**NTNU**
Norwegian University of
Science and Technology

# Internal Blast Loading of Submerged Floating Tunnels in Concrete

## Erika Krone

**Department of Structural Engineering**
Faculty of Engineering Science and Technology
**NTNU- Norwegian University of Science and Technology**

# MASTER THESIS 2018

| SUBJECT AREA: Computational Mechanics | DATE: June 11, 2018 | NO. OF PAGES: 11 + 151 + 13 |
|---|---|---|

TITLE:

### Internal Blast Loading of Submerged Floating Tunnels in Concrete

Indre eksplosjonslast i rørtunellbru i betong

BY:

Erika Krone

SUMMARY:

A submerged floating tunnel (SFT) has been proposed for crossing the fjords which today are operated by ferries along the Norwegian highway E39. One concern with a potential SFT, which probably would be built using reinforced concrete, is if an explosion is to go off inside it, either accidentally or intentionally. Since full-scale experimental testing is out of the question, one must resort to numerical analyses and component tests.

Uniaxial compression tests were performed for concrete cubes and digital image correlation (DIC) analyses of the tests provided satisfactory results. The tests were then simulated using both the concrete damaged plasticity (CDP) model in ABAQUS and the Karagozian & Case (K&C) model in LS-DYNA and both were found to provide adequate results. The CDP parameters were obtained by scaling previous results and the model displayed pathological mesh dependency. The K&C model proved simpler to use as the only necessary input was the concrete strength. However, for LS-DYNA it was found that an unnaturally low friction coefficient was needed and that the model displayed unphysical post-peak behavior.

Concrete pipes were subjected to blast loads by using C4 charges. The charge placement clearly affected the failure and the effects of confinement and scaled distance were evident. Increasing the wall thickness and adding reinforcement proved to be effective design measures with regard to blasts. For both ABAQUS and LS-DYNA, Lagrangian analyses overpredicted the damage, despite underestimating the blast. Eulerian analyses of the blast were performed in ABAQUS but underestimated the pressure. Lastly, coupled Eulerian-Lagrangian (CEL) analyses were performed in ABAQUS, but the analyses eventually stagnated, there was pressure leakage, the pressure-time curves fluctuated excessively, the pressure was underestimated, and the damage of the pipe was overpredicted. For both the Eulerian and CEL analyses deciding on a proper time step scaling factor proved challenging.

Furthermore, methods of incorporating stochastic behavior for concrete were investigated for simulating both the compression and blast tests. For the pipes, these methods reduced the amount of damage.

RESPONSIBLE  TEACHER: Professor Tore Børvik

SUPERVISOR(S): Professor Tore Børvik and postdoc Martin Kristoffersen

CARRIED OUT AT: SIMLAB, Department of Structural Engineering, NTNU

# MASTEROPPGAVE 2018

TITTEL:

**Indre eksplosjonslast i rørtunellbru i betong**

Internal Blast Loading of Submerged Floating Tunnels in Concrete

UTFØRT AV:

Erika Krone

SAMMENDRAG:

En rørtunellbru har blitt foreslått som en mulig løsning for flere av fjordkrysningene i prosjekt 'Ferjefri E39'. En utfordring med en slik potensiell rørtunellbru er dersom den, enten ved et uhell eller med vilje, utsettes for en eksplosjon. I og med at fullskala forsøk er uaktuelt, må man ty til numeriske analyser og komponenttester.

Enaksielle trykktester ble utført for betongkuber og DIC-analyser av testene ga tilfredsstillende resultater. Testene ble dermed simulert både ved bruk av CDP betongmodellen i ABAQUS og K&C betongmodellen i LS-DYNA, hvorav begge modellene ga akseptable resultater. Ved å skalere tidligere resultater ble CDP-parameterne bestemt, men CDP-modellen viste klar meshavhengighet. K&C-modellen var enklere å benytte i og med at betongstyrken var neste påkrevde inndata. Det viste seg imidlertid at en unaturlig lav friksjonskoeffisient var nødvendig i LS-DYNA og at modellen viste ufysisk residualoppførsel.

Betongrør ble utsatt for eksplosjonslaster ved bruk av C4-ladninger. Ladningens plassering hadde åpenbar innvirkning på bruddmekanismen og effektene av avgrensning og skalert avstand var også tydelige. Å øke veggtykkelsen og armere betongen viste seg å være effektive dimensjoneringstiltak med tanke på eksplosjonslast. Lagrangeanalyser overestimerte skaden i både ABAQUS og LS-DYNA, til tross for at eksplosjonstrykket ble underestimert. Euleranalyser av eksplosjonen ble gjennomført i ABAQUS, men også disse undervurderte trykket. Til slutt ble koblede Euler-Lagrangeanalyser gjennomført i ABAQUS, men analysene stagnerte etterhvert, det var trykklekkasje, trykkurvene oscillerte, trykket ble undervurdert og rørets skade ble overvurdert. Å definere en passende tidsstegskaleringsfaktor viste seg dessuten å være utfordrende for både Euler- og de koblede analysene.

Videre ble metoder for implementering av stokastisk variasjon i numerisk modellering av betong undersøkt, både for trykk- og eksplosjonsforsøkene. Ved bruk av disse metodene ble skaden av rørene redusert.

**Department of Structural Engineering**
FACULTY OF ENGINEERING SCIENCE
NTNU – Norwegian University of Science and Technology

# MASTER'S THESIS 2018

for

*Erika Krone*

# Internal blast loading of submerged floating tunnels in concrete

## 1. INTRODUCTION

The Norwegian Public Roads Administration is conducting a large research project aimed at replacing the ferry connections along the E39 coastal highway route along the west coast of Norway with fixed connections. For the wide and deep fjords, a submerged floating tunnel (SFT) made of concrete has been suggested as an alternative. Reinforced concrete allows more or less any cross-sectional profile to be cast, and the buoyancy can easily be adjusted to the desired level. A potential hazard for such a structure is internal blast loading caused either by an accident or by a terrorist attack. It is important to verify that the structure is able to withstand a realistic blast load, or at least minimise the damage as a breach could have disastrous consequences. To assess the blast performance of concrete structures, plane concrete slabs and off-the-shelf precast concrete tubes have been subjected to blast loading. In addition, numerical simulations of these tests have been carried out. In this master's thesis, blast experiments using live explosives will be performed in collaboration with the Norwegian Defence Estates Agency. The data generated will be used for validation and verification of some frequently used numerical methods involving blast loading. Computational methods are now available to predict both the loading and structural response in these extreme loading situations, and experimental validation of such methods is necessary in the development of safe and cost-effective structures. In addition to simulating the experiments, full-scale simulations of an SFT is a viable goal.

## 2. OBJECTIVES

The main objective of the research project is to determine how concrete tubes behave under blast loading, and to validate to which extent this can be predicted using computational tools.

## 3. A SHORT DESCRIPTION OF THE RESEARCH PROJECT

The main topics in the research project will be as follows:

1. A comprehensive literature review should be conducted to understand the blast load phenomenon, blast load design, constitutive and failure modelling of concrete materials exposed to extreme loadings, explicit finite element methods, and possibly fluid-structure interaction.
2. Instrumented material testing of concrete cubes for validation of material models.
3. Proper constitutive relations and failure criteria are chosen and calibrated based on the material tests.
4. Experimental work on concrete tube components: Precast concrete tubes will be subjected to blast load from a C-4 charge. Three main charge positions will be used – centrically in the cross-section, and in contact with the concrete on both the outside and the inside.
5. Nonlinear finite element simulations of the field experiments will be performed, and the numerical results shall be compared and discussed based on the experimental findings.

*Supervisors:*    Tore Børvik (NTNU) and Martin Kristoffersen (NTNU)

The thesis must be written according to current requirements and submitted to the Department of Structural Engineering, NTNU, no later than June 11th, 2018.

NTNU, January 15th, 2018

Tore Børvik
Professor

# Acknowledgements

*Trondheim, June 11, 2018*

Erika Krone

# Abstract

A submerged floating tunnel (SFT) has been proposed for crossing the fjords which today are operated by ferries along the Norwegian highway E39. One concern with a potential SFT, which probably would be built using reinforced concrete, is if an explosion is to go off inside it, either accidentally or intentionally. Since full-scale experimental testing is out of the question, one must resort to numerical analyses and component tests.

Uniaxial compression tests were performed for concrete cubes and digital image correlation (DIC) analyses of the tests provided satisfactory results. The tests were then simulated using both the concrete damaged plasticity (CDP) model in ABAQUS and the Karagozian & Case (K&C) model in LS-DYNA and both were found to provide adequate results. The CDP parameters were obtained by scaling previous results and the model displayed pathological mesh dependency. The K&C model proved simpler to use as the only necessary input was the concrete strength. However, for LS-DYNA it was found that an unnaturally low friction coefficient was needed and that the model displayed unphysical post-peak behavior.

Concrete pipes were subjected to blast loads by using C4 charges. The charge placement clearly affected the failure and the effects of confinement and scaled distance were evident. Increasing the wall thickness and adding reinforcement proved to be effective design measures with regard to blasts. For both ABAQUS and LS-DYNA, Lagrangian analyses overpredicted the damage, despite underestimating the blast. Eulerian analyses of the blast were performed in ABAQUS but underestimated the pressure. Lastly, coupled Eulerian-Lagrangian (CEL) analyses were performed in ABAQUS, but the analyses eventually stagnated, there was pressure leakage, the pressure-time curves fluctuated excessively, the pressure was underestimated, and the damage of the pipe was overpredicted. For both the Eulerian and CEL analyses deciding on a proper time step scaling factor proved challenging.

Furthermore, methods of incorporating stochastic behavior for concrete were investigated for simulating both the compression and blast tests. For the pipes, these methods reduced the amount of damage.

# Contents

# Nomenclature

## Abbreviations

| | |
|---|---|
| ALE | Arbitrary Lagrangian-Eulerian |
| B$x$ | Concrete with uniaxial cylinder compressive strength of $x$ MPa after 28 days |
| BLEVE | Boiling liquid expanding vapor explosion |
| C$x/y$ | Concrete with uniaxial cylinder and cube compressive strengths of $x$ and $y$ MPa after 28 days |
| C3D8R | Solid brick element with eight nodes, reduced integration, and hourglass control |
| C4 | Plastic explosive composition C4 |
| CDP | Concrete damaged plasticity |
| CEL | Coupled Eulerian-Lagrangian |
| CFD | Computational fluid dynamics |
| ConWep | Conventional weapons |
| CPU | Central processing unit |
| CSD | Computational structural dynamics |
| DIC | Digital image correlation |
| DOF | Degree of freedom |
| DPDC | Dynamic plastic damage concrete |
| EC3D8R | Eulerian brick element with eight nodes, reduced integration, and hourglass control |
| EOS | Equation of state |
| EVF | Eulerian volume fraction |
| fc | Friction coefficient |
| FE | Finite element |
| FEMA | Federal Emergency Management Agency |

| | |
|---|---|
| FRC | Fiber-reinforced concrete |
| FRP | Fiber-reinforced polymer |
| FSI | Fluid-structure interaction |
| HE | High explosives |
| HJC | Holmquist-Johnson-Cook |
| JWL | Jones–Wilkins–Lee |
| K&C | Karagozian & Case |
| MRES | Modified random element strength |
| MS | Mesoscale |
| NDEA | Norwegian Defence Estates Agency |
| NPRA | Norwegian Public Roads Administration |
| NTNU | Norwegian University of Science and Technology |
| P-I | Pressure-impulse |
| PBIED | Personnel-borne improvised explosive device |
| RES | Random element strength |
| SFT | Submerged floating tunnel |
| SIMLab | Structural Impact Laboratory |
| Std | Standard deviation |
| TNT | Trinitrotoluene |
| TSF | Time step scaling factor |
| UHPC | Ultra-high performance concrete |
| VBIED | Vehicle-borne improvised explosive device |
| w/c ratio | Water-cement ratio |

# Greek Letters

| | |
|---|---|
| $\alpha$ | Incident angle of blast wave |
| $\chi$ | Scaling factor of explosion |
| $\Delta t$ | Time increment |
| $\Delta t_{cr}$ | Stable/critical time increment |
| $\Delta \sigma$ | Failure surface for deviatoric stress |
| $\Delta \sigma_m$ | Failure surface for maximum stress |
| $\Delta \sigma_r$ | Failure surface for residual stress |
| $\Delta \sigma_y$ | Failure surface for yield stress |
| $\eta$ | K&C scaling factor for $\Delta \sigma$ |
| $\gamma$ | JWL parameter |
| $\lambda$ | K&C damage function |
| $\omega$ | Natural frequency |
| $\rho_0$ | Density of explosive |
| $\sigma$ | Stress |
| $\varepsilon$ | Strain |
| $\varepsilon^e$ | Elastic strain |
| $\varepsilon^p$ | Plastic strain |
| $d\bar{\varepsilon}^p$ | Effective plastic strain increment |
| $\bar{\varepsilon}^e$ | Elastic strain with stiffness degradation |
| $\bar{\varepsilon}^p$ | Plastic strain with stiffness degradation |

# Roman Letters

| | |
|---|---|
| $A$ | JWL parameter |
| $a_0$, $a_1$, $a_2$ | K&C material parameters for $\Delta\sigma_m$ |
| $a_{f1}$, $a_{f2}$ | K&C material parameter for $\Delta\sigma_r$ |
| $a_{y0}$, $a_{y1}$, $a_{y2}$ | K&C material parameter for $\Delta\sigma_y$ |
| $B$ | JWL parameter |
| $b$ | Decay coefficient of Friedlander equation |
| $b_1$ | K&C damage scaling parameter which determines damage rate for uniaxial tension |
| $b_2$ | K&C damage scaling parameter which determines damage rate for uniaxial compression |
| $c$ | Speed of sound moving though a medium |
| $c_d$ | Dilatational wave speed |
| $d$ | CDP damage variable |
| $E$ | Elasticity/Young's modulus |
| $E_D$ | Detonation energy density |
| $f_c$ | Compressive strength |
| $f_t$ | Tensile strength |
| $f_{c,m}$ | Matrix compressive strength |
| $f_{c,p}$ | Particle compressive strength |
| $i$ | Increment number |
| $i_{r+}$ | Specific impulse |
| $L^e$ | Characteristic length of the smallest element in a finite element model |
| $M$ | Mach number |
| $P$ | Pressure |
| $P_a$ | Ambient pressure |
| $P_r$ | Peak reflected pressure |
| $P_{so}$ | Peak incident pressure |
| $R$ | Stand-off distance of explosion |
| $R_1$,$R_2$ | JWL parameters |
| $r_f$ | K&C dynamic increase factor which accounts for strain rate effects |
| $t$ | Time |
| $t_+$ | Duration of positive phase |

| | |
|---|---|
| $t_-$ | Duration of negative phase |
| $t_d$ | Load duration |
| $U$ | Heat of explosion |
| $u$ | Translational or rotational degree of freedom |
| $V$ | Ratio of volume of detonation products to volume of undetonated HE |
| $v$ | Speed of an object moving through a medium |
| $v_D$ | Detonation wave speed |
| $W$ | Weight of explosive |
| $Z$ | Scaled distance of explosion |
| $\mathbb{M}$ | Mass matrix |
| $\mathbb{R}^{ext}$ | Applied load vector |
| $\mathbb{R}^{int}$ | Internal load vector |

# Chapter 1

# Introduction

Safety is always the number one concern in structural design. This is also the case when the Norwegian Public Roads Administration (NPRA) plans to massively overhaul the Norwegian west coast highway. The project is commonly referred to as 'Ferry-Free E39' due to its intent of ridding the highway of its many ferry-crossings. By doing so the travel time between Kristiansand and Trondheim could be reduced by up to 40 %. However, as the fjords along the route are both deep and wide, replacing the ferries will require pioneering technology. One solution that has been proposed for several of the crossings, but has never before been built, is a submerged floating tunnel (SFT) which combines the concept of a bridge and a tunnel.

One major safety concern for a potential SFT is internal blast loading, either accidentally or intentionally. Although the probability of such an occurrence is rather low, the consequences could worst case be tremendous. Since it is practically impossible to remove the risk completely, it is essential to limit the potential damage.

Due to reinforced concrete's low cost and high versatility, it will most likely be the preferable choice of material if an SFT is to be built. Even though reinforced concrete is one of the most used construction materials, it can be a challenge to model numerically. And even if the use of numerical simulations is extensive, it is also increasing. For in addition to possibly being both cost and time saving, as well as providing more flexibility in the design phase, numerical analyses can be crucial when experimental tests are impractical, as they are for blast loads in SFTs for instance.

This thesis will look closer into the concepts of SFTs, concrete, blast loads, and numerical simulations. The behavior of concrete will then be investigated both experimentally using digital image correlation (DIC), and numerically. These results will then be used to assess numerical simulations of tubular concrete structures subjected to blast loads, which will be compared to experimental tests.

# Chapter 2

# State of the Art

Since the topic of submerged floating tunnels (SFT) subjected to blast loads is rather complex, it is useful to first obtain an overview of previously conducted work related to the topic.

Digital image correlation (DIC) is a useful tool for engineering purposes and it has previously also been used for concrete. Several studies have been published on the topic of DIC for three-point bending of concrete beams. For example Skarzynski et al. focused on notched concrete beams [1], Skarzynski and Tejchman looked at various concrete mixes for both plain and reinforced beams, and Fayyad and Lees also examined reinforced beams [2]. In addition, Fagerholt et al. [3] have evaluated DIC for analyses of metal specimens with large deformations and a single propagating crack, which perhaps could be applicable to concrete as well since it cracks in tension. However, for this thesis it is intended to use DIC for concrete compression tests, and there does not seem to be any available research on this exact topic.

Furthermore, concrete will be modeled in ABAQUS using the concrete damaged plasticity (CDP) model. Since the CDP model requires numerous input parameters, there has already been considerable research on the identification and calibration of these parameters. Sümer and Aktas [4], Michal and Anfdrezej [5], and Nikaido et al. [6] are just some of those who have investigated this topic, along with Jankowiak and Lodygowski whose results will be used in this thesis. Since the CDP model is intended to be an all-round model, it has been used to simulate a range of different problems. Chaudhari and Chakrabarti used CDP for uniaxial compression tests [7], Birtel and Mark used it for shear failure in reinforced concrete beams [8], and Wahalathantri et al. used it for flexural crack simulation in reinforced concrete [9]. The CDP model has also been used to model more specific problems such as partial-depth precast prestressed concrete bridge decks under increasing static loading (Ren et al. [10]), cracking development prediction in concrete gravity dams (Zappitellia et al. [11]), concrete-to-fiber-reinforced polymer (FRP) bond behavior (Tao and Chen [12]), and soft missile impact (Kawamoto and Stepan [13] and Martin [14]).

The concrete will also be modeled using the K&C model developed by Malvar et al. [15] for LS-DYNA. Various verification and calibration studies have been performed for the

model by e.g. Markovich et al. [16], Brannon and Leelavanichkul [17], Wu and Crawford [18], and Xu and Willie [19]. This concrete model has as well been used to model a diversity of problems, including blasts (Shukla et al. [20]), projectile impact (Kong et al. [21] and Kim et al. [22]), ultra-high performance concrete (UHPC) (Wu et al. [23] and Hor et al. [24]), and FRP-to-concrete bond behaviour (Li et al. [25]).

Mesoscale modeling is when one in numerical models distinguish between the particles and matrix of concrete. It is a relatively recent topic which has received quite a lot of attention. Mesoscale modelling has a broad field of application such as fracture in uniaxial tension (Grassl and Jirasek [26]), tensile failure at high strain rates (Zhou and Hao [27]), FRP-to-concrete bond behaviour (Li et al. [25]), chloride diffusion in cracks (Wang and Ueda [28]), fibre reinforced concrete under compressive impact loading (Xu et al. [29]), and contact detonations [30], just to mention a few.

Since concrete is one of the most used construction materials, also in protective structures, there has been extensive research conducted on concrete subjected to blast loads. Blast loading has for instance been investigated for structural concrete elements such as walls and panels (Tiwari et al. [31], Mays et al. [32], Ngo et al. [33], Lok and Xiao [34], Lin et al. [35], and Tabatabaei et al. [36]), slabs (Zhou et al. [30] and Wang et al. [37]), columns (Kravchenko et al. [38]), plates (Xu and Lu [39]), and bridge decks (Foglar and Kovar [40]). The list of research on concrete subjected to blast loading is nearly endless. However, the work of Tiwari et al. is especially relevant for this thesis as they used coupled Eulerian-Lagrangian (CEL) analyses, in combination with John-Wilkins-Lee (JWL) equation of state, to model reinforced concrete tunnels in soil subjected to internal blast loads in ABAQUS [41].

Postdoc Martin Kristoffersen at the Norwegian University of Science and Technology (NTNU) has been one of the supervisors for this thesis. His field of research is submerged floating tunnels subjected to internal blast loading. This thesis is therefore closely linked to his work on the topic [42, 43, 44, 45, 46]. The experimental testing of concrete pipes subjected to blast loading conducted for this thesis, is a continuation of tests previously performed by Kristoffersen [42, 43]. The results from these previous tests will therefore be included and discussed in this thesis.

This master's thesis is not the first on the topic of internal blast loading in concrete SFTs. In 2015 Haug and Osnes [47] wrote their master's thesis on the same subject, and so did Hillestad and Pettersen in 2016 [48]. Both theses were carried out for the Structural Impact Laboratory (SIMLab) at the Department of Structural Engineering at NTNU and form a basis for this thesis. However, the theses from 2015 and 2016 had slightly different focuses and thereby also approaches and areas of study. Short summaries of the theses are presented below, along with their key findings and suggestions for further work.

### Master's Thesis of Haug and Osnes (2015)

The master thesis by Haug and Osnes from 2015 [47] was an initial study on numerical simulation of plain concrete plates subjected to blast loading.

Haug and Osnes first performed tests on fresh B45 concrete from which they cast cubes, cylinders, and plates for further testing. They then performed compression tests of the cubes after the concrete had cured for 28 and 40 days and of the cylinders after 28 days of curing. From these tests, Young's modulus was calculated to be 40.9 GPa. The actual

cylinder compression strength of the B45 concrete was measured to be 55 MPa. For the cylinders, tensile splitting tests were also performed. From these tests, the tensile strength was found to be approximately 4 MPa.

Before experimentally subjecting concrete plates to blast loading in a shock tube, preliminary analytic and numerical studies were carried out. This was done to get an impression of expected results, in addition to determining the pressures and configuration of the experimental setup. Furthermore, a steel plate with sensors was tested in the shock tube in order to calibrate the shock tube. Five 50 mm thick unreinforced concrete plates were then subjected to various pressures in the shock tube and the results are summarized in Table 2.1 below.

**Table 2.1:** Summary of results from testing of concrete plates subjected to blast loading by Haug and Osnes.

| Plate number | Peak pressure (MPa) | Comment | Damage |
|---|---|---|---|
| 1 | 7.40 | | Minimal, only small surface cracks |
| 2 | $\sim$7, 11.99, $\sim$12 | The plate was subjected to three blast loads | Minimal, only small surface cracks |
| 3 | 6.62 | The plate was perforated by four bullets before testing | None |
| 4 | $\sim$22.5 | The pressure profile did not resemble a Friedlander curve | Complete failure |
| 5 | 18.78 | | Large cracks resembling bending failure |

For further experimental work, the thesis has several suggestions. Firstly, Haug and Osnes suggest repeating the conducted tests in order to study variations in the results. Secondly, they propose studying the effect of varying the thickness of the plates and the strength of the concrete, in addition to including reinforcement. Furthermore, it is suggested using a less rigid clamping plate to vary the boundary conditions. The thesis also proposes possibly using other bases for comparison in the experiments, e.g. displacement or launch velocity of broken material.

After the experiments in the shock tube, Haug and Osnes attempted to simulate the tests numerically. This was done using both the Holmquist-Johnson-Cook (HJC) concrete model in IMPETUS Afea Solver and the Karagozian & Case (K&C) concrete model in LS-DYNA. The main focus was on the HJC model and it was found that it provided a too ductile behavior which overestimated the capacity, despite immense tuning. The K&C model, on the other hand, provided reasonable results even with no tuning. In addition, Haug and Osnes used the Dynamic Plastic Damage Concrete (DPDC) model in Europlexus in order to simulate the fluid-structure interaction (FSI) of the experiment. From this they concluded that FSI analyses were redundant if there were no through-thickness cracks.

Haug and Osnes concluded that there is still work to be done on concrete models as they

are not as mature as for e.g. metals. For further work, they amongst other suggested to introductory simulate the material tests, e.g. the compression tests. This in order to evaluate possible material models based on less complex tests than the blast tests. They also suggest using more exact numerical models that include e.g. shear reinforcement, bolts, and bolt holes. Furthermore, they suggest investigating the effect of varying the boundary conditions and plate thickness in the numerical model. Haug and Osnes also propose including statistical distribution and initial damage in the numerical model. Lastly, they advise to numerically simulate part of an SFT using correct dimensions.

### Master Thesis of Hillestad and Pettersen (2016)

The master thesis of Hillestad and Pettersen from 2016 [48] was a direct continuation of the work from the previous year by Haug and Osnes. They chose to follow the recommendations for further work suggested in the thesis from 2015, and their focus was therefore on incorporating the stochastic behavior of concrete in numerical simulations of plain and reinforced concrete plates subjected to blast loading.

First, Hillestad and Pettersen performed tests on fresh B45 concrete from which they cast cubes, cylinders, beams, and plates for further testing. They then performed compression tests on the cubes after 2, 7, 14, 28, 49, and 84 days of curing. This was done in order to study the concrete strength as a function of time and thereby account for this in subsequent simulations of concrete plates subjected to blast loading. After 28 days of curing, 20 cube compression tests were performed. This was done such that the stochastic concrete behavior could be studied. In addition, after 28 days, cylinder compression tests were also performed. To determine the tensile strength of the concrete, both tensile splitting and three-point bending tests were carried out. The results of the concrete tests can be seen in Table 2.3. Since reinforcement steel was cast into some of the concrete plates, pieces of the rebar steel were tested in uniaxial tension to determine its yield strength and fracture strain, see Table 2.2.

**Table 2.2:** Results of rebar testing performed by Hillestad and Pettersen.

| Test type | Number of tests | Yield strength (MPa) | Fracture strain (-) |
|---|---|---|---|
| Uniaxial tension | 14 | 794 | 0.8796±0.041 |

**Table 2.3:** Results of concrete testing performed by Hillestad and Pettersen.

| Test type | Number of tests | Strength (MPa) | Standard deviation (MPa) |
|---|---|---|---|
| Cube compression | 20 | 46.35 | 0.73 |
| Cylinder compression | 5 | 39.62 | 0.75 |
| Tensile splitting | 5 | 3.50 | 0.34 |
| Three-point bending | 3 | 6.74 | - |

The concrete tests were then modeled numerically in ABAQUS using the concrete damaged plasticity (CDP) model, and in LS-DYNA using the K&C model. For the CDP

model, material parameters from literature were tuned to correspond with the experimental tests, while the K&C model did not require tuning. Both the CDP and the K&C models were able to capture the confinement effect in the cube compression test. Both material models also provided higher tensile strength for the bending test than the tensile splitting test. However, the CDP model represented the post-peak, load-softening behavior better.

Next, two methods were developed to describe the stochastic behavior of concrete. The first such method was the random element strength method which assigned normally distributed random strength to each element in a finite element method. It was found that the relationship between the element strength distribution and the cube strength distribution, was not straightforward. The method also had to be calibrated for each mesh size and when the element strength distribution was kept constant, finer meshes provided narrower cube strength distributions. The second stochastic method was a mesoscale method which divided the mesh into aggregates and cement. This method was able to recreate the cube strength distribution from the experiments, as well as produce intricate and reasonable crack patterns.

For further work on material testing, Hillestad and Pettersen recommend obtaining stress-strain curves from the compression test in order to procure a better basis of comparison for numerical simulation of concrete. Further, they suggest testing cubes of various sizes for the purpose of advanced studies of concrete's stochastic behavior.

Furthermore, shock tube experiments were carried out. Four plates were subjected to blast pressures. Two of the plates were plain, while two were reinforced. Digital image correlation (DIC) was used to measure the deformation of the plates during testing. None of the plates experienced collapse or through-thickness cracking. A summary of the results from the shock tube testing is provided in Table 2.4.

**Table 2.4:** Summary of results from testing of concrete plates subjected to blast loading by Hillestad and Pettersen.

| Test ID | Reinforcement | Peak pressure (bar) | Damage |
|---|---|---|---|
| P-41 | X | 12.05 | Surface cracks. Small piece detached from the back center |
| R-41 | ✓ | 12.27 | Surface cracks |
| P-77 | X | 16.55 | Surface cracks. More cracks on the back. Continuous crack along the bolt holes in the front |
| R-77 | ✓ | 17.27 | Surface cracks. Less cracks on the back. More cracks in the front |

Hillestad and Pettersen suggest performing more shock tube experiments since by testing several plates at the same pressure, as well as at a wider range of pressures, a better basis for comparison with numerical simulations, is obtained. They also suggest using a laser to measure the midpoint deflection of the plate during testing for verification of the DIC measurements. To eliminate uncertainties, they also recommend measuring the

pre-tension in the bolts and the displacement of the shock tube.

Using the same codes and material models as for the simulation of the material tests, also the shock tube experiments were simulated numerically. Both ABAQUS and LS-DYNA provided reasonable results although for both codes the extent of cracking was exaggerated but still in overall good agreement with the experiments. Both codes were also able to capture the difference in crack pattern due to the reinforcement. However, the simulated displacement histories were not in perfect correlation with the experiments, though it was better for low pressures. LS-DYNA proved to be most accurate for the plain plates, while ABAQUS was best for the reinforced plates. The ultimate load capacity predicted by ABAQUS was in good agreement with analytical and elastic calculations, while LS-DYNA predicted it to be a little high. However, the collapse pressure predicted by LS-DYNA was more realistic than that of ABAQUS. Furthermore, the plate response in ABAQUS responded well with theory when altering the blast load impulse, when LS-DYNA did not. Both codes had significant fractions of hourglass energy, despite attempting different hourglass control formulations in LS-DYNA. Hillestad and Pettersen further implemented a strain based erosion criteria in ABAQUS. This made it easier to assess the inflicted damage, but at the same time it reduced the plate capacity. In addition, a strain rate dependent material formulation was implemented in LS-DYNA which overestimated the plate capacity. The random element strength method was also examined. This method gave little change in displacement, but more erratic and realistic crack patterns. The mesoscale modeling overestimated the damage which indicates that there is still work that needs to be done on the tensile properties of the method.

For further work on numerical simulations, Hillestad and Pettersen suggest studying more sophisticated approaches for the random element strength method as it currently needs to be calibrated for each mesh. This, they propose, can be done by for example imposing probability field on the mesh instead of distributing element strength randomly. For the mesoscale method, they suggest calibrating it to the material tests and testing different material models for the aggregate and cement. Hillestad and Pettersen also recommend looking into the implementation of stochastic variation of aggregate strength. Further, they put forward the idea of testing the mesoscale model also in ABAQUS. Since including an element erosion criteria in the numerical simulations gave excessive damage, Hillestad and Pettersen suggest examining a more sophisticated criteria with multiple parameters. Another suggestion is to run fluid-structure interaction analyses as this would simulate a more realistic blast load and could therefore influence the collapse sequence if element erosion is enabled. The last recommendation regarding numerical simulation is to examine the effect of including the shear rebar in the numerical simulations.

For further work on blast loading on submerged floating tunnels (SFT), Hillestad and Pettersen suggest carrying out experiments with contact charges. This could cause more damage and material models for such a case should therefore be investigated. Another suggestion is to perform scaled experiments with blast loading on concrete tubes as this would provide a more realistic scenario with regard to an SFT.

# Chapter 3

# Underlying Theory

## 3.1 Ferry-Free E39

Today it takes 21-22 hours to drive on highway E39 along the western coast of Norway from Kristiansand to Trondheim, see Figure 3.1, a route which is approximately 1100 km long [49]. The main reason for the excessive travel time is the eight ferry crossings. By making route E39 ferry-free, in addition to improving the pre-existing roads, the Norwegian Public Roads Administration (NPRA) hopes to reduce the travel time by 7-9 hours [49]. If all goes according to plan, project ferry-free E39 is estimated to cost 340 billion NOK, that is approximately 43.2 billion USD [50].

Many of the fjords whose crossings today are operated by ferries, are both deep and wide, making alternative ways of crossing challenging. The fjord considered to be the most difficult to cross is the Sognefjord which is about 4 km wide and up to 1300 m deep, with 200-300 m of bottom deposits above the rock [49]. In comparison, the longest existing suspension bridge



**Figure 3.1:** Highway E39 from Kristiansand to Trondheim. *Credit:* NPRA.

is the Akashi Strait Bridge in Japan which has a main span of 1991 m [51], while the longest floating bridge is the SR 520 bridge in Washington State with its 2350 m [52]. Proposed solutions for crossing the Sognefjord include a suspension bridge on fixed foundations with a 3700 m long main span, a multi-span cable-stayed or suspension bridge on floating foundations with 700-800 m long spans, and a traditional floating bridge [53]. A combination of two or more of the different options is also a possibility. However, another pioneering option is the never before built concept of a submerged floating tunnel (SFT). One way or another, innovative engineering is thus necessary in order to realize the ferry-free E39 project.

## 3.2 Submerged Floating Tunnels

A submerged floating tunnel combines the principles of a bridge and a tunnel as it is a tunnel that floats in the water. It is also called an Archimedes bridge as it based on Archimedes' principle of buoyancy, stating that if the weight of an object submerged in water is less than the weight of the water suppressed by that object, the object will float [54]. Therefore, by adjusting the mass of the tunnel, and thereby also its buoyancy, the means of anchoring the SFT can be decided. By decreasing the mass of the SFT, the buoyancy increases and the SFT has to be anchored to the foundation by tension legs, also often referred to as tethers or mooring cables. On the other hand, by increasing the SFT mass, the buoyancy decreases, and the SFT must be anchored to the foundation by column supports or to pontoons on the water surface. For short spans and modest loading, the SFT can be unanchored, only with connections to land [55]. Figure 3.2 illustrates the different methods of anchoring an SFT.



**(a)** Tethers      **(b)** Column support      **(c)** Pontoons      **(d)** No anchoring
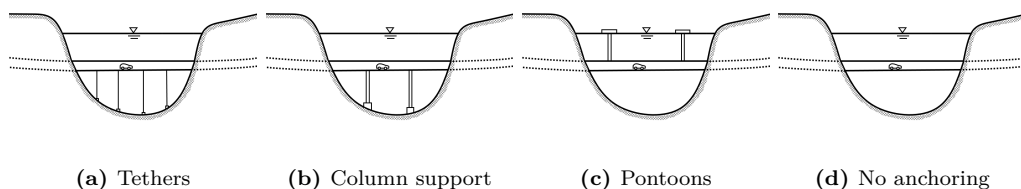
**Figure 3.2:** Different methods of anchoring an SFT.

For the ferry-free E39 project, the two most viable anchoring options are tethers and pontoons. An illustration of what these anchoring methods could look like in reality is shown in Figure 3.3. A simple way of providing horizontal stiffness for a tether anchored SFT is to incline the tethers. For a pontoon anchored SFT, horizontal anchors may be utilized, or the SFT may be formed as a horizontal arch with two connected parallel tubes [56], see Figure 3.4. Using two connected tubes is also convenient as it provides a good opportunity for evacuation in the case of an emergency. A combination of methods for horizontal stiffening can also be used.

The main advantage with an SFT is that it can be used for crossings where traditional options such as bridges and subsea tunnels prove difficult, or even impossible, to build. The wide and deep fjords along route E39 are examples of such crossings. The topography of the crossing will also affect the anchoring of an SFT. While tethers have many advantages that are to be further discussed, both tethers and column supports can become challenging and thus costly if the crossing is very deep. Besides, they are dependent on the soil conditions as they are anchored to the foundation. This also makes them vulnerable to landslides. The length of the tethers should be adjustable to compensate for possible settlements in the foundation [56]. For the Bjørnafjord along route E39, geologists have therefore been studying the ground conditions in order to help decide which mean of crossing is most suitable [57]. Because of the extreme depth of the Sognefjord, pontoon anchoring is the favorable concept [58].

Another significant advantage with an SFT is that it is less visible in the scenery. If another anchoring method than pontoons is utilized, the SFT will even be invisible above the water surface. Additionally, an SFT will shield its surroundings from both traffic noise and dust.
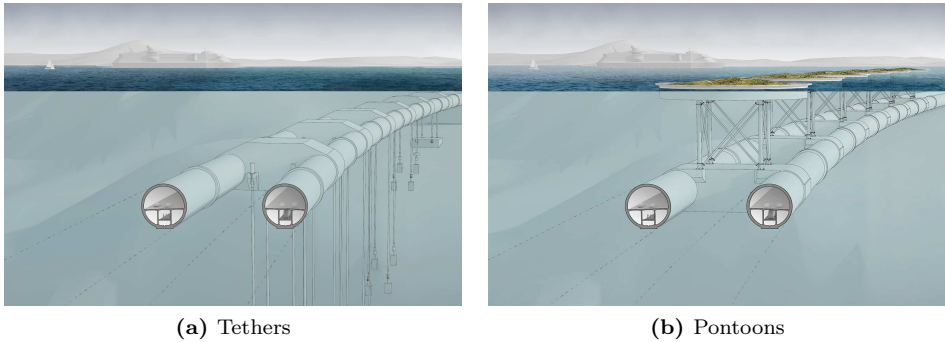


**(a)** Tethers

**(b)** Pontoons

**Figure 3.3:** Illustration of how a tether or pontoon anchored SFT may look. *Credit:* Snøhetta.

The cross-section of an SFT tunnel, also often referred to as the tube, can basically be any geometric shape. Yet, when designing the SFT cross-section, traffic, evacuation, ventilation, ballast, inspection, maintenance, and repair work, should be taken into account. However, due to hydrodynamic considerations a circular cross-section such as the one shown in Figure 3.3, is often preferred [56].

An additional benefit with an SFT is that it can be constructed at a dry dock at a secondary location. The SFT may be constructed in sections or as a whole, before it is towed to the actual site where it is joined together and ballasted to the desired depth [59]. Since there is no experience with SFTs yet, measures should be taken in order to strive for optimal usage of the structure throughout its whole life. One such measure should be to design for the possibility to repair or replace parts of the structure with shorter service life, such as the anchoring system and movable joints. Another such measure is to design the structure in a way that, if necessary, improvements are possible to implement [56]. In addition, the SFT should be robust against changes that may occur over time such as corrosion, or variation in the static system and material properties [56]. As for all structures, an SFT has a limited service life and will have to be demolished sooner or later and this should also be kept in mind during the design stage. Since the SFT is a floating structure, it may easily be towed away in sections to be reused or recycled [59].
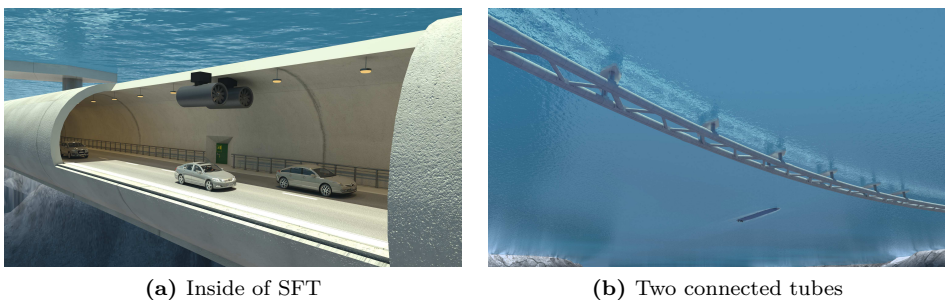


**(a)** Inside of SFT

**(b)** Two connected tubes

**Figure 3.4:** Suggested design of an SFT. *Credit:* NPRA/Vianova.

Another major convenience with SFTs is that they permit ships to pass easily, in contrast to a bridge which would possibly need a deck height of up to 90 m [60]. Nonetheless, this requires the SFT to be submerged deep enough to allow ships to pass overhead, that is some 30 m below the surface [61]. Furthermore, by constructing the SFT sufficiently deep in the water, the structure is less subjected to weather. It is, however, undesirable to place the tunnel so deep that the high hydrostatic pressure needs to be dealt with.
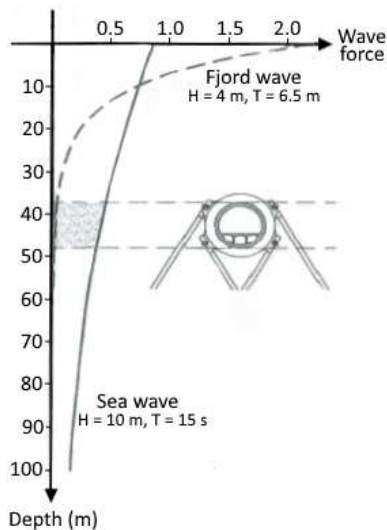


**Figure 3.5:** Force of typical wind and sea waves as a function of water depth. *Credit:* Jakobsen [56].

A potential SFT would be subjected to various dynamic loads, one of which is waves. There are several origins for waves and for a fjord like the Sognefjord one would have to account for wind waves, sea waves, and internal waves. While waves caused by wind in the fjord are rather superficial with a force quickly decaying with water depth, waves coming in from the sea have larger wave heights and periods and are therefore forceful also at greater depths, see Figure 3.5. Another source of waves in a fjord is the layering of water due to salinity varieties. A fjord with a significant supply of fresh water may be susceptible to such a phenomenon which is called internal or secondary waves. An SFT would also be exposed to current, which may cause vortex induced vibration.

Other dynamic loads include those due to earthquakes. Earthquakes could impose loads on an SFT both by ground transmission and pressure waves in the water, so-called seaquakes. Another possible result of an earthquake is a tsunami, although in a Norwegian fjord a tsunami might as well be caused by a rockslide into the fjord. Traffic in the SFT might also be included as a dynamic load case.

When designing a slender structure prone to dynamic loading, such as an SFT, dynamic analyses should be performed in order to avoid resonance and fatigue. There has been substantial research on dynamic loading on SFTs, but Jakobsen's [56] article, supplemented by the work of Perotti et al. [62], provides an adequate overview upon which these preceding paragraphs are based.

In addition to designing for static and dynamic loading, accidental loading needs to be accounted for. For the absolute worst case scenario of structural failure and water intrusion into the SFT, the SFT should be designed such that the water inflow rate is sufficiently limited for people to have time to evacuate [56]. Accidental loading includes for example ship collision, explosion, and fire. While there is no risk of ship collision for an SFT anchored with tethers, an SFT anchored with pontoons could risk a ship colliding with one of the pontoons, or even two pontoons, although that risk is only 0.01 % [58]. How it may look when a ship passes a pontoon anchored SFT, is illustrated in Figure 3.6. For a tether anchored SFT, though less likely, a submarine colliding with the tethers is a possible scenario that needs to be taken into consideration. For either anchoring systems, the anchoring should be redundant [56], meaning that if a pontoon is punctured or lost, or a tether is slack or snapped, the SFT structure will not fail completely and

remain operable. For the pontoon anchored SFT, this can be achieved by having a weak link in the connections between the tube and the pontoons [58]. The possibility of a ship losing its anchor, impacting the SFT, has also been considered, but analysts found the probability to less than 0.01 % [58]. 0.01 % is the limit probability NPRA requires in order to design for a load. The probability of a ship sinking on the SFT has also been found to be less than this limit [58].

Besides accidental loads involving ships, the safety of an SFT would need to be considered with regard to fire and explosions. Fires may be accidental due to e.g. vehicles catching fire. If this vehicle is carrying dangerous goods, it could also cause an explosion. However, explosions may also be intentional and caused by the use of explosives in a terrorist attack or warfare. Either way, whether a fire or explosion is accidental or intentional, an SFT must be designed to withstand such loads in order to be safe to use. The blast load phenomena and design with regard to blast loading will be further investigated in the following section.



**Figure 3.6:** Visualization of a ship passing over a pontoon anchored SFT. *Credit:* NPRA.

For the ferry-free E39 project it is not only for the Sognefjord that an SFT is considered a potential solution. For three other fjord crossings, Bjørnafjord, Sulefjord and Halsafjord, SFTs are also considered [63]. It is nor the first time an SFT has been proposed in Norway. For Høgsfjord, an SFT was a carefully considered and developed concept which got the green light from the NPRA concerning feasibility and safety. The NPRA were even ready to establish construction contracts, but the SFT was not built due to political reasons [56, 59]. The potential for SFTs is large in Norway as there are many other challenging fjords and crossings than only those along route E39. Design criteria for SFTs have even been included in NPRA's handbook for the design of bridges [64]. However, the interest for SFTs also spans globally. Studies on SFTs have been carried out for various locations, including Lake Washington in the US, Lugano Lake in Switzerland, Messina Strait in Italy, and several places in Japan. In addition, the construction of an SFT prototype at Qiandao Lake in China is under planning [65].

Often when deciding on which alternative to move forward with, it tends to boil down to cost. For the Sognefjord, NPRA has attempted to assess the different fjord crossing alternatives economically, but there are no reference projects and many uncertainties at this early stage of the project. Their conclusion so far, based on very rough calculations, is that the bridges, including an SFT, in general seem economically preferable since the service and maintenance costs of subsea tunnels are higher [53].

Since an SFT has never been built before and full-scale experiments are practically impossible, numerical analyses will be crucial when, sooner or later, designing an SFT.

## 3.3   Concrete

If an SFT is built for the ferry-free E39 project, the tube will most likely be constructed using reinforced concrete because of its versatility and low cost.

### 3.3.1   Properties

Concrete is a composite material consisting of aggregates, i.e. sand and gravel, bonded together by cement paste, i.e. cement and water. It is also porous as it contains a varying degree of air voids. Supplementary, admixtures may be added to the concrete to alter its properties such as plasticity and curing time. Typically, the density of concrete is approximately 2400 kg/m$^3$ [66], but it may vary depending on the concrete composition.

Because of the random distribution of variously sized aggregates of various strength, concrete's homogeneity is dependant on the scale of interest. That is, at a large scale concrete behaves homogeneously while on a smaller scale it is highly heterogeneous.
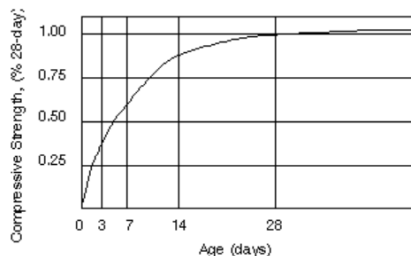


**Figure 3.7:** How concrete typically strengthens with time. *Credit:* University of Memphis [67].

A concrete's compressive strength is perhaps its most important property with regard to engineering design. Typical concrete strengths may range from C20/25 to C45/55, where 20 and 45 refer to the minimum required cylindrical compressive strength measured in megapascal after 28 days, while 25 and 55 denote the same value only for cubical test specimens. The cube strength is higher than the cylinder strength since the cube's slenderness ratio is lower and thus the confining pressure is higher. Often concretes are simply referred to as e.g. B50 and then 50 denotes the cylinder compressive strength.

When one talks about concrete strength, one usually refers to the concrete's 28-day compressive strength. The concrete strength is namely dependent on the curing time, as illustrated in Figure 3.7 where it can be seen that the concrete strength increases most rapidly in the beginning. If the concrete is kept moist during curing, after 28 days it will have reached approximately 90 % of its strength [67]. Should the concrete dry out or freeze during curing, its potential strength will be significantly reduced.

It is not only a concrete's curing conditions that determine its strength. Many factors have an effect, including for example the proportion and quality of the concrete components, and the degree of compaction. However, the most important factor is the water-cement ratio (w/c ratio) which is a concrete's weight of water compared to its weight of cement [67]. A higher w/c ratio leads to a more porous concrete as the water excess to the curing process eventually evaporates. The concrete strength, and also the durability, therefore decreases as the w/c ratio increases. Nevertheless, a higher w/c ratio is beneficial with regard to concrete workability. If the w/c ratio is too low the concrete will therefore not be able to compact properly, also resulting in a decrease in strength. The concrete strength's dependency on the w/c ratio is illustrated in Figure 3.8.

The concrete compressive strength is also dependant on the rate of loading. As the load rate increases, so does the compressive strength, along with the Young's modulus and the slope of the descending portion of the stress-strain curve [70].

Figure 3.9 displays typical stress-strain curves for compression of concretes of various strengths. The elastic part of the stress-strain curves are not completely, but nearly, linear up to approximately 30 % of the ultimate strength [66, 69]. When the curves reach their yield strength and become non-linear, small increases of stress lead to large increases in strain due to microcracking in the concrete [71]. The post-peak response is characterized by strain-softening.

In uniaxial tension, the stress-strain curve for concrete is approximately linearly elastic up until its ultimate strength, and the post-peak behavior decreases gradually to zero [69]. This is illustrated in Figure 3.10 where the difference in compressive and tensile strength is also shown. For concrete is strong in compression, but weak in tension. The tensile strength is generally only about 10 % of the compressive strength and concrete is therefore usually reinforced with rebar steel.

Equation (3.1) is taken from the Eurocode standard for design of concrete structures [72] and is used to determine how the modulus of elasticity (also called Young's modulus) $E$ for concrete varies with time, provided that the cylindrical compressive strength $f_c$ is known. The secant modulus of elasticity is used since the elastic part is slightly non-linear.

$$E(t) = (f_c(t)/f_c)^{0.3} E \qquad (3.1)$$

Concrete is classified as a ceramic which characteristically is strong, stiff, hard, and brittle [66]. However, although concrete is often defined as brittle, it is a quasi-brittle material as it is tougher than most ceramics due to the microcracking [73]. Under low confining pressures, the concrete behavior is more brittle, and the main failure modes are cracking in tension and crushing in compression [74]. As the confining pressure increases, the macroscopic response increasingly resembles that of ductile materials with work hardening as the micropores of the concrete either merge under tension or collapse under compression [74]. This is thus
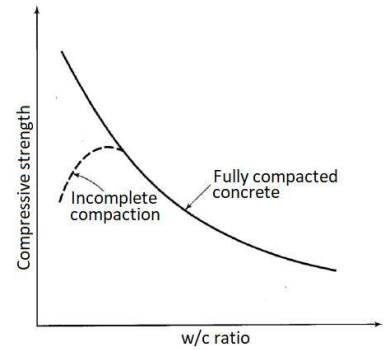


**Figure 3.8:** Compressive strength as a function of w/c ratio. *Credit:* National Concrete Pavement Technology Center [68].
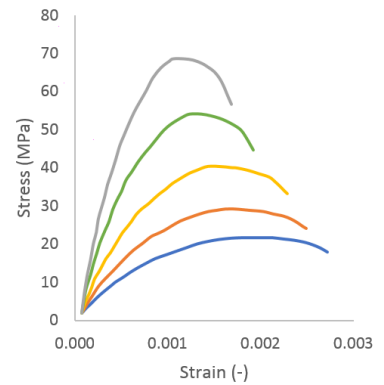


**Figure 3.9:** Typical compressive stress-strain curves for concrete. *Credit:* Modified from University of Memphis [67].
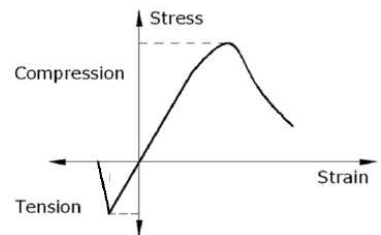


**Figure 3.10:** Typical uniaxial compressive and tensile stress-strain curve for concrete. *Credit:* Islam et al. [69].

the reason for why the confining pressure causes the concrete strength to differ for cubic and cylindrical test specimens.

Concrete can suffer damage due to many reasons such as shrinkage, creep, corrosion of the reinforcement due to carbonation or chlorides, aggregate expansion, or freeze-thaw. However, these types of damage are not the focus of this thesis. Instead, the focus will be on failure due to blast loading.
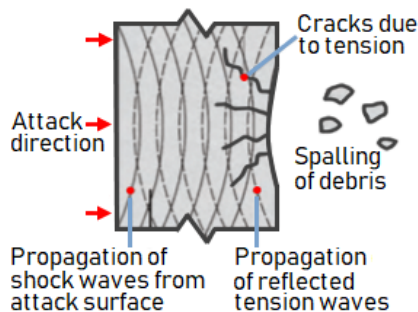
Blast loads have high energy and short duration. This affects both the global and local responses and failure modes. Localized response is fundamentally determined by material properties [75]. For concrete subjected to contact or close-in blast loads, some typical failure modes are cratering, spalling/scabbing, breaching, cracking, and fragmentation.

Craters may form on the side of the target facing the blast when the target material is pushed away laterally [76]. Spalling/scabbing may occur on the opposite side of the target. It is often difficult to practically distinguish between spalling and scabbing since the damage appears similar. The difference between scabbing and spalling is their cause. While spalling occurs as a result of deformation, scabbing is caused by tensile failure when the compressive shock pressure wave propagating through the target is reflected at the targets surface, forming a tensile pressure wave [76]. However, spalling is commonly used as a hypernym for both spalling and scabbing. The concept of scabbing, although denoted spalling, is illustrated in Figure 3.11. If a crater and a spall merge, the target is breached [75].

**Figure 3.11:** Concept of spalling/scabbing. *Credit:* Dynasystems Ltd.

High tensile forces as a result of a blast load, may also lead to cracking. The cracks may only be superficial or extend through the thickness of the target. If the amount of cracking through the target's thickness is substantial, the cracks may merge and lead to fragmentation.

## 3.3.2 Numerical Modelling

The numerical simulations for this thesis will be performed using two finite element programs, namely ABAQUS and LS-DYNA. Concrete is modeled differently for the two codes, and the concrete models are described in brief below.

### Concrete Damaged Plasticity Model

The concrete damaged plasticity model is a material model for concrete, and other quasi-brittle materials, implemented in ABAQUS [74]. The theory of the following paragraphs therefore mainly originates from the ABAQUS user manual [74], unless stated otherwise. The purpose of the CDP model is to be a general capability concrete model with a wide range of applications. The model can therefore be used to model concrete in all types of

structures subjected to monotonic, cyclic, or dynamic loading, but under low confining pressures and mainly for reinforced concrete.

The model is a continuum, plasticity-based, damage model based on the work by Lubliner et al. [77] and Lee and Fenves [78]. By combining the concepts of damaged elasticity with isotropic tensile and compressive plasticity, the model is able to represent the inelastic non-linear behavior of concrete. A very brief explanation of the main concept of the model is provided in the following paragraph, but as the model is rather complex, the reader is referred to the ABAQUS user manual [74] for its full description.
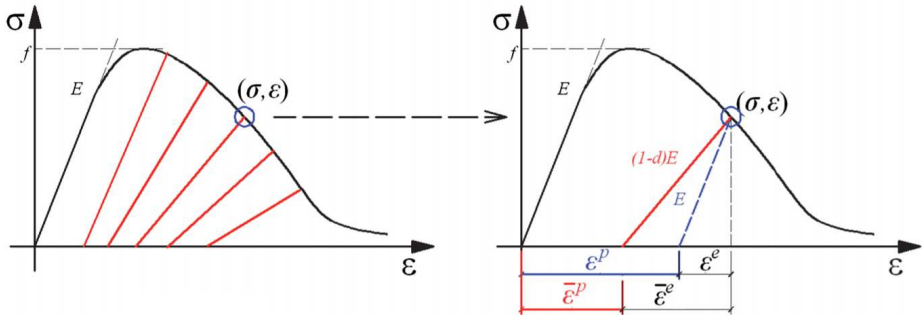


**Figure 3.12:** Compressive stress-strain curve for concrete. *Credit:* Tao and Chen [12].

As the CDP model is intended for low confining pressures, it assumes that the main failure mechanisms are cracking in tension and crushing in compression. Figure 3.12 shows a somewhat simplified but typical stress-strain curve for concrete under uniaxial compression. The figure illustrates how the unloading response is weakened due to damage $d$ when the concrete is unloaded from any point on the post-peak strain-softening part of the curve. $\sigma$ and $\varepsilon$ naturally denote the stress and strain, superscript $e$ and $p$ indicate whether the strain is elastic or plastic, while the bar denotes stiffness degradation. The damage variable $d$ is assumed to be a function of the plastic strains, temperature, and field variables and it varies from zero to one, where zero is undamaged and one is completely damaged. There are two damage variables, one for each of the main load cases, compression and tension. The shape of the stress-strain curve for tensile loading is slightly different, but the concept is the same.

Primarily CDP is intended for reinforced concrete, although it can be used for plain concrete as well. Lack of reinforcement in significant regions of the model will introduce pathological mesh dependency due to the specification of a post-failure stress-strain relation. If the cracking failure occurs at localized regions, as it does e.g. for close-in blasts, this problem with pathological mesh dependency may typically occur. In attempt to avoid this problem, the mesh should be sufficiently large such that each element contains rebar. Rebars can be modeled with metal plasticity models as one-dimensional rods which are embedded in the concrete.

To determine all the parameters required for the CDP model, uniaxial compression, uniaxial tension, biaxial failure in plane state of stress, and triaxial tests need to be performed [79]. Since this amount of testing is extensive, a simplified method is to use parameters that have already been identified for another concrete. To acquire the desired compressive strength the compressive stresses and strains should be scaled. Figure 3.13 displays all

necessary input parameters for the CDP model, along with values determined for a B50 concrete by Jankowiak and Lodgowski. The compressive stresses and strains that need scaling are highlighted in red.

| Material's parameters | B50 | The parameters of CDP model | |
|---|---|---|---|
| | | $\beta$ | 38° |
| Concrete elasticity | | $m$ | 1 |
| $E$[GPa] | 19.7 | $f=f_{b0}/f_c$ | 1.12 |
| $v$ | 0.19 | $\gamma$ | 0.666 |
| Concrete compression hardening | | Concrete compression damage | |
| Stress [MPa] | Crushing strain [-] | DamageC [-] | Crushing strain [-] |
| 15.0 | 0.0 | 0.0 | 0.0 |
| 20.197804 | 0.0000747307 | 0.0 | 0.0000747307 |
| 30.000609 | 0.0000988479 | 0.0 | 0.0000988479 |
| 40.303781 | 0.000154123 | 0.0 | 0.000154123 |
| 50.007692 | 0.000761538 | 0.0 | 0.000761538 |
| 40.236090 | 0.002557559 | 0.195402 | 0.002557559 |
| 20.236090 | 0.005675431 | 0.596382 | 0.005675431 |
| 5.257557 | 0.011733119 | 0.894865 | 0.011733119 |
| Concrete tension stiffening | | Concrete tension damage | |
| Stress [MPa] | Cracking strain [-] | DamageT [-] | Cracking strain [-] |
| 1.99893 | 0.0 | 0.0 | 0.0 |
| 2.842 | 0.00003333 | 0.0 | 0.00003333 |
| 1.86981 | 0.000160427 | 0.406411 | 0.000160427 |
| 0.862723 | 0.000279763 | 0.69638 | 0.000279763 |
| 0.226254 | 0.000684593 | 0.920389 | 0.000684593 |
| 0.056576 | 0.00108673 | 0.980093 | 0.00108673 |

**Figure 3.13:** Material parameters of CDP model for B50 concrete. The highlighted parameters are the ones to be scaled. *Credit:* Jankowiak and Lodygowski [79].

One way to scale the compressive stresses and strains is to firstly simulate a concrete compression test with unscaled parameters in ABAQUS. A scaling factor can then be determined by dividing the desired compressive strength by the one obtained from the simulation. The compressive stresses and strains in Figure 3.13 can then be multiplied by this scaling factor. If the analysis of the compression test is re-run with the updated parameters, it should provide the desired compressive strength.

### Karagozian & Case Concrete Damage Model

There are several concrete material models available in the finite element software LS-DYNA. One of these is the third release of the Karagaozian & Case (K&C) concrete damage model (keyword *MAT_CONCRETE_DAMAGE_REL3 or *MAT_072R3) which was developed for simulating concrete subjected to blast loading [21].

The material model requires no less than 49 parameters, in addition to an equation of state. However, what distinguishes the third release of the K&C model from its predecessors, is the capability of automatic generation of all material model parameters based solely on the concrete's unconfined compressive strength. The user is still able to tune any

of the model's parameters, but the compressive strength is thus the only required input of the model. The material model is therefore straightforward to use as the necessary experimental testing is limited to only uniaxial compression tests, a test which is anyhow required for quality control when constructing with concrete.

The K&C model was developed by Malvar et al. and for the full explanation of the material model, the reader is referred to [15]. However, a brief summary of the concept of the model is provided in the following paragraphs.



(a) Uniaxial compression        (b) Failure surfaces
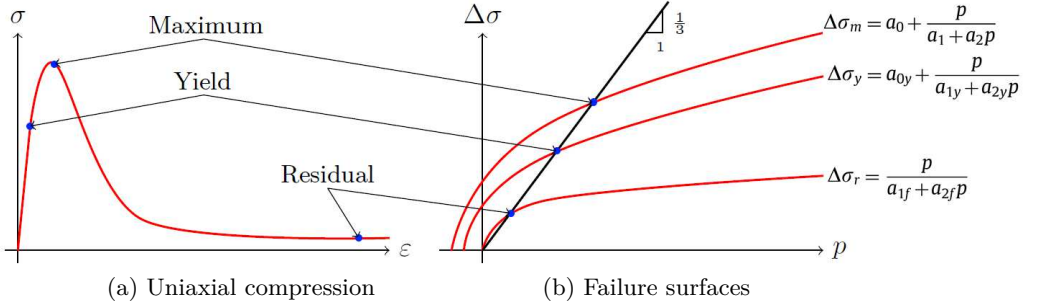
**Figure 3.14:** Principle of CDP model. *Credit:* Modified from Hillestad and Pettersen [48].

K&C is a three-invariant model which uses three shear failure surfaces and includes both damage and strain-rate effects [80]. In this model, the volumetric and deviatoric responses are decoupled. While an equation of state (EOS) describes the relationship between the hydrostatic pressure and the volumetric strain, the deviatoric response is described by the three failure surfaces illustrated in Figure 3.14 which are used to calculate the current failure surface provided in Equation (3.2) [15]. $\Delta\sigma = \sqrt{J_2}$ is the failure surface for the deviatoric stresses, while subscripts $m$, $y$ and $r$ detonate the maximum, yield, and residuals strengths respectively. $p$ is the pressure, and $a_0$, $a_1$, and $a_2$ are material parameters.

$$\Delta\sigma = \eta\left(\Delta\sigma_m - \Delta\sigma_i\right) + \Delta\sigma_i \quad \text{where} \quad i = \begin{cases} y & \text{for} \quad \Delta\sigma_y < \Delta\sigma < \Delta\sigma_m \\ r & \text{for} \quad \Delta\sigma_m < \Delta\sigma < \Delta\sigma_r \end{cases} \tag{3.2}$$

In Equation (3.2) $\eta$ is a value which ranges from 0 to 1, and is a function of the damage function $\lambda$ which is also sometimes referred to as the 'modified' effective plastic strain [80]. The function for $\lambda$ is provided in Equation (3.3) where $d\bar{\varepsilon}^p$ is the effective plastic strain increment, $r_f$ is a dynamic increase factor that accounts for strain rate effects, $f_t$ is the concrete tensile strength, and $b_1$ and $b_2$ are damage scaling parameters, for uniaxial tension and compression, respectively, which determine at which rate the damage occurs [15].

$$\lambda = \int_0^{\bar{\varepsilon}^p} \frac{d\bar{\varepsilon}^p}{r_f(1 + p/r_f f_t)^{b_j}} \quad \text{where} \quad j = \begin{cases} 1 & \text{for} \quad p \geq 0 \\ 2 & \text{for} \quad p < 0 \end{cases} \tag{3.3}$$

When using the K&C model in LS-DYNA, the scaled damage measure $\delta$ is often used to visualize the damage after completing a simulation. The scaled damage $\delta$ is a function of the damage function $\lambda$ and is defined by Equation (3.4) [80].

$$\delta = 2\lambda/(\lambda + \lambda_m) \quad \text{where} \quad \begin{cases} 0 \leq \delta < 1 & \text{for} \quad \Delta\sigma_y < \Delta\sigma < \Delta\sigma_m \\ 1 \leq \delta < 2 & \text{for} \quad \Delta\sigma_m < \Delta\sigma < \Delta\sigma_r \end{cases} \tag{3.4}$$

### 3.3.3 Statistical Variation

The concrete compressive strength will always vary somewhat, mainly due to the random distribution of aggregates of various sizes and strengths.

Hillestad and Pettersen found for their master thesis in 2016 [48] that the compressive strength of concrete can be approximately described using a normal distribution. They therefore used two different methods for incorporating stochastic variation in their numerical models. These two methods are described below, along with a third method which is a combination of the two.

***Random Element Strength***

For their master thesis in 2016, Hillestad and Pettersen developed a MATLAB script for a method they named random element strength (RES) [48]. The random element strength method assigns strengths to the model elements randomly according to a normal distribution. The principle of random element strength is illustrated in Figure 3.15 where every color corresponds to different material strengths.

Hillestad and Pettersen's MATLAB script for RES in ABAQUS was provided as an attachment to their thesis. A second version of this script has been developed to be used for LS-DYNA. These MATLAB scripts modify an ABAQUS input file or LS-DYNA keyword file for concrete.



**Figure 3.15:** Principle of random element strength.

The script developed for ABAQUS assigns elements to sets randomly according to a normal distribution. The sets are then given different material strengths. The number of different material strengths is user-defined. The different material strengths are non-randomly predefined according to a normal distribution with a user-defined mean and standard deviation. The different material strengths do therefore not vary for each time a modified input file is generated using the script, while the element sets do. However, in order for the element sets to vary it is important that the variables in MATLAB not be cleared as the MATLAB random function is not truly completely random. I.e., if the MATLAB memory is cleared in between the generation of modified ABAQUS input files, the script will generate the same element sets each time. Scaling of the concrete material parameters, as described in Section 3.3.2, is included in the script.

In an LS-DYNA keyword file, every element is assigned a part ID. The RES MATLAB script therefore changes this part ID to be a random number according to a normal distribution. A user-defined number of parts are generated and assigned different material strengths which are non-randomly predefined according to a normal distribution with a user-defined mean and standard deviation. As for the ABAQUS RES MATLAB script, the MATLAB memory must not be cleared between every modified keyword file generation.
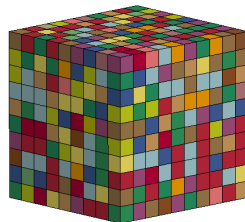
Additionally, a modified version of the random element strength method is developed. This method is identical to the RES method, except that it also generates the material strengths randomly. This modified random element strength (MRES) method should therefore provide greater variation in the numerical simulation results.

### *Mesoscale Modeling*

A concrete mesoscale model distinguishes between particles (aggregates) and matrix (cement), and it may also include the transition zones. The basic principle of mesoscale modeling is illustrated in Figure 3.16 where the red elements make up the matrix while the yellow elements are the aggregates. Mesoscale modeling can be made much more complex than this by for example including the transition zones or including the irregular geometries of the aggregate.
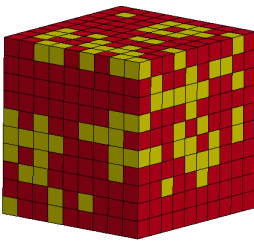


**Figure 3.16:** Basic principle of mesoscale modeling.

For their master thesis in 2016 Hillestad and Pettersen also developed a MATLAB script such that mesoscale modeling of concrete could be implemented [48]. Hillestad and Pettersen's script was developed for LS-DYNA and a second script has therefore been created to be used for ABAQUS. These MATLAB scripts incorporate mesoscale modeling by altering the ABAQUS input file or LS-DYNA keyword file.

Both scripts first generate particles and their placement randomly based on a user-defined minimum and maximum particle size. The scripts then check that the whole particles are placed within the user-defined geometry and that they do not intersect. It is then checked which elements are located inside the particles and these elements are saved as particle elements. Once the user-defined particle volume fraction is reached, the particle generation is terminated.

After it is determined which elements are particle elements, they are given a user-defined strength. The remaining matrix elements are given another user-defined strength. In ABAQUS this is done by establishing two element sets which are assigned different material strengths. In LS-DYNA two different parts with corresponding material strengths are established and every element is then assigned to the correct part by altering its part ID reference.

### *Combination of Random Element Strength and Mesoscale Modeling*

Since it is the aggregates whose strengths vary the most, while the matrix is much more homogeneous, the random element strength and mesoscale modeling methods are combined such that only the particles are given random strengths. The principle of this combined method is illustrated in Figure 3.17 where all the matrix elements are red, and all the particle elements are of various colors corresponding to the different strengths.



**Figure 3.17:** Principle of combination of RES and MS.
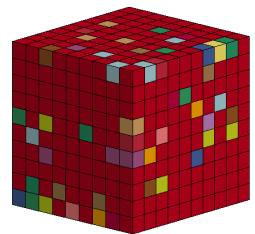
MATLAB scripts for including this combined method are established for both ABAQUS and LS-DYNA by simply combining the previous scripts.

# 3.4 Blast Loading

Since an intentional or accidental explosion could occur in a potential SFT, blast loading needs to be accounted for in the design in order to protect both civilians and infrastructure. For an SFT the most likely cause of an explosion would be if a tanker carrying dangerous goods such as compressed gas or explosives, were to be involved in an accident. Another possible cause of an explosion would be if explosives were used in a terrorist attack. Since chemical explosions involving high explosives are more severe, they will be the focus of this thesis, but gas explosions will also be briefly discussed. The following section is mainly based on the work by Aune et al. [81], unless otherwise is stated.

## 3.4.1 Explosives

There are three main types of explosions. The first explosion type is physical explosions which may occur for example if a tank containing compressed gas ruptures, a volcano erupts, or if liquids of different temperatures are mixed. The second type of explosion is nuclear explosions which are caused by atom fission or fusion. The third explosion type is chemical explosions caused by explosives.

Explosives are often categorized as high or low according to their burn rate. High explosives (HE), also called detonating, burn very rapidly and produce high pressures, while low explosives, also called deflagrating, burn more slowly producing lower pressures.

For experiments in this thesis, the high explosive C4 will be utilized. C4 is a plastic explosive which can easily be molded into any desired shape. It is an extremely stable secondary explosive which requires a detonator to ignite it. A detonator can be a primary explosive which is easily ignited, causing a high-velocity shock wave to spread to the secondary explosive. This shock wave causes adiabatic heating in the secondary explosive and thereby detonates it. Some characteristic properties of C4, along with TNT, are provided in table 3.1.

**Table 3.1:** Characteristic properties of TNT and C4 [75].

| Explosive type | Explosive density (g/cm$^3$) | Detonation velocity (km/s) | Heat of detonation (kJ/kg) |
|:---:|:---:|:---:|:---:|
| TNT | 1.64 | 6.90 | 4100-4900 |
| C4 | 1.59 | 8.04 | 5860 |

The high explosive trinitrotoluene (TNT) is commonly used as a basis for comparison of the energy released in explosions. The TNT equivalent is the free air equivalent weight of TNT required to produce a particular shock wave parameter of a magnitude equal to that produced by a unit weight of the explosive [75]. The TNT equivalent for C4 is therefore provided in Table 3.2. Note that the values in Table 3.2 are only validated up to pressures of approximately 700 kPa and might therefore not be accurate for close-in detonations where pressures can be much larger.

**Table 3.2:** TNT equivalent mass factors for design purpose [82].

| Explosive type | TNT equivalent mass factor | |
|:---:|:---:|:---:|
| | Peak pressure | Impulse |
| C4 | 1.37 | 1.19 |

TNT equivalency is for example used when the American Federal Emergency Management Agency (FEMA) has assessed what maximum amount of explosive could reasonably fit into a container or vehicle [83]. Their findings are presented in Figure 3.18 where the potential threats have been categorized into personnel- and vehicle-borne improvised explosive devices (abbreviated PBIED and VBIED respectively). These findings can be useful when designing for a potential terrorist attack where the exact threat is unknown.

| Threat description | | Explosive mass (TNT equivalent) [kg] |
|:---:|:---:|:---:|
| PBIED | Pipe bomb | 2.3 |
| | Suicide belt | 4.5 |
| | Suicide vest | 9.0 |
| | Briefcase/suitcase bomb | 23.0 |
| VBIED | Car bomb (compact sedan) | 227.0 |
| | Car bomb (sedan) | 454.0 |
| | Passenger/cargo van | 1,814.0 |
| | Small van/ delivery truck | 4,536.0 |
| | Moving van/ water truck | 13,608.0 |
| | Semitrailer | 27,216.0 |

**Figure 3.18:** Maximum amount of explosive that could reasonably fit into a container or vehicle. *Credit:* Aune et al. [81], adapted from FEMA [83].

### 3.4.2 Blast Phenomena

*Detonation and Deflagration*

The detonation of a high explosive is a rapid chemical reaction where oxidation of fuel elements in the explosive generates a large amount of gas and heat. The rapid expansion of gas is the source of a high-intensity shock wave. Approximately one-third of the explosive's chemical energy is released in the detonation. The remaining two-thirds of energy is released more slowly through burning. The burning can affect the later stages of an explosion, especially if the explosion takes place in a confined space.

$$M = \frac{v}{c} \tag{3.5}$$

A detonation only occurs if the Mach number is greater than one. The Mach number is the relationship between the speed of an object, e.g. a shock wave, moving through a medium, e.g. air, $v$ and the speed of sound in that same medium $c$, see Equation (3.5). If the Mach number is less than one, instead of a detonation one gets a deflagration. While

a deflagration is characterized by slower burning, a detonation is characterized by a shock wave and rapid burning.

### Shock Wave

A shock wave expands outward from the source of the detonation since the pressure generated from the detonation is higher than the surrounding pressure. When a shock wave propagates in air it is also called a blast wave. If the shock wave propagates in a solid medium, it is often referred to as a shock pressure. A shock wave behaves like an ordinary wave, but it is defined by a sudden increase in pressure, temperature, and density. As a shock wave propagates its strength decays, its duration lengthens, and its velocity and pressure decreases. Fragments are accelerated by blast waves and can cause considerable damage. Fragments which originate from parts of the explosive device are called primary, while fragments of external objects are called secondary.
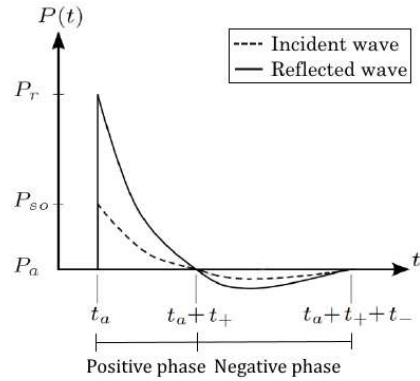


**Figure 3.19:** Characteristic blast wave from an explosion. *Credit:* Modified from Aune et al. [81].

Figure 3.19 illustrates a characteristic pressure-time curve for an incident and reflected blast wave. Here $P$ is the pressure and index $a$ implies the ambient pressure and index $r$ implies the peak reflected pressure. $t$ is the time and $t_+$ and $t_-$ is the duration of the positive and negative phase respectively. The area under the pressure-time curve is the specific impulse, $i_{r+}$, i.e. the energy of the explosion.

$$P(t) = P_a + P_r \left( 1 - \frac{t}{t_+} \right) \exp \left( \frac{-bt}{t_+} \right) \tag{3.6}$$

As shown in Figure 3.19, the incident blast wave is characterized by an incident overpressure which arises almost instantly to a peak value $P_{so}$ and then decays exponentially. The negative phase of the blast wave has a longer duration due to the momentum of the gas which causes the suction. A blast wave can be described by the Friedlander equation which is provided in Equation 3.6 where $b$ is a decay coefficient. When a blast wave interacts with a surface that is not parallel to the direction of the wave, it is reflected and amplified. The reflected pressure has the same shape as the incident wave, but the peak pressure is higher. The reason for this is that there is a congestion of air particles at the reflecting surface.

### Reflection

The reflected pressure varies with the incident angle of the blast wave, $\alpha$. If the blast load is head-on, $\alpha = 0°$, the reflected pressure is maximized, and if the blast load is side-on, $\alpha = 90°$, the reflected pressure is minimized. Head-on and side-on pressure is illustrated in Figure 3.20. Since the reflected pressure is larger than the incident pressure, it is commonly used for design purposes. However, it is important to remember

that explosives of the same weight and geometry will not necessarily provide the same pressure-time curve if the physical conditions are varied [84].



**(a)** Side-on, $\alpha = 90°$            **(b)** Head-on, $\alpha = 0°$
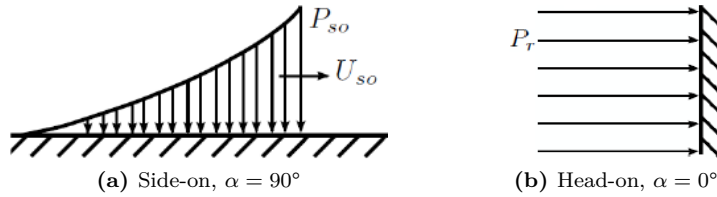
**Figure 3.20:** Pressure loading. *Credit:* Aune et al. [81].

If the angle of incident, $\alpha$, is between zero and approximately forty degrees, the reflection is categorized as regular, Figure 3.21a. On the other hand, if $\alpha \gtrsim 40°$ the reflected wave interacts with the incident wave forming a Mach front whose direction is parallel to the surface, Figure 3.21b. For design purposes, a Mach front is assumed to be a plane wave with uniform pressure distribution and a pressure magnitude equal to that of the incident wave. A Mach front can occur for example if the detonation is air burst, Figure 3.21c.



(a) Regular       (b) Mach       (c) Air burst detonation
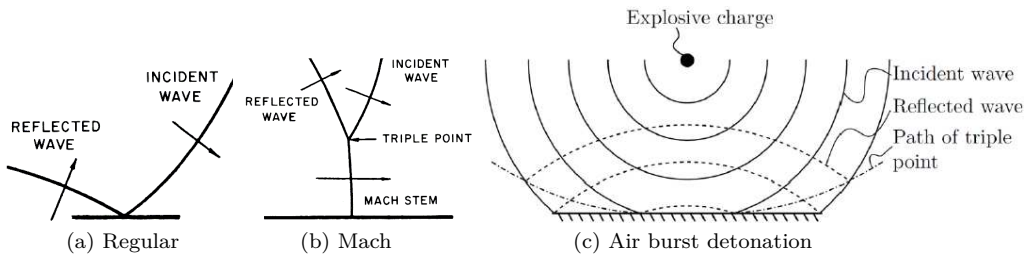
**Figure 3.21:** Reflection of shock waves. *Credit:* (a,b) Military Story [85], (c) Aune et al. [81].

### Confined Explosions

If an explosion is confined, as it partly would be in an SFT, the pressure-time curve has a high peak pressure as the pressure is amplified by its numerous reflections. The accumulation of gases from the explosion leads to both additional pressure and increased duration [86]. A confined explosion has two phases. The first phase is the shock pressure phase which is of short duration and resembles that of unconfined explosions, but with several reflected waves from internal surfaces. The second phase is the gas pressure phase which is of longer duration. This phase is complicated as reflected waves interact with internal surfaces, generating new reflected waves which then again interact with each other. Simultaneously, gases of high pressure and temperature expand. Eventually, the pressure will decay to ambient pressure due to leakage from confined space and cooling of gasses. A typical and an idealized pressure-time curve for confined explosions are displayed in Figure 3.22. Notice that for the simplified pressure-time curve, the shock and gas pressures overlap and could therefore overestimate the impulse [75].

**(a)** Typical

**(b)** Idealized
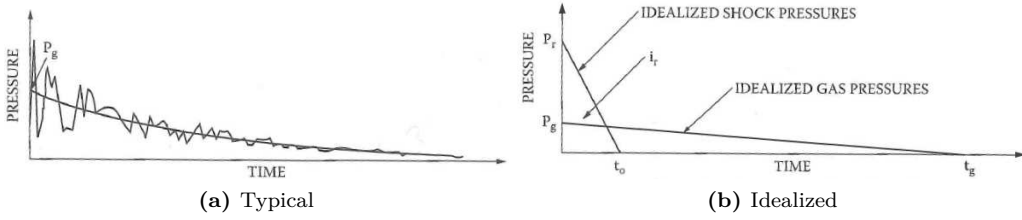
**Figure 3.22:** Confined explosion. *Credit:* Krauthammer [75].

### Scaling Laws and Load Categorization

To be able to predict characteristics of blast waves based on experimental testing, scaling laws can be utilized. A commonly used such scaling law is the Hopkinson-Cranz, also called cube-root, scaling. The Hopkinson-Cranz scaling laws can be used for spherical charges and are provided in Equation 3.7 where $W$, $U$, and $R$ is the weight, heat, and stand-off distance of the reference explosion. Subindex 1 refers to the explosion which is to be scaled. If one chooses $W_1$ and $U_1$ to be unit measures, one can obtain the scaled distance $Z$ by Equation 3.8. The scaling factor $\chi$ can also be used to scale the duration and impulse. Bear in mind, to be able to use the scaling laws, the blast environments must be similar and the shock wave must propagate spherically. Spherical shock wave propagation requires a spherical charge or far-field detonations. For cylindrical charges and close-in detonations, for example, square root scaling may be more suitable.

$$\frac{R}{R_1} = \left(\frac{U}{U_1}\right)^{1/3} = \left(\frac{W}{W_1}\right)^{1/3} \tag{3.7}$$

$$Z = R_1 = \frac{R}{U^{1/3}} = \frac{R}{W^{1/3}} = \chi R \tag{3.8}$$

The scaled distance $Z$ can be used to categorize the loading, which is useful since the structural response is highly dependent on distance. If $Z < 0.5$ the blast load is categorized as close-in and is highly localized. Typical failure modes, depending on the target thickness and material, include shear, spalling and petalling. Since simplified methods such as Kingery and Bulmash (to be further discussed in Section 3.4.3) are based on an ideal blast environment, the use of such methods might be questionable for close-in detonations. If $0.5 < Z \lesssim 2$ the detonation is defined as near-field and a non-uniform pressure from a shock wave can cause both global and local effects. The blast loading is called far-field if $Z > 2$, in which case a uniform shock wave pressure can evoke global response.

### Gas Explosions

This section has focused on explosions caused by detonation of high explosives, but there are several ways that a gas tanker could cause an explosion in an SFT. One such way is if a pressure vessel bursts. This may happen if the internal pressure is large and the pressure vessel fails. Failure of the pressure vessel could happen due to for example

impact, corrosion, or fatigue. Increased internal pressure due to eg. fire could also cause the pressure vessel to rupture. If the contained gas is flammable, the pressure vessel burst could also cause a fireball. If the tank contains liquid or liquefied gas at temperatures above their atmospheric-pressure boiling points, a boiling liquid expanding vapor explosion (BLEVE) may occur as the instantaneous pressure reduction could result in explosive vaporization. Most gas explosions are deflagrations which happen less rapidly and have lower peak pressures and longer duration than chemical explosions, but therefore the impulse may also be large. However, a gas detonation such as a BLEVE may resemble an explosion caused by explosives. Gas explosions are described in more detail by Albright [87], whose book this paragraph is mostly based on.

An example of a submerged tunnel explosion caused by a gas tanker happened in Bremanger in Norway in 2015. A tank trailer was transporting 16 500 liters of gasoline when it crashed into the tunnel wall. The crash caused the tank to rupture, and gasoline leaked out. The gasoline was then most likely ignited by heat/ignitions from the engine of a close-by car, causing an explosion. The tunnel was severely damaged, sea water leaked in, and if was feared that the tunnel would collapse [88].

### 3.4.3 Load Prediction

The magnitude, duration, and distribution of blast loading on structures are functions of several factors. Amongst these factors are explosive properties such as the material, weight, and shape of the explosive. The location of the detonation relative to the structure is another such factor along with the magnitude and amplification of the pressure by its interaction with the ground and structure. There is a variety of methods which can be used when predicting a blast load. These methods can be divided into three main categories: empirical, semi-empirical, and numerical methods. The methods are listed with increasing complexity, and the more complex methods are usually used at later design stages.

#### *Empirical Methods*

The perhaps most commonly used empirical method for predicting blast loading is the Kingery-Bulmash equations. Kingery and Bulmash gathered data from literature on explosions in idealized conditions and, by using Hopkinson-Cranz scaling, they curve-fitted this data to higher-order polynomials as functions of the TNT equivalent blast parameters. The Kingery-Bulmash equations predict blast properties such as peak pressure, impulse, and duration. As the equations are empirical, they are highly idealized and should not be used outside the range of the experimental data on which they are based. This implies that the equations are only valid for either spherical free air bursts or hemispherical surface explosions and that they should not be used for complex blast environments. In Figure 3.25a the equations for spherical free air bursts are provided. Similar equations are also available for hemispherical surface explosions in Figure 3.25b. Note that the equations are only provided for scaled distances greater than approximately 0.5 and 0.7, respectively, and that they are therefore not valid for close-in blasts.

ConWep is short for 'conventional weapons' and is a computer program that bases itself on the Kingery-Bulmash equations. Additionally, ConWep has been implemented in several

finite element programs, including both ABAQUS and LS-DYNA. ConWep automatically calculates pressures produced by a blast based on only four user-defined inputs, namely the point of detonation, amount of explosive (provided in TNT-equivalent mass), charge type (air or surface burst), and which surface is subjected to the blast. ConWep also automatically applies the pressure to the surfaces and is therefore simple to use. However, since ConWep is based on the Kingery-Bulmash equations, the same limitations regarding blast environment and validity apply.

Eurocode 1, part 7 on accidental actions, provides empirical equations for calculating the pressure due to gas explosions in road and rail tunnels [89]. The pressures for both gas deflagration and detonation are provided in Figure 3.23 and 3.24 respectively.



$$p(t) = 4p_0 \frac{t}{t_0}(1 - \frac{t}{t_0}) \text{ for } 0 \le t \le t_0$$

where :

$p_0$   is the peak pressure (=100 kN/m$^2$ for a typical liquefied natural gas fuel;

$t_0$   is the time constant (= 0,1 s);

$t$   is the time.

The pressure may be used for the entire interior surface of the tunnel.
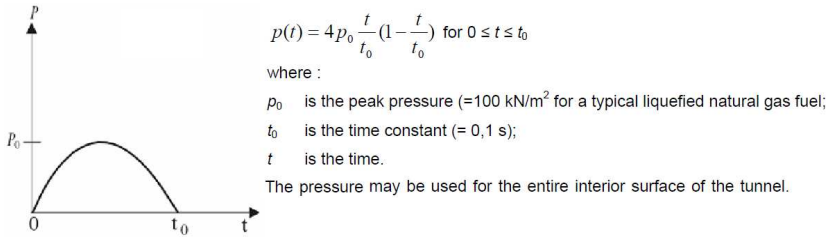
**Figure 3.23:** Pressure due to gas deflagration in tunnels according to EC1. *Credit:* EN 1991-1-7 [89].



$$p(x,t) = p_0 \exp\left\{-\left(t - \frac{|x|}{c_1}\right)/t_0\right\} \text{ for } \frac{|x|}{c_1} \le t \le \frac{|x|}{c_2} - \frac{|x|}{c_1}$$

$$p(x,t) = p_0 \exp\left\{-\left(\frac{|x|}{c_2} - 2\frac{|x|}{c_1}\right)/t_0\right\} \text{ for } \frac{|x|}{c_2} - \frac{|x|}{c_1} \le t \le \frac{|x|}{c_2}$$

$$p(x,t) = 0 \text{ for all other conditions}$$

where:

$p_0$   is the peak pressure (=2 000 kN/m$^2$ for a typical liquefied natural gas fuel;

$c_1$   is the propagation velocity of the shock wave (~ 1 800 m/s);

$c_2$   is the acoustic propagation velocity in hot gasses (~ 800 m/s);

$t_0$   is the time constant (= 0,01 s);

$|x|$   is the distance to the heart of the explosion;

$t$   is the time.
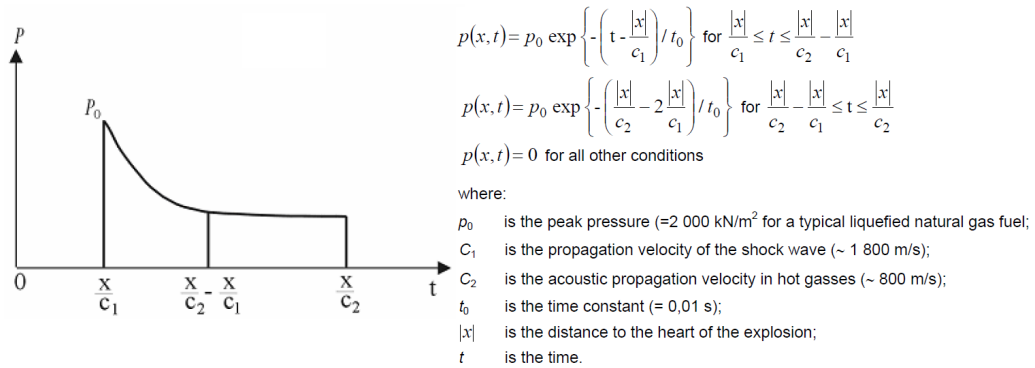
**Figure 3.24:** Pressure due to gas detonation in tunnels according to EC1. *Credit:* EN 1991-1-7 [89].

(a) Spherical charge detonated in free air



(b) Hemispherical surface charge
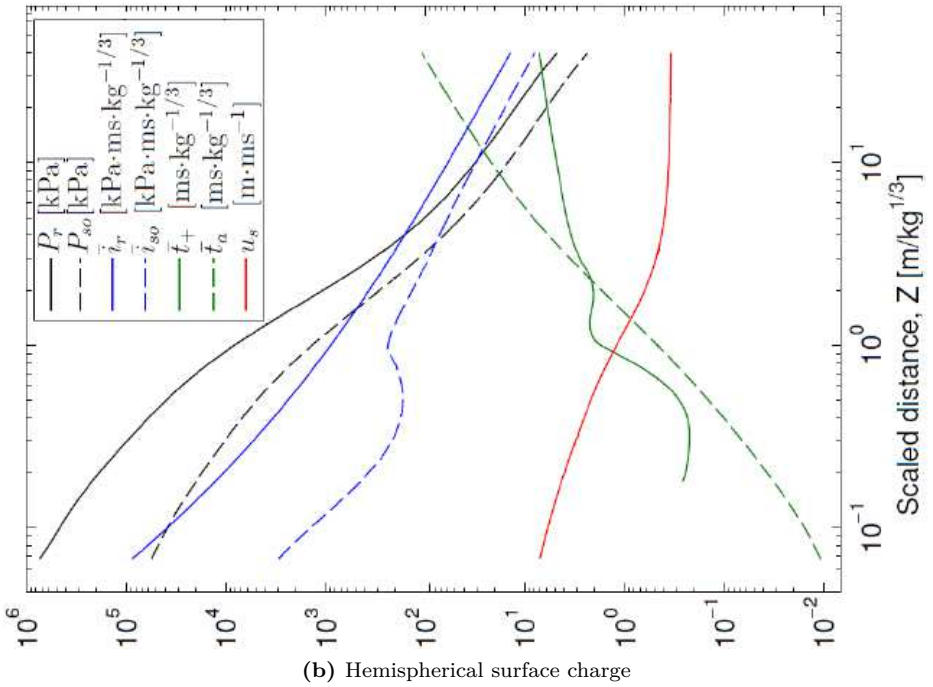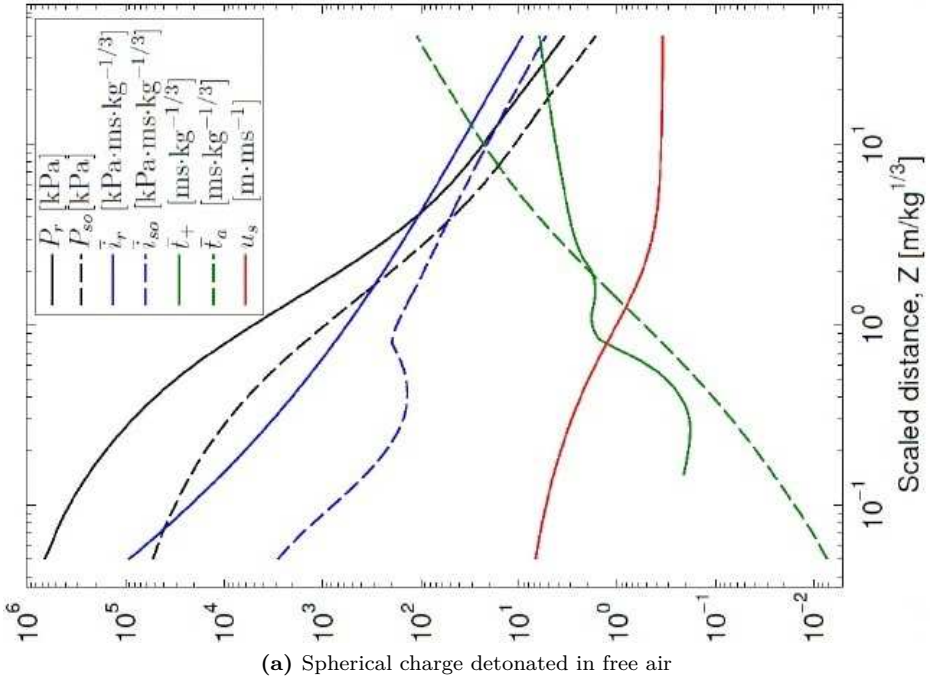
**Figure 3.25:** Kingery and Bulmash blast parameters for TNT. *Credit:* Aune et al. [81].

### Semi-Empirical Methods

Semi-empirical methods are based on empirical methods and do not solve the governing equations, but they also take simplified geometrical aspects into account and can therefore include multiple reflecting surfaces. These methods are often restricted since they are mostly developed for defense-related agencies.

### Numerical Methods

The numerical method of computational fluid dynamics (CFD) solves the governing equations for fluid flow (conservation of mass, momentum, and energy) numerically for user-defined initial and boundary conditions. These methods can therefore be used for complex blast environments. CFD solves the governing equations by dividing the fluid domain into small discretized control volumes. During each time step, all variables (pressure, density, and velocity) are assumed to be constant in each control volume. When simulating blast loading, finite volume, finite difference, or finite element method discretization is typically used in combination with explicit time integration schemes. Besides, an Eulerian formulation where the mesh is fixed, and the fluid particles move relative to the mesh, is preferable for the simulation of shock waves. While a fine mesh is computationally expensive, a too coarse mesh will lead to a loss of resolution of the blast wave, under-predicting the peak pressure and thereby also the load. A possible solution might therefore be adaptive meshing where a coarse mesh is used, but with a mesh refinement when needed. CFD does usually not consider structural response since structures are assumed to be infinitely strong and stiff. This is generally no problem as long as the structural deformations are small. If this is not the case fully coupled analyses, need to be considered. A simplified alternative is to say that a structural element fails abruptly and that the corresponding boundary condition is removed from the analysis if the combination of peak pressure and impulse exceeds the structural element's capacity.

There are several methods for simulating a blast load in a CFD analysis. One such method is to use the John-Wilkins-Lee (JWL) equation of state (EOS) which models the pressure generated by detonating high explosives [74]. The JWL EOS defines the pressure $P$ by equation (3.9) and is available in several finite element programs, including ABAQUS and LS-DYNA.

$$ p = A \left( 1 - \frac{\gamma}{R_1 V} \right) \exp(-R_1 V) + B \left( 1 - \frac{\gamma}{R_2 V} \right) \exp(-R_2 V) + \frac{\gamma E_D}{V} \qquad (3.9) $$

$E_D$ is the detonation energy density, while $V$ is the ratio of the volume of detonation products to the volume of undetonated HE [90]. This ratio $V$ can be calculated using the detonation wave speed $v_D$, the distance of the material point from the detonation point, and the density of the explosive $\rho_0$ [74]. $A$, $B$, $R_1$, $R_2$, and $\gamma$ are JWL material parameters. All the required JWL parameters have been calibrated for several explosive types by Dobratz and Crawford [90] and have been included for TNT and C4 in Table 3.3.

**Table 3.3:** Parameters for JWL EOS for TNT and C4 [90].

| Type of explosive | $\rho_0$ (kg/m$^3$) | $E_D$ (GPa) | $v_D$ (m/s) | A (GPa) | B (GPa) | $R_1$ (-) | $R_2$ (-) | $\gamma$ (-) |
|---|---|---|---|---|---|---|---|---|
| TNT | 1630 | 7.0 | 6930 | 371.2 | 3.23 | 4.15 | 0.95 | 0.30 |
| C4 | 1601 | 9.0 | 8193 | 609.8 | 12.95 | 4.1 | 1.25 | 0.44 |

### 3.4.4 Structural Response and Design

Although the probability of an explosion is low, blast loading is an extreme load which needs to be considered as the potential consequences are substantial. The main principles of blast loading design are, if possible, to increase the stand-off distance, encompass initial protective design of a structure and its built-in components, harden and reinforce existing structures, and install protective elements in the vicinity of structures. For an SFT some of these measures are difficult to incorporate, and good initial design is therefore essential.

For very simple systems the structural response due to blast loading can be obtained analytically. However, most structures are more complex and the use of analytical solution methods quickly becomes complicated. Nevertheless, there are other means of calculating the response of complex structures subjected to blast loading.

#### *Pressure-Impulse Diagram*

A pressure-impulse (P-I) diagram is a useful tool to easily assess whether a structure will be damaged by a blast loading. Traditionally, P-I diagrams are obtained for single-degree-of-freedom systems using simplified material models, but they can also be generated by carrying out FE analyses for multiple pressure-impulse load combinations to determine if the structure fails or not. A typical P-I diagram can be seen in Figure 3.26. The horizontal asymptote represents the structure's quasi-static load capacity, while the vertical asymptote represents the structure's impulsive load capacity. The part of the curve that does not fall within the impulsive or quasi-static regime, is the dynamic regime.
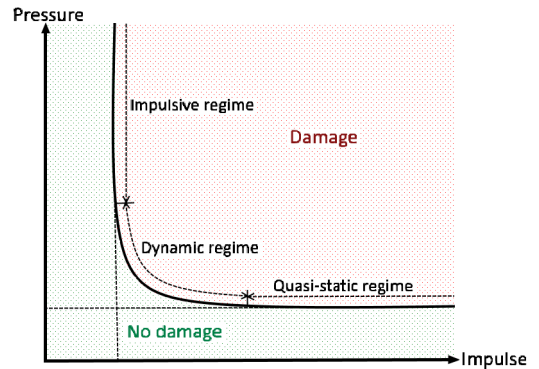


**Figure 3.26:** P-I diagram.

Baker et al. [91] established limits for the different load regimes for an undamped perfectly elastic system. They stated that if the product of the system's natural frequency $\omega$ and the load duration $t_d$ was less than 0.4, the load was in the impulsive regime. If $\omega t_d$ was greater than 40, the loading was quasi-static. For any values between these asymptotes, $0.4 < \omega t_d < 40$, the loading is categorized as dynamic. The different load regimes are illustrated and compared with a typical structural response in Figure 3.27. For the impulsive loading regime, the maximum structural response is assumed to be independent of the shape of the load pulse since the duration of the load is short compared to the

response time of the system. For the dynamic regime, the load duration and structural response time are of the same magnitude, and therefore the response is more complex and highly dependent on the load shape. For the quasi-static regime, the load duration is longer than the structural response time, and the maximum response is therefore only dependent on the peak load and the structural stiffness [75].
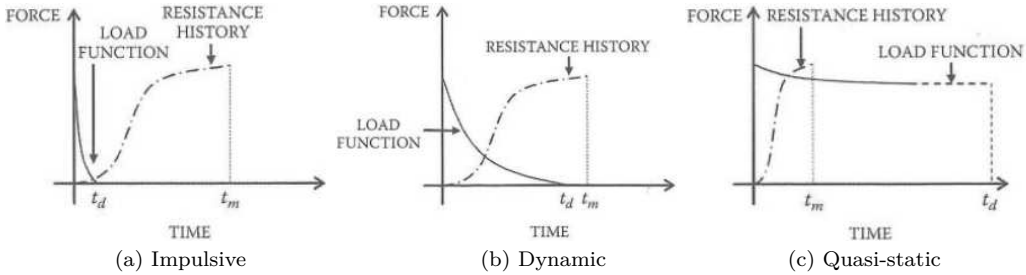


**Figure 3.27:** Loading regimes. *Credit:* Krauthammer [75].

### Uncoupled Simulations

P-I diagrams can only be used to assess whether or not a structure is damaged by a blast load, and not to determine the structural response. If one wishes to do so, there are two main methods, the first of which is uncoupled analyses where two separate analyses are performed. First, a CFD analysis is carried out as described in the previous subsection. This is done in order to obtain the pressure-time curve of the blast load which is then used as input for a computational structural dynamics (CSD) analysis. Since the structural parts are assumed infinitely stiff and strong for the CFD analysis, the blast load may be overly conservative as the failure of structural elements, e.g. windows, can change the properties of the fluid flow.

### Coupled Simulations

The second method for determining the structural response is a coupled analysis where there is full coupling between the fluid and the structure. By fully coupling the simulations of CSD and CFD, the fluid-structure interaction (FSI) is accounted for. There are two main approaches for performing coupled analyses. The arbitrary Lagrangian-Eulerian (ALE) method utilizes an Eulerian mesh for the fluid which is then coupled to a Lagrangian mesh for the structure. While an Eulerian mesh is a fixed reference mesh where the particles move with respect to the mesh, a Lagrangian mesh is fixed to the particles, see Figure 3.28. The coupling of the meshes can be done using a strong approach where the nodes of the fluid and structure meshes are distinct and superposed, and their velocity vectors are constrained. The strong approach is limited to moderate structural deformations, and therefore a weak approach may sometimes be preferable. For a weak approach, the pressure forces are transmitted directly from the fluid to the structure without using constraints. If the mesh gets too distorted for an ALE simulation, re-meshing is possible. However, re-meshing can be computationally costly, and one can get artificial diffusion and loss of accuracy.

**(a)** Eulerian

**(b)** Lagrangian
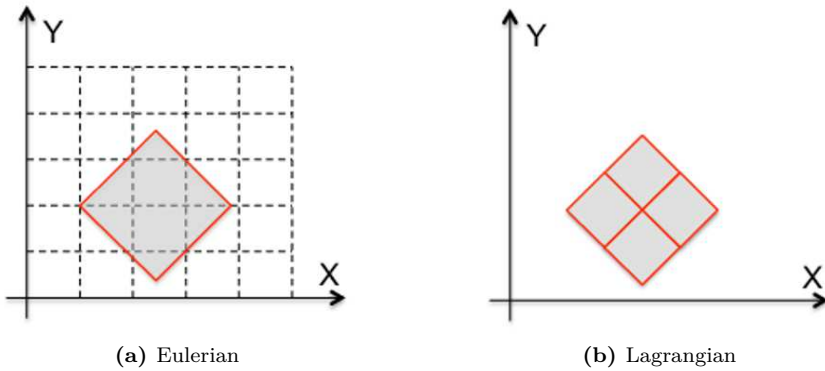
**Figure 3.28:** Mesh types. *Credit:* Spicher et al. [92].

For the second main coupled analysis approach, fluid mesh distortion is not an issue as the structural mesh is embedded in the fluid mesh. This method is therefore referred to as embedded mesh method or alternatively immersed, fictitious domain, or overlapping mesh method. The fluid still uses an Eulerian mesh, and the structure still uses a Lagrangian mesh. The two meshes are superposed, and both strong and weak coupling can be used in the same way as for ALE. To choose which fluid nodes are at the fluid-structure interface, spheres of a given radius are created around the structural nodes. The spheres are then connected forming a volume, and all fluid nodes that fall within this volume are part of the influence domain. The ALE and embedded method may seem very similar, but the difference is made clearer in Figure 3.29.



**(a)** ALE

**(b)** Embedded
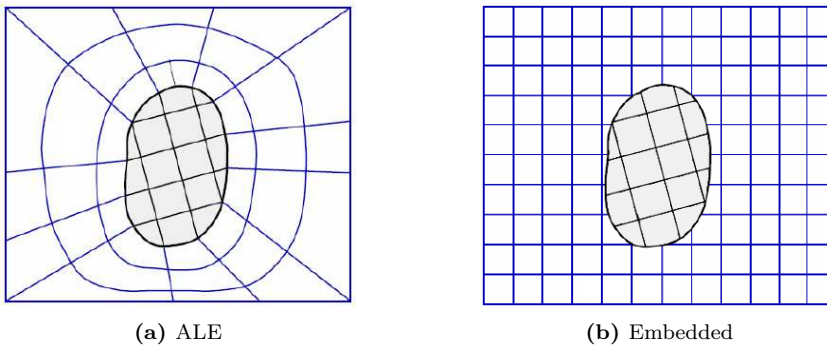
**Figure 3.29:** Mesh methods for coupled analyses. *Credit:* Aune et al. [81].

## 3.5   Explicit Finite Element Method

When designing an SFT with regard to blast loading, full-scale testing is naturally out of the question. Instead, numerical methods will have to be made use of. Numerical simulations can be both cost and time efficient, provided that they are properly executed.

Blast loads have very short durations and therefore call for small time steps. Since explicit analyses are only conditionally stable, they also require small time increments and are therefore well-suited for fast transient problems, such as structural impacts and blast loads [81]. In addition, the method is suitable for problems involving other non-linearities such as material strain-softening or contact.

Explicit analyses can be performed in both ABAQUS and LS-DYNA, which are the finite element codes that are used for numerical simulations in this thesis.

### 3.5.1   Central Difference Time Integration Scheme

Compared to direct-integration which is used for implicit analyses, the increments for explicit analyses are relatively inexpensive [74]. The reason for this is that explicit analyses utilize the central difference time integration scheme which does not require equation-solving at every time step. For the half-step central difference with a varying time step, Equations (3.10), (3.11), and (3.12) are used to determine the nodal displacement (or rotation), velocity, and acceleration, respectively, at each increment $i$ [74]. The method is also illustrated in Figure 3.30. For the full derivation of the equations, the reader is referred to e.g. [93] or [94].
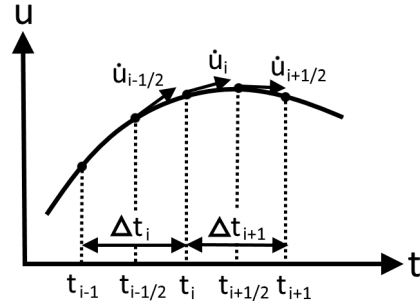


**Figure 3.30:** Illustration of the central difference time integration scheme.

$$u_{(i+1)} = u_{(i)} + \Delta t_{(i+1)} \dot{u}_{(i+1/2)} \tag{3.10}$$

$$\dot{u}_{(i+1/2)} = \dot{u}_{(i-1/2)} + \frac{\Delta t_{(i+1)} + \Delta t_{(i)}}{2} \ddot{u}_{(i)} \tag{3.11}$$

$$\ddot{u} = \mathbb{M}^{-1} \left( \mathbb{R}^{ext}_{(i)} - \mathbb{R}^{int}_{(i)} \right) \tag{3.12}$$

When the equations above are combined, the calculation only calls for values from the previous time increment. This is what makes the method explicit. It is also what makes every increment computationally cheap, given that the mass is lumped such that the mass matrix $\mathbb{M}$ is diagonal and thus easily inverted for Equation (3.12). $\mathbb{R}^{ext}$ and $\mathbb{R}^{int}$ are the applied and internal load vectors, respectively.

At the first increment $t = 0$, a value needs to be prescribed for $\dot{u}_{(-1/2)}$. A common way of doing this is by backward approximation, provided in Equation (3.13). This method is also used in for example ABAQUS where the default values of $u_{(0)}$ and $\dot{u}_{(0)}$ are zero [93].

$$\text{At} \quad t = 0 \quad \dot{u}_{(1/2)} = \dot{u}_{(0)} + \frac{\Delta t_1}{2} \ddot{u}_{(0)} \quad \implies \quad \dot{u}_{(-1/2)} = \dot{u}_{(0)} - \frac{\Delta t_{(0)}}{2} \ddot{u}_{(0)} \tag{3.13}$$

### 3.5.2 Stability

Although the cost of each time increment is low, the explicit method requires many increments. For as was mentioned introductory, the explicit method is only conditionally stable, which means that its stability is dependent on adequately small time increments. An adequately small time step is such that during a single time step, information does not propagate more than the distance between adjacent nodes [94]. The stable, also commonly referred to as critical, time increment $\Delta t_{cr}$ for an undamped material can therefore be calculated from Equation (3.14). By introducing damping to the material, the stable time increment would be reduced [94].

$$\Delta t_{cr} = \frac{L^e}{c_d} \tag{3.14}$$

$L^e$ is the characteristic length of the smallest element in the finite element model, and $c_d$ is the dilatational wave speed. Equation (3.15) provides $c_d$ for when Poisson's ratio is zero, where $E$ is the elasticity modulus of the material, and $\rho$ is its density. Note that a single element with either small size or mass, can therefore significantly reduce $\Delta t_{cr}$ for the entire analysis, even if the importance of that single element is physically negligible [93].

$$c_d = \sqrt{\frac{E}{\rho}} \tag{3.15}$$

Even when using a time step which is smaller than $\Delta t_{cr}$, the stability of the analysis is not guaranteed [93]. To ensure that an analysis truly is stable, an energy balance check must be performed. Solutions which oscillate with increasing amplitudes are often also an indication of the presence of numerical instabilities [74].

If it is desirable to decrease the critical time step even further, in order to ensure stability in highly nonlinear analyses, for instance, $\Delta t_{cr}$ can be multiplied by a constant time step scaling factor. In LS-DYNA it is for example recommended to use a time step scaling factor of 0.67 for blast loads [80].

### 3.5.3 Scaling

Because of the small time steps required for explicit analyses, they are commonly used for transient problems. However, it is often also advantageous to use explicit methods for other problems involving nonlinear effects, such as e.g. material strain-softening or contact. By introducing either mass or time scaling, the use of explicit finite element analyses can be expanded to include quasi-static problems.

Mass scaling aims at increasing the stable time increment $\Delta t_{cr}$ by upscaling the density of the material $\rho$ (see Equations (3.14) and (3.15)). There are two ways of doing so, namely fixed and variable mass scaling [74]. For fixed mass scaling the density is scaled uniformly for all elements. The scaling is performed only once and at the beginning of the load step. For variable mass scaling the scaling is performed in a similar manner, but periodically throughout the analysis, i.e. the amount of scaling varies.

Time scaling also aims at increasing the stable time increment but does so by speeding up the whole analysis. As time scaling increases the strain rates, it should only be used for constitutive models that are not rate dependant [93].

Neither mass nor time scaling should be used for dynamic problems where the response is dependant on inertia forces [93, 74]. To ensure that there are no dynamic effects present when applying mass or time scaling for a quasi-static problem, it should be checked that the ratio of kinetic to internal energy is less than approximately 10 % [74]. For the same reason, loads should be applied smoothly and are therefore typically ramped up during the first 10 % of the simulation time [93].

### 3.5.4   Mesh Dependency

It is not only the stable time increment which is dependant on the mesh size. Materials that undergo strain-softening, such as concrete, for example, may experience pathological mesh dependency. Pathological mesh dependency is a nonphysical phenomenon where the damage tends to zero as the mesh size tends to zero. The cause of this phenomena is that strain-softening leads to a loss of uniqueness which may cause the deformation to localize in narrow bands whose dimensions are determined by the characteristic element size [93].

Another mesh dependent parameter is element erosion. Element erosion is commonly used to model fracture propagation by removing an element from the finite element model if its damage has reached a critical value [93]. The modeling of damage by element erosion is therefore naturally mesh dependent.

# Chapter 4

# Experimental Testing of Concrete in Compression

To form a basis of comparison for numerical concrete models, uniaxial compression tests of concrete cubes are performed. Ideally, to validate the concrete models, the whole force-displacement curve is required, not only the compressive strength which is usually found from concrete compression tests.



**Figure 4.1:** Cube before testing.

## 4.1   Setup and Execution

Three B20 concrete cubes are tested in uniaxial compression. The cubes of approximately 50x50x50 mm are partitions of the concrete cubes cast in conjunction with the master thesis of Hillestad and Pettersen [48]. The concrete receipt can therefore be found as an attachment to their thesis. Since the cubes are partitions, the aggregates are clearly visible, see Figure 4.1.

**Table 4.1:** Measurements of concrete cubes for compression tests

| Cube no. | Length (mm) | Width (mm) | Weight in air (g) | Weight in water (g) | Density (g/cm$^3$) |
|---|---|---|---|---|---|
| 1-8 | 49.9 | 46.8 | 278.5 | 165.9 | 2.47 |
| 27-8 | 49.6 | 47.0 | 278.4 | 164.7 | 2.45 |
| 40-8 | 50.5 | 47.0 | 291.2 | 173.5 | 2.47 |

Before testing, the cubes are measured and inspected for imperfections. Only minor damages at the edges are observed. The measurements of the cubes can be viewed in Table 4.1. The density is calculated using Archimedes' principle [54], i.e. by dividing the weight in air by the difference between the weight in air and water, and multiplying it by the density of water.

In order to obtain the whole force-displacement curves, the tests are performed using a 250 kN Instron 5985. The cubes are compressed at a rate of 0.5 mm/min. The setup of the experiment is shown in Figure 4.2.

The force is directly logged from the machine, while the strain is afterward acquired using digital image correlation (DIC) . Therefore, for the DIC analyses, one side of the concrete cubes is painted with a speckle pattern, as can be seen in Figure 4.1. This painted side faces a camera which continuously takes pictures throughout the experiment, with a frequency of two frames per second.

**Figure 4.2:** Setup of compression tests.

## 4.2   Digital Image Correlation

Digital image correlation (DIC) is a method that allows for the measuring of e.g. strains by using an image series taken of an experiment. This is done by creating a kind of virtual extensometer. For the concrete compression tests, the displacements and strains are small, and there is extensive cracking. DIC may therefore not be optimal, but this is what will be examined.

The DIC software eCorr is used to perform the analyses. In the pre-processor, the first image of the series is uploaded and a mesh is generated. All cubes are analyzed using a structured Q4 mesh of 50x50 pixels. To prevent spalling from becoming an issue, the meshes are created well within the outer borders of the specimen. Finite element (FE) DIC analyses are then performed with the meshed reference frames and whole image series as input. Cube 40-8 is also analyzed using 25x25 and 100x100 pixels meshes in order to study the effect of mesh size.



**Figure 4.3:** Vectors for obtaining engineering strains from DIC analysis.

After the DIC analyses are completed, it is observed that the displacements are excessive at the later stages of the analyses. This is due to considerable cracking causing the meshes to severely distort. The analyses are therefore re-run using the multiscale coarse search function. This function is used for where the displacements from one frame to the next are large and correlation is lost. For this, an FFT mask size of 100 and super Q4 is utilized.

The engineering strain (denoted vElong in eCorr) is measured for ten vectors spanning in the load direction in the middle of the cube surface. For all images, the load direction is horizontal from left to right. The vectors are numbered from top to bottom, and the placement and numbering of the vectors can be seen in Figure 4.3. An average engineering strain is calculated from the vectors.

Additionally, the first principal strain distribution is examined in the DIC analyses. Note that principal strain is not the same as engineering strain. A principal strain plane is a plane where all the shear strains are zero, and the first principal strain is the largest of the normal strains in this plane. Furthermore, it is important to note that after cracking the strains in the cracks are not real.

### 4.2.1 Cube 1-8

For cube 1-8, multiscaling is used for frame number 383 since the displacements from frame 382 to 383 seem to be particularly large. The effect of multiscaling is illustrated by the first principal strains in Figure 4.4 and the residuals in Figure 4.5. When not using multiscaling, the poor correlation can be observed from how the mesh is distorted and from how the high strains and residuals are not localized at the cracks.



**(a)** Frame 383      **(b)** Before      **(c)** After
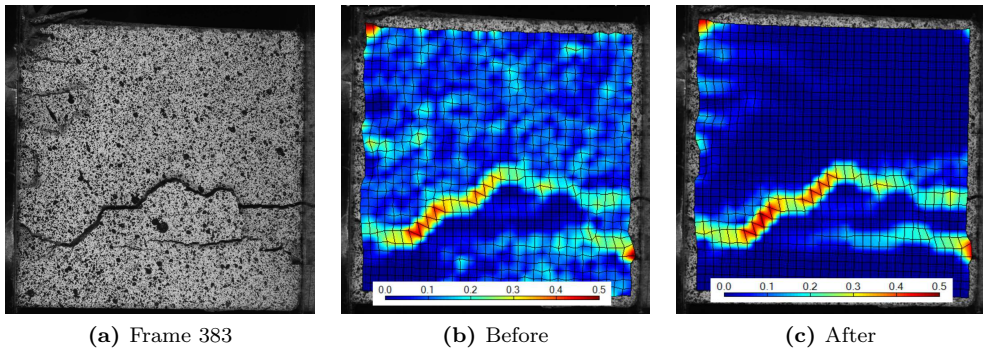
**Figure 4.4:** First principal strains for frame 383 before and after using multiscaling for DIC analysis of cube 1-8.



**(a)** Frame 383      **(b)** Before      **(c)** After
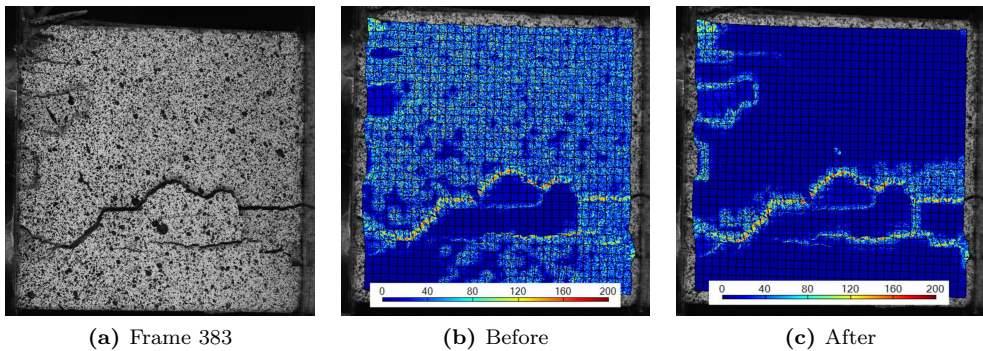
**Figure 4.5:** Residuals for frame 383 before and after using multiscaling for DIC analysis of cube 1-8.

The engineering strains obtained from the DIC analysis of cube 1-8 using multiscaling are presented in Figure 4.6. Up to a certain point, all vectors produce almost exactly the same engineering strain. For cube 1-8 there seem to be two points where there are possible losses of correlation. The first such point occurs for frame 332 where the engineering strains of four of the vectors deviate from the remaining strains, see Figure 4.8. These four vectors are the upper vectors. Frame 332 and the preceding frame are therefore more closely



**Figure 4.6:** Engineering strains obtained from DIC analysis of cube 1-8.

examined in Figure 4.8. However, from these images, it is difficult to determine the reason for the discrepancies, but nothing suggests that the correlation is poor as the mesh structure remains intact.

Furthermore, the residuals of frame 331 and 332 are examined in Figure 4.7 by using an inverted grey color map and manual scaling such that small residuals are more visible. It is now observable that a piece of concrete is beginning to detach from the cube in the middle left part of Figure 4.7b. The crack propagation and the evolvement of the detaching concrete piece can also be seen in Figure 4.10. Since the six lower vectors are attached to this piece of concrete that breaks off, while the upper four vectors are not, the strains differ.



(a) Frame 331      (b) Frame 332
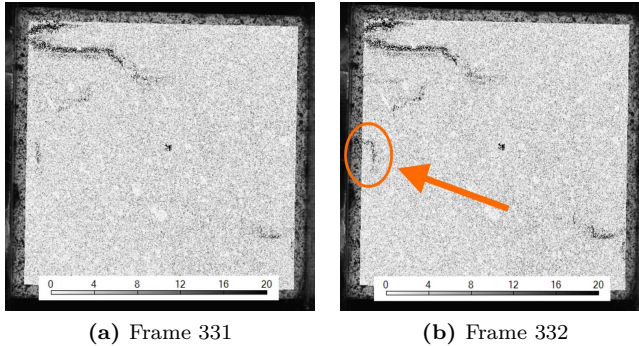
**Figure 4.7:** Residuals for selected frames from DIC analysis of cube 1-8.

The second point of possible loss of correlation for cube 1-8 seems to be at frame 383, see Figure 4.8a. This is the frame for which multiscaling was applied. When examining and comparing the cracking for frame 382 and 383 in Figure 4.8, it can be seen that there is no bad correlation, except for in the cracks. However, the vectors for obtaining the engineering strains span in the area with significant cracking, and this is most probably the reason for why the strains deviate after frame 382.

Figure 4.9 displays some selected frames and the corresponding first principal strains from the DIC analysis of cube 1-8. For frame 330 and 340, there is only minor cracking in the very utmost top part of the left corner. For frame 350, a longer crack through the slight lower middle is barely visible, and for frame 360, this crack is more visible, along with

other smaller cracks. For frame 370 and 380, the cracks are evident. It is apparent that the DIC analysis is able to render the cracking long before it is visible to the naked eye. The crack propagation is also clearly visible when the corresponding residuals from the DIC analysis are plotted using a grey inverted color map in Figure 4.10.
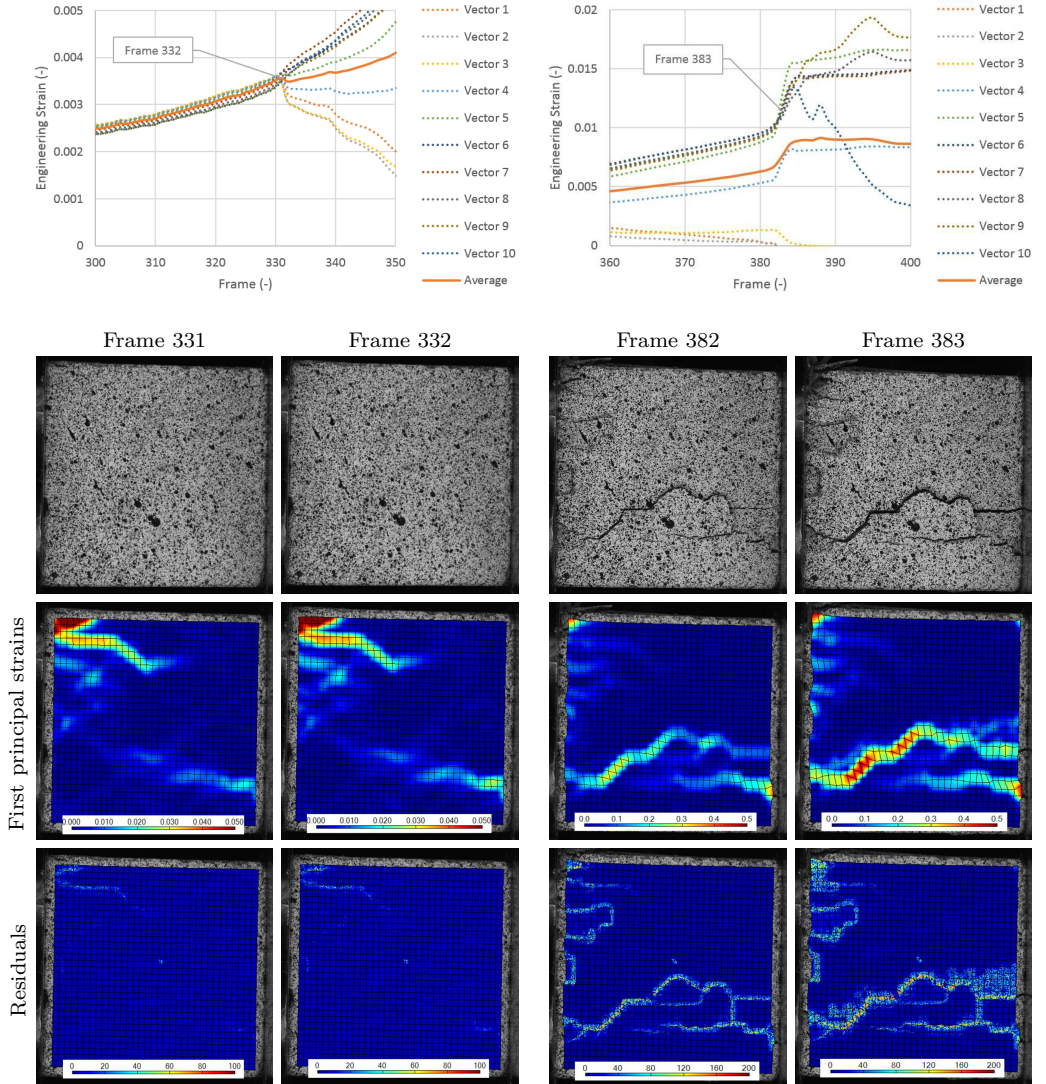


**Figure 4.8:** Examination of possible loss of correlation for DIC analysis of cube 1-8.

**(a)** Frame 330      **(b)** Frame 340      **(c)** Frame 350

**(d)** Frame 360      **(e)** Frame 370      **(f)** Frame 380
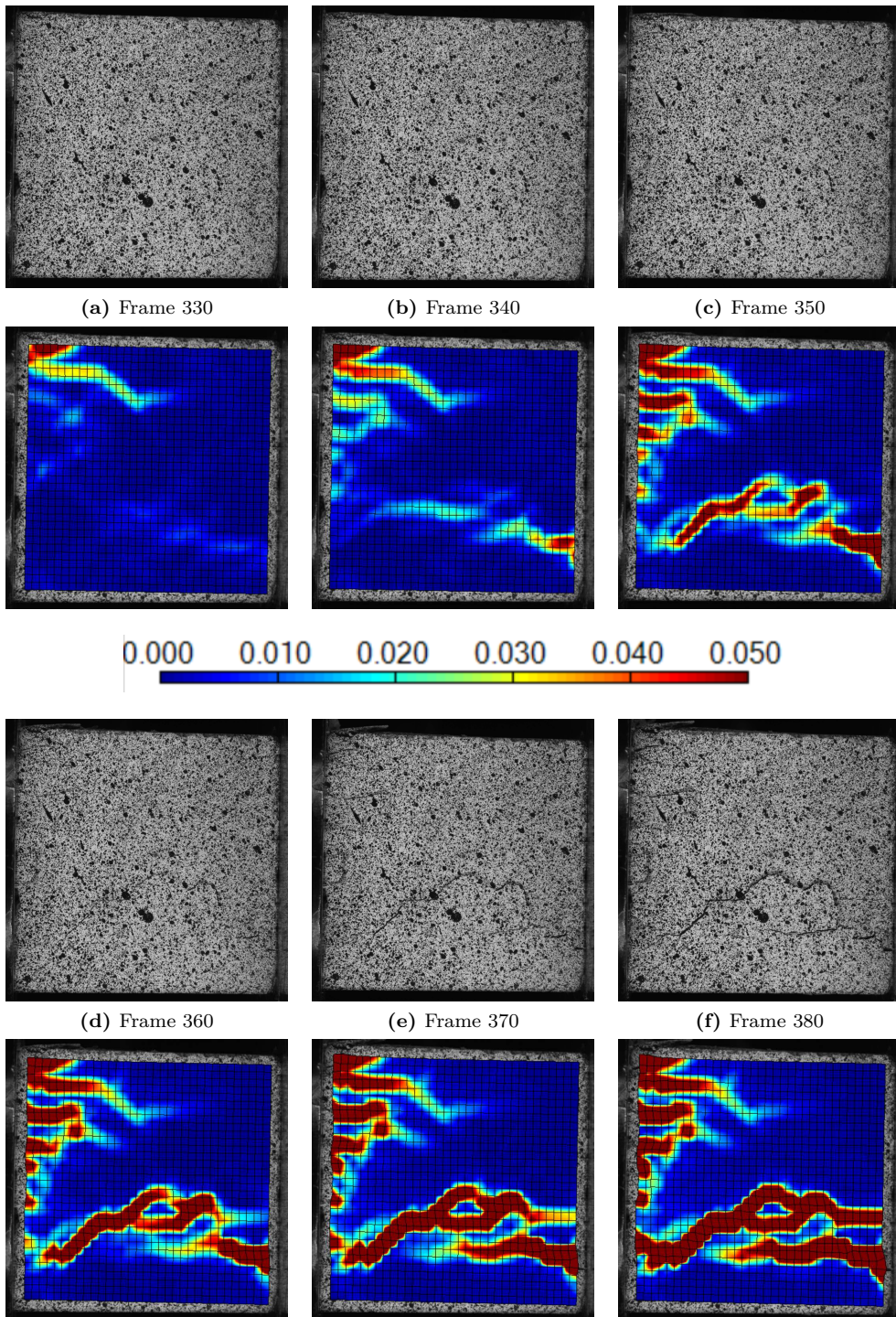
**Figure 4.9:** Selected frames and the corresponding first principal strains from the DIC analysis of cube 1-8.

**(a)** Frame 330        **(b)** Frame 340        **(c)** Frame 350



**(d)** Frame 360        **(e)** Frame 370        **(f)** Frame 380
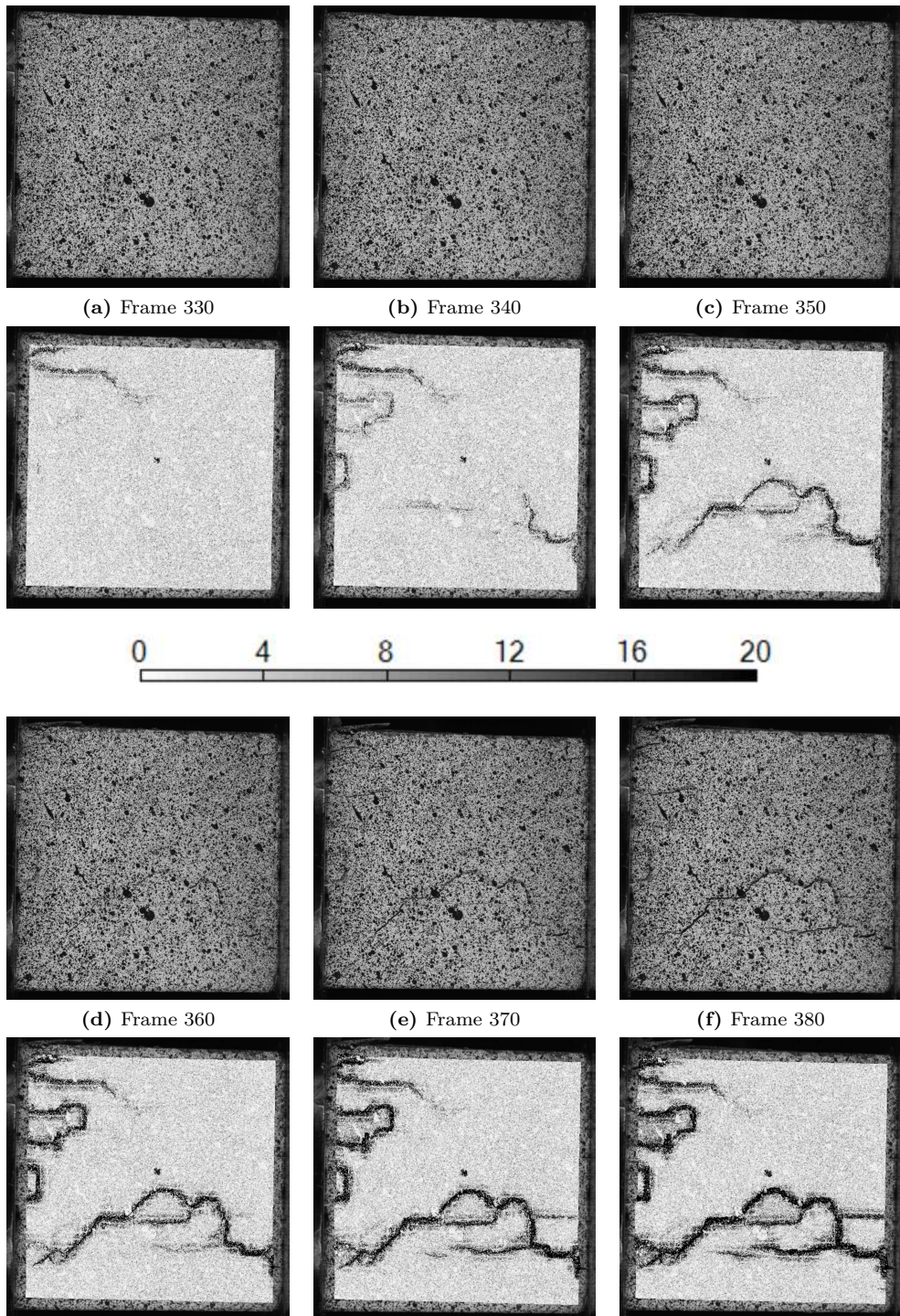
**Figure 4.10:** Selected frames and the corresponding residuals from the DIC analysis of cube 1-8.

## 4.2.2   Cube 27-8

A DIC analysis is performed for cube 27-8 using the same approach as for cube 1-8. Multiscaling is used for frame 499 since the displacements from frame 498 to 499 are large.
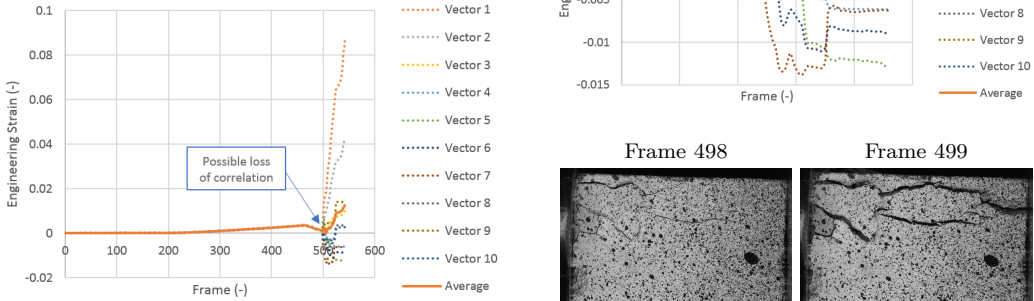


**Figure 4.11:** Engineering strains obtained from DIC analysis of cube 27-8.

The engineering strains obtained from the DIC analysis of cube 27-8 is presented in Figure 4.11. Similarly to cube 1-8, all vectors provide the same engineering strain up to a certain frame. It is therefore examined if there is a loss of correlation for this frame. The frame in question is frame 499 for which multiscaling was used. From Figure 4.12 it is clearly an increase in first principal strains, mesh distortion, and residuals from frame 498 to 499, and thus correlation is apparently lost.
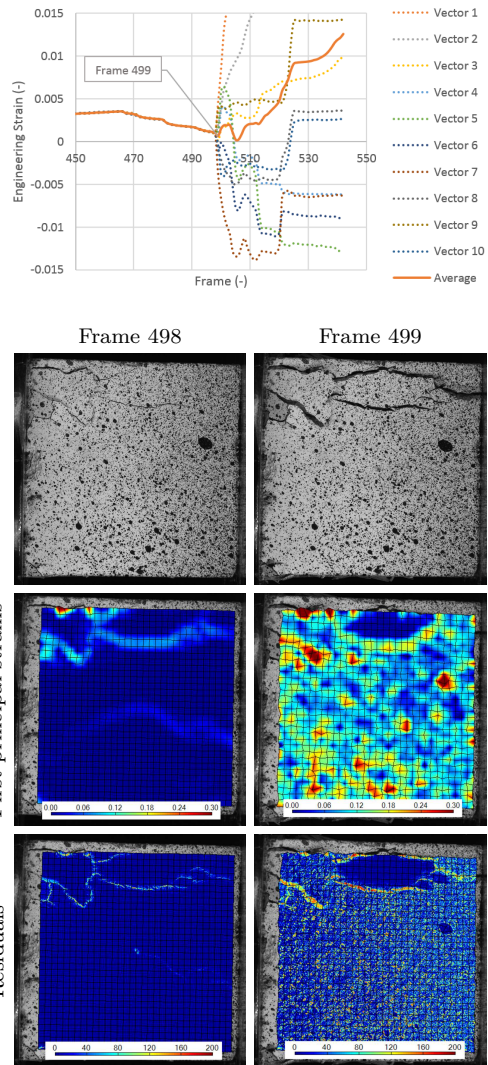


**Figure 4.12:** Examination of possible loss of correlation for DIC analysis of cube 27-8.

In an attempt to improve the correlation for frame 499, the DIC analysis is re-run using multiscaling with several steps. The first multiscaling step uses an FFT mask size of 40, along with a rigid body DIC type. The second step uses a mask size of 80, along with super Q4, while the last step uses mask size 120 and super Q8. The first principal strains and residuals are again examined (Figure 4.14) and now there only seems to be poor correlation in the upper part of the cube which is severely cracked. The engineering strains are once again obtained, and the significantly improved results are presented in Figure 4.13.
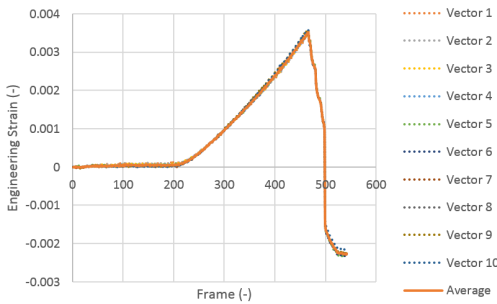


**Figure 4.13:** Engineering strains obtained from DIC analysis of cube 27-8 using several steps of multiscaling.
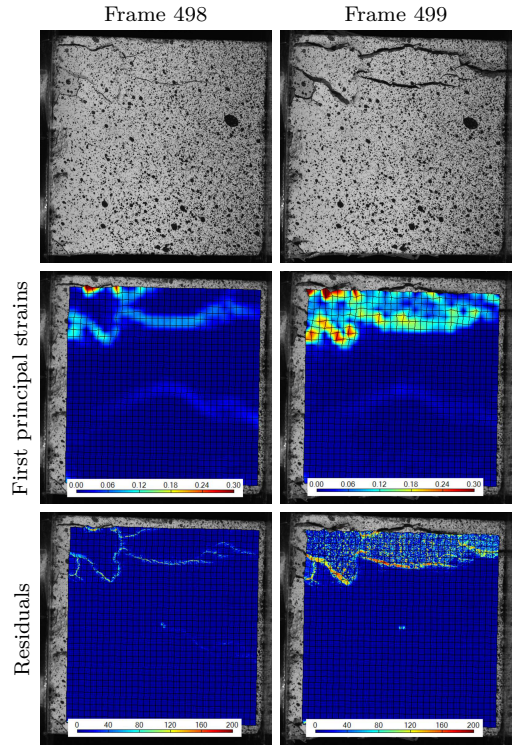


**Figure 4.14:** Examination of possible loss of correlation for DIC analysis of cube 27-8 when using several steps of multiscaling.

### 4.2.3 Cube 40-8

The compression of cube 40-8 is also analyzed using DIC. Multiscaling is applied for frame 362 where the displacements are large. The engineering strains from the analysis are provided in Figure 4.15. Unlike the results for the previous cubes, there are no large deviations after a certain frame number, and there is therefore no obvious loss of correlation.

Although there seems to be no loss of correlation in Figure 4.15, the frame for which multiscaling was used is examined in Figure 4.16. Although the correlation is
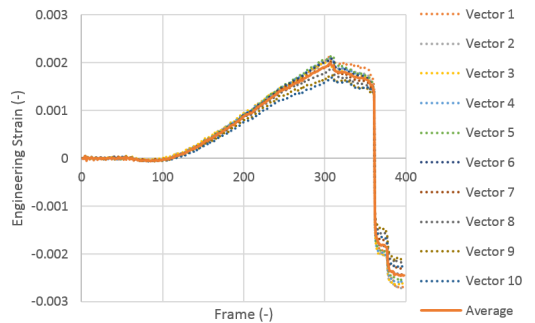


**Figure 4.15:** Engineering strains obtained from DIC analysis of cube 40-8.

clearly bad for the upper part of the cube, the correlation is good for the middle part where the engineering strains are measured. In Figure 4.16 it is also checked to see if this

is also the case for the last frame. Despite substantial cracking and mesh distortion, the middle part of the cube is relatively intact. Since all the engineering strains are measured within this area that is most likely the reason for why there was seemingly no loss of correlation in Figure 4.15.
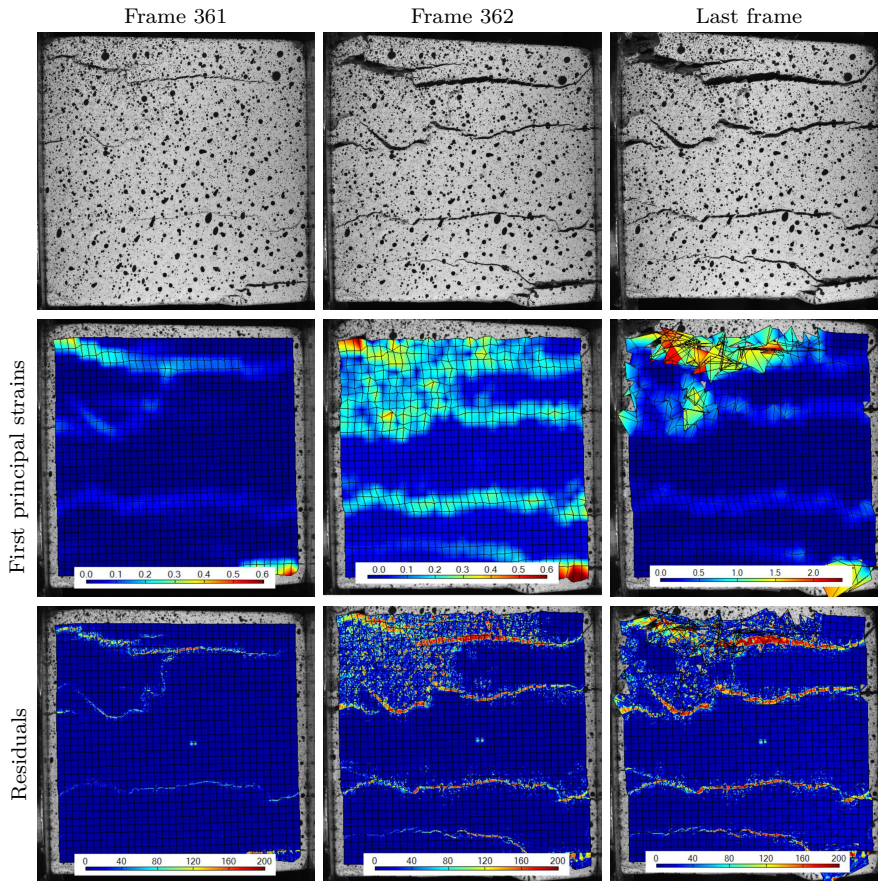


**Figure 4.16:** Examination of why there seems to be no loss of correlation in the DIC analysis of cube 40-8.

### 4.2.4 Effect of Mesh Size

Furthermore, the effect of mesh size in the DIC analyses is examined. Since there were little deviations in the results for cube 40-8, this cube will be used for the DIC mesh size study. A 50x50 pixels mesh was used for the analyses of all three cubes. Cube 40-8 is therefore additionally analyzed using 25x25 and 100x100 pixels meshes. Except for mesh size, no parameters are changed and the analyses are conducted in the exact same manner as previously. The resulting engineering strains can be seen in Figure 4.17.

**(a)** 25x25 mesh
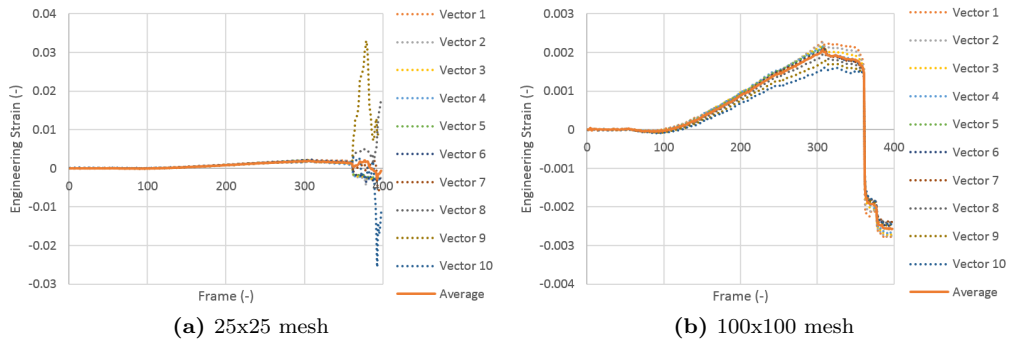
**(b)** 100x100 mesh

**Figure 4.17:** Engineering strains obtained from DIC analysis of cube 40-8 using various mesh sizes.

While the 100x100 mesh provides what seems to be an almost identical solution to that of the 50x50 mesh, the results obtained using the 25x25 mesh differ. The reason for this is that a smaller mesh will generate more numerical noise, while this noise is damped out for the larger meshes. A comparison of the average engineering strains obtained for the different mesh sizes is available in Figure 4.18.
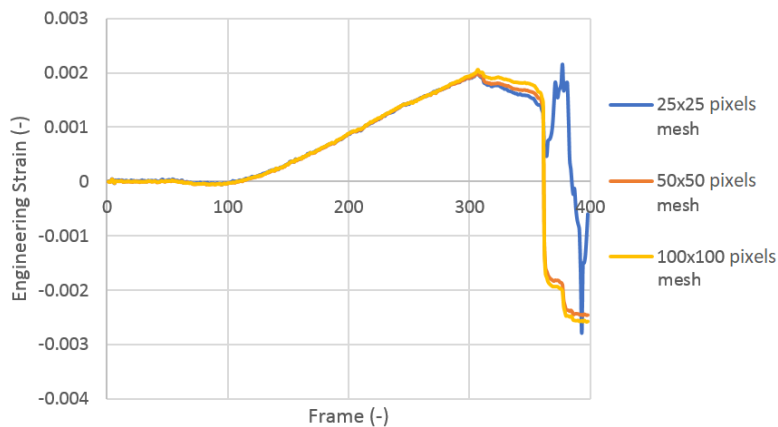


**Figure 4.18:** Average engineering strains obtained from DIC analyses of cube 40-8 using various mesh sizes.

Although numerical noise is a disadvantage of smaller meshes, the crack propagation is not as clear if the mesh is too large. This is illustrated in Figure 4.19. Also visible in Figure 4.19 is the numerical noise for the 25x25 mesh. This noise can be seen in the form of severe mesh distortion and large first principle strains in the middle of the specimen. In reality there seems to be no cracking at this location, but instead a small shade. This shade can in fact be observed in the residuals of the DIC analyses of all three cubes (Figure 4.20), and is therefore most likely caused by insufficient cleaning of the camera lens. Another disadvantage of a smaller mesh is that the analysis takes longer.

**(a)** Frame 358    **(b)** 25x25 mesh    **(c)** 50x50 mesh    **(d)** 100x100 mesh
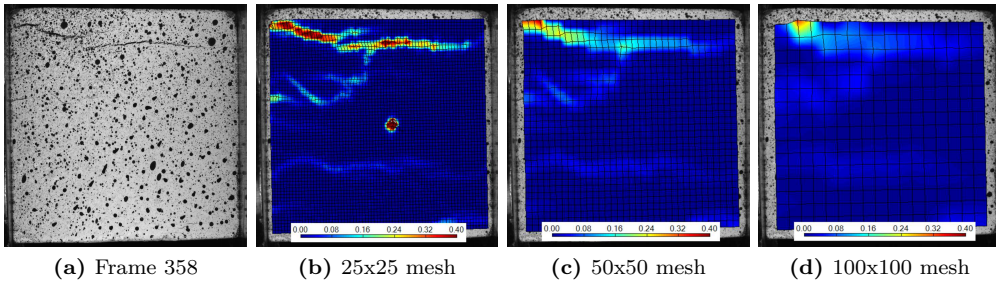
**Figure 4.19:** First principle strains for frame 358 from DIC analysis of cube 40-8 using various mesh sizes.



**(a)** Frame 358    **(b)** 25x25 mesh    **(c)** 50x50 mesh    **(d)** 100x100 mesh
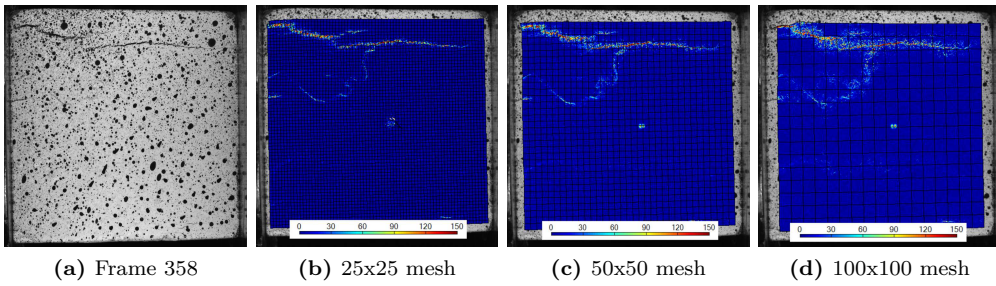
**Figure 4.20:** Residuals for frame 358 from DIC analysis of cube 40-8 using various mesh sizes.

In conclusion, a mesh size of 50x50 pixels appears suitable for this problem since it produces little numerical noise and at the same time renders the crack propagation with sufficient accuracy.

## 4.3   Results

Concrete cube 27-8 after testing is shown in Figure 4.21 where substantial cracking and spalling can be observed.

In Table 4.2 the compressive strength is calculated for each concrete cube by dividing the maximum force by the load surface area of the cube. Recall that the force was logged directly from the test rig.



**Figure 4.21:** Cube 27-8 after testing.

**Table 4.2:** Calculation of compressive strength.

| Cube no. | Area (mm$^2$) | Maximum force (kN) | Compressive strength (MPa) |
|---|---|---|---|
| 1-8 | 2335.3 | 164.90 | 70.61 |
| 27-8 | 2331.2 | 183.73 | 78.1 |
| 40-8 | 2373.5 | 161.67 | 68.11 |

Since the cubes are small, the concrete behavior is heterogeneous resulting in large strength differences for the three cubes. The average compressive strength is 72.51 MPa, and the standard deviation is 5.60 MPa. However, three tests are not really a sufficiently large sample set to represent a stochastic process.

The concrete cubes originate from Hillestad and Pettersen's master thesis in 2016 [48]. Since then the cubes have been kept soaked in water. Hillestad and Pettersen studied the effect of curing time on the compressive strength. They found that the strength $f_c$ could be expressed by Equation (4.1) where $t$ is the curing time in days. This function for $f_c$ is compared to their test results ain Figure 4.22.

$$f_c(t) = \frac{217.8t}{10.29 + 4.22t} \tag{4.1}$$

If Equation (4.1) is used to estimate the compressive strength of the cubes tested for this thesis, and thus the curing time is approximately two years, one gets $f_c = 51.44$ MPa. This is much lower than the results from the experimental testing (Table 4.2). However, as seen in Figure 4.22, Hillestad and Pettersen also got a large discrepancy from the function for the concrete cubes that were tested after 84 days. Besides, Equation (4.1) was fitted to results from compression tests of larger cubes which may also explain the large deviance between the estimated and measured strength of the cubes tested in this thesis.
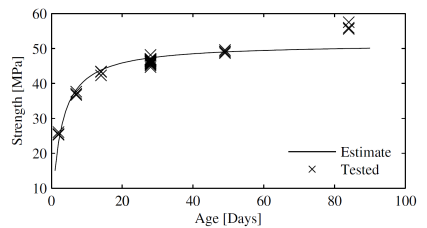


**Figure 4.22:** B20 concrete strength as a function of curing time. Credit: Hillestad and Pettersen [48].

While the engineering strains are obtained using DIC as described in the previous section, the forces are logged directly from the test rig during testing. Since the engineering stress is simply the force divided by the initial load surface area, the engineering stress-strain curves in Figure 4.23a are established. Note that only the smooth continuous parts of the curves are plotted.



**(a)** Obtained from DIC



**(b)** Measured from test rig
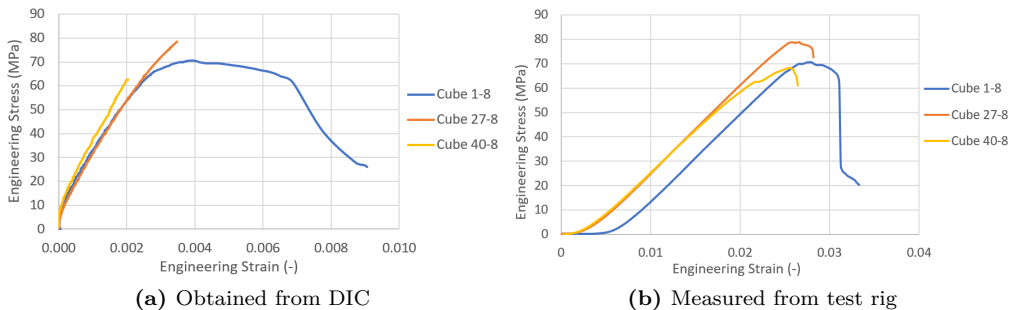
**Figure 4.23:** Engineering stress-strain curves for all cubes.

In addition to logging the force, the test rig also logs the displacements. The engineering stress-strain curve in Figure 4.23b is obtained using these logged displacements. It is observed that these strains are much larger than those obtained using DIC. Since the forces for these tests are large and the displacements are very small, the large differences in strain could be due to deformations in the test rig.
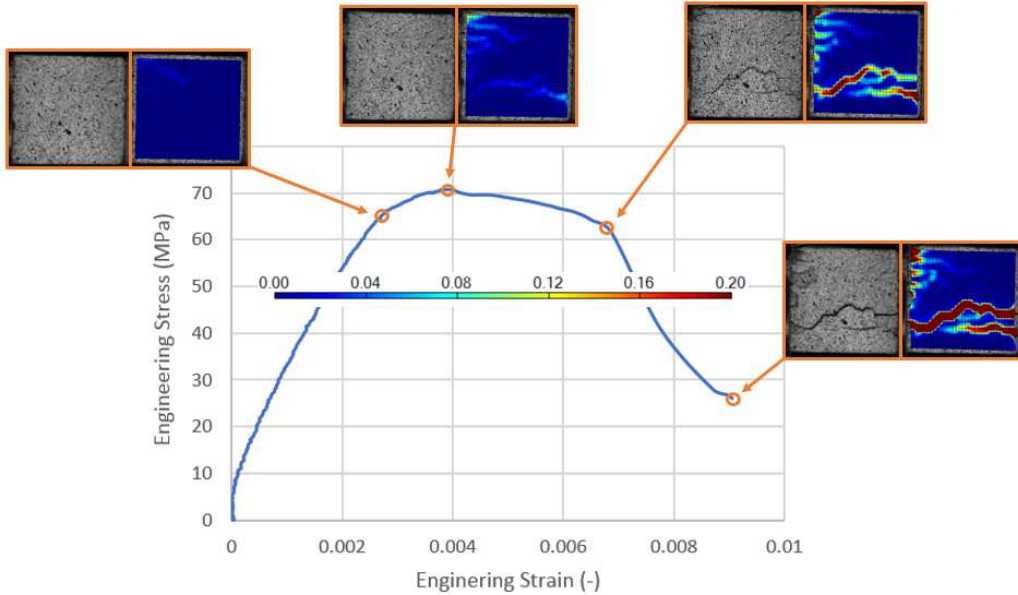


**Figure 4.24:** Engineering stress-strain curve for cube 1-8 obtained using DIC. Images of the cube with corresponding first principle strain distribution are displayed for selected frames. The scale for the first principal strain distributions is provided in the center of the figure.

In Figure 4.24 certain interesting points along the engineering stress-strain curve for cube 1-8 are selected, and the corresponding images and DIC first principal strains are displayed. Note that there is almost no visible cracking for the maximum force, except for a small crack in the upper left corner.

# Chapter 5

# Numerical Simulation of Concrete in Compression

The uniaxial compression test of concrete cube 1-8 is simulated numerically using FE codes. This is done in an attempt to calibrate and assess the numerical concrete models before proceeding to more complex simulations involving blast loads.

## 5.1 ABAQUS

### 5.1.1 Reference Model

A reference model of the compression test of concrete cube 1-8 is established in ABAQUS. Cube 1-8 is chosen since it was the only experiment for which the DIC analysis provided the post-peak part of the engineering stress-strain curve. The actual measured size of the cube, 49.9x46.8x48.6 mm, is modeled.

Since the confining contact forces are large for cubes in compression, an explicit numerical method is used. Because the experimental test was quasi-static, time-scaling is applied, and while the experiment took 209 s, the simulation time of the ABAQUS model is set to 209 ms. Double precision is used for better accuracy as the number of increments may get large.

Despite high confining pressures, the CDP model is used to describe the concrete material properties which are defined as described in Section 3.3.2. No scaling of the material parameters is used for the reference model.

For the concrete cube, solid elements with eight nodes, reduced integration, and hourglass control, that is C3D8R elements, are utilized with a mesh size of approximately 5x5x5 mm. This results in a total of 900 elements.

The test rig is modeled as two analytically rigid plates. One of the plates is kept completely fixed. For the second plate, all degrees of freedom (DOF) are fixed, except the displacement in the load direction since the load is imposed as a velocity on this plate.

The load velocity is ramped up over the first ten percent of the simulation time to try to avoid unwanted dynamic effects due to time-scaling.

Contact is defined between the cube and the plates using penalty method. The friction coefficient is set to 0.57 as this is the friction coefficient between dry concrete and steel recommended in [95].



(a) Engineering stress-strain curve          (b) Energy balance check
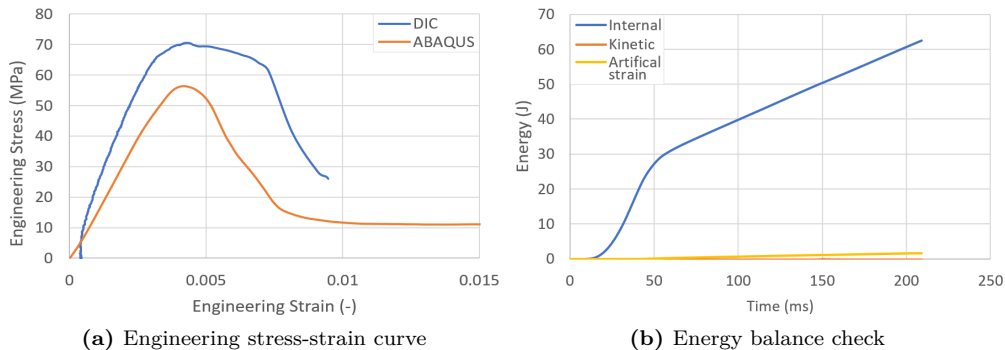
**Figure 5.1:** ABAQUS reference model of concrete compression test.

The displacements and contact forces of the load plate are used to calculate the engineering stress and strain. The resulting engineering stress-strain curve for the ABAQUS reference model of the compression test can be seen in Figure 5.1a. The shape of the curve looks similar to that obtained by DIC analysis of the experimental test. The ABAQUS model of the compression test even renders a residual strength of the concrete. The peak value, however, is too low, but this is to be expected as the concrete material parameters have not yet been scaled.

Since time-scaling is used, it is important to perform an energy balance check in order to examine that there are no numerical instabilities. From Figure 5.1b it is observed that the kinetic energy is very low compared to the internal energy and nothing suggests that there are any numerical instabilities present. However, the artificial strain and internal energy ratio is 2.5 % and therefore slightly high as it according to [96] should not exceed 1-2 %.

### 5.1.2 Parametric Study

The effect of varying parameters of the ABAQUS reference model is checked. This is done by varying one parameter at a time. The effect of varying multiple parameters simultaneously is not studied. The energy balance is examined for every simulation.

#### *Friction Coefficient*

Since the confining forces are high for cubes in compression, the effect of varying the friction coefficient is the first to be studied. In Figure 5.2a the reference model is the one with a friction coefficient of 0.57.

**(a)** Engineering stress-strain curve

**(b)** Energy balance check for frictionless model
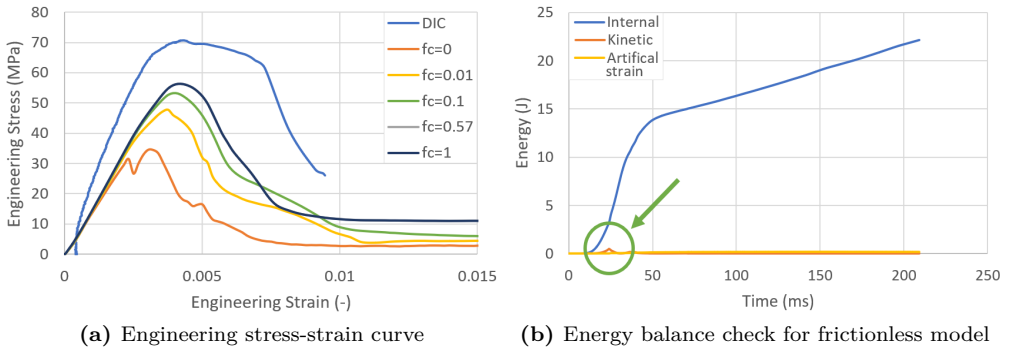
**Figure 5.2:** ABAQUS model of compression test with varying friction coefficient (fc).

From Figure 5.2a it is observed that including friction makes a large difference compared to a frictionless analysis, even if the friction coefficient is very small. If the friction coefficient is 0.1 or 1 does, however, not make much difference. Furthermore, when the analysis is frictionless there is a small leap in the kinetic energy, Figure 5.2b, suggesting that the solution might be numerically unstable.

### *Mesh Size*

The mesh size affects both the CPU time and often also the solution. Mesh size is therefore the second parameter to be examined. In Figure 5.3 the mesh size of the reference model with 900 elements is halved and doubled. The results of the simulations using various mesh sizes can be seen in Figure 5.4a.



**(a)** 125 elements      **(b)** 900 elements      **(c)** 7220 elements
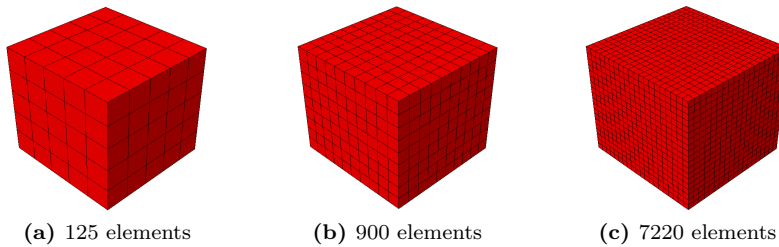
**Figure 5.3:** Various mesh sizes for ABAQUS model of compression test.

As expected from the theory presented in Section 3.3.2, the model displays a pathological mesh dependence as the concrete is not reinforced. The pathological mesh dependency can be observed in Figure 5.4a where mesh refinement leads to a narrower stress-strain curve. Further mesh refinement would eventually lead to a nonphysical stress-strain curve. Pathological mesh dependency is described more detailedly in Section 3.5.4.

**(a)** Engineering stress-strain curve        **(b)** CPU time
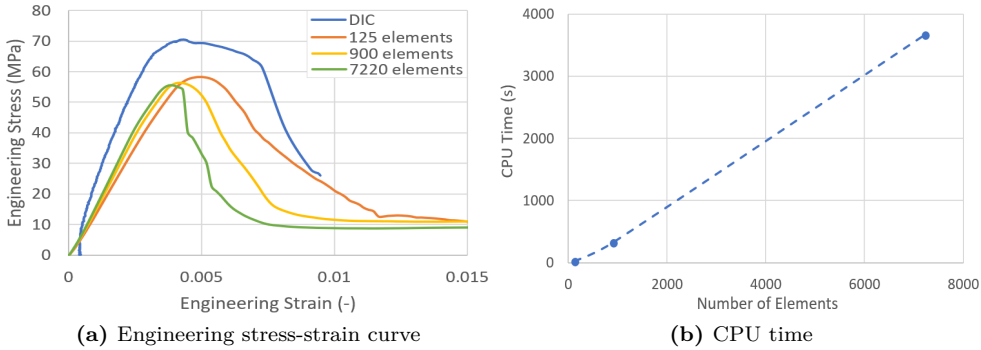
**Figure 5.4:** ABAQUS model of concrete compression test with varying mesh size.

In Figure 5.4b the CPU time is plotted for the various mesh sizes and, not surprisingly (see Section 3.5.2), the CPU time increases when the mesh is refined.

### *Time Scaling*

Time scaling was used for the reference model in order to reduce the computational time. The effect of varying the simulation time is checked, and the result is presented in Figure 5.5 where a simulation time of 209 ms corresponds to the reference model.



**(a)** Engineering stress-strain curve     **(b)** Number of increments (Note that the y-axis is logarithmic)
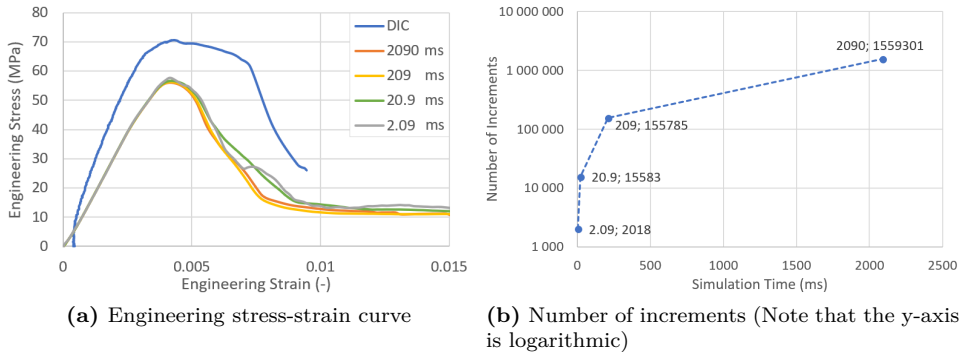
**Figure 5.5:** ABAQUS model of concrete compression test with varying simulation time.

As seen in Figure 5.5a, the simulation time does not considerably impact the result. However, the stress-strain curve seems to eventually become unstable when the simulation time is increased. By increasing the simulation time the number of increments also decreases drastically as illustrated in Figure 5.5b. Even though double precision is used, round-off error is most likely the explanation for the instabilities observed for the analysis with a simulation time of 2090 ms. Furthermore, the stress-strain curve is less smooth when the simulation is run very fast at only 2.09 ms, but even then the kinetic energy level is acceptable.

### Mass Scaling

Since concrete is known to be rate dependent, mass scaling may be preferable to time scaling (see Section 3.5.3). The semi-automatic mass scaling function of ABAQUS is therefore examined. This is done by firstly increasing the simulation time of the reference model to equal the actual duration of the experiment, i.e. 209 s instead of 209 ms. The load rate is thus decreased correspondingly. The target increment time of the mass scaling is chosen such that the total number of increments is approximately equal to when time scaling was used.



**Figure 5.6:** Engineering stress-strain curve for ABAQUS model of concrete compression test using time and mass scaling.

From Figure 5.6 it seemingly makes no difference whether one uses time or mass scaling for this particular problem. The energy levels are also examined, as always, but also these are the same.

### Scaling of Material Parameters

The material parameters for the reference model correspond to a B50 concrete. These can be scaled by multiplying the input compression stresses and strains by a scaling factor, as explained in Section 3.3.2. Since the simulation is already performed with no scaling, the scaling factor can easily be obtained by dividing the desired strength by the strength from the unscaled simulation. A scaling factor of 1.245 is therefore used, and the result is presented in Figure 5.7.



**Figure 5.7:** Engineering stress-strain curve for ABAQUS model of concrete compression test with scaled compression stress and strain.

The scaled model renders the compressive strength of the experimental test well, but the experimental stress-strain curve is stiffer.

### Young's Modulus

In an attempt to increase the stiffness of the stress-strain curve of the numerical model, Young's modulus $E$ is examined. The Young's modulus determined by Jankowiak and Lodygowski [79] in Figure 3.13 for a B50 concrete, and which has been used for the reference model, is 19.7 GPa. In Section 3.3.1 the equation for scaling of Young's modulus with respect to time, proposed by Eurocode 2, was presented (Equation (3.1)). By applying this equation with $E = 19.7$ GPa for the B50 concrete, for the concrete of the cubes

with a strength of 70.61 MPa, an estimate of Young's modulus is found to be $E = 21.8$ GPa.



**(a)** Scaling of only $E$

**(b)** Scaling of compressive material parameters when $E = 32$ GPa
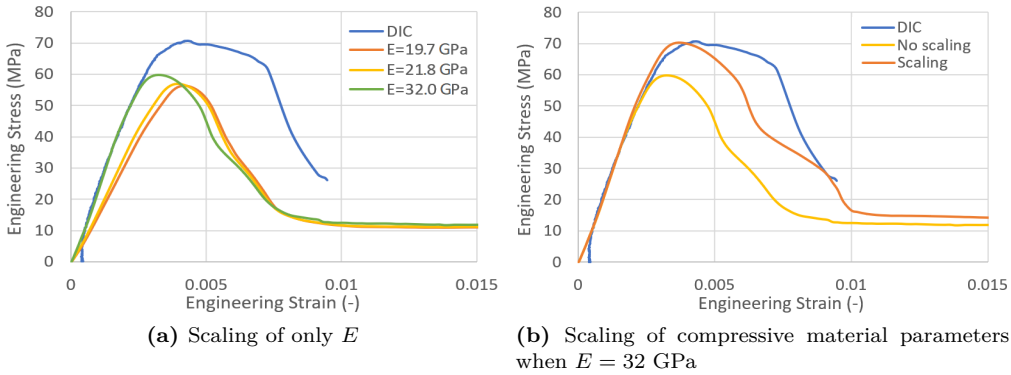
**Figure 5.8:** Engineering stress-strain curve for ABAQUS model of concrete compression test with varying Young's modulus $E$.

In Figure 5.8a the suggested values of $E$ are applied for the reference model. It is observed that when $E$ is scaled according to the Eurocode, $E = 21.8$ GPa, the resulting stress-strain curve is very similar to that with the unscaled $E = 19.7$ GPa. Therefore, a third value of $E$ is obtained by trial and error to best possible fit the experimental stress-strain curve. This value is found to be much higher, $E = 32.0$ GPa, and a very good fit to the elastic part of the experimental stress-strain curve. In Figure 5.8b it is therefore attempted to scale the compressive material parameters when $E = 32.0$ GPa. Up until the ultimate strength, the numerical model is now an almost perfect match. However, the post-peak behavior is slightly underestimated.

### Random Element Strength

The random element strength (RES) method assigns the concrete elements randomly to sets with different strengths according to a user-defined normal distribution. The method is described in Section 3.3.3 and a MATLAB script is used to implement RES in ABAQUS by altering the input file.



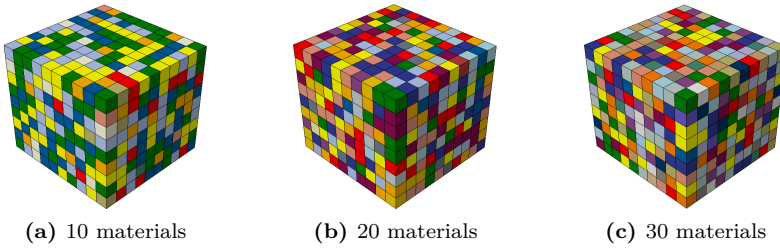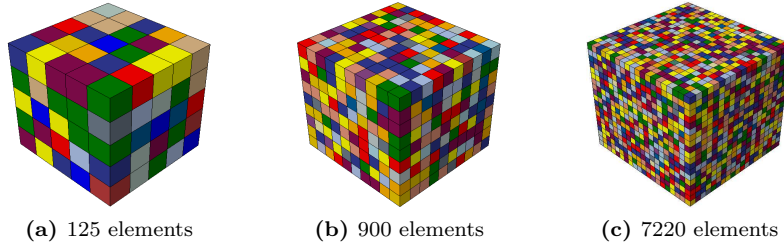**(a)** Sim. 1　　　　　　　**(b)** Sim. 2　　　　　　　**(c)** Sim. 3
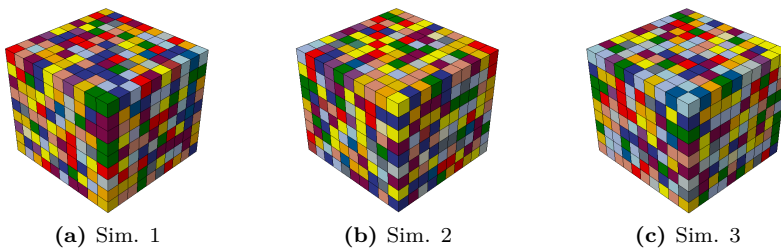
**Figure 5.9:** Distribution of element strengths for the three first ABAQUS simulations of the concrete compression test using random element strength modeling. Each color corresponds to a different strength.

When the script is used with 20 material strengths with a mean of 72.51 MPa and a standard deviation of 5.60 MPa (as calculated in 4.3), the engineering stress-strain curves

in Figure 5.10a are obtained. Figure 5.9 shows how the elements are assigned various strengths for the three first simulations using RES, where each color represents a concrete material with a slightly different strength. Ten simulations are run with the same mean strength and standard deviation in order to see how much the results differ. The results vary very little and the strength is overestimated.



**(a)** RES            **(b)** Modified RES
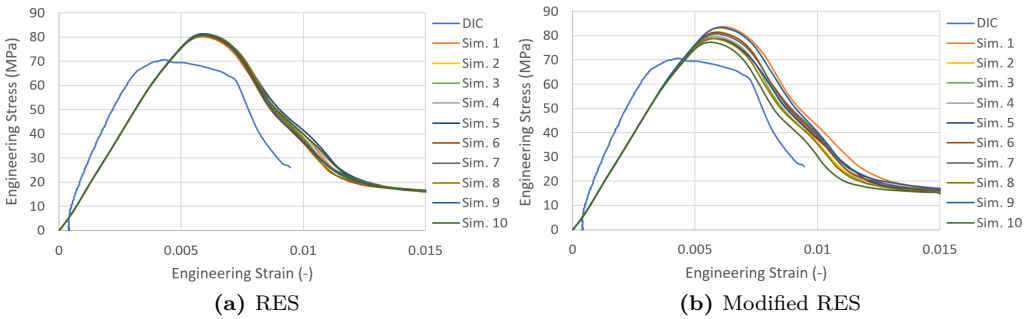
**Figure 5.10:** Engineering stress-strain curves for ten ABAQUS simulations of concrete compression test using regular and modified random element strength method (RES).

In an attempt to increase the variation for the numerical simulations and make it resemble the variation in the results from the experimental testing, the MATLAB script is modified such that also the different material strengths are generated randomly according to a normal distribution.

Ten new simulations are run using the modified script. The number of materials, the mean, and the standard deviation remain unchanged, and the results are presented in Figure 5.10b. The results now vary much more from one simulation to another. Since this modified random element strength method seems more promising, it will be further examined.

As was shown in Figure 5.10b the stress-strain curves vary even when the user-defined input is kept constant. Therefore, it will be difficult to perform a parameter study on the user-defined inputs without conducting a very large number of simulations to observe a trend. However, a small parameter study with few simulations is still performed to see if the method behaves as expected.

As discussed in Section 4.3, the sample set is small and thus the calculated mean strength and standard deviation may not be representative. The effect of varying these two parameters is therefore examined. For Figure 5.11a the mean is varied while the standard deviation is kept constant, and opposite for Figure 5.11b.

**(a)** Varying mean strength

**(b)** Varying standard deviation (Std)
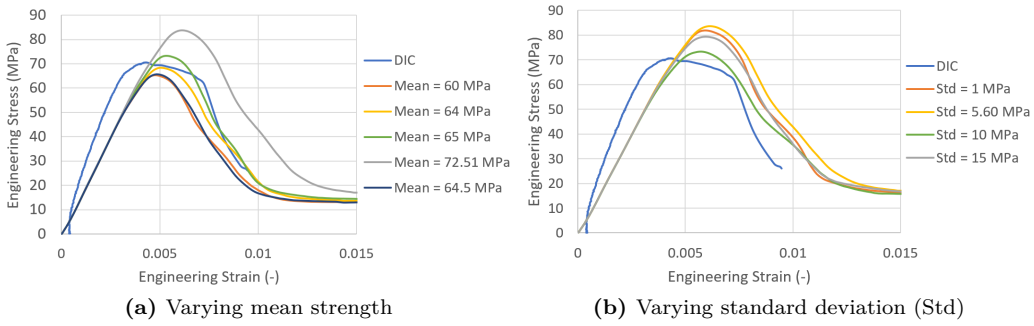
**Figure 5.11:** Engineering stress-strain curve for ABAQUS model of concrete compression test using modified random element strength.

Reducing the mean concrete strength should consequently reduce the stress, which does in fact seem to be the trend in Figure 5.11a. A mean strength of roughly 64-65 MPa appears to best render the experimental results. Increasing the standard deviation should also decrease the stress. If this is the case for this method is difficult to say for certain from Figure 5.11b, although there clearly is an effect of altering the standard variation.



**(a)** 10 materials

**(b)** 20 materials

**(c)** 30 materials

**Figure 5.12:** Distribution of element strengths for ABAQUS simulations of the concrete compression test using random element strength modeling with a various number of materials. Each color corresponds to a different strength.

Figure 5.12 shows the distribution of element strengths when the number of material strengths is varied. In Figure 5.13a it is illustrated that the effect of varying the user-defined number of material strengths, is relatively small.



**(a)** Varying number of materials

**(b)** Varying mesh size
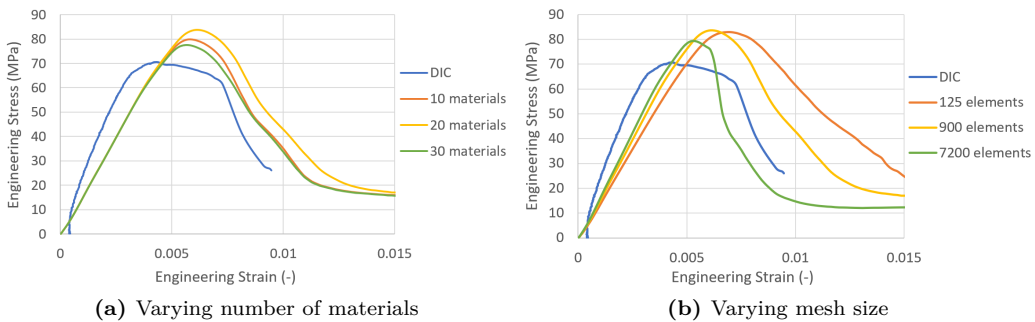
**Figure 5.13:** Engineering stress-strain curve for ABAQUS model of concrete compression test using the modified random element strength method.

Lastly, the effect of mesh size is studied for when the modified random element strength method is used. The result is presented in Figure 5.13)b where the same pathological mesh dependency can be observed as when not using random element strength (Figure 5.4). Figure 5.14 illustrates the distribution of element strengths for different mesh sizes.



**(a)** 125 elements      **(b)** 900 elements      **(c)** 7220 elements

**Figure 5.14:** Distribution of element strengths for ABAQUS simulations of the concrete compression test using random element strength modeling with various mesh sizes. Each color corresponds to a different strength. .

### *Mesoscale Modeling*

Mesoscale modeling distinguishes between concrete matrix and particles. The concept of mesoscale modeling is further described in Section 3.3.3 and a MATLAB script has been developed in order to alter the ABAQUS input file to include mesoscale modeling.



**(a)** Sim. 1      **(b)** Sim. 2      **(c)** Sim. 3
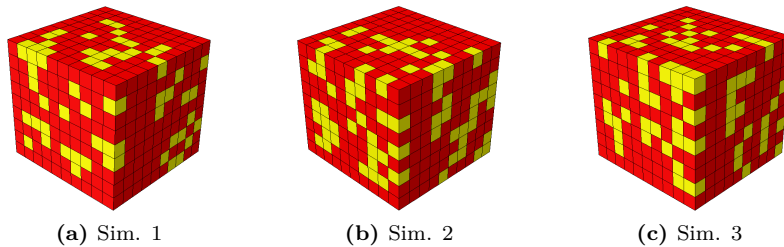
**Figure 5.15:** Distribution of particles for the three first ABAQUS simulations of the concrete compression test using mesoscale modeling. The yellow elements are particle elements, while the red are matrix elements.

In their thesis, Hillestad and Pettersen used a matrix strength of 30 MPa and a particle strength of 200 MPa. These values are therefore used to run ten simulations of the compression test, along with a minimum and maximum particle size of 2 and 4 mm respectively. How the distribution of the particles vary for the first three simulations can be seen in Figure 5.15 where the particle elements are yellow. The resulting engineering stress-strain curves for the ten simulations using mesoscale modeling are provided in Figure 5.16. It is observed
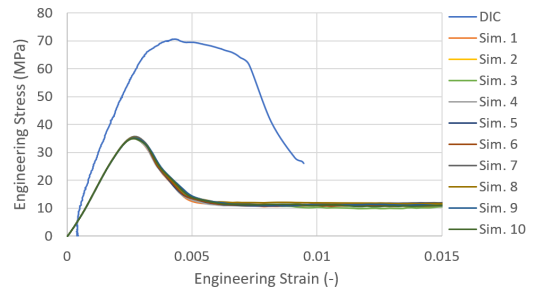


**Figure 5.16:** Engineering stress-strain curves for ten ABAQUS simulations of concrete compression test using mesoscale modeling.

that the results vary very little and that the stress is greatly underestimated.

The user-defined input parameters for the mesoscale modeling script are varied one by one in order to study their effects. The first parameter to be studied is the matrix strength. From Figure 5.17a it is observed that by doubling the matrix strength to 60 MPa, the correct compressive strength is obtained.

The particle strength is also varied in order to examine its effect. From Figure 5.17a it can be seen that varying the particle strength greatly, has minimal effect.



**(a)** Varying matrix strength $f_{c,m}$

**(b)** Varying particle strength $f_{c,p}$
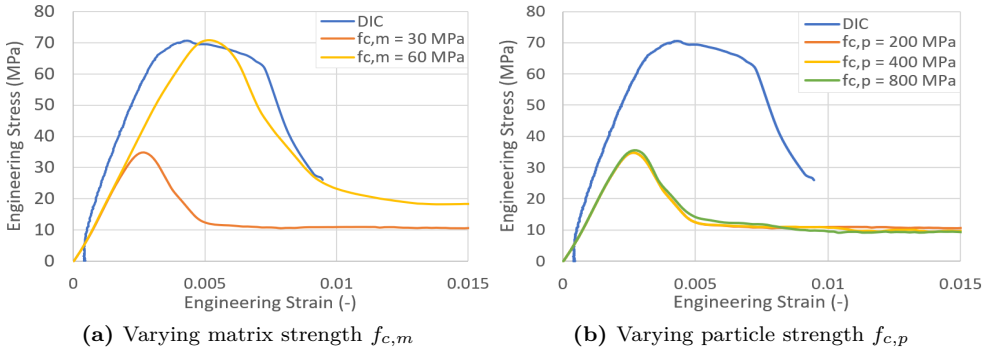
**Figure 5.17:** Engineering stress-strain curves for ABAQUS simulations of concrete compression test using mesoscale modeling.

The desired particle volume fraction is another user-defined input for the mesoscale model, and its effect is therefore studied in Figure 5.18. From these figures, it is observed that although the fraction of particles is increased it barely affects the results.



**(a)** 20 % particles

**(b)** 65 % particles

**(c)** Engineering stress-strain curve
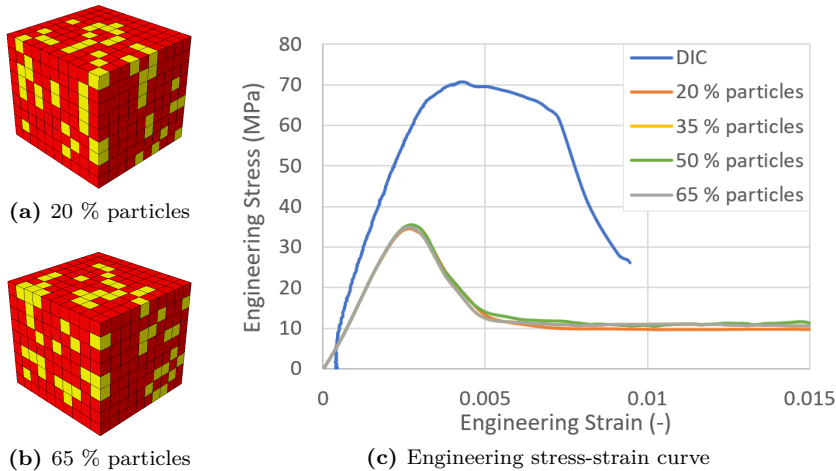
**Figure 5.18:** ABAQUS simulations of concrete compression test using mesoscale modeling with varying volume fractions of particles. The yellow elements in a) and b) are particle elements, while the red are matrix elements.

The minimum and maximum particle sizes are also varied, and the results are provided in Figure 5.19a and b respectively. The effect of varying either parameter seems minor.

**(a)** Varying minimum particle size

**(b)** Varying maximum particle size
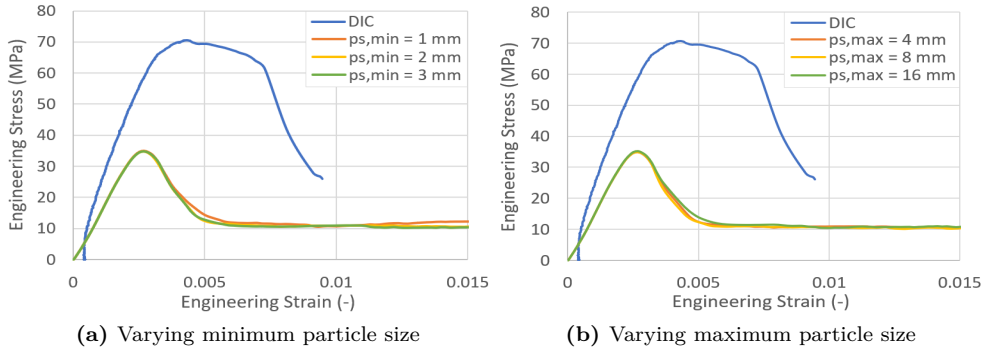
**Figure 5.19:** Engineering stress-strain curves for ABAQUS simulations of concrete compression test using mesoscale modeling.

The mesh size is also varied, and the distribution of the particles for the different mesh sizes is shown in Figure 5.20. The same pathological mesh dependency as was observed previously, can be seen in Figure 5.21.



**(a)** 125 elements

**(b)** 900 elements

**(c)** 7220 elements
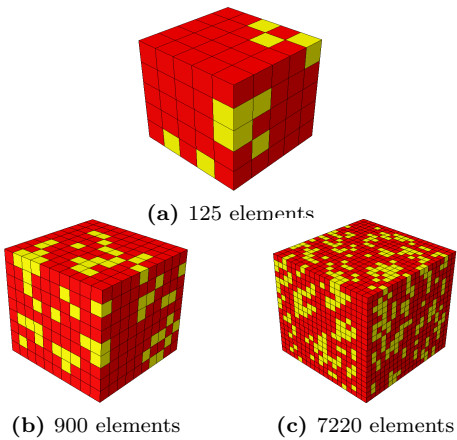
**Figure 5.20:** Distribution of particles for ABAQUS simulations of concrete compression test using mesoscale modeling with varying mesh size. The yellow elements are particle elements, while the red are matrix elements.
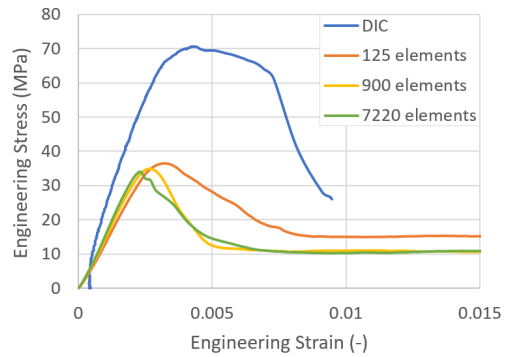


**Figure 5.21:** Engineering stress-strain curves for ABAQUS simulations of concrete compression test using mesoscale modeling with varying mesh size.

### *Combination of Random Element Strength and Mesoscale Modeling*

The modified random element strength method is combined with mesoscale modeling by merging the two MATLAB scripts. The merged script assigns the same strength to all the matrix elements, while all the particle elements are given random strengths according to a normal distribution with a user-defined mean strength and standard deviation. The method is described more detailedly in Section 3.3.3.

**(a)** Sim. 1      **(b)** Sim. 2      **(c)** Sim. 3
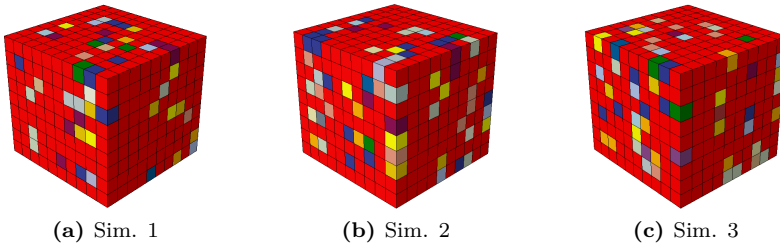
**Figure 5.22:** Distribution of particles for the three first ABAQUS simulations of the concrete compression test using a combination of random element strength and mesoscale modeling. Each color corresponds to a different strength, while the red elements are matrix elements.

The same input which was used for the random element strength and mesoscale modeling methods are used. The particle element strength is given a large standard deviation of 30 MPa. How the distribution of particles and their strengths vary, is shown in Figure 5.22 for the three first simulations. Ten simulations are run to study the variation, which from Figure 5.23a proves to be small. The stress is still significantly underestimated and since the matrix strength was seen to be of greater importance than the particle strength for mesoscale modeling, the matrix strength is increased in Figure 5.23b with the desired effect.



**(a)** Ten simulations      **(b)** Varying matrix strength $f_{c,m}$
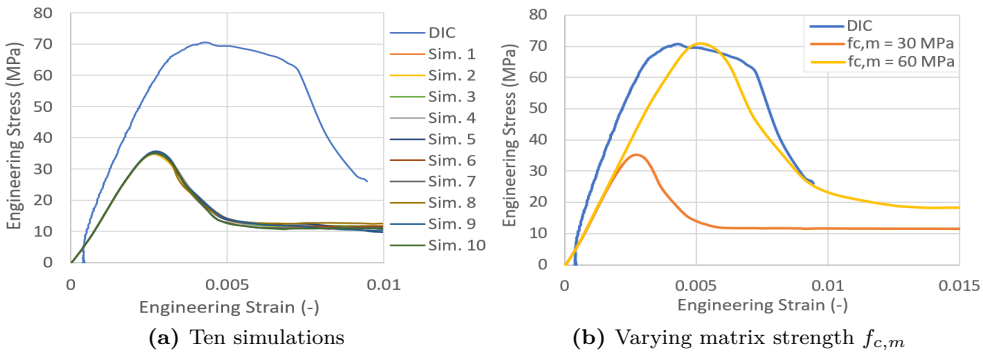
**Figure 5.23:** Engineering stress-strain curves for ABAQUS simulations of concrete compression test using a combination of modified random element strength method and mesoscale modeling.

*Discussion*

The most promising ABAQUS models of the compression test are compared in Figure 5.24. The most reasonable models include the reference model with scaled material parameters, both with and without scaling of Young's modulus $E$. Also promising is the modified random element strength model with a higher mean strength. Besides, the mesoscale model, and the combination of modified random element strength method and mesoscale model, both with increased matrix strength, have also shown potential.
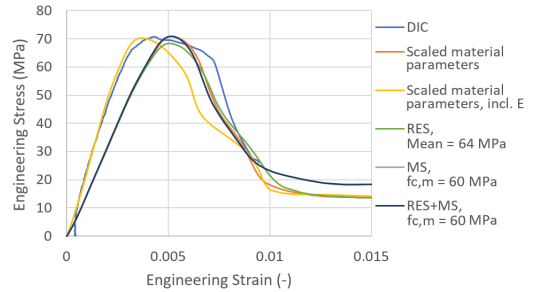


**Figure 5.24:** Comparison of engineering stress-strain curves for the most promising ABAQUS models of the concrete compression test.

From Figure 5.24 it is observed that the most promising ABAQUS models provide quite similar results. The greatest difference is seen when Young's modulus is scaled such that the stiffness equals that of the experimental test.

## 5.2 LS-DYNA

### 5.2.1 Reference Model

A reference model of the uniaxial compression test of concrete cube 1-8 is established in LS-DYNA as well. For eased comparison, it is attempted to make the LS-DYNA model as similar as possible to the ABAQUS model. Therefore, the same geometry, time-scaling, mesh, and load application as for ABAQUS is used, along with an explicit method.

The concrete material is defined using the K&C model, as described in Section 3.3.2, and the only necessary material input is therefore the compressive strength which in Section 4.3 was found to be 70.61 MPa.

For the concrete cube, solid elements are used in combination with reduced integration and stiffness Flanagan-Belytschko hourglass control. The test rig is modeled as two rigid plates, similarly to in ABAQUS, but the plates now require meshing. The plates are meshed using a finer mesh than for the cube such that the nodes of the different parts do not coincide.

Contact is established between the cube and the plates using the surface-to-surface contact formulation with penalty method. In their thesis work, Hillestad and Pettersen [48] found that the friction coefficient had to be small for the LS-DYNA simulations of the compression test. Thus, a friction coefficient of 1 % of that used in ABAQUS, is chosen for the LS-DYNA reference model. This corresponds to a friction coefficient of 0.0057. This is an unnaturally low friction coefficient, and the friction coefficient will therefore be closer examined in the parametric study. Unlike ABAQUS, LS-DYNA distinguishes between the static and dynamic friction coefficient. However, for the LS-DYNA reference model, the static and dynamic friction coefficient are set to be equal.

**(a)** Engineering stress-strain curve



**(b)** Energy balance check
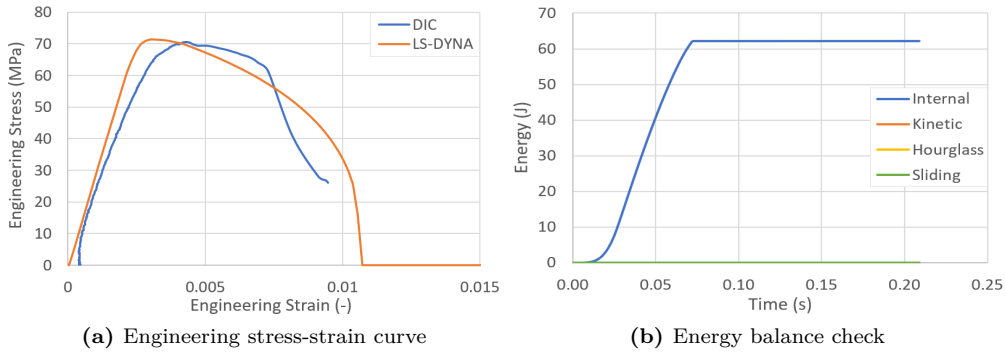
**Figure 5.25:** LS-DYNA reference model of concrete compression test.

The resulting displacements and contact forces of the load plate are used to calculate the engineering stress and strain provided in Figure 5.25a. As can be seen in Figure 5.25a, the LS-DYNA reference model renders both the shape and the peak value of the experimental stress-strain curve quite well. However, the numerical model has no residual strength.

An energy balance check is performed for the reference model, and the result is shown in Figure 5.25b. All other energies are negligible compared to the internal energy.

## 5.2.2   Parametric Study

A parametric study is conducted in the same manner as for the ABAQUS model, by altering one parameter at a time.

### *Friction Coefficient*

Since a very low friction coefficient was used between the concrete and steel for the reference model, this is the first parameter to be examined. Here the friction coefficient refers to both the static and dynamic friction coefficient as they are set equal to each other. The result of varying the friction coefficient for the LS-DYNA reference model can be seen in Figure 5.26 where a friction coefficient of 0.0057 corresponds to the reference model.

From Figure 5.26 it is observed that an unnaturally low friction coefficient provides reasonable results, while the recommended friction coefficient of 0.57 [95] provides poor results.
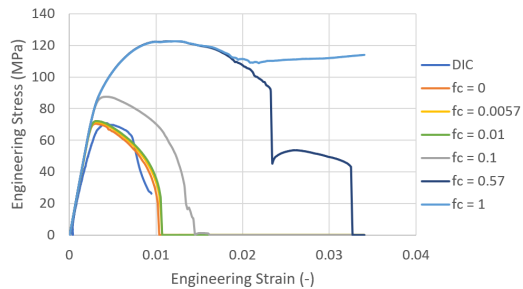


**Figure 5.26:** Engineering stress-strain curve for LS-DYNA model of concrete compression test with varying friction coefficient (fc).
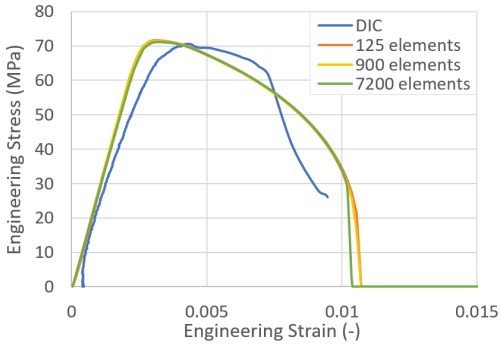
**Figure 5.27:** Engineering stress-strain curve for LS-DYNA model of concrete compression test with varying mesh size.

### Mesh Size

The mesh size of the concrete cube is also varied in the same manner as for ABAQUS, i.e. it is halved and doubled. In Figure 5.27 900 elements corresponds to the reference model.

In Figure 5.27 it can be seen that the mesh size has minimal effect on the resulting engineering stress-strain curve. However, the mesh size does affect the computational cost greatly, as discussed in Section 3.5.2.

### Time Scaling

The LS-DYNA reference model's simulation time is varied just like for ABAQUS, and the result can be seen in Figure 5.28 where the reference model has a simulation time of 209 ms.

From Figure 5.28 it is observed that the simulation time greatly affects the solution. When the simulation time is very short, 2.09 ms, the results are completely off as the stresses are negligible. When the simulation is run very slowly at 2090 ms, the solution also deviates from both the reference model and the experimental results. The simulation time also affects the computational cost, as discussed in Section 3.5.2.



**Figure 5.28:** Engineering stress-strain curve for LS-DYNA model of concrete compression test with varying simulation time.

### Random Element Strength

The modified random element strength method is explained in Section 3.3.3 and Hillestad and Pettersen's MATLAB script for random element strength in LS-DYNA [48] is modified to include random material strength, just like it was done for ABAQUS.

Ten simulations are run using the modified random element strength method. The distribution of the various element strengths can be seen for the three first simulations in Figure 5.29 where every color corresponds to a different element strength. 20 materials with a mean strength of 72.51 MPa and a standard deviation of 5.60 MPa (as calculated in 4.3) is used, and the results are provided in Figure 5.30 where there is a clearly visible variation in the results.
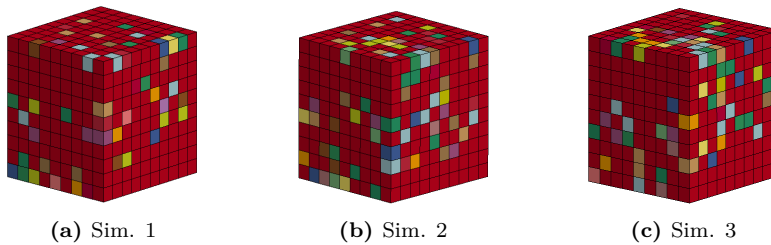
**(a)** Sim. 1



**(b)** Sim. 2

**(c)** Sim. 3



**Figure 5.29:** Distribution of element strengths for the three first LS-DYNA simulations of the concrete compression test using the modified random element strength method. Each color corresponds to a different strength.
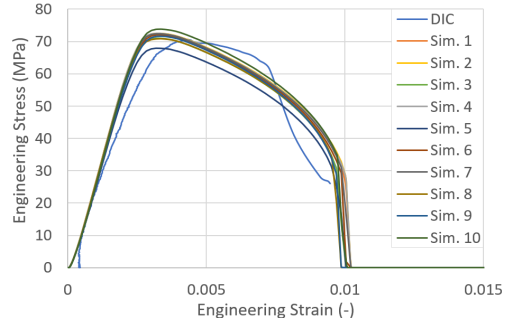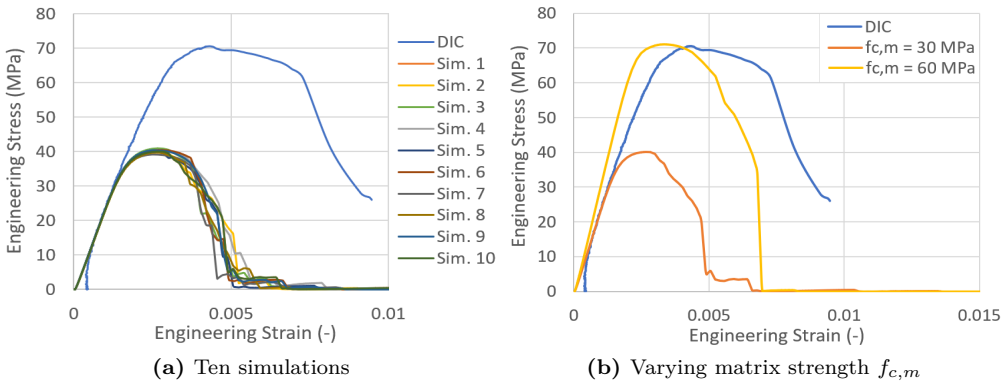
**Figure 5.30:** Engineering stress-strain curve for LS-DYNA model of concrete compression test using the modified random element strength method.

### Mesoscale Modeling

Mesoscale modeling is also examined in LS-DYNA by using Hillestad and Pettersen's MATLAB script to alter the LS-DYNA keyword file [48]. The theory behind the mesoscale modeling script is described in Section 3.3.3.



**(a)** Sim. 1

**(b)** Sim. 2

**(c)** Sim. 3
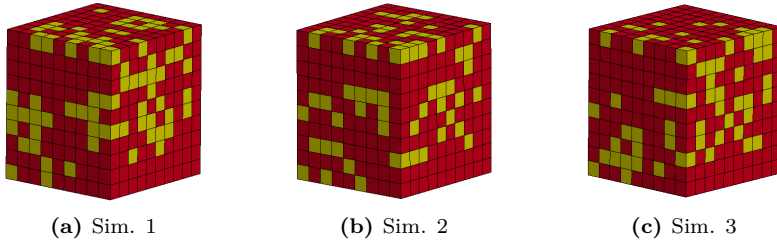
**Figure 5.31:** Distribution of particles for the three first LS-DYNA simulations of the concrete compression test using mesoscale modeling. The yellow elements are particle elements, while the red are matrix elements.

In Figure 5.31 the distribution of particles (yellow) in the matrix (red) can be seen for the three first simulations using mesoscale modeling in LS-DYNA. Ten such simulations are run in order to examine the variation. A matrix strength of 30 MPa and a particle strength of 200 MPa is utilized along with a minimum and maximum particle size of 2 and 4 mm, and the results are displayed in Figure 5.32a). There is a clear variation in the results, but the stresses are underestimated.

**(a)** Ten simulations

**(b)** Varying matrix strength $f_{c,m}$
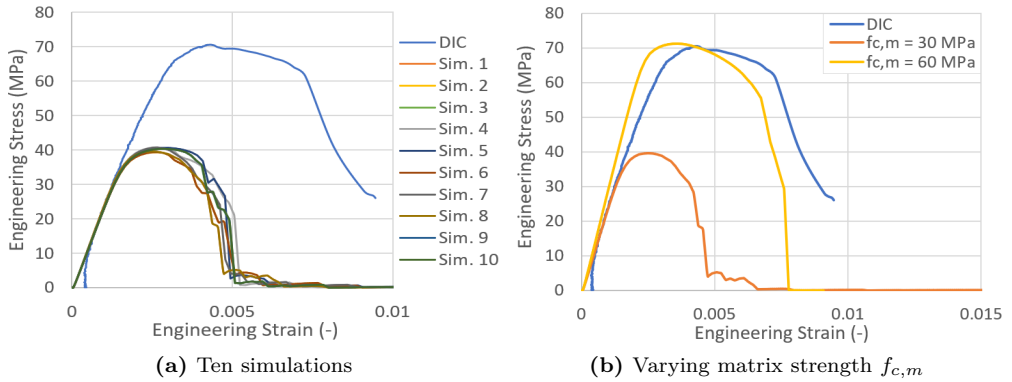
**Figure 5.32:** Engineering stress-strain curves for LS-DYNA model of concrete compression test using mesoscale modeling.

Since varying the matrix strength proved efficient in ABAQUS with respect to increasing the stress, the same is attempted for the LS-DYNA model. In Figure 5.34b the matrix strength is increased from 30 MPa to 60 MPa. The resulting stress-strain curve is then in quite good agreement with the experimental test results.

### *Combination of Random Element Strength and Mesoscale Modeling*

Combining the modified random element strength method with mesoscale modeling is also done in LS-DYNA using a MATLAB script as described in Section 3.3.3.



**(a)** Sim. 1        **(b)** Sim. 2        **(c)** Sim. 3

**Figure 5.33:** Distribution of particles for the three first LS-DYNA simulations of the concrete compression test using a combination of modified random element strength method and mesoscale modeling. Each color corresponds to a different strength, while the red elements are matrix elements.

The distribution of particles with various strengths can be seen for the three first simulations in Figure 5.33 where the matrix is red and the particles are of various colors where each color corresponds to a different strength. All the matrix elements are given the same strength of 30 MPa while all the particle elements are given random strengths according to a normal distribution with a mean strength of 200 MPa and a large standard deviation of 30 MPa. All other user-defined inputs are the same as for the random element strength and mesoscale modeling method. A total of ten simulations are run, and the results are available in Figure 5.34a. Again there is an evident variation, but the stresses are underestimated. Therefore, the matrix strength is attempted increased from 30 to 60 MPa in Figure 5.34b, and the desired effect is observed.

**(a)** Ten simulations

**(b)** Varying matrix strength $f_{c,m}$

**Figure 5.34:** Engineering stress-strain curve for LS-DYNA model of concrete compression test using a combination of modified random element strength method and mesoscale modeling.

### Discussion

The LS-DYNA reference model has been found to render both the shape and peak value of the experimental engineering stress-strain curve quite well. However, the LS-DYNA model of the compression test has no residual strength. In an attempt at finding an explanation for this, the damage of the concrete cube is examined in Figure 5.35. In Section 3.3.2 it was explained how the damage in LS-DYNA ranges from 0 to 2, where 0 is undamaged, and 2 is complete damage. From Figure 5.35 it is thus observed that the engineering stress tends to zero once all the elements are completely damaged, emphasized by the orange dashed vertical asymptote.
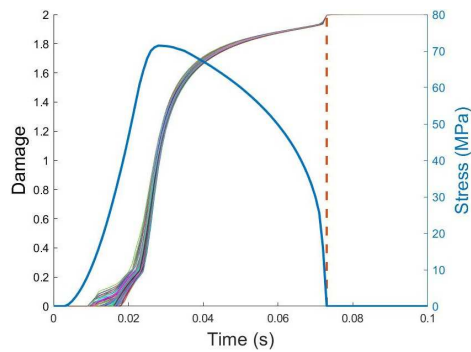


**Figure 5.35:** Damage-time curve for all elements of the LS-DYNA reference model of the concrete compression test, and the corresponding stress-time curve.

The most promising LS-DYNA models include the reference model, the modified random element strength method, and the mesoscale modeling and modified random element strength mesoscale modeling combination models with an increased matrix strength. These models are compared in Figure 5.36. While the elastic parts of the curves are practically identical, the post-peak behavior differs significantly. Nevertheless, none of the models render the residual strength of the concrete.
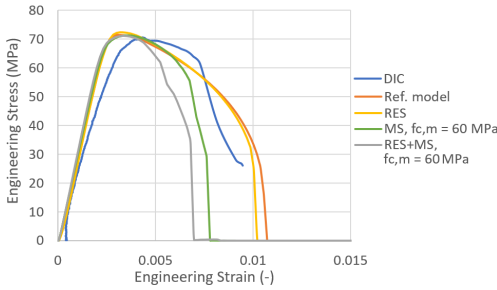
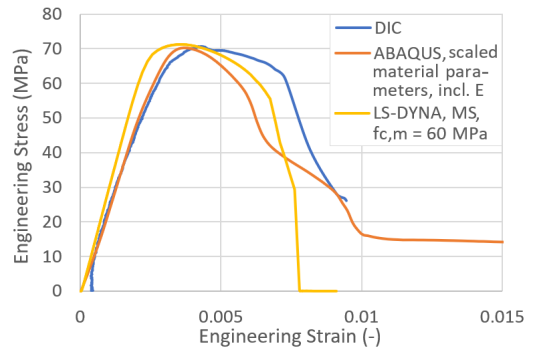**Figure 5.36:** Comparison of engineering stress-strain curves for the most promising LS-DYNA models of the concrete compression test.
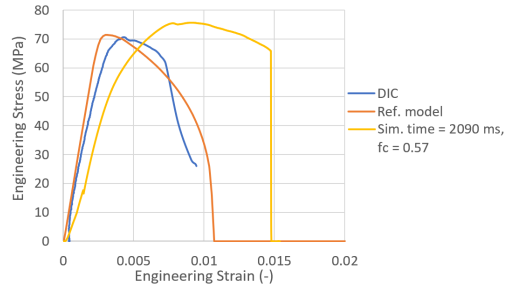
**Figure 5.37:** Engineering stress-strain curve for LS-DYNA model of concrete compression with increased simulation time and friction coefficient (fc).

Since the LS-DYNA reference model underestimates the stress when it is run slowly at 2090 ms, it is checked whether this allows for a more realistic friction coefficient of 0.57. The result is presented in Figure 5.37 and is a significant improvement from when the parameters were examined separately.

## 5.3 Discussion

Two of the most promising stress-strain curves simulated using ABAQUS and LS-DYNA are in Figure 5.38 compared with the curve obtained using DIC for experimental test. The ABAQUS model with the scaled material parameters, including Young's modulus, and the LS-DYNA mesoscale model with an increased matrix strength, are chosen as the most promising models.

From Figure 5.38 it is observed that the elastic part of the LS-DYNA model is slightly too stiff. It is also observed that the ABAQUS model approaches a horizontal asymptote of approximately 15 MPa after reaching its peak value. The LS-DYNA model, on the other hand, approaches zero. As the concrete cube will still have some strength remaining even after severe cracking, the LS-DYNA model approaching zero is nonphysical.



**Figure 5.38:** Comparison of engineering stress-strain curves for the most promising ABAQUS and LS-DYNA models of the concrete compression test.

Another nonphysical aspect of the LS-DYNA model is the unnaturally low friction coefficient which is required in order to obtain reasonable results. A more realistic friction coefficient can be used in ABAQUS.

While it was shown that the ABAQUS model displays pathological mesh dependency as

it is not reinforced, it is fairly insensitive to time-scaling. The simulation can therefore be run very quickly without the solution becoming unstable, but choosing a suitable mesh size can be problematic. Conversely, the LS-DYNA model seemed to be almost independent on mesh size, but sensitive to the amount of time-scaling.

The modified random element strength method gave a much more realistic spread in results for the ABAQUS model than the original method. It also provided a good spread for the LS-DYNA model. While the mesoscale modeling provided little variation for the ABAQUS model, its results were more promising for the LS-DYNA model. However, it was shown that the matrix strength was of much greater importance than the particle strength and although the concrete compression strength is known, it may be difficult to decide on a suitable matrix strength.

An advantage of the LS-DYNA model compared to the ABAQUS model is that the concrete material parameters require no scaling and the compressive strength is the only necessary input.

The ABAQUS model is computationally cheaper than the LS-DYNA model. This may be due to the fact that the cube is immensely distorted in the LS-DYNA analysis and not in the ABAQUS analysis, see Figure 5.39. Neither of the deformed cubes resembles the cube from the experimental test as it was very little deformed before cracking.



**(a)** ABAQUS          **(b)** LS-DYNA
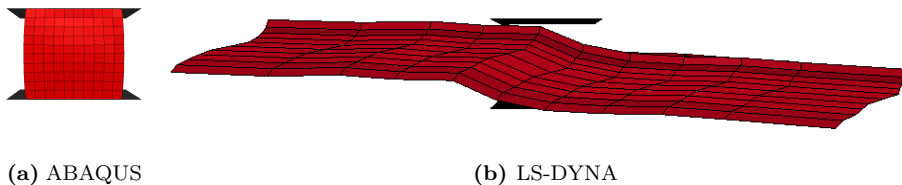
**Figure 5.39:** Deformed concrete cubes for the last increment in numerical simulations of the concrete compression test.

Energy balance checks are performed for every simulation as time-scaling and an explicit method is used. Except for the frictionless ABAQUS simulation, the kinetic energy is always very low compared to the internal energy for both ABAQUS and LS-DYNA. In fact, all other energies are very low compared to the internal energy for all LS-DYNA simulations. For the ABAQUS simulations, however, the artificial strain and internal energy levels vary between approximately 0.9 and 4.6 %, and is generally higher when using mesoscale modeling. According to ABAQUS recommendations, this level should not exceed 1-2 % [96]. However, for LS-DYNA the equivalent recommendation is 10 % [97]. While the value suggested by LS-DYNA might be excessively high, the value recommended by ABAQUS is perhaps too strict. An artificial strain versus internal energy level of maximum 4.6 % is therefore not considered a problem as the model seems to perform well otherwise.

# Chapter 6

# Experimental Testing of Concrete Pipes Subjected to Blast Loading

In an attempt to asses the performance of tubular concrete structures subjected to blast loading, experimental blast tests on plain and reinforced concrete pipes are conducted.

## 6.1 Setup and Execution

The experimental testing of concrete pipes subjected to blast loading conducted for this thesis is a continuation of tests previously performed by Kristoffersen et al. [43]. For the previous tests, a total of 16 pipes were examined by varying the placement and size of C4 charges. The geometry of the smaller pipes used for testing in this thesis is similar to the pipes used in the previous testing, except for the length. The experimental setup and execution of the tests for this thesis are also similar to that of the previously conducted tests, except for the number and placement of pressure sensors. The results from the previous tests (smaller pipes I to XVI) are therefore included in this thesis.
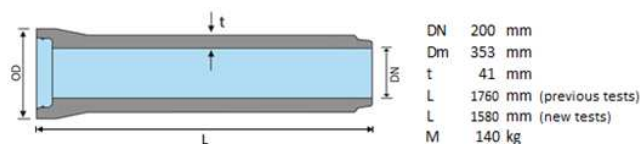


**Figure 6.1:** Geometry of the 200 mm diameter (smaller) concrete pipes which are tested.
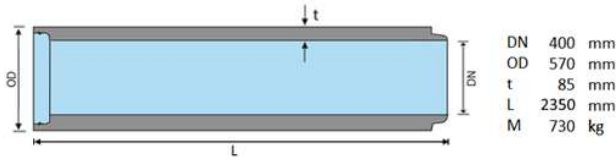
**Figure 6.2:** Geometry of the 400 mm diameter (larger) concrete pipes which are tested.

For the experimental tests conducted in conjunction with this thesis, an additional 18 concrete pipes are subjected to blast loading. Six of the pipes are smaller and plain, similar to those from the 16 previous tests. The geometry of these pipes is shown in Figure 6.1. Note that the length of the smaller pipes differs for the previous and new tests. The remaining 12 pipes are larger with the geometry provided in Figure 6.2. Of these larger pipes, six are plain, and six are reinforced. Onwards the 200 mm diameter pipes are referred to as 'the smaller pipes', while the 400 mm diameter pipes are referred to as 'the larger pipes'. An overview of the experimental tests, including the previously conducted tests, is presented in Figure 6.3. For all variations of the experimental tests, the size of the explosive charge is varied.
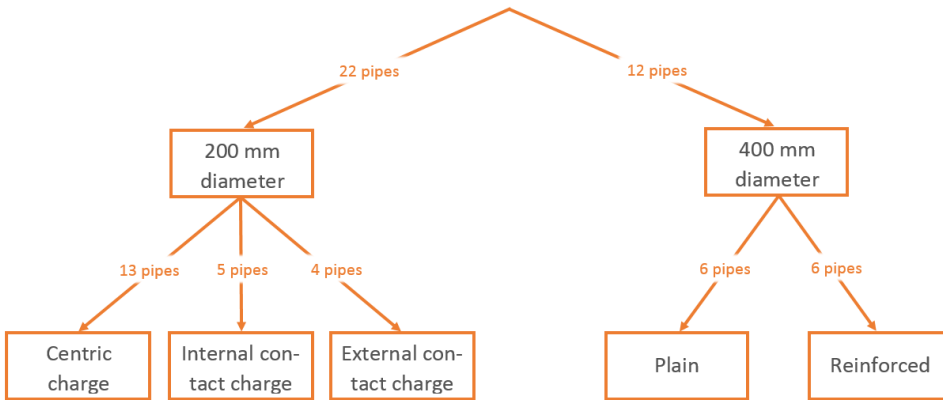


**Figure 6.3:** Overview of the experimental tests of concrete pipes subjected to blast loading.

The pipes are all made of a concrete with a 28-day cube compressive strength of 83.3 MPa. The strength is also measured after one and seven days of curing and is presented in Figure 6.4. The water-cement ratio is 0.37, and the maximum aggregate size is 8 mm. The concrete's water absorption is measured to be 3.84 % in average, reflecting its high density.

For the reinforced concrete pipes there are 12 longitudinal rebars without ribs and of 8 mm diameter. The reinforcement in the ring direction is ribbed with a diameter of 6 mm, and lies in a spiral with a slope of 100 mm per coil, on the outside of the longitudinal reinforcement.
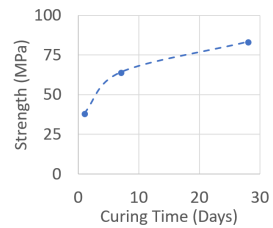


**Figure 6.4:** The cube strength of the pipes' concrete as a function of curing time.

All pipes are commercially available and off-the-shelf, with the intended use for drainage. Since the pipes are mass produced, there is minimal deviation in geometry and material properties.
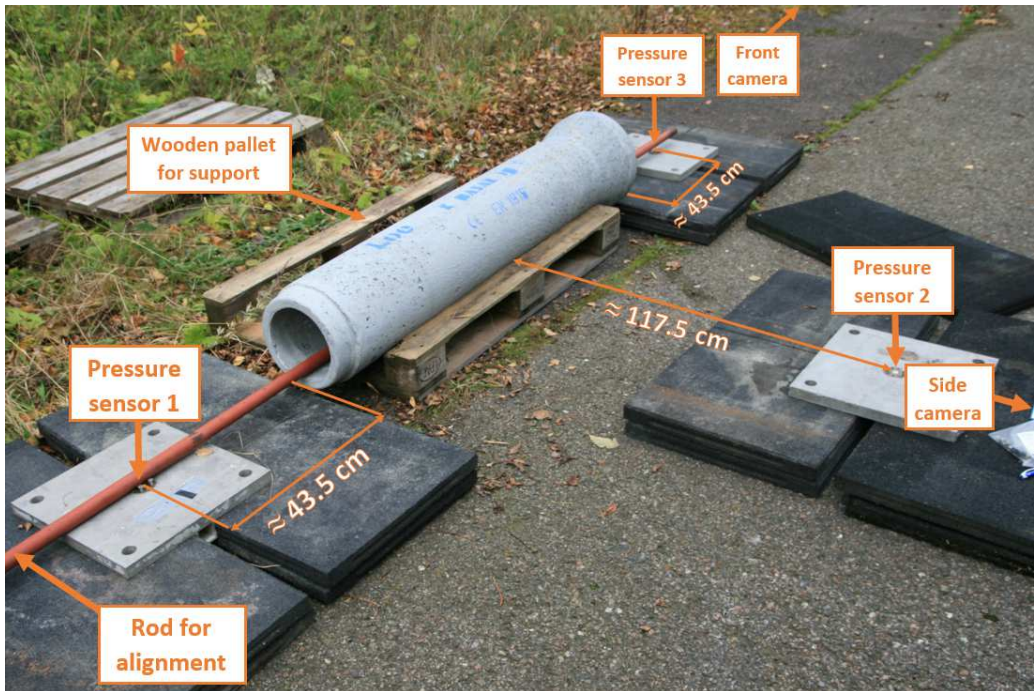


**Figure 6.5:** Experimental setup of previously conducted tests of concrete pipes subjected to blast loading.

The setup of the previously conducted experimental tests is shown in Figure 6.5, and the setup of the tests conducted for this thesis is shown in Figure 6.6. For all tests, wooden pallets or planks are used to support the concrete pipes.

One camera films the cross-section of the pipes and the other films the pipes from the side. High-speed, high-resolution cameras of models Phantom Miro LC310 and Phantom v2012 are used. The cameras take 1280 by 800 pixels images at 3268 and 22629 frames per second respectively. For the first round of testing only the latter camera model was used. For the second round of testing mainly the first camera model is used, but for the last tests one of the cameras needed to be replaced and thus the latter camera model is used.
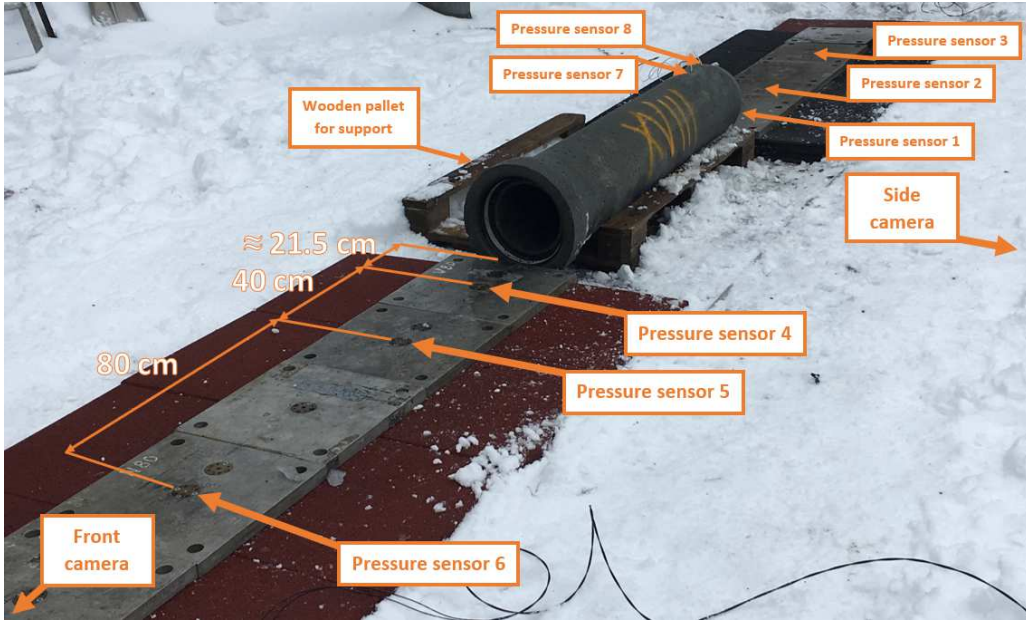
**Figure 6.6:** Experimental setup of new testing of concrete pipes subjected to blast loading.

Kistler 603B piezoelectric pressure sensors with a sampling frequency of 1 MHz are used to measure the pressure throughout the testing. In order to keep the pressure sensors in place during the tests, they are flush-mounted in 400x400x30 mm aluminum plates. The number and placement of sensors differ for the previously and newly conducted tests. For the previous tests, three pressure sensors were placed approximately 131.5 cm from the charge, one at each end of the pipe in the longitudinal axis and one perpendicular to the main axis (see Figure 6.5). Since it was found that the sensor perpendicular to the main axis provided data which was difficult to interpret, no sensors are used in the this axis for the new tests. Instead, the number of pressure sensors in the longitudinal axis is increased. For the new tests, a total of eight pressure sensors are utilized. Sensors 1 and 4 are placed approximately 21.5 cm from the pipe opening, sensors 2 and 5 an additional 40 cm from



**Figure 6.7:** Pressure sensors inside pipe for new tests.

the opening, and sensors 3 and 6 another 80 cm away (see Figure 6.6). For the smaller pipes, holes are drilled into the pipe 10 and 20 cm from the narrow end. For the larger pipes, the corresponding measurements are 10 and 25 cm. Pressure sensor 8 is placed in the hole closest to the pipe opening, while sensor 7 is placed in the other hole. The positioning of pressure sensors 7 and 8 is illustrated in Figure 6.7 where also some scabbing around the drilled holes can be observed. The placement of all the sensors for the new tests is summarized in Table 6.1.

**Table 6.1:** Distances from the sensors to the charge for the second round of experimental testing of concrete pipes subjected to blast load.

| | Distance from charge (cm) | |
|---|---|---|
| Sensor | Smaller pipes | Larger pipes |
| 7 | 59 | 92.5 |
| 8 | 69 | 102.5 |
| 1+4 | 100.5 | 139 |
| 2+5 | 140.5 | 179 |
| 3+6 | 220.5 | 259 |



**Figure 6.8:** Spherical charge placed centrically within pipe.

Spherical charges of composite C4 are placed centrically within the pipes. Cardboard, styrofoam, or thin wooden sticks are used to place and support the charges, as illustrated in Figure 6.8. For the previous tests also cubic contact charges were placed both internally and externally on the pipe. All charges, including the contact charges, are centered with regard to the pipe's longitudinal direction. For each test variation, the amount of C4 is varied. The charges are detonated using electrically ignited blasting caps containing primary explosives equivalent to approximately 1 g of C4.

## 6.2 Results

The results from the experimental testing of concrete pipes subjected to blast loading are presented in the following subsection where they are categorized and presented according to Figure 6.3.

### 6.2.1 Smaller Pipes

For the smaller pipes, the results are sorted by charge placement. All the smaller pipes were plain, i.e. not reinforced. Results from both rounds of testing are included.

#### *Centric Charge*

The damage of the smaller plain concrete pipes subjected to blast loading by centrically placed charges, is summarized in Table 6.2. The results from the previously conducted tests are also included and correspond to pipe I to VI and XIV. Recollect that the pipe length differed for the new and previous test specimens. If the pipe fragmented, a photo is included displaying the fragments approximately sorted by size. The TNT equivalent is calculated as described in Section 3.4.1 using the peak pressure TNT equivalent mass factor of 1.37.

**Table 6.2:** Summary of the damage of the smaller plain concrete pipes subjected to blast loading by centrically placed charges. Pipe I to VI and XIV are from the previously conducted tests.

| Pipe ID | Amount of C4 (g) | TNT equi- valent (kg) | Damage | |
|---------|------------------|-----------------------|--------|---|
| III | 10 | 0.0137 | No visible damage | |
| XVIII | 10 | 0.0137 | No visible damage | |
| XIX | 12 | 0.01644 | One long, narrow, longitudinal crack | |
| IV | 12.5 | 0.17125 | One long, narrow, longitudinal crack | |
| XIV | 13 | 0.01781 | Fragmentation |  |
| VI | 13.5 | 0.018495 | Fragmentation |  |
| V | 14 | 0.01918 | Fragmentation |  |
| XX | 14 | 0.01918 | Fragmentation |  |
| II | 15 | 0.02055 | Fragmentation |  |
| XXI | 16 | 0.02192 | Fragmentation |  |
| XXII | 18 | 0.02466 | Fragmentation |  |
| XVII | 20 | 0.0274 | Fragmentation |  |
| I | 25 | 0.03425 | Fragmentation |  |

13 g of C4 was required to fragment the smaller plain concrete pipe when the charge was placed centrically within the pipe. The pipe then fragmented in oblong pieces due to mainly longitudinal cracking. Larger charges caused the pipe to fragment into smaller oblong pieces which were scattered further away. All end sections remained intact, although they were more damaged during the second round of testing where the pipes were shorter.

(a) Frame 0 (0 ms)



(b) Frame 21 ($\sim$0.9 ms)



(c) Frame 38 ($\sim$1.7 ms)



(d) Frame 67 ($\sim$3.0 ms)

**Figure 6.9:** Selected frames for the smaller plain concrete pipe XIV where a charge of 13 g C4 was centrically placed within the pipe.
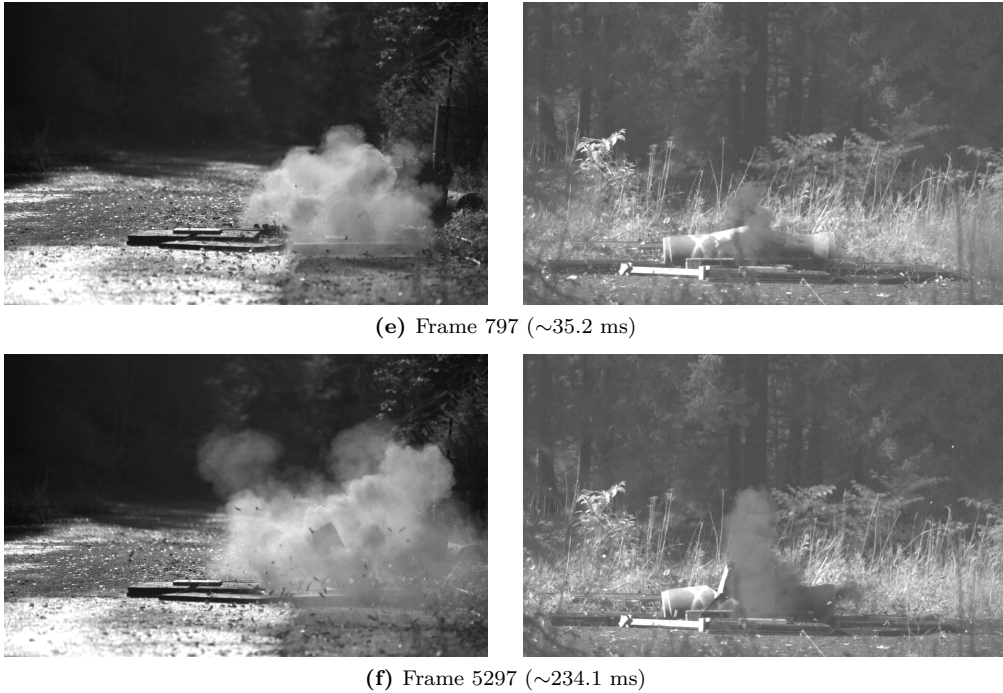
**(e)** Frame 797 ($\sim$35.2 ms)



**(f)** Frame 5297 ($\sim$234.1 ms)

**Figure 6.9:** Selected frames for the smaller plain concrete pipe XIV where a charge of 13 g C4 was centrically placed within the pipe.

Figure 6.9 displays a time series for one of the smaller plain concrete pipes with a centrically placed charge. For this time series, 13 g of C4 was used, which was the minimum charge size required in order for the smaller pipe to fragment when the charge was centrically placed. The time series shows selected frames from both cameras such that the pipe can be seen from both the front and side. The creation and expansion of the fireball is clearly visible. Also visible, though less distinctly, is the shock wave which can be observed when closely examining frame 38 and 67 from the front. The formation of longitudinal cracks is especially apparent when the pipe is seen from the side in frame 38. How these cracks then form oblong fragments which are then scattered around, is observable in frame 797 and 5297.

All pressure time-curves are available in Appendix A. A general observation for the previously conducted tests is that the pressures measured at sensor 1 and 3 are fairly similar and mostly resemble the characteristic blast wave presented in Figure 3.19 in Section 3.4, with a sudden increase in pressure at the arrival of the blast wave, followed by a slower decrease and a negative phase until the pressure again stabilizes at the ambient pressure. Some pressure fluctuations are present due to the burning of the fireball. For the new tests, the same observations are made. In addition, it can be seen that the peak pressure decreases as the distance from the charge increases and that the pressures measured inside the pipe are significantly larger than those measured outside the pipe. The pressures measured orthogonally to the pipe length, at sensor 2 for the previously conducted tests, are more difficult to make sense of. Nevertheless, it is emphasized that these observations are only general and deviations do occur. For instance, for the new tests, sensor 2 seems defect for several of the tests while sensor 7 provides irregular readings for one test.

Since sensors 1+4, 2+5, and 3+6 for the new tests are placed symmetrically with regard to the pipe, it is checked whether the pressure measurements equal for these sensor pairs. For the new tests, 14 g of C4 was the smallest centrically placed charge for which the pipe fragmented, and pipe XX is therefore used as an example. From Figure 6.10 it can be seen that the peak pressures are slightly higher at sensors 1, 2, and 3 compared to at sensors 4, 5, and 6 respectively. It is also observed that the shock wave reaches these sensors 1, 2, and 3 shortly before sensors 4, 5, and 6. Both these observations may indicate that the pipe or charge is not completely centered in the longitudinal direction. Another possible explanation is that the sensors may also not be entirely aligned. The different geometries at the pipe ends may also affect the results.



**(a)** Sensors 1 and 4      **(b)** Sensors 2 and 5      **(c)** Sensors 3 and 6
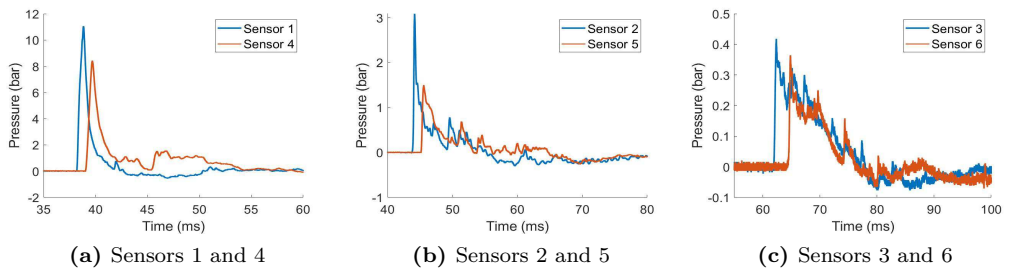
**Figure 6.10:** Pressure-time curves for the smaller plain concrete pipe XX where a charge of 14 g C4 is centrically placed within the pipe.

For the smaller plain concrete pipes with centrically placed charges, the peak pressure is plotted as a function of charge size in Figure 6.11. Results from both rounds of testing are included. Since the pressures measured within the pipe were much larger than the ones measured outside the pipe, the plots are separated into two figures. For both plots, the charge size which was required to fragment the pipe (13 g) is highlighted as a vertical asymptote. As the distance from the charge increases, the peak pressure displays a more and more linear dependence on the charge size. Furthermore, whether or not the pipe fragments does not seem to affect the peak pressure.
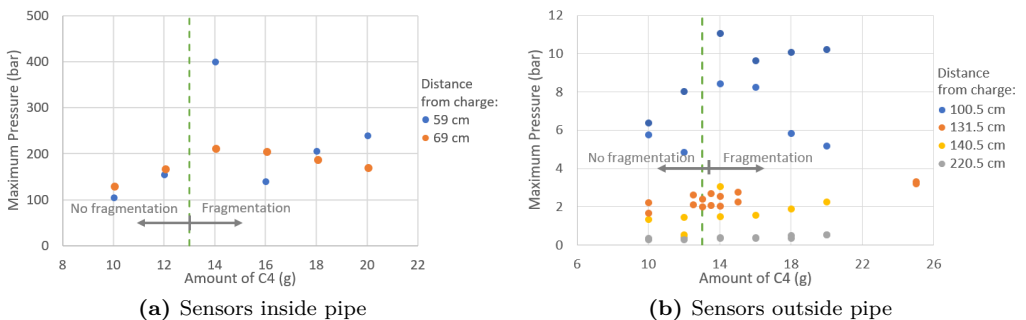


**(a)** Sensors inside pipe      **(b)** Sensors outside pipe

**Figure 6.11:** Peak pressure plotted against charge size for the smaller plain concrete pipes with centric charges.

By utilizing a logarithmic scale for the y-axis, all peak pressures can be plotted in one figure (see Figure 6.12). Logarithmic y-axes will therefore be made use of for all further similar plots, but it is important to be aware of this when assessing the results. However,

since the x-axis is still linear, the same observations are made from Figure 6.12 as before. Nevertheless, now the peak pressures measured closer to and within the pipe also seem to display an almost linear dependency on the charge size although this may not be entirely representative (as was shown in Figure 6.11).
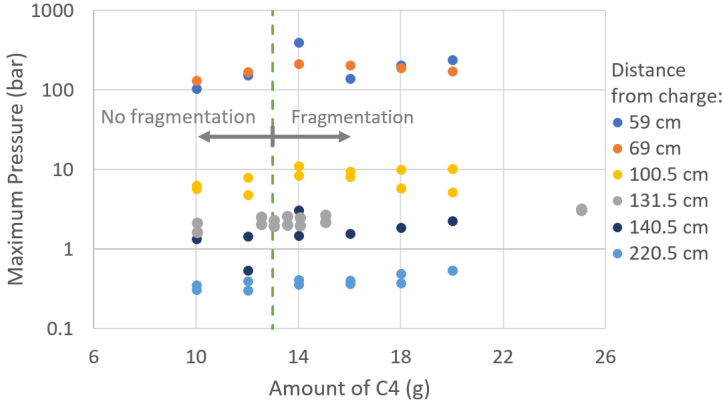


**Figure 6.12:** Peak pressure plotted against charge size for the smaller plain concrete pipes with centric charges. Note that the y-axis is logarithmic.

By making use of the peak pressure TNT equivalent mass factor of 1.37 (see Section 3.4.1) the scaled distance can be calculated as described in Section 3.4.2. The peak pressure can then be plotted against the scaled distance and thereby be compared with the Kingery-Bulmash equations which were presented in Figure 3.25 in Section 3.4.3. In Figure 6.13 this is done for the smaller plain concrete pipes with centrically placed charges. Since the Kingery-Bulmash equations are not meant for complex, close-in, partly confined blasts as for these experimental tests, for the sake of comparison both the incident and reflected pressure are included for both spherical air bursts and hemispherical surface explosions. The Kingery-Bulmash equations are usually plotted with both logarithmic x- and y-axes. However, since the scaled distances for these experimental tests are all within the same range, linear x-axes are used for both plots in Figure 6.13. Logarithmic y-axes as in Figure 6.13a will be utilized for further similar plots, but to clearly emphasize the actual deviances, a linear y-axis is used in Figure 6.13b.
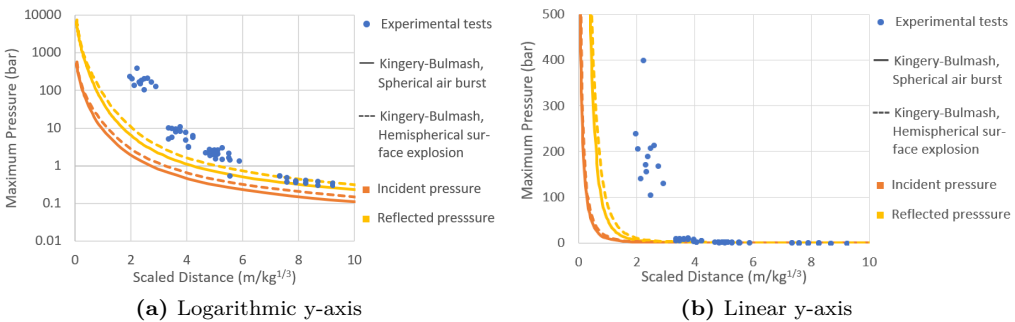


**(a)** Logarithmic y-axis

**(b)** Linear y-axis

**Figure 6.13:** Peak pressure plotted against scaled distance for the smaller plain concrete pipes with centric charges. The Kingery-Bulmash equations for both the incident and reflected pressure are included for both spherical air bursts and hemispherical surface explosions.

When examining Figure 6.13, several interesting observations can be made. From Figure 6.13a, it is especially clear that the experimental test results follow the same curve shape as the Kingery-Bulmash equations. For larger scaled distances, the peak pressures even coincide almost perfectly with the Kingery-Bulmash reflected pressure for surface explosions. However, as the scaled distance decreases, the experimental results differ more and more, which is particularly clear with the linear y-axis in Figure 6.13b. This is likely due to the confinement effect of the blast wave inside the pipe. It is therefore non-conservative to estimate the blast parameters using the Kingery-Bulmash equations.

### *Internal Contact Charge*

The damage of the smaller plain concrete pipes subjected to internal contact charges is summarized in Table 6.3. All the results are from the first round of testing. If the pipe fragmented, a photo is included displaying the fragments approximately sorted by size.

**Table 6.3:** Summary of the damage of the smaller plain concrete pipes subjected to blast loading by internal contact charges.

| Pipe ID | Amount of C4 (g) | TNT equivalent (kg) | Damage | |
|---------|------------------|---------------------|--------|---|
| VIII | 5 | 0.00685 | Spalling/scabbing outside. Small crater inside. More damage on the side opposite to the charge | |
| XV | 6 | 0.00822 | Fragmentation. Through-thickness breach |  |
| IX | 7.5 | 0.010275 | Fragmentation. Through-thickness breach when pieced together |  |
| X | 7.5 | 0.010275 | Fragmentation. Through-thickness breach when pieced together |  |
| VII | 10 | 0.0137 | Fragmentation |  |

When the charge was placed internally on the pipe wall, 6 g of C4 was required to fragment the smaller plain concrete pipe. Craters were formed on the inside of the pipe wall where the contact charge was placed, while spalling/scabbing was observed on the outside of the pipe wall. Typically the damage was larger on the outside of the pipe, i.e. on the side opposite to the charge. For the pipes that fragmented, the fragmentation initiated at the location of the charge. Larger charges produced smaller fragments which were more scattered around. All end sections remained intact.

In Figure 6.14 a time series is shown for an internal contact charge. For this pipe, 6 g of C4 was used, which was the minimum internal contact charge size required in order for the smaller pipe to fragment. The time series shows selected frames from both cameras such that the pipe can be seen from both the front and side. The creation and expansion of the fireball is clearly visible. Also visible, though less distinctly, is the shock wave which can be observed when closely examining frame 52 from the front. It is also observable how the concrete pipe initially breaches at the top of the pipe where the contact charge is placed.

(a) Frame 0 (0 ms)



(b) Frame 30 (∼1.3 ms)



(c) Frame (∼2.3 ms)



(d) Frame 418 (∼18.5 ms)

**Figure 6.14:** Selected frames for the smaller plain concrete pipe XV with an internal contact charge of 6 g C4.

**(e)** Frame 1318 ($\sim$58.2 ms)
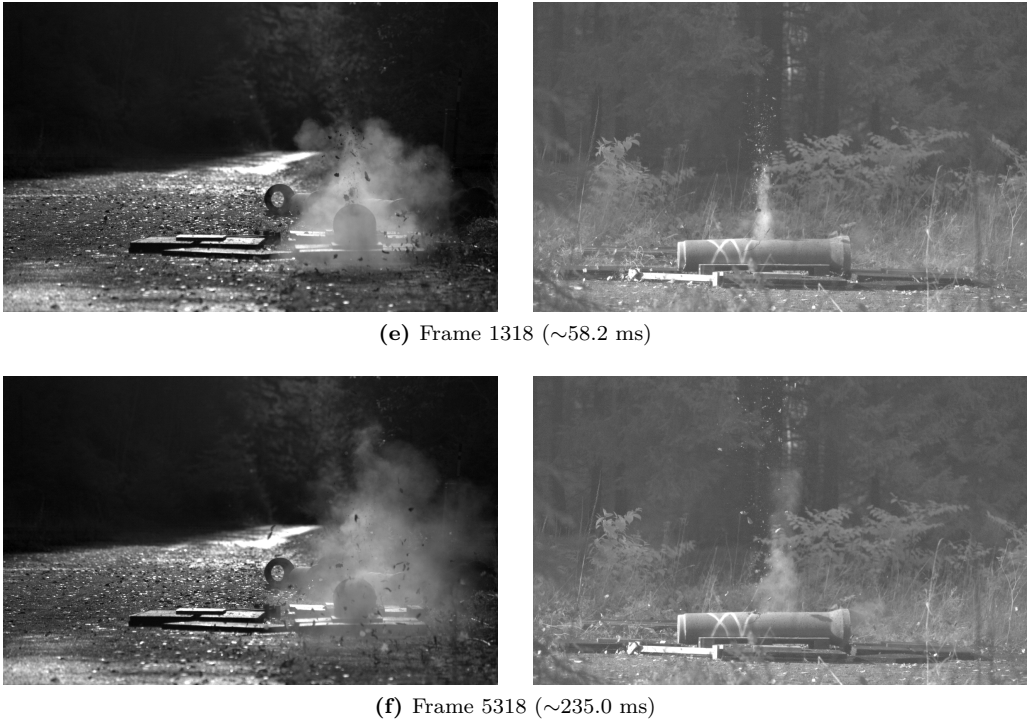


**(f)** Frame 5318 ($\sim$235.0 ms)

**Figure 6.14:** Selected frames for the smaller plain concrete pipe XV with an internal contact charge of 6 g C4.

All pressure measurements for the smaller pipes with internal contact charges are presented in Appendix A. The pressures measured at sensor 1 and 3 are, in general, fairly similar, and most resemble the characteristic blast wave. However, some pressure fluctuations are present due to the burning of the fireball. The pressures measured orthogonally to the pipe length at sensor 2, are more difficult to make sense of.

The peak pressures for the smaller plain concrete pipes with the internal contact charges are compared in Figure 6.15. In Figure 6.15a the peak pressure is plotted as a function of the charge size, and a linear dependency is observable. The minimum charge required to fragment the pipe is highlighted, but whether or not the pipe fragments does not seem to affect the peak pressure. In Figure 6.15b the experimental results are plotted as a function of the scaled distance, and compared with the Kingery-Bulmash equations for incident and reflected pressure for both spherical air bursts and hemispherical surface explosions. It is observable that the experimental test results resemble the curve shape of the Kingery-Bulmash equations. However, the experimental pressures are significantly larger, due to the confinement of the blast wave, and therefore it would be non-conservative to use the Kingery-Bulmash equations to predict the blast parameters.
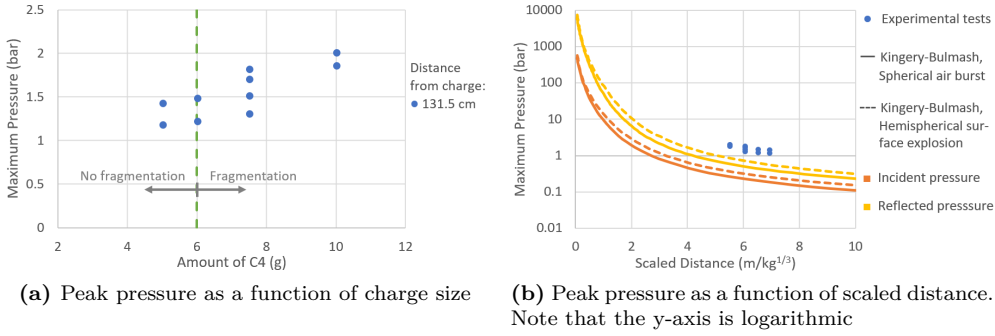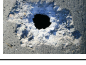
**(a)** Peak pressure as a function of charge size



**(b)** Peak pressure as a function of scaled distance. Note that the y-axis is logarithmic

**Figure 6.15:** For the smaller plain concrete pipes with internal contact charges, the peak pressure is plotted against charge size and scaled distance respectively.

### External Contact Charge

The damage of the smaller plain concrete pipes subjected to blast loading by external contact charges, is summarized in Table 6.4. All the results are from the previously conducted tests. Photos zoomed in on the damage are included.

**Table 6.4:** Summary of the damage of the smaller plain concrete pipes subjected to blast loading by external contact charges.

| Pipe ID | Amount of C4 (g) | TNT equivalent (kg) | Damage | |
|---|---|---|---|---|
| XI | 10 | 0.0.0137 | Small crater on outside. Spalling/scabbing inside |  |
| XVI | 12.5 | 0.017125 | Small crater on outside. Spalling/scabbing inside. Small hole through wall |  |
| XII | 15 | 0.02055 | Small crater on outside. Spalling/scabbing inside. Hole through wall |  |
| XIII | 20 | 0.0274 | Small crater on outside. Spalling/scabbing inside. Larger hole through wall |  |

12.5 g of C4 was required to breach the 200 mm plain pipe when the charge was placed externally on the pipe wall. Craters were formed on the outside of the pipe wall where the contact charge was placed, while spalling/scabbing was observed on the inside. Typically the damage was larger on the inside of the pipe, i.e. on the side opposite to the charge. Larger charges produced larger through-thickness holes.

In Figure 6.16 a time series is shown for an external contact charge. For this pipe, 15 g of C4 was used. It was desirable to use the time series of the minimum charge size required to breach the pipe (12.5 g), but this video was very dark. The time series shows selected frames from both cameras such that the pipe can be seen both from the front and from the side. The creation and expansion of the fireball is clearly visible. Also visible, though less distinctly, is the shock wave which can be observed when closely examining frame 2 and 6 from the front. Except for fragments being projected in the last couple of frames, it is difficult to observe the damage evolution of the pipe as the damage is relatively small, and the fireball obstructs the view of the pipe.

**(a)** Frame 0 (0 ms)



**(b)** Frame 2 (∼0.1 ms)



**(c)** Frame 6 (∼0.3 ms)



**(d)** Frame 129 (∼5.7 ms)

**Figure 6.16:** Selected frames for the smaller plain concrete pipe XII with an external contact charge of 15 g C4.

**(c)** Frame 3329 (∼147.1 ms)



**(d)** Frame 5329 (∼235.5 ms)

**Figure 6.16:** Selected frames for the smaller plain concrete pipe XII with an external contact charge of 15 g C4.

All pressure-time curves for the smaller plain pipes subjected to external contact charges are available in Appendix A. These pressures do not necessarily distinctly resemble the characteristic blast wave as they fluctuate conspicuously. The irregularity of the results is also apparent in Figure 6.17a where there is a relatively large scatter, although the peak pressure generally seems to increase with the charge size. The minimum charge required to breach the pipe is highlighted in the plot, but the peak pressure does not seem affected by whether or not the pipe breaches. In Figure 6.17b the peak pressure is plotted as a function of the scaled distance and compared with the Kingery-Bulmash equations for both the incident and reflected pressure for spherical air bursts as well as hemispherical surface explosions. The experimental test results do not coincide with one of the Kingery-Bulmash curves, but they fall well within the confinement of the various Kingery-Bulmash pressure curves. The reason for this is probably that the blast is not confined by the pipe wall and, therefore, the blast environment is more similar to those of the experiments on which the Kingery-Bulmash equations are based.
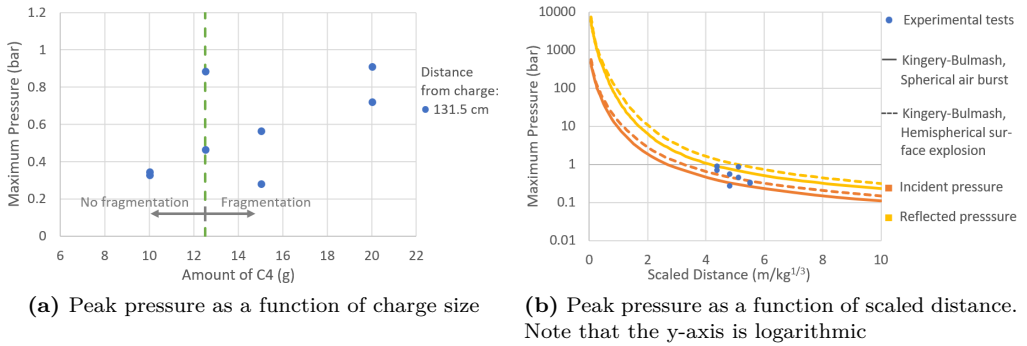
**(a)** Peak pressure as a function of charge size

**(b)** Peak pressure as a function of scaled distance. Note that the y-axis is logarithmic

**Figure 6.17:** For the smaller plain concrete pipes with external contact charges, the peak pressure is plotted against charge size and scaled distance respectively.

### *Discussion*

From the previous tests, Kristoffersen et al. were able to determine the minimum charge size required to breach the pipe wall. They also observed that when the pipes fragmented, oblong fragments were formed by longitudinal cracking. For the centrically placed charges, the cracks were mainly longitudinal, and larger charges produced smaller fragments which were more scattered around, as illustrated in Figure 6.18. For the contact charges, the damage was typically larger on the side of the pipe wall opposite to the charge. For all tests the end sections were intact, indicating that blast loading is a local problem. Another key observation with regard to SFT design was that after a certain distance the shock waves became one-dimensional along the pipe axis. All observations and findings from the previous tests still stand after conducting additional tests.



**(a)** 13 g of C4 (pipe XIV)

**(b)** 25 g of C4 (pipe I)
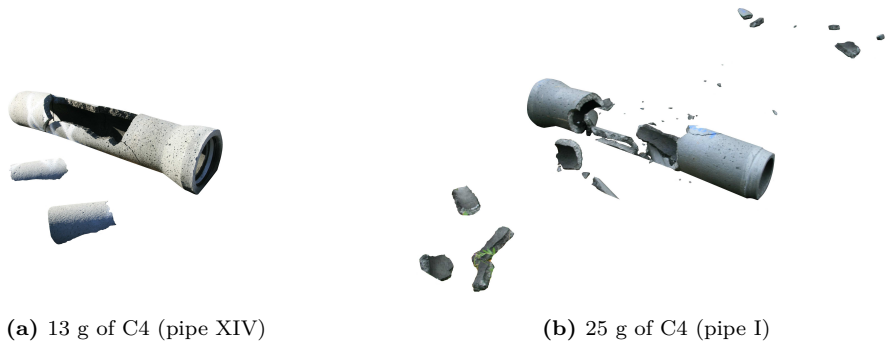
**Figure 6.18:** Damage of two the smaller plain concrete pipes with centrically placed charges.

13, 6, and 12.5 g of C4 was required to obtain through-thickness damage of the pipes when the charges were placed centrically within, internally in contact, and externally in contact, respectively. I.e. a much smaller charge was required to severely damage the pipe if the charge was placed in contact on the inside of the pipe (6 g), compared to when it was laced centrically within the pipe (13 g). This emphasizes the importance of stand-off distance.

The smallest contact charge required to severely damage the pipe was much smaller when the charge was placed on the inside of the pipe (6 g), compared to when the charge was placed on the outside of the pipe (12.5 g). This emphasizes the effect of confinement which was discussed in Section 3.4.2. The significance of charge placement is illustrated in Figure 6.19 where a contact charge of 10 g C4 was placed internally and externally on the pipe wall. While the internal contact charge fragmented the pipe, the external contact charge merely caused a small crater on the outside of the pipe wall and some spalling/scabbing on the inside. When a 10 g C4 charge was placed centrically within the pipe, there was no visible damage.



**(a)** Internal contact charge (pipe VII)  **(b)** External contact charge (pipe XI)
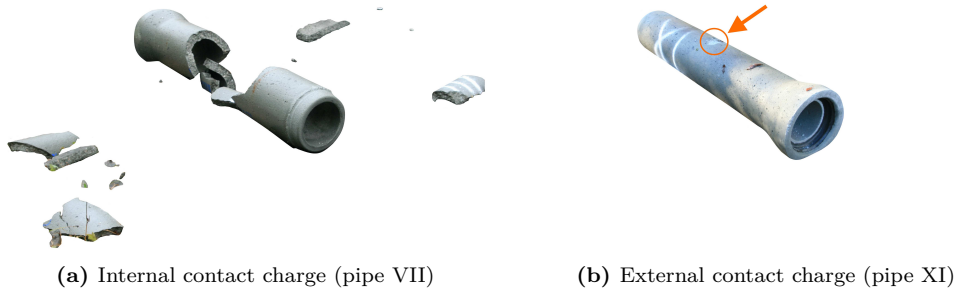
**Figure 6.19:** Damage of two the smaller plain concrete pipes with contact charges of 10 g C4.

The results from the new tests, with holes drilled into the pipe wall for pressure sensors, are in compliance with the previously conducted tests which had no drilled holes. Furthermore, for the pipes with drilled holes that fragmented, the cracks did not propagate through the drilled holes. Both these observations indicate that the drilled holes did not affect the damage of the pipes.

All pressure-time curves fluctuated due to the burning of the fireball. While it for both centric and internal contact charges was found that, in general, the pressures measured in the pipes' longitudinal direction resembled the characteristic blast wave, this was typically not the case for the external contact charges.
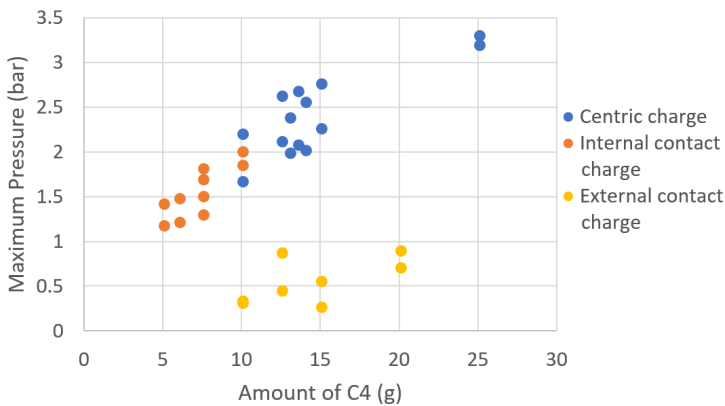


**Figure 6.20:** Peak pressure plotted against charge size for the smaller plain concrete pipes with charges of C4 placed centrically within the pipe and in contact internally and externally.

Figure 6.20 provides the peak pressure as a function of the charge size for all charge placements. From this figure, it can be seen that for both the centric and internal contact charges, the peak pressures display an approximate linear dependency on the charge size, while the peak pressures due to external contact charges are more scattered. In addition, the external contact charges produce significantly lower pressures. This is in good compliance with the damage observations, and again illustrates the significance of confinement for a blast load.

While it was shown that using the Kingery-Bulmash equations for the centric and internal contact charges would be non-conservative, the equations could seemingly safely be used for the external contact charges. Again, the reason for this is most likely that the external contact charge blast is not confined by the pipe wall. However, if the Kingery-Bulmash equations are used, to be on the safe side, one should use the Kingery-Bulmash equation for the reflected pressure caused by a surface explosion.

## 6.2.2   Larger Pipes

The larger pipes are subcategorized into 'plain' and 'reinforced'. All tests are from the second round of testing and all charges were centrically placed within the pipes.

### *Plain Concrete*

The damage of the larger plain concrete pipes subjected to blast loading by centrically placed charges is summarized in Table 6.5. All of the results are from the second round of testing. For some of the pipes that fragmented, a photo is included displaying the fragments approximately sorted by size. Some of the pipes fragmented in large heavy pieces which were difficult to move and arrange by size, thus there are no pictures of these fragments.

**Table 6.5:** Summary of the damage of the larger plain concrete pipes subjected to blast loading by centrically placed charges.

| Pipe ID | Amount of C4 (g) | TNT equivalent (kg) | Damage |
|---------|------------------|---------------------|--------|
| VI | 50 | 0.0685 | No visible damage |
| X | 65 | 0.08905 | Split in two along vertical, longitudinal axis |
| VII | 75 | 0.10275 | Few and large, oblong fragments |
| VIII | 75 | 0.10275 | Similar to pipe VII |
| V | 100 | 0.137 | Fragmentation  |
| I | 150 | 0.2055 | Fragmentation  |

65 g of C4 was required to fragment the larger plain concrete pipe when the charge was placed centrically within the pipe. The pipe then fragmented in two pieces. Larger charges caused the pipe to fragment into oblong pieces formed by longitudinal cracking. Increasing the charge further, resulted in smaller fragments which were more scattered around.

Figure 6.21 displays a time series of a larger plain concrete pipe subjected to blast loading caused by a centrically placed charge. Since the minimum charge required to fragment the pipe (65 g) caused the pipe to fragment into only two large pieces, there was not too much to see for that time series. Therefore, the time series in Figure 6.21 is instead of a blast when 100 g of C4 was used. The time series shows selected frames from both cameras such that the pipe can be seen from both the front and side. The creation and expansion of the fireball is clearly visible. For frame 26 from the side, one can also quite clearly see the shock wave. Also visible is the formation of oblong fragments due to longitudinal cracking and how these fragments are scattered around.

(a) Frame 0 (0 ms)



(b) Frame 26 (∼1.1 ms)



(c) Frame 81 (∼3.6 ms)



(d) Frame 218 (∼9.6 ms)

**Figure 6.21:** Selected frames for the larger plain concrete pipe V where a charge of 100 g C4 was centrically placed within the pipe.

**(e)** Frame 631 (∼27.9 ms)



**(f)** Frame 1263 (∼55.8 ms)

**Figure 6.21:** Selected frames for the larger plain concrete pipe V where a charge of 100 g C4 was centrically placed within the pipe.

All pressure-time curves for the larger plain pipes with centrically placed charges are available in Appendix A. In general, all pressure-time curves resemble the characteristic blast wave, but with some fluctuations due to burning of the fireball. It should be noted that sensor 7, and especially sensor 2, did not always provide reasonable results.

In Figure 6.22a the peak pressure is plotted as a function of the charge size. With an increased distance from the charge, the peak pressures display increasingly linear dependency on the charge size. The minimum charge required to fragment the pipes is marked in the plot, but the damage of the pipes does seemingly not affect the peak pressure. In Figure 6.22b the peak pressure is plotted against the scaled distance and compared with the Kingery-Bulmash peak and reflected pressure for both spherical air bursts and hemispherical surface explosions. The experimental test results form a curve of similar shape as the Kingery-Bulmash equations, but of higher values, particularly as the scaled distance diminishes. This is likely due to the confinement of the blast, and making use of the Kingery-Bulmash equations would therefore be non-conservative in this case.
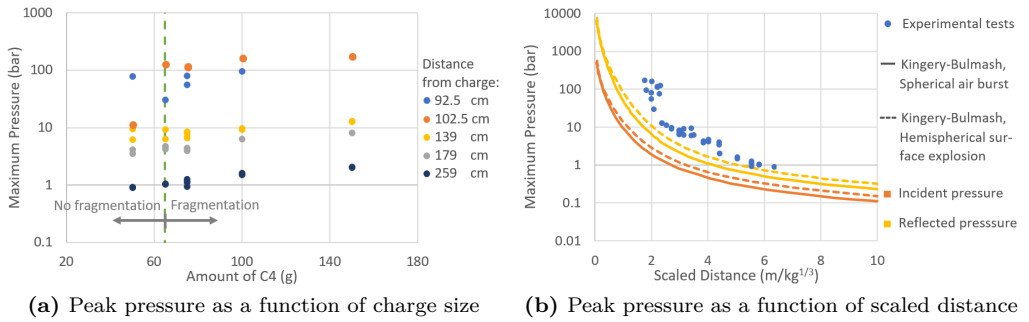
**(a)** Peak pressure as a function of charge size



**(b)** Peak pressure as a function of scaled distance

**Figure 6.22:** For the larger plain concrete pipes with centric charges, the peak pressure is plotted against charge size and scaled distance respectively. Note that the y-axes are logarithmic.

### Reinforced Concrete

The damage of the larger reinforced concrete pipes subjected to blast loading by centrically placed charges is summarized in Table 6.5. All results are from the second round of testing.

**Table 6.6:** Summary of the damage of the larger reinforced concrete pipes subjected to blast loading by centrically placed charges.

| Pipe ID | Amount of C4 (g) | TNT equivalent (kg) | Damage |
|---|---|---|---|
| II | 150 | 0.2055 | In center, one surface crack in ring direction and several in longitudinal direction with an avg. length of 69.22 mm (Std = 22.58 mm). Narrow end fragmented. |
| III | 200 | 0.274 | Similar to pipe II, but longer, deeper and wider cracks. Avg. longitudinal crack length 96.86 mm (Std = 17.19 mm). Narrow end fragmented. |
| IV | 300 | 0.411 | Similar to pipe III, but longer, deeper and wider cracks. Avg. longitudinal crack length 119.38 mm (Std = 30.80 mm). Through-thickness cracks. Cracking at narrow end. Narrow end fragmented. |
| IX | 400 | 0.548 | Similar to pipe IV, but longer, deeper and wider cracks. Avg. longitudinal crack length 121.00 mm (Std = 26.04 mm). Through-thickness cracks. One very small fragment detached from middle and one larger piece from the narrow end. Narrow end fragmented. |
| XII | 400 | 0.548 | Similar to pipe IX. Avg. longitudinal crack length 146.33 mm (Std = 42.82 mm). Narrow end fragmented. |
| XI | 500 | 0.685 | Similar to pipe XII, but longer, deeper and wider cracks. Avg. longitudinal crack length 150.00 mm (Std = 52.85 mm). Through-thickness cracks. Severe spalling/scabbing in center. Narrow end fragmented. |

**Figure 6.23:** Characteristic crack pattern for reinforced concrete pipes subjected to blast loading (pipe XII).

When the charge was placed centrically within the larger reinforced concrete pipes, one crack formed in the center of the pipe in the ring direction, and several cracks formed in the center in the longitudinal direction (see Figure 6.23). When the charge was enlarged, the crack length, depth, and width also increased. 300 g of C4 was required to produce through-surface cracks, as shown in Figure 6.24. Increasing the charge also caused larger fragments to detach from the pipe end. For a charge size of 500 g, there was also severe spalling/scabbing on both the in- and outside of the center of the pipe.

For all tests, the narrow end of the pipe fragmented, as illustrated in Figure 6.25. At first, this was thought to be mainly due to the narrowing of the pipe cross-section, in combination with the fact that at the end of the pipe the shock pressure propagating in the pipe wall is reflected and amplified. However, the cross-section also narrows at the other end of the pipe. When examining the pipe more closely, it was found that there was no reinforcement in the narrow end that fragmented. When the shock pressure propagating in the pipe wall reached this part, it therefore fractured.
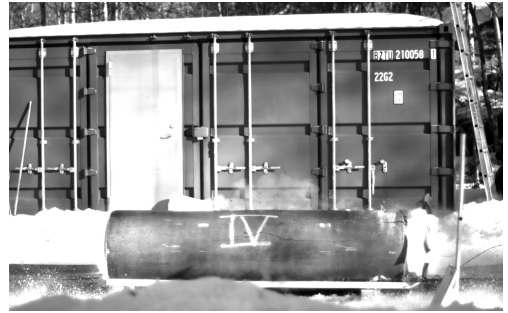


**Figure 6.24:** Through-thickness cracks in reinforced concrete pipe (pipe IV).



**(a)** Before

**(b)** After
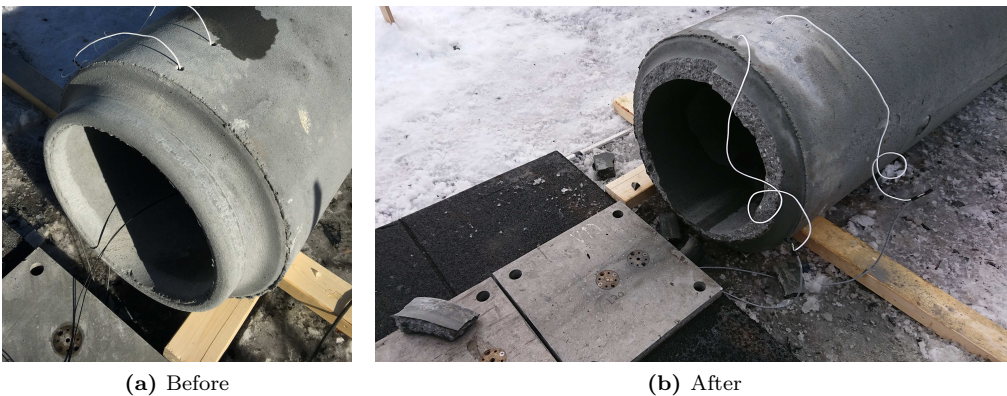
**Figure 6.25:** For all tests of the reinforced concrete pipes, the narrow end fragmented.

**(a)** Frame 0 (0 ms)
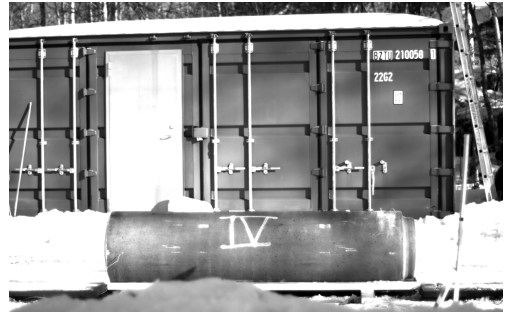


**(b)** Frame 100 (∼4.4 ms)



**(c)** Frame 400 (∼17.7 ms)



**(d)** Frame 1000 (∼44.2 ms)

**Figure 6.26:** Selected frames for the larger reinforced concrete pipe IV where a charge of 300 g C4 was centrically placed within the pipe.
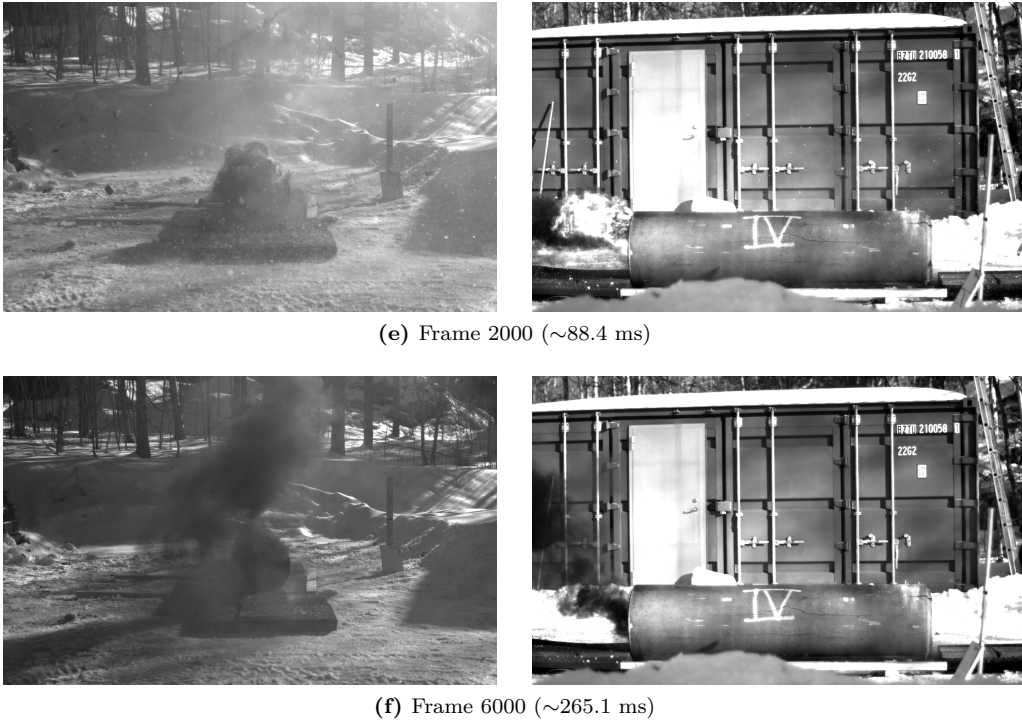
**(e)** Frame 2000 (∼88.4 ms)



**(f)** Frame 6000 (∼265.1 ms)

**Figure 6.26:** Selected frames for the larger reinforced concrete pipe IV where a charge of 300 g C4 was centrically placed within the pipe.

Figure 6.26 displays a time series for a larger reinforced concrete pipe subjected to a blast load caused by centrically placed charge. For this time series, 300 g of C4 was used, which was the minimum charge size required to produce through-thickness cracks. The time series shows selected frames from both cameras such that the pipe can be seen both from the front and from the side. The creation and expansion of the fireball is clearly visible. From frame 100 and outward it can also be observed how the narrow end fragments. In the time series, one can also see snow being whirled up by the blast wave. From the frames showing the side of the pipe, the formation of longitudinal cracks is apparent and, if one looks more closely, also the crack in the center of the pipe in the ring direction.

With the exception of pipe XII for which the sensors failed to record the pressure, all pressure measurements for the larger reinforced concrete pipes subjected to blast loading are provided in Appendix A. The pressure-time curves mostly resemble the characteristic blast wave, but with some fluctuations due to burning of the fireball. Note that for some of the tests sensors 2 and 7 were out of order.

The peak pressure is plotted against the charge size in Figure 6.27a. As the distance from the charge increases, the peak pressure displays a seemingly more and more linear dependency on the charge size. This dependency does not seem to be affected by whether or not there are through-thickness cracks. In Figure 6.27b the peak pressure is plotted as a function of the scaled distance, and compared with the Kingery-Bulmash peak and reflected pressure for both spherical air bursts and hemispherical surface explosions. The

experimental peak pressures coincide remarkably well with the Kingery-Bulmash equations considering that one would expect the confinement effect to be even larger in this situation.
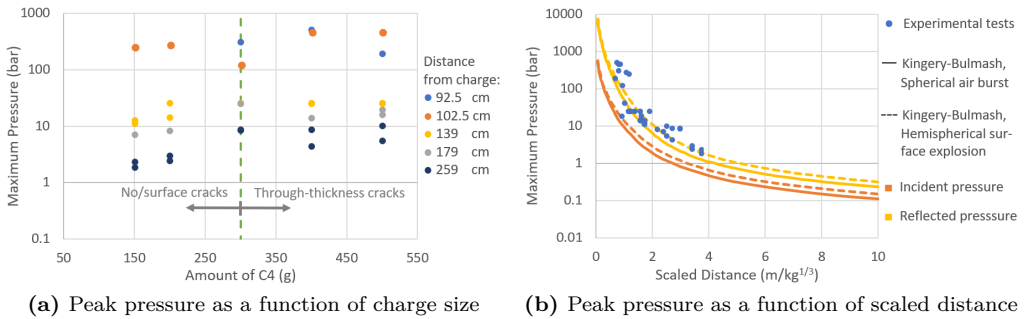


**(a)** Peak pressure as a function of charge size



**(b)** Peak pressure as a function of scaled distance

**Figure 6.27:** For the larger reinforced concrete pipes with centric charges, the peak pressure is plotted against charge size and scaled distance respectively. Note that the y-axes are logarithmic.

### Discussion

The larger plain concrete pipes fragmented in a similar manner to the smaller plain concrete pipes, in oblong fragments caused by cracking in the longitudinal direction. Increasing the charge size decreased the fragment size and scattered the fragments more. This is illustrated in Figure 6.28 where a 65 g charge of C4 caused the pipe to split into two large pieces, while a 150 g charge caused the pipe to fragment into many small pieces which were spread around. It was found that a charge of 65 g fragmented the pipe, while a charge of 50 g only caused one barely visible longitudinal surface crack.



**(a)** 65 g of C4 (pipe X)

**(b)** 150 g of C4 (pipe I)

**Figure 6.28:** Damage of two of the larger plain concrete pipes.

While 65 g of C4 was required to fragment the larger plain concrete pipe, 300 g of C4 was necessary to produce through-thickness cracks for the same size reinforced concrete pipes. For the reinforced concrete pipes, a very distinct crack pattern was observed at the center of the pipe where there was one crack in the ring direction and several in the longitudinal direction. For sufficiently large charges also spalling/scabbing was observed in the center of the pipe. The narrow end of the pipes fragmented for all tests probably due to the lack of reinforcement and pressure amplification in this part. The effect of increasing the charge size for the reinforced concrete pipes is illustrated in Figure 6.29. Comparing the pipes in Figure 6.28b and 6.29a for which the same charge size is used, clearly demonstrates the effect of reinforcement as the plain concrete pipe is completely fragmented, while the reinforced concrete pipe only has surface cracks.
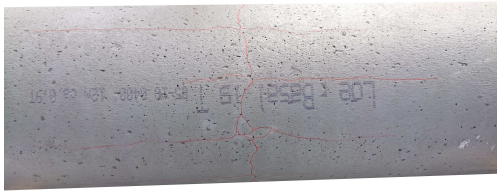
**(a)** 150 g of C4 (pipe II)        **(b)** 500 g of C4 (pipe XI)

**Figure 6.29:** Damage of two of the larger reinforced concrete pipes.

For the larger pipes, there were pin lift anchors cast into the pipe wall. For plain concrete pipe X, a crack had propagated through one of these lifting points (see Figure 6.30a). For reinforced concrete pipe IV a crack had propagated through the holes drilled for the pressure sensors (see Figure 6.30b). Nevertheless, since both these incidents occurred only once, nothing indicates that the holes drilled into the pipe wall or the lifting points affect the damage of the pipes.



**(a)** Lifting point (pipe X)        **(b)** Drilled holes (pipe IV)

**Figure 6.30:** Crack propagation through irregularities in pipe.

Overall the pressure-time curves for both the plain and reinforced larger pipes resembled the characteristic blast wave, although fluctuations were present due to the fireball burning. Figure 6.31 displays the peak pressure as a function of charge size for pipes both with and without reinforcement. For both pipe types, the peak pressure seems to depend linearly on the charge size, more and more so as the distance from the charge increases. While the Kingery-Bulmash equations were shown to be non-conservative for the plain concrete pipes, presumably due to the confinement effect, they were shown to be a good estimate for the reinforced concrete pipes. The reason for why the confinement of the blast seemingly did not affect the pressure in the reinforced pipes, is unidentified.
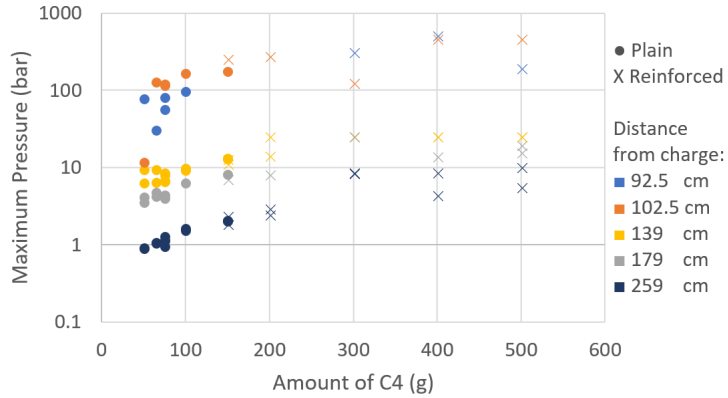
**Figure 6.31:** Peak pressure plotted against charge size for the larger plain and reinforced concrete pipes with charges of C4 placed centrically within the pipe.

If one compares the test results for the larger plain concrete pipes to the smaller pipes with centrically placed charges, one finds that although the pipe wall thickness was approximately doubled, the minimum charge size required to fragment the pipe was quintupled. For the larger pipes, the minimum charge required to damage the pipes severely was 4.6 times higher by adding reinforcement. It can therefore be concluded that increasing the wall thickness and adding reinforcement appear to be effective measures when designing tubular concrete structures with regard to blast resistance.

# Chapter 7

# Numerical Simulation of Concrete Pipes Subjected to Blast Loading

In an attempt to asses the performance of tubular concrete structures subjected to blast loading, the experimental blast tests of concrete pipes are simulated numerically. Different ways of modeling are examined.

## 7.1   Lagrangian Analyses of Pipe

Although confined blast loads are complex and therefore usually require more sophisticated methods of analysis, Lagrangian analyses with explicit time integration are extensively used to model structures subjected to blast loading [15], and their capabilities will therefore be examined.

As was explained in Section 3.4.4, in a Lagrangian analysis the mesh is fixed to the material, and the elements deform with the material. Lagrangian meshes are mainly used in structural analyses. In this thesis, all preceding analyses of the compression tests have been Lagrangian.

### 7.1.1   ABAQUS

Lagrangian analyses of the pipes subjected to blast loading are performed in the finite element software ABAQUS. A reference model is first established, and a parametric study is performed for some key parameters.

### Reference Model

In ABAQUS it is necessary to scale the concrete material parameters such that they correspond to the concrete used for the pipes, i.e. have a cube compressive strength of 83.3 MPa. This is done in the same manner as in Chapter 5, only now using a 10x10x10 cm cube and an 8 mm mesh, which corresponds to the concrete's maximum aggregate particle size. Young's modulus is estimated using Equation (3.1) from Eurocode 2 [72] and is therefore $E = 23$ GPa. The resulting stress-strain curves from the numerical simulations of the compression tests, both with and without material parameter scaling, can be seen in Figure 7.1.
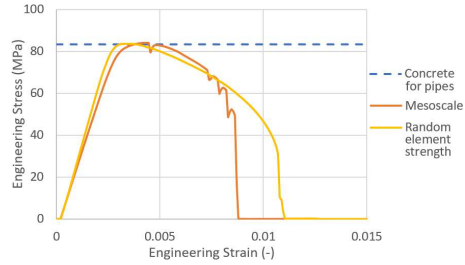


**Figure 7.1:** Scaling of concrete material parameters such that the CDP model in ABAQUS corresponds to the concrete of the pipes.

Once the material scaling factor is determined, the pipes subjected to blast loading can be simulated numerically using an explicit method.

To begin with, only the smaller pipes are modeled. The full geometry of the pipe, as shown in Figure 6.1, is created using solid elements. Since reduced integration is also used, the elements are of type C3D8R. Default hourglass control is utilized. The pipe is meshed using a mesh size of 8 mm, corresponding to the maximum particle size.

It is desirable that the simulation time of the reference model is no longer than necessary since a parameter study is to be performed. The simulation time is therefore set to 5 ms as this should be sufficiently large to capture the peak of the shock wave.
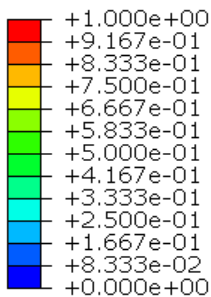


**Figure 7.2:**
Damage scale in ABAQUS.

From the experimental tests, it was found that the Kingery-Bulmash equations in most cases were non-conservative due to the confinement effect. Even though ConWep is based on these equations, ConWep is a simple method for imposing a blast load since the only required input is blast type, which surface is subjected to the blast, and the charge's position and TNT equivalent mass. For the reference model, ConWep is therefore used with a centrically placed charge of 14 g C4 (∼19.2 g TNT). For the second round of experimental testing, 14 g of C4 was the smallest centric charge that caused the pipe to fragment. Unless stated otherwise, the blast is modeled as an air blast.

Since the analyses are not coupled, there is no simulated shock wave pressure which can be compared with the experimental results. Only the pressure which is applied to the pipe can be displayed. Instead, the damage of the pipes is compared visually. Unless specified otherwise, the term damage will for ABAQUS be used for the tensile damage of concrete. Figure 7.2 displays the damage scale in ABAQUS where 1 is complete damage, and 0 is no damage. This scale is applicable for all the numerical simulations of damage conducted in ABAQUS for this chapter, unless another scale is provided. Since the peak pressure is very sudden, high, and short, one thousand field outputs are requested in an attempt of better capturing the peak. For some simulations, the total number of increments will be less than this, and then the number of field outputs will be equal to the number of increments.

All analyses are performed using four CPUs and double precision. The reference model then takes approximately 5.5 minutes to run.

### *Load Application and Charge Size*

ConWep was used for the reference model, even though the Kingery-Bulmash equations were found to mostly be non-conservative for the experimental tests. Alternative methods of predicting and applying the blast load are therefore assessed.

One way of imposing the blast load is by applying it as a pressure on the inside of the pipe. However, in the experimental tests, the pressure was only measured at the end of, and outside of, the pipe. Therefore, in order to estimate the pressure at various locations inside the pipe, the Friedlander equation (Equation 3.6 in Section 3.4.2) is curve-fitted to the pressure measured inside the pipe at sensor 8. The curve-fitting is done using the least squares method. The pressure at sensor 8 is used instead of the pressure at sensor 7, since sensor 7 seemed malfunctioned for some tests. By using the difference in time of arrival of the shock wave at sensor 8 and 1, as well as the distance between the sensors, the wave speed



**Figure 7.3:** Example of how Friedlander is curve-fitted and extrapolated.

is calculated. Once the wave speed is known, one can estimate the time of arrival of the shock wave at different locations inside the pipe. The Friedlander equation can then be extrapolated to estimate the pressure at these locations. In Figure 7.3 the Friedlander curve-fitting and extrapolation is illustrated for the smaller plain concrete pipe with a 14 g charge of C4 centrically placed within the pipe.
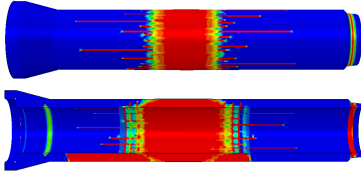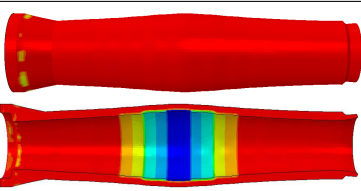
Once the pressure is estimated by curve-fitting and extrapolating the Friedlander curve, it needs to be decided how to apply the pressure to the inside of the pipe. One easy method, yet overly conservative, is to apply the pressure estimated for the center of the pipe, uniformly to the whole inside of the pipe. Another method is to partition the inside of the pipe into equally large segments, estimate the pressure at each of these partitions, and then apply the respective pressures uniformly at each partition. For these simulations, partitions with an approximate width of 10 cm are chosen. The last method that will be assessed for imposing the pressure is to define the Friedlander equation as a function of the pipe's longitudinal axis. These three different ways of imposing the Friedlander pressure will from now on be referred to as 'uniform Friedlander', 'uniform Friedlander with partitioning', and 'varying Friedlander' respectively. For all these Friedlander methods, the pressure is applied simultaneously to the whole inside of the pipe.

In Figure 7.1 all these different methods of subjecting the pipes to blast load numerically are compared, including ConWep. Images are provided showing the damage of both the in- and outside of the pipe model. As the Friedlander methods eventually cause severe deformations and damage, as well as mesh distortion, the pipes are compared at 0.5 ms. All methods are checked for two charge sizes, one that caused the pipe to fragment (14 g of C4), and one that did not (12 g of C4). This corresponds to the experimental tests of the smaller pipes XX and XIX respectively. Photographs of the damage of these pipes are also included for the sake of comparison.

**Table 7.1:** Damage of pipes with various charge sizes, simulated in ABAQUS with various methods of load prediction and application. Images of both the in- and outside of the pipes are provided at 0.5 ms.

| Method | Amount of C4 | |
| --- | --- | --- |
| | **12 g** | **14 g** |
| Experiment |  |  |
| ConWep |  |  |
| Uniform Friedlander |  |  |
| Uniform Friedlander with partitioning |  |  |
| Varying Friedlander |  |  |

The first observation that is made from studying the results in Figure 7.1, is that although the damage is slightly greater for the larger charge, the damage is very similar regardless of charge size, even though this was not the case for the experimental results. All methods cause severe damage to the pipes and therefore appear to be conservative, despite not accounting for reflections.
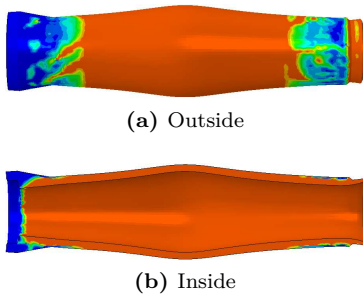
**(a)** Outside



**(b)** Inside

**Figure 7.4:** Compressive damage of smaller pipe simulated in ABAQUS when applying varying Friedlander pressure for a 14 g charge of C4.

Another conspicuous observation from Table 7.1 is that the different ways of applying the pressure, provide different deformations and damages. Applying the Friedlander pressure as a function of the pipe's length axis, or as uniform pressures on partitions of the pipe, results in similar damage where the whole outside of the pipe is damaged, as well as the end sections. In addition, there are large deformations in the center of the pipe. Although the center of the inside of the pipe seems intact, it is important to remember that it is only the tensile damage which is displayed. Thus, in Figure 7.4 also the compressive damage is plotted for the pipe that was simulated using varying Friedlander pressure for the 14 g charge of C4. It is then clear that the whole pipe is completely damaged. The same goes for when using the uniform Friedlander pressure, although the deformation of these pipes is clearly different, as well as unrealistic.

The most promising method of imposing the blast load in the Lagrangian analyses is therefore ConWep. Unlike the Friedlander methods, ConWep does not cause damage to the whole pipe and is able to capture the locality of the problem. Therefore, the ConWep method will be further investigated, while the other methods are discarded. Nevertheless, also ConWep overpredicts the damage for the 12 g C4 charge. It is therefore checked what is the maximum charge size that does not cause severe damage to the pipe. This is done by repeatedly decreasing the charge size and inspecting the damage until the amount of damage is satisfactorily small. According to ABAQUS with ConWep, as little as approximately 1.2 g of C4 will be just enough to cause severe damage to the pipe. In comparison, from the experimental tests, the same number was found to be 13 g. As ConWep is based on the Kingery-Bulmash equations, which from the experimental testing, in general, were found to be non-conservative, it is unexpected for ConWep to be so overpredictive of the damage.
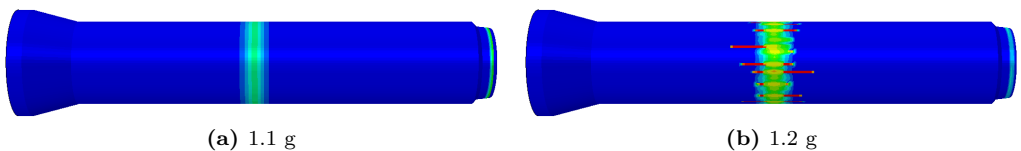


**(a)** 1.1 g



**(b)** 1.2 g

**Figure 7.5:** Numerically simulated damage of pipes with various charge sizes in ABAQUS.

To check whether it is ConWep or the material model which is the cause of the unexpected high damage, the pressure calculated and applied to the pipe by ConWep is plotted for both 12 and 14 g charges. The pressures in Figure 7.6 are plotted for elements on the inside of the pipe wall, in the center and at the locations corresponding to sensors 7 and 8. The pressures measured at sensors 7 and 8 for the experimental tests are also included for comparison. It is then evident that the ConWep pressure is in fact much lower than the experimentally measured pressure. This therefore indicates that it is the material model which is the cause of the overpredicted damage.
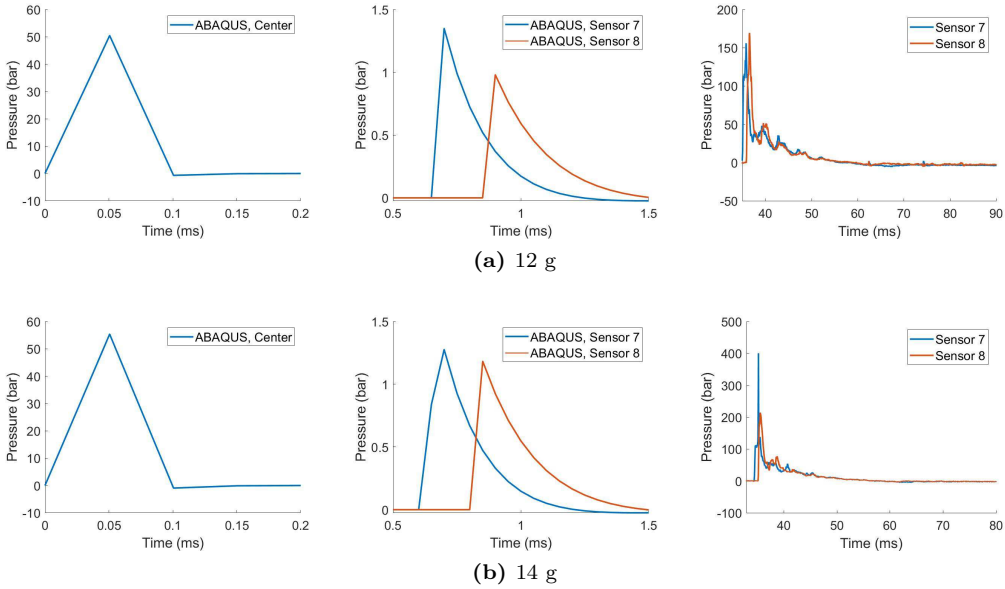
**(a)** 12 g



**(b)** 14 g

**Figure 7.6:** ConWep pressures for 12 and 14 g charges of C4, measured at the inside of the pipe wall in the center and at sensors 7 and 8. The plots to the right display the pressures at sensors 7 and 8 from the corresponding experimental tests.

### Simulation Time

In the column furthermost to the right in Table 7.2, a time series of the damage propagation is shown for when ConWep is utilized for the smaller plain concrete pipe with a 14 g centric charge of C4. It can be seen that the damage commences in a band around the center of the pipe. The width of the damage band then increases, without creating fragments, and cracks start forming from the band and outwards in the longitudinal direction. The narrow end of the pipe is also damaged. In the corresponding experimental test, the damage was also greatest in the center of the pipe, but fragments were formed due to longitudinal cracking. The narrow end remained intact in the experimental test.

**Table 7.2:** Damage of pipe simulated in ABAQUS with various simulation times.

| Simulation time | Damage | |
| --- | --- | --- |
| | **At 0.5 ms** | **At last increment** |
| **0.5 ms** |  |  |
| **5 ms** |  |  |
| **50 ms** |  |  |

From the experimental test results in Appendix A, it can be seen that the total duration of the shock wave is less than 50 ms. In the numerical model, however, there seems to be

no end to the damage propagation. Since the damage is excessive already at 5 ms, from now on the damage will only be compared at 0.5 ms.

It is also examined whether the total simulation time affects the damage at a certain time increment. This is done by running the reference model at a total simulation time of 0.5, 5, and 50 ms. The damage is then compared at 0.5 ms and displayed in the left column in Table 7.2. For all three simulation times, the width of the damage bands appears to be equal, and the narrow end is damaged similarly. Nevertheless, the longitudinal cracks vary somewhat and with no obvious trend.

### *Young's Modulus*

Since the damage is overpredicted, even though the pressure is underestimated, Young's modulus $E$ is scaled in hope that increasing the elasticity will decrease the damage. For the reference model, Young's modulus was determined according to the Eurocode to be $E = 23.0$ GPa. However, for the compression tests in Chapter 5 it was found that Young's modulus could be increased even further. Since there are no compression tests to scale Young's modulus to for the pipes, the results from Chapter 5 and linear approximation are used to provide an estimate of $E = 45.5$ GPa. The unscaled $E = 19.7$ GPa for a B50 concrete provided by Jankowiak et al. [79] is also evaluated.
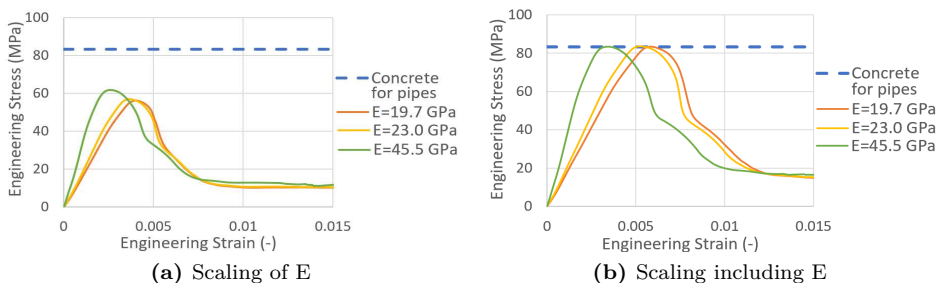


**(a)** Scaling of E  **(b)** Scaling including E

**Figure 7.7:** Scaling of concrete material parameters, including Young's modulus $E$, such that the CDP model in ABAQUS corresponds to the concrete of the pipes.

To provide a compressive strength of 83.3 MPa the concrete material parameters are then scaled in the same manner as described in Chapter 5. This is done by first only scaling $E$ and simulating the compression test numerically (Figure 7.7a), and afterwards scaling the remaining concrete material parameters and simulating the compression test numerically once more (Figure 7.7b).

The scaled material models, including scaling of $E$, are then used to simulate the smaller pipes subjected to blast loads. However, from Figure 7.8 it is observed that whether or not Young's modulus is scaled, seems to be of minor importance with regard to damage. Although the cracking of the concrete varies somewhat for the different values of $E$, the width of the damage band is seemingly unchanged and the damage is still excessive.
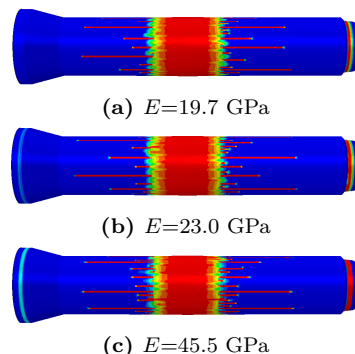


**(a)** $E$=19.7 GPa

**(b)** $E$=23.0 GPa

**(c)** $E$=45.5 GPa

**Figure 7.8:** Damage of pipe simulated in ABAQUS with various values of Young's modulus $E$.

## *Mesh Size*

When simulating the cube compression tests in Chapter 5 it was confirmed that the concrete damaged model plasticity model (CDP) in ABAQUS is highly mesh sensitive. From what is known about the CDP model, the same mesh sensitivity is to be expected for the pipe as it is both plain and subjected to the highly localized loading of a blast. In Figure 7.10 it is checked whether this indeed is the case and the mesh size of the pipe is therefore both halved and doubled. The pathological mesh dependency is then clear also for the pipes. As the mesh size is decreased, the damage becomes more and more localized. The mesh size also greatly affects the CPU time, as is illustrated in Figure 7.9. Deciding on an appropriate mesh size is therefore challenging and it is decided to keep the 8 mm mesh for further simulations since this is the mesh size that the concrete material model is scaled for.
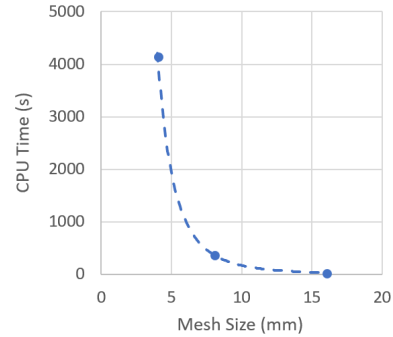


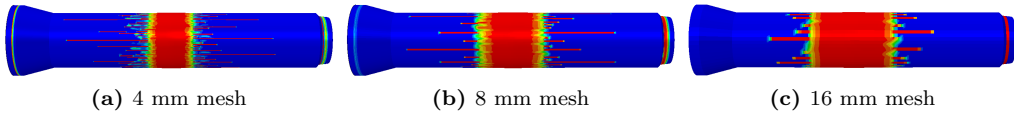**Figure 7.9:** CPU time in ABAQUS as a function of mesh size.



| **(a)** 4 mm mesh | **(b)** 8 mm mesh | **(c)** 16 mm mesh |
|---|---|---|

**Figure 7.10:** Damage of pipe simulated in ABAQUS with various mesh sizes.

## *Blast Type*

One of the input parameters of ConWep is blast type, i.e. whether the blast is a spherical air blast or a hemispherical surface blast. From the experimental testing, it was found that in some cases the Kingery-Bulmash equations for hemispherical surface blasts, were a better match due to the effect of reflections.

In Figure 7.12 the ConWep pressures are compared for both blast types, and it is confirmed that the surface blast does indeed provide higher pressures. While the pressure at the center of the pipe is much higher for the surface blast, and therefore more realistic with regard to the pressures measured experimentally at sensors 7 and 8, the pressures simulated at sensors 7 and 8 are still much too low.
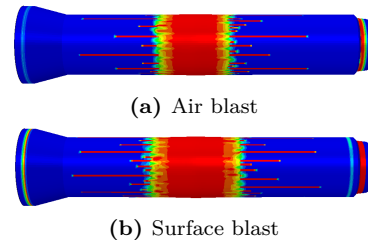


**(a)** Air blast



**(b)** Surface blast

**Figure 7.11:** Damage of pipe simulated in ABAQUS both with air and surface blast formulation for ConWep.

Since the pressures are higher for the surface blast, the damage is also larger, as is shown in Figure 7.11.
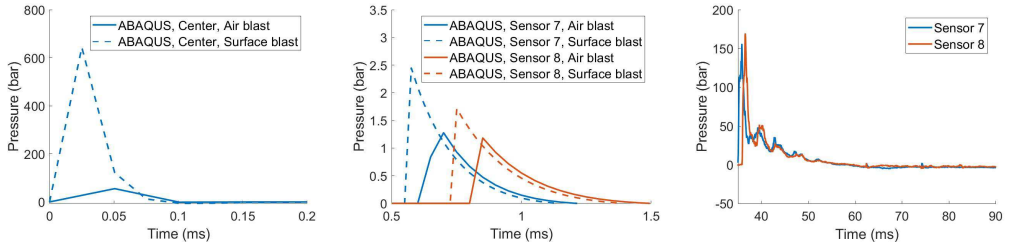
**Figure 7.12:** ConWep pressures for both air and surface blasts of a 14 g charge of C4, measured at the inside of the pipe wall in the center and at sensors 7 and 8. The plot to the right displays the pressures at sensors 7 and 8 from the corresponding experimental test.

### Charge Placement

From the experimental tests, it was found that the charge placement had a considerable effect on the damage of the pipes. It is therefore desirable to check whether it is possible to render this effect with numerical simulations.

All charges are of 10 g C4 such that the results can be compared to both each other and to experimental test results. For the contact charges, the charges are placed on the top of the pipe and hemispherical surface blast formulation is utilized for ConWep.
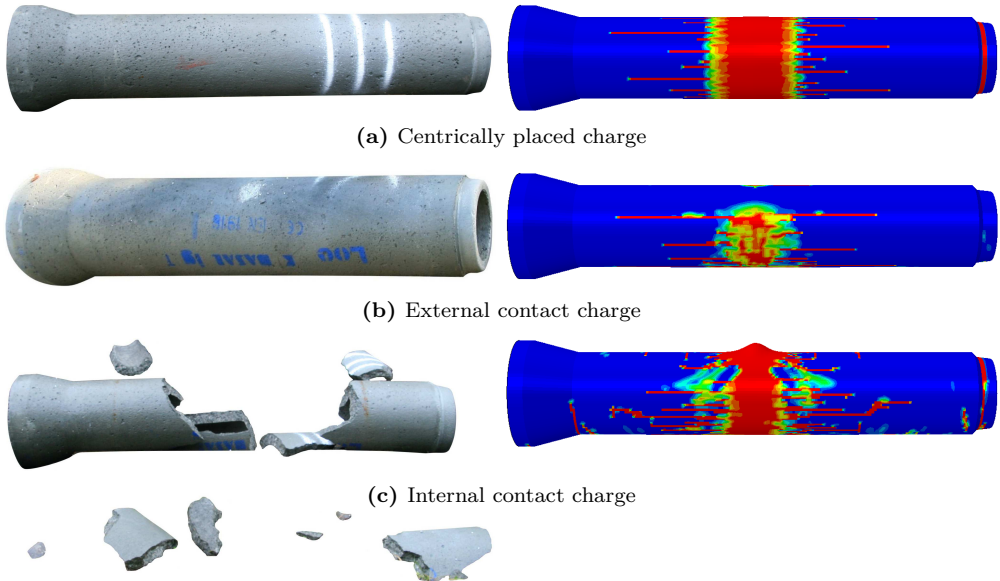


**(a)** Centrically placed charge



**(b)** External contact charge



**(c)** Internal contact charge

**Figure 7.13:** Damage of pipes with charges of 10 g C4 at various placements. Both the experimental tests results and the results from the numerical simulations in ABAQUS are provided.

From Figure 7.13 it is clear that varying the placement of the charge significantly affects the damage of the pipe, both experimentally and numerically. However, the numerically simulated damages do not resemble that of the experimental tests.

### Reinforcement

From the experimental testing, it was also found that whether the pipes were reinforced or not, greatly affected the damage of the pipes when subjected to blast loads. Additionally, as discussed in Section 3.3.2, the concrete damaged plasticity model in ABAQUS is primarily intended for reinforced concrete. The numerical model of a smaller pipe is therefore replaced by a larger pipe with the same material properties, and reinforcement is added.

The properties of the reinforcement steel are unknown, and the rebars in the model are therefore given a standard steel material with a density of 7850 kg/m$^3$, Young's modulus 210 GPa, and a Poisson ratio of 0.3. Since the reinforcement did not obtain much damage in the experimental tests, it is not assigned any plastic material properties in the numerical model. The rebars are modeled as beam elements with sections and placement as described in the previous chapter. The rebar beam elements are then embedded in the numerical model of the larger concrete pipe.
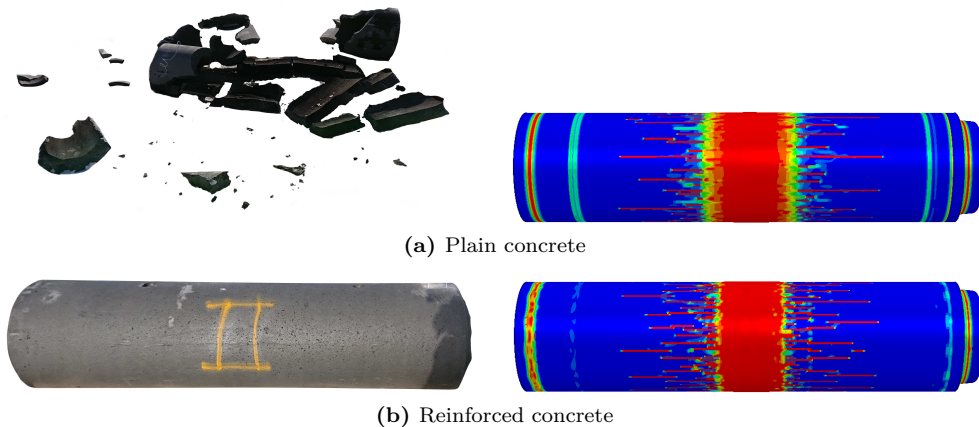


**(a)** Plain concrete



**(b)** Reinforced concrete

**Figure 7.14:** Damage of larger pipes from experimental tests and ABAQUS simulations, both with and without reinforcement, for charges of 150 g C4.

In Figure 7.14 the larger concrete pipes, both with and without reinforcement, are simulated numerically for centrically placed charges of 150 g C4. The experimental test results are also included for the sake of comparison. The plain concrete pipe was in reality completely damaged, while for the reinforced pipe only the narrow end fragmented and some surface cracks were observed. For the numerical simulations, however, the difference is far less. The damage band of the plain pipe is wider than for the reinforced pipe, but there are more cracks for the reinforced pipe.

### Statistical Variation

Although the amount of damage has varied somewhat, the damage has looked similar for almost all simulations, except for when varying the charge placement. It is desirable to check whether it is possible to obtain a more random and realistic crack pattern. Therefore, two of the methods for introducing statistical variation to the concrete's behavior (modified random element strength and mesoscale modeling) which were both evaluated for the numerical simulation of the concrete compression tests, will now be assessed for the concrete pipes.

Firstly, as before, the concrete needs to be scaled such that it has a compressive strength of 83.3 MPa. The compression tests are modeled with the same input as their corresponding reference models in Chapter 5, but now the concrete cube is 10x10x10 cm, and a mesh size of 8 mm is used. Scaling is included in the modified random element strength method, while the mesoscale method requires manual scaling. Since the matrix strength was found to have the most effect on the mesoscale model's compressive strength, it has been altered until it provided a satisfactory compressive strength



**Figure 7.15:** Scaling of concrete material parameters for the modified random element strength and mesoscale methods such that they provide compressive strengths in ABAQUS corresponding to the concrete of the pipes.

for the numerical simulation of the compression test. As the method is meant to provide variation, the resulting compressive strength will not always be exactly the same, but a matrix compressive strength of 71.4 MPa seems to provide a reasonable result (see Figure 7.16). The modified random element strength method is also meant to provide variation, but from Figure 7.25 it is seen the compressive strength is acceptable.
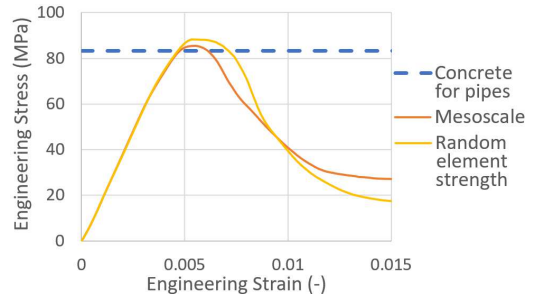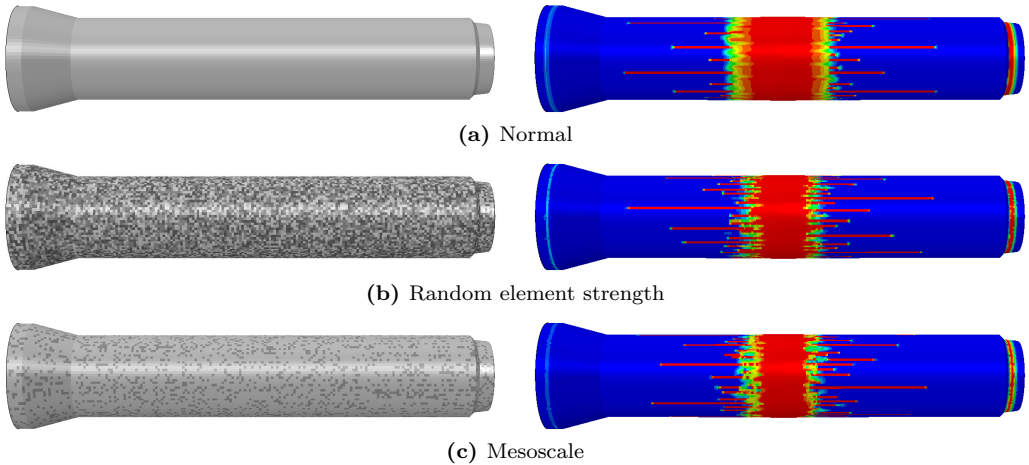


**(a)** Normal



**(b)** Random element strength



**(c)** Mesoscale

**Figure 7.16:** Damage of pipe simulated in ABAQUS both with normal concrete damaged plasticity, modified random element strength method, and mesoscale modeling.

Once it has been confirmed that the methods provide the correct concrete strength, they can be applied to the pipes. The result can be seen in Figure 7.16 where also images of the undamaged input models are displayed to emphasize the concept of the methods. For the random element strength model, each shade of grey corresponds to slightly different concrete strengths. For the mesoscale model, the darker grey elements correspond to the particles, while the lighter grey elements make up the matrix. The reference model has also been included for comparison.

Although both of the methods for statistical variation provide the same looking damage as before, with a band in the center and longitudinal cracking, there are some differences. Both methods namely seem to decrease the width of the damage band, the mesoscale modeling method slightly more than the other. Note that these methods have only been tested for the 8 mm mesh and that perhaps the difference would have been greater if the mesh was refined.

### *Integration Method*

It is briefly controlled whether there is a notable effect of using full versus reduced integration. Additionally, for the model with reduced integration, both default and stiffness hourglass control is tested. Note that the model with reduced integration and default hourglass control is the reference model. From Figure 7.17 there seems to be relatively little difference for the damage. However, for these simulations the CPU time is 41.5 minutes when using full integration, compared to 6 (stiffness) and 6.5 (default) minutes when using reduced integration.
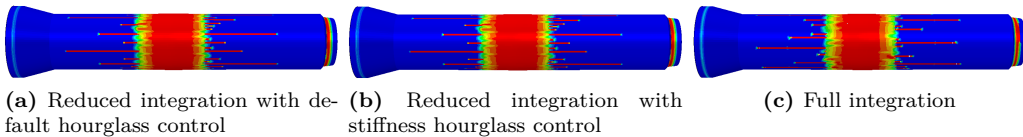


**(a)** Reduced integration with default hourglass control    **(b)** Reduced integration with stiffness hourglass control    **(c)** Full integration

**Figure 7.17:** Damage of pipe simulated in ABAQUS with both full and reduced integration with various hourglass control.

### *Precision*

Lastly, it is decided to examine if single precision could have been used to save computational cost and if this would have affected the damage. In Figure 7.18 the tensile damage of the pipes are compared for single and double precision, and it is observed that the difference is modest. The double precision simulation took 22.3 % longer to run than the one with single precision.
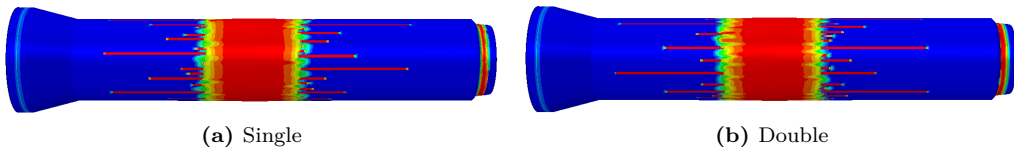


**(a)** Single      **(b)** Double

**Figure 7.18:** Damage of pipe simulated in ABAQUS with both single and double precision.

## 7.1.2 LS-DYNA

Since a different concrete material model is used for LS-DYNA, Lagrangian analyses of the pipes subjected to blast loading are performed in LS-DYNA as well. Since the main goal of the LS-DYNA analyses is to asses the material model, the parametric study is slightly more limited than the one performed for ABAQUS.

### Reference Model

The advantage of the K&C concrete model in LS-DYNA is that it is not necessary to scale the material parameters. Still, a numerical analysis of the compression test is performed in the same manner as in Chapter 5, only now with a 10x10x10 mm cube and 8 mm mesh, to ensure that the concrete model does in fact provide the correct compressive strength. The result is presented in Figure 7.19 and it is observed that the compressive strength is of satisfactory magnitude.
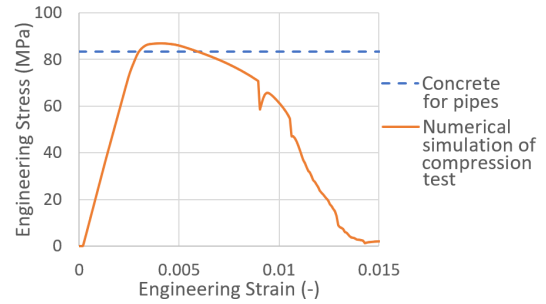


**Figure 7.19:** Numerical simulation of compression test in LS-DYNA in order to validate the concrete material model.

Once the validity of the material model has been confirmed, the pipes can be simulated numerically. A reference model is established as similar to the one in ABAQUS as possible. Therefore, an explicit method, an 8 mm mesh, reduced integration with default hourglass control, a 14 g charge of C4, and ConWep, are used.
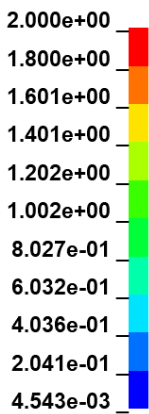


**Figure 7.20:** Legend for damage in LS-DYNA.

From preliminary simulations, it is found that the LS-DYNA reference model appears to be rather slow and therefore it is decided to use single precision to reduce the computational cost. If this affects the results, will be examined in the parametric study. In addition, in order to decrease the computational cost, the reference model is only simulated for 0.5 ms. This effect will also be examined in the parameter study. The reference model then takes approximately 6 minutes to run.

Like it was done for the ABAQUS analyses, the damage of the pipes will be compared visually. However, the damage definition in the two codes is different. Unlike ABAQUS, LS-DYNA does not distinguish between tensile and compressive damage. In LS-DYNA the damage is instead referred to as "scaled damage measure" and in Chapter 3, Section 3.3.2, it is further described. A damage scale that is applicable for all simulations of damage in LS-DYNA in this chapter is provided in Figure 7.20. A scaled damage of value 0 corresponds to the yield failure surface, while values of 1 and 2 correspond to the maximum and residual failure surfaces respectively [80].

### Charge Size

For the experimental testing, 12 g of C4 centrically placed within the pipe did not cause any visible damage to the pipe, while 14 g caused the pipe to fragment. When simulated in LS-DYNA both charge sizes cause similar and severe damage to the pipe, as can be seen in Figure 7.21. The damage is mostly localized in a band in the center of the pipe from which longitudinal cracks, which eventually propagate diagonally, emerge. The edges of the cracks are rather indistinct. There are also several cracks in the ring direction.
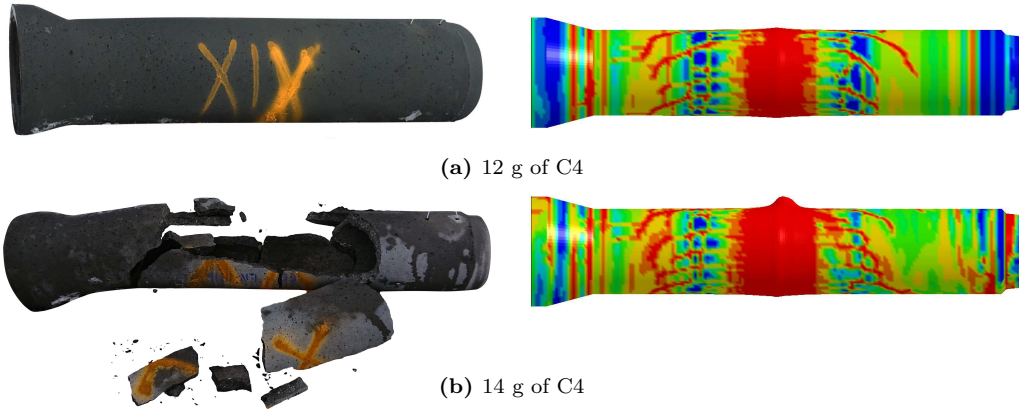
**(a)** 12 g of C4



**(b)** 14 g of C4

**Figure 7.21:** Damage of pipe with various charge sizes, from experimental testing and numerical simulations in LS-DYNA.

### Simulation Time

The simulation time is investigated next. The simulation time is set to 0.5, 5 and 50 ms. In Table 7.3 the damage of the pipes is compared at 0.5 ms for all three simulation times, in addition to at the last increment. It is observable that the damage appears to be quite similar at 0.5 ms for all simulation times, although the amount of deformation in the center of the pipe, as well as the crack pattern, varies somewhat. When the damage at the last increment is compared for the different simulation times, it is notable that the damage does not spread with time, but instead the deformations in the center of the pipe increase. For 50 ms simulation time the deformation is unrealistic at the last increment, but since these elements are completely damaged, one can disregard them. It is also observed that the narrow end is highly damaged and deformed for this increment.

**Table 7.3:** Damage of pipe simulated in LS-DYNA with various simulation times.

| Simulation time | Damage | |
|:---:|:---:|:---:|
| | **At 0.5 ms** | **At last increment** |
| **0.5 ms** |  |  |
| **5 ms** |  |  |
| **50 ms** |  |  |

### *Mesh Size*

The effect of mesh size is examined by halving and doubling the mesh size of the reference model. The results are provided in Figure 7.22. When the mesh is refined, it is observed an increased amount of cracking and a more distinct crack pattern with narrower cracks. In addition, the pipe ends seem to become more damaged when reducing the mesh size.
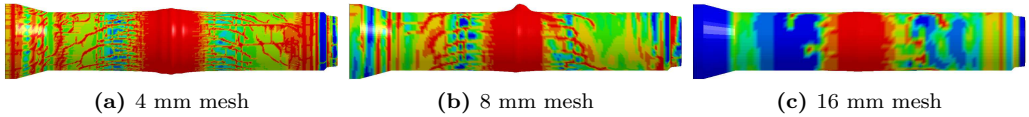


**(a)** 4 mm mesh                **(b)** 8 mm mesh                **(c)** 16 mm mesh

**Figure 7.22:** Damage of pipe simulated in LS-DYNA with various mesh sizes.

### *Charge Placement*

The location of the charge is investigated in Figure 7.23. Charges equivalent to 10 g of C4 are used such that the simulated results can be compared to the experimental results. For the contact charges ConWep surface blasts are used. The damage of the pipe is clearly affected by the charge placement. Still, a common feature for all the charge placements is that the numerical simulations greatly overpredict the damage. Nevertheless, some characteristics that were observed from the experimental testing can also be observed for the simulations. The numerical model of the external contact charge, for instance, displays deformations which resemble cratering, the internal contact charge causes the most damage in the center of the pipe, while longitudinal cracking can be seen for the centrically placed charge.



**(a)** Centrically placed charge



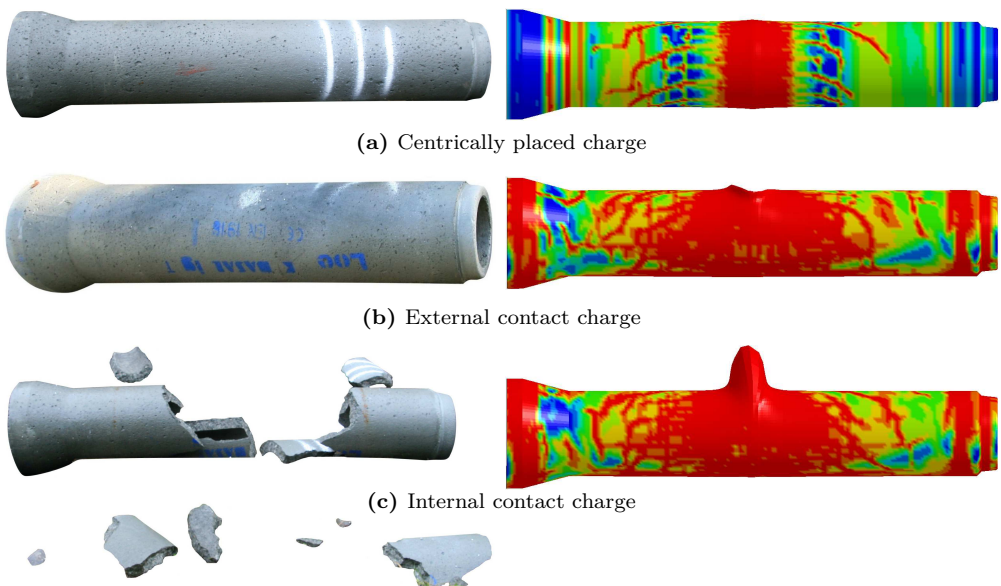**(b)** External contact charge



**(c)** Internal contact charge

**Figure 7.23:** Damage of pipe with charges of 10 g C4 at various placements. Both the experimental tests results and the results from the numerical simulations in LD-DYNA are provided.

### *Statistical Variation*

In the same manner as for the ABAQUS simulations, statistical variation is introduced for the concrete by the methods of modified random element strength and mesoscale modeling.

It is first examined that the methods provide satisfactory compressive strengths when simulating the compression tests, which it from Figure 7.24 can be confirmed that they do. For the mesoscale model, a matrix strength of 71.4 MPa is used, just like in ABAQUS.
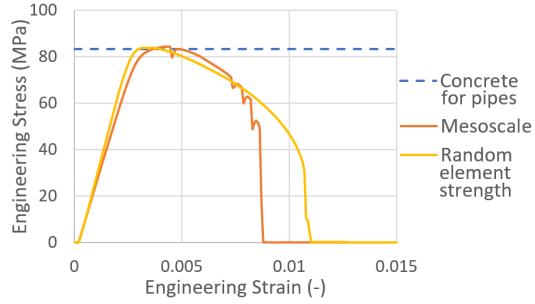


**Figure 7.24:** Numerical simulation of compression test in LS-DYNA in order to validate the concrete material model when using the modified random element strength and mesoscale methods.

Once the material models have been verified, they are applied for the pipes. The results are presented in Figure 7.25 where also images of the input models are included in order to clarify the principle of the methods. In the random element strength model, each shade of grey corresponds to concrete materials with slightly different strengths. In the mesoscale model, the darker grey elements correspond to the particles. In addition, the reference model has been included for comparison. It observed that the modified random element strength method does not seem to notably affect the damage, although the deformations in the pipe center are reduced. Mesoscale modeling, on the other hand, seems to reduce the damage remarkably. In addition, the cracks seem to be a bit more random and the deformations in the pipe center are reduced.
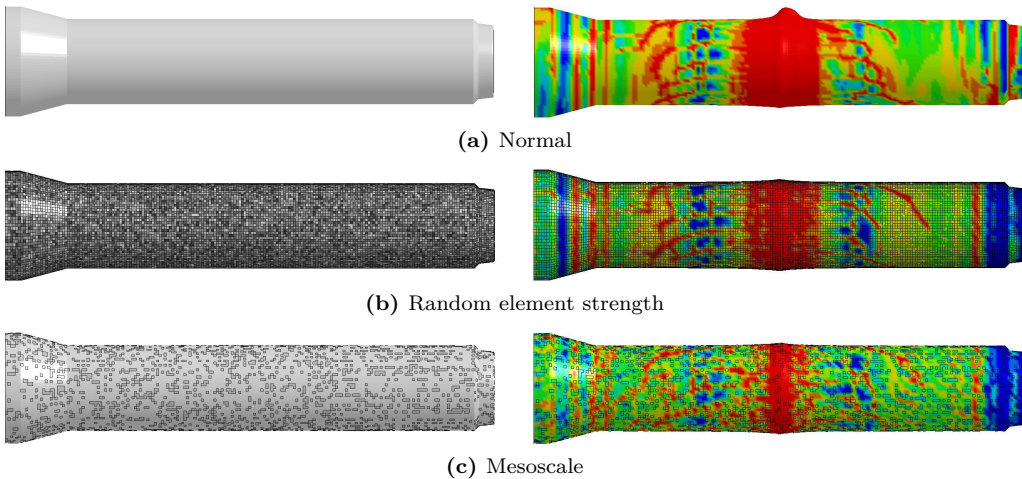


**(a)** Normal



**(b)** Random element strength



**(c)** Mesoscale

**Figure 7.25:** Damage of pipe simulated in LS-DYNA both with normal concrete damaged plasticity, modified random element strength method and mesoscale modeling.

### *Integration Method*

It is also examined whether it makes a difference for the damage if it is used reduced or full integration. Both default and stiffness hourglass control are tested for the reduced integration. Recall that reduced integration with default hourglass control corresponds to the reference model. From Figure 7.26 it is clear that both integration method and hourglass control affects the damage. The amount of deformation in the center of the pipe, crack pattern, and width of the damage band, varies for all three simulations. Nevertheless, for all simulations the damage is still overpredicted and confined to a band in the center with cracks spreading out from it. There is little difference with regard to CPU time. While both simulations with reduced integration take just under 6 minutes, the one with full integration only takes approximately 20 seconds longer.
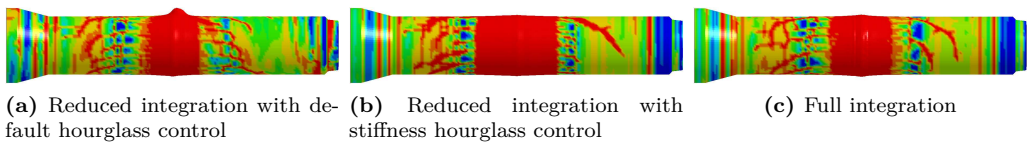


**(a)** Reduced integration with default hourglass control    **(b)** Reduced integration with stiffness hourglass control    **(c)** Full integration

**Figure 7.26:** Damage of pipe simulated in LS-DYNA with both full and reduced integration with various hourglass control.

### *Precision*

Lastly, single versus double precision is briefly inspected. In Figure 7.27 it can be observed that the damage of the two simulations is quite similar, although the crack pattern varies a little and the deformations in the pipe center are slightly larger when using single precision. Single precision was used for the reference model in an attempt to make the simulation computationally cheaper. Simulating with single precision takes just less than 6 minutes, while double precision takes approximately 2 minutes longer.
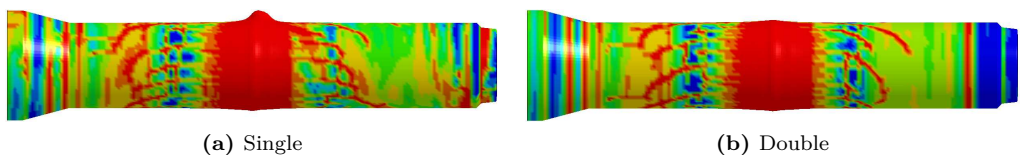


**(a)** Single      **(b)** Double

**Figure 7.27:** Damage of pipe simulated in LS-DYNA with both single and double precision.

## 7.1.3 Discussion

Lagrangian analyses of the pipes subjected to blast loads have been performed using the two finite element software ABAQUS and LS-DYNA, which both use different concrete material models. While the ABAQUS concrete model is more tedious to use as it requires scaling of its input parameters, the concrete model in LS-DYNA only requires the strength and is therefore straightforward to use. At first, it was examined in ABAQUS how to best apply the blast load. It was found that ConWep best rendered the locality of the problem, in addition to being easy to use. However, when using ConWep for both ABAQUS and LS-DYNA, the damage was overpredicted. Besides, in ABAQUS the damage did not

seem to stop evolving. In Figure 7.28 the damage of the reference models of ABAQUS and LS-DYNA are displayed for eased comparison of the two. While no deformations were observed for any of the ABAQUS simulations, there were deformations in the pipe center for most simulations in LS-DYNA.

Note that it was attempted to make the two reference models almost identical, but that single precision and a shorter simulation time was used for the LS-DYNA model since its computational cost was significantly larger. Despite these measures, the ABAQUS reference model is still slightly less costly than the one for LS-DYNA, but only by approximately 30 seconds.

By comparing the pressures that were applied to the pipe when using ConWep to the corresponding ones from the experimental testing, it was clear that ConWep greatly underestimated the pressures. This was to be expected since ConWep is not intended to be used for complex blast environments and does not take reflections into account. However, since the damage was overpredicted, despite the low pressures, this also suggests that it is the material models which possibly are not ideal when modeling blast load problems such as these.
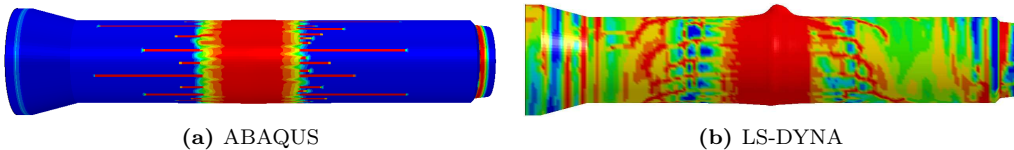


(a) ABAQUS  (b) LS-DYNA

**Figure 7.28:** Numerically simulated damage of reference models.

While the mesh distinctly restricted the cracking of the concrete in ABAQUS, the cracking appeared to be more realistic in LS-DYNA. The ABAQUS model showed a clear pathological mesh dependency, which was to be expected from the description of the material model. Refining the mesh of the LS-DYNA model seemed to cause more cracking and narrower cracks, in addition to cause more damage to the pipe ends. The reason for why the pipe ends become more damaged with a smaller mesh size is unknown.

Reinforcement was added for a concrete pipe in ABAQUS, but the simulated damage was little affected by this. Due to time limitations, reinforcement was not examined for the LS-DYNA model.

For both the ABAQUS and LS-DYNA models, the concrete behavior was attempted to be made more random to account for the statistical variation that is observed for experimental testing of concrete. The methods of modified random element strength and mesoscale modeling were therefore applied. For both methods in both software, the damage did in fact seem to become more localized. In LS-DYNA these methods also seemed to affect the crack pattern.

The placement of the charge was also varied for both ABAQUS and LS-DYNA and for both codes the damage was clearly affected by the charge placement.

The ABAQUS model seemed less affected than the LS-DYNA model by whether it was used full or reduced integration, default or stiffness hourglass control, single or double precision.

## 7.2 Eulerian Analyses of Blast

In Eulerian analyses, the mesh is fixed in space, not to the material, and instead the material flows through the mesh. The Eulerian elements may therefore not always be completely filled with material, or they may simultaneously be filled with several materials. Eulerian analyses in ABAQUS are based on the volume-of-fluid method where the Eulerian volume fraction (EVF) is computed for each increment [74]. The volume fraction of an element is 1 if the element is completely filled with material, and 0 if it is completely empty. If the volume fraction is less than 1, the remainder of the element is filled with void material which has neither mass nor strength.

Since the mesh is fixed, Eulerian analyses are effective when the deformations are large or for fluid flow. Eulerian analyses should therefore be well suited to simulate blast pressure.

Due to time limitations, the Eulerian analyses are only performed in ABAQUS and not LS-DYNA. When deciding on which software to use it is taken into account that the Eulerian analyses will form the basis of the coupled Eulerian-Lagrangian analyses that will be performed later. Although the concrete model in LS-DYNA is easier to use and seemed to best render the crack pattern in concrete, the LS-DYNA Lagrangian analyses also had longer CPU times. This, in addition to the fact that the user manual for ABAQUS is more detailed and that there generally is more literature available for ABAQUS, is why ABAQUS was the chosen software.

### 7.2.1 Reference Model

An Eulerian reference model is established in ABAQUS using explicit method. The reference model needs to be well-functioning and computationally relatively inexpensive as a parameter study is to be performed.

It is decided to explore the use of symmetry as the Eulerian analyses will form the basis for the computationally costly coupled Lagrangian-Eulerian analyses that will be performed in the subsequent section. The Eulerian domain is therefore modeled as a 0.4x04x2.9 m box. This geometry is chosen such that it can include one-eight of the pipe, but be slightly larger than the pipe in the ring direction and to include the location of sensors 1, 2, 4, and 5 in the longitudinal direction.

Another method of reducing the computational cost is to use a coarse mesh. A mesh of 20 mm is therefore chosen for the reference model. The elements are Eulerian brick with reduced integration and default hourglass control, i.e. EC3D8R.

The JWL equation of state is used to define how the shock wave propagates through the air. The method of JWL is described in further detail in Section 3.4.3 where also the properties for C4 are provided in Table 3.3. In ABAQUS, JWL needs to be defined as a material with a detonation point, which is then assigned to the Eulerian fluid part. However, the default material is then void, and it is necessary to specify where there is to be assigned non-void material. By using the density of C4 provided in Table 3.3, the radius of a spherical C4 charge of 14 g can be calculated and added as a part in the model. Since symmetry is used, only one eight of the spherical charge is modeled. The charge is only a reference geometry and it needs not be meshed or assigned a material.

For the charge geometry is only used to define which part of the Eulerian domain is to be assigned non-void material, which is done using the volume fraction tool and a predefined discrete field. The Eulerian part is assigned boundary conditions which allow the fluid to flow freely in and out of the domain.

By using the wave speed provided in Table 3.3 it is found that because the shock wave propagates so quickly, 0.02 ms is a sufficiently long simulation time for the shock front to reach the boundary of the Eulerian domain. For LS-DYNA it is recommended to use a time step scaling factor of 0.67 in order to reduce the stable time step when using high explosives which propagate quickly [80]. Since there is no such recommendation for ABAQUS, a time step scaling factor of 0.67 is used for the reference model.

Because the peak pressure is very sudden, one thousand field outputs, optionally the maximum number of increments, are requested. Four CPUs and double precision is used to run the simulation of the reference model, which then only takes 18 seconds.

Figure 7.29 displays a time series of how the pressure propagates for the Eulerian reference model. It should be noted that the model has been mirrored about two of its symmetry axes and that not the whole width of the model is shown. The figures to the left displays the pressure with no averaging and the figures to the right display the same pressures with maximum amount of averaging. Since the pressure looks more realistic when averaged, onwards a maximum amount of averaging will be used for the pressures. Despite the coarse mesh, it is observed that the pressure propagates in a quite spherical manner. Since the pressure varies considerably, a fixed pressure scale is not well suited and a scale for the pressure in Pascals is included for every image.
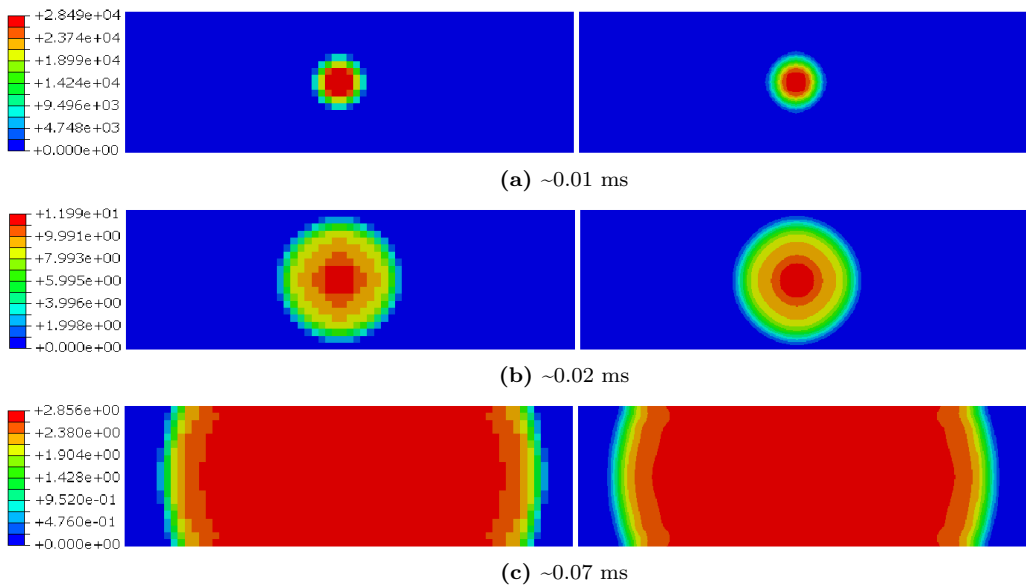


**(a)** ~0.01 ms



**(b)** ~0.02 ms



**(c)** ~0.07 ms

**Figure 7.29:** Time series of the pressure for the Eulerian reference model, including a scale for its magnitude with units in Pascals. No averaging has been used for the pressures to the left, while a maximum amount of averaging has been used for the pressures to the right.
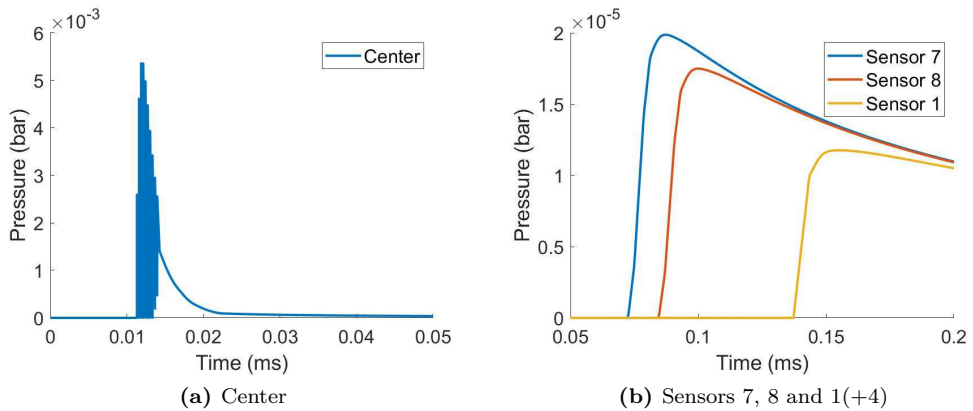
**(a)** Center



**(b)** Sensors 7, 8 and 1(+4)

**Figure 7.30:** Pressures simulated at various locations for the Eulerian reference model.

In Figure 7.30 the pressure-time curves have been plotted at locations corresponding to sensors 7, 8 and 1+4, as well as at the pipe wall in the center of the pipe. The pressure-time curves for the corresponding experimental test (small pipe XX) are available in Appendix A, but in Table 7.4 the peak pressures have been summarized, along with those for the 12 g charge. Recall that sensors 7 and 8 are located inside the pipe while all others are outside. It is clear that the pressures in Figure 7.30 are much all lower than the pressures from the experimental testing in Table 7.4. The reason for this is likely the lack of confinement and reflections in the numerical simulation, or it could possibly be due to JWL incorrectly representing the blast. Furthermore, it is observed that the pressure simulated at the center of the pipe fluctuates, but that it does not do so at the sensors. The reason for this is unknown.

**Table 7.4:** Peak pressures from experimental testing of concrete pipes subjected to blast loading due to centric charges of 12 and 14 g of C4.

| Sensor | Distance from charge (cm) | Peak pressure (bar) | |
|:---:|:---:|:---:|:---:|
| | | 12 g of C4 | 14 g of C4 |
| 7 | 59 | 155.99 | 400.53 |
| 8 | 69 | 169.53 | 214.26 |
| 1+4 | 100.5 | 8.03, 4.87 | 11.06, 8.43 |
| 2+5 | 140.5 | 1.47, 0.54 | 3.09, 1.50 |
| 3+6 | 220.5 | 0.40, 0.30 | 0.42, 2.92 |

## 7.2.2 Parametric Study

A study is conducted for some of the parameters in the Eulerian analyses of the blast. It is decided not to vary the parameters of the JWL equation of state since no experimental testing has been performed for only the blast, without a pipe, and therefore there is no experimental tests to calibrate these parameters for.

### Symmetry

Theoretically, it should make little or no difference if symmetry is made use of or not. Still, it is checked if this indeed is the case. From Figure 7.31, however, it is observed that the pressures are significantly higher when there is no symmetry. The reason for this is unknown, although the definition of boundary conditions could possibly have something to do with it. Nevertheless, the pressures are still low compared to the experimental testing. Additionally, by not exploiting the symmetry of the problem the simulation takes more than 15 times longer to run.



(a) Center   (b) Sensors 7, 8, and 1(+4)
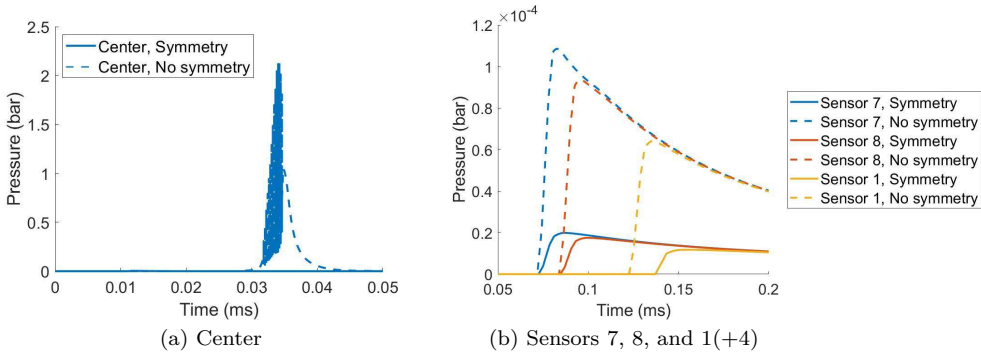
**Figure 7.31:** Pressures simulated at various locations for Eulerian analyses both with and without making use of symmetry.

### Mesh Size

The Eulerian mesh size is examined next in Figure 7.33. When later running coupled simulations, it is desirable to use an Eulerian mesh that is smaller than the Lagrangian mesh. Mesh sizes of 4, 6, and 8 mm are therefore assessed. When the analyses are run with the same time step scaling factor of 0.67 as the reference model, they all abort prematurely. After some trial and error, it is found that time step scaling factors of respectively 0.2, 0.3, and 0.4 allow the analyses to complete without any errors.



**Figure 7.32:** Computational time as a function of mesh size for Eulerian analyses.

From Figure 7.33 it is observed that the mesh size affects both the magnitude of the pressure and the amount of fluctuations. However, it is difficult to decide which mesh size is better as decreasing the mesh size seems to cause more fluctuations and lower pressures as the distance from the charge increases, while the opposite is observed when increasing the mesh size. An appropriate mesh size would therefore perhaps be smaller closer to the charge and increase with the distance from the charge. Furthermore, decreasing the mesh size, as well as the time step scaling factor, leads to an increase in computational time, which is clearly illustrated in Figure 7.32.
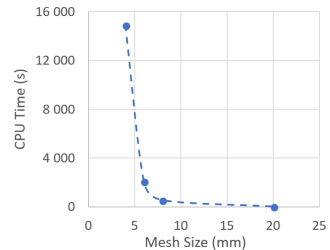
(a) Center



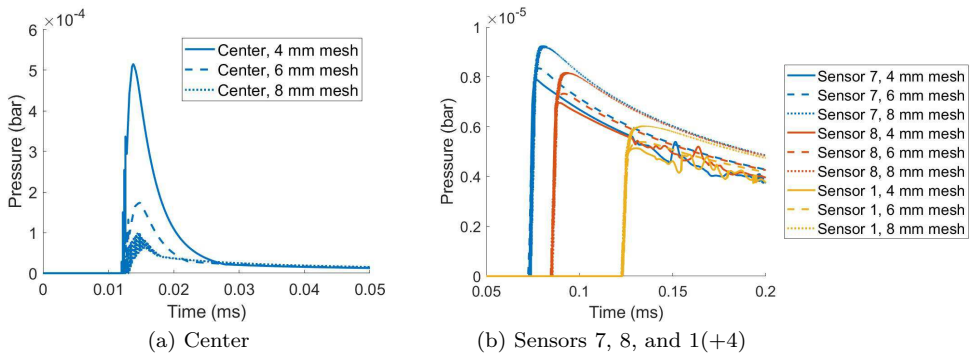(b) Sensors 7, 8, and 1(+4)

**Figure 7.33:** Pressures simulated at various locations for Eulerian analyses with various mesh sizes.

### Time Step Scaling Factor

When varying the mesh size, the time step scaling needed to be adjusted in order for the analyses to not abort. It is therefore examined whether adjusting the time step scaling factor could have affected the results. In Figure 7.34 the time step scaling factor of the reference model is varied. It is clear that the time step scaling factor does indeed affect the results. When decreasing the time step scaling factor the peak pressure is slightly increased at all three sensors, and at sensor 1+4 even the time of arrival is different. The reason for these differences is unknown.
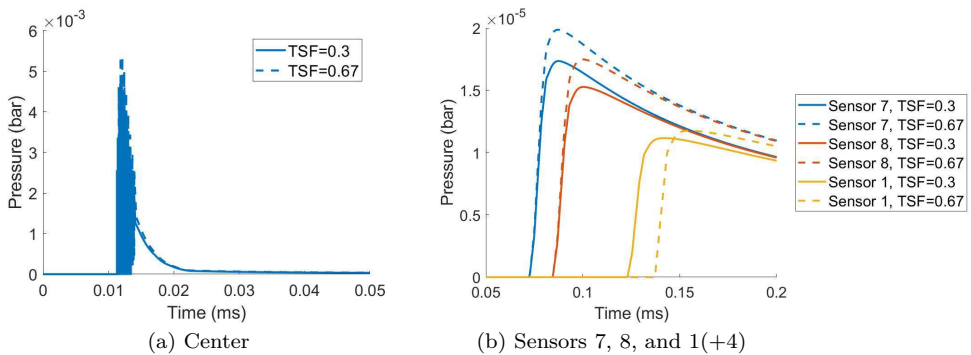


(a) Center



(b) Sensors 7, 8, and 1(+4)

**Figure 7.34:** Pressures simulated at various locations for Eulerian analyses with various time step scaling factor (TSF).

### Charge Size

From the experimental tests, it was found that a charge size of 14 g C4 caused the pipe to fracture, while a charge of 12 g did not. In Figure 7.35 these charge sizes are simulated using Eulerian analyses. It is observed that at the pipe wall in the center of the pipe and at the locations of sensors 7 and 8, there seems to be no difference in the pressures of the two charge sizes. At sensor 1+4, however, the pressure is larger for the smaller charge, as well as the time of arrival of the shock wave is shorter. The reason for these peculiar findings is unaccounted for.
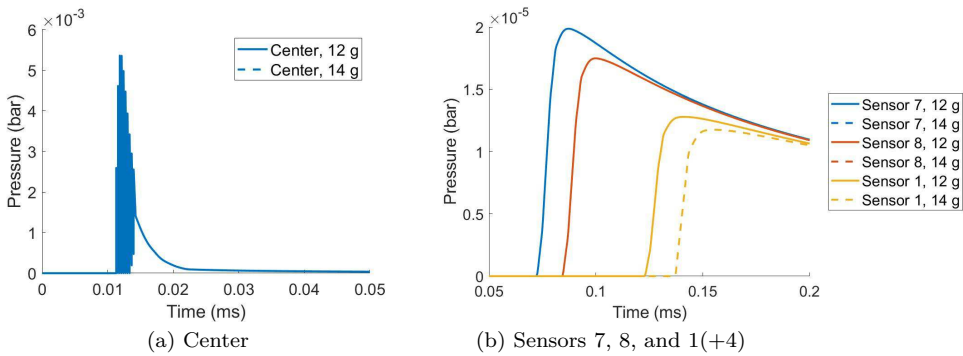
**Figure 7.35:** Pressures simulated at various locations for Eulerian analyses with various charge sizes.

### Charge Shape

For the experimental testing, all non-contact charges were spherical. For a plastic explosive such as C4, the charge could practically be almost any shape. In a potential terrorist attack, the most reasonable charge shape would perhaps be brick-like. Therefore a scenario with a cubic charge is also evaluated. From Figure 7.36 it is observed that the same explosive amount, only with a different shape of the charge, produces very similar pressures. At the location of sensor 1+4, however, the pressures deviate more, in addition to the time of arrival being slightly earlier for the cubic charge. The propagation of the pressure wave has also been examined, but as it looked very similar to the time series for the reference model (Figure 7.29) it has not been included.
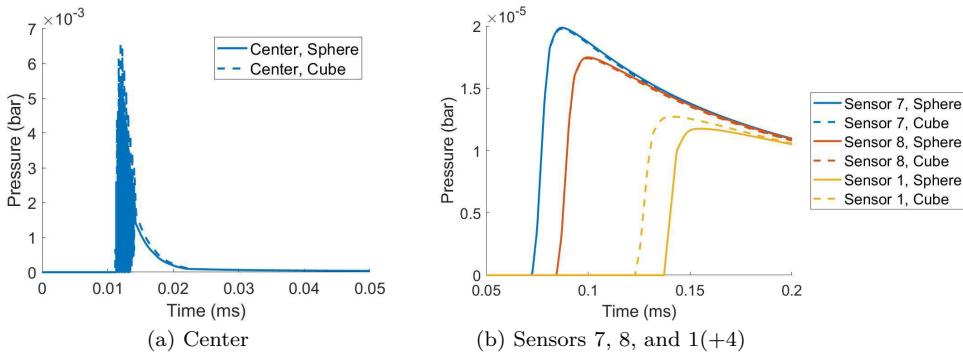


**Figure 7.36:** Pressures simulated at various locations for Eulerian analyses with various charge shapes.

### Flux Limit Ratio

The stable time increment is automatically calculated such that material does not flow across more than one element during a single increment. The flux limit ratio is a parameter that can be added to restrict material flow in an increment to only a fraction of an element [74]. Its default value is 1, but it may be decreased to as low as 0.1, which could be

necessary for e.g. blasts where the material velocity approaches the speed of sound.

The difference between the time step scaling factor and the flux limit ratio is investigated. For one simulation the time step scaling factor is set equal to 0.67 while the flux limit ratio is set equal to its default value of one. This simulation thereby corresponds to the reference model. For the second simulation, the two parameters are given the opposite values. However, the second simulation aborts after only three increments. It can therefore be concluded that even though time step scaling factors and flux limit ratios aim to reduce the stable time increment, their means of doing so are different and consequently also the result.

### *Bulk Viscosity*

For explicit analyses in ABAQUS, a small amount of numerical damping is by default added to damp out any high-frequency oscillations [74]. This is done in the form of bulk viscosity. There are two bulk viscosity parameters, one linear and one quadratic, whose default values are 0.6 and 1.2 respectively. In Figure 7.37 the damping is disabled by setting both bulk viscosity parameters to zero. The peak pressures are then observed to decrease, also at the center of the pipe although it is not clear from Figure 7.37a. Besides, the time of arrival at sensor 1+4 has decreased. Nevertheless, no oscillations are observed, except for at the center of the pipe.
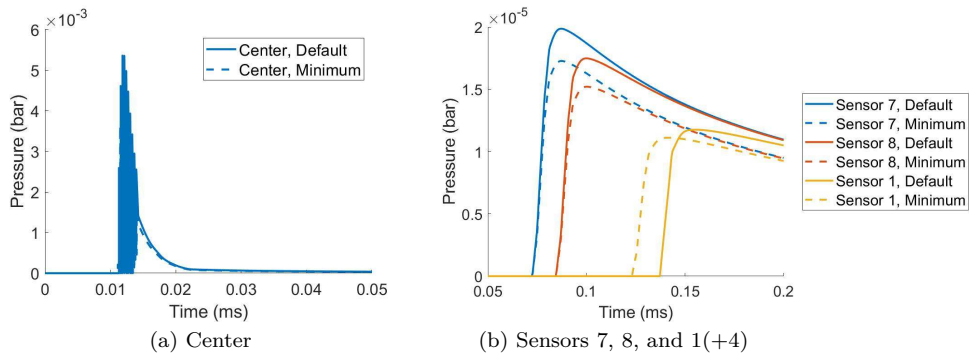


(a) Center  (b) Sensors 7, 8, and 1(+4)

**Figure 7.37:** Pressures simulated at various locations for Eulerian analyses with both default and minimum values for the bulk viscosity parameters.

### *Reflecting Boundary Conditions*

Lastly, it is attempted to simulate an explosion where the shock wave is reflected. For this to resemble the experiments with the pipes, the geometry of the fluid is changed to a cylinder. It was first attempted to exploit the symmetry of the problem and only model one-eighth of the cylinder, but this proved difficult when defining the boundary conditions. For in order to make the surface corresponding to the pipe reflecting, the velocities in the radial direction of the surface are fixed to zero. The geometry and boundary conditions of the model is illustrated in Figure 7.38. The mesh is naturally not exactly the same as for when the fluid was modeled as a cube, but the mesh size is still approximately 20 mm.
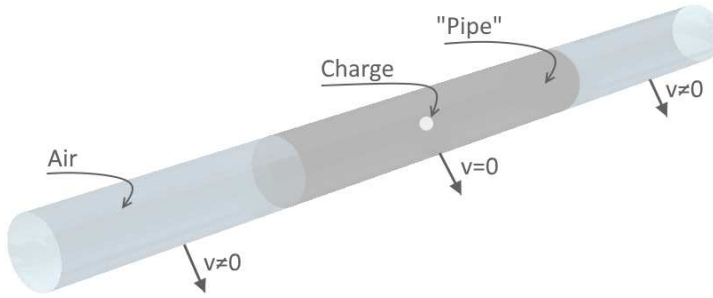
**Figure 7.38:** Model for Eulerian analysis of blast with reflecting boundary conditions at the location of the pipe.

In Figure 7.39 the pressures are plotted for the same locations as before (center and sensors 7, 8, and 1). It is seen that by making the boundaries reflecting, the pressures are greatly increased. The pressures with the non-reflecting boundaries are also included in Figure 7.39, but they are negligible in comparison to those with reflecting boundaries. The pressure-time curves for the model with the reflecting boundaries also much more resemble the characteristic blast wave. In addition, there are some fluctuations present, probably due to the reflections. Once the pressure is no longer confined by the reflecting boundaries, i.e. at sensor 1+4, it decreases significantly. The same observation was made for the experimental tests. However, even though the pipe fragmented for 14 g C4 in the experimental test, the pressures simulated with reflecting boundaries are still way too low in comparison. Nevertheless, the pressure simulated at the center of the pipe is approximately ten times higher than what was measured experimentally at sensors 7 and 8. In the numerical simulation, the pressure therefore decreases immensely from the center to the location of sensor 7. Since there is no experimental pressure data available from the center of the pipe, it is unknown if this was also the case for the experimental tests.
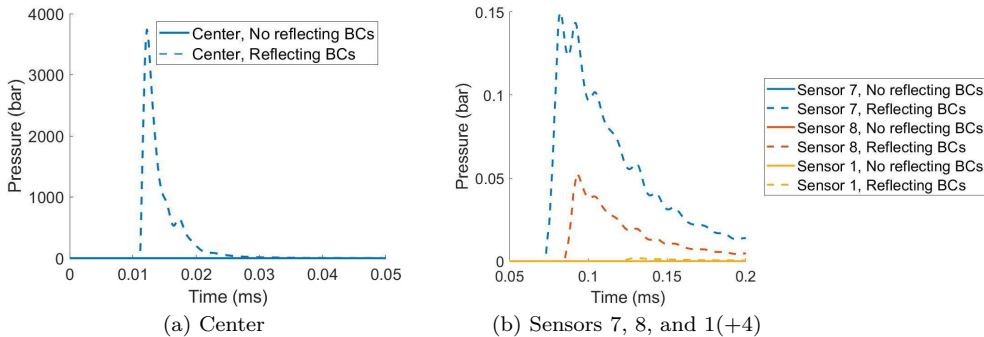


**Figure 7.39:** Pressures simulated at various locations for Eulerian analysis of blast with reflecting boundary conditions (BC) at the location of the pipe.

A time series displaying the pressure propagation is provided in Figure 7.40. The images show the pressures at a longitudinal partition in the center of the cylinder. Note that a maximum amount of averaging has been used when displaying the pressure. At the beginning (Figure 7.40a), the pressure propagates in the same spherical manner as was

observed in Figure 7.29. However, when reaching the boundary, the pressure is reflected, and the pressure state is immediately more complex. Therefore, many more images than previously are included in an attempt to better show how the blast pressure evolves. It should be noted that the time difference between the images is not constant since more images are required at the beginning when the shock wave first reaches the boundary. When first reaching the boundary the pressure is reflected and interacts with itself (Figure 7.40c). At this time the pressure is therefore at its highest and at the boundary. The pressure is then reflected and is highest in the center of the pipe when it once again interacts with itself (Figure 7.40e). Then the pressure starts propagating in the longitudinal direction. The pressure then propagates in a more spherical manner similar to when there was no reflection at the boundary. However, as the pressure propagates it also seems to almost pulsate, in the sense that the shock front alters between being convex and concave (Figure 7.40f-j). At the last increment at 0.2 ms (Figure 7.40k), it does not appear that the pressure has propagated outside the location of the pipe. Nevertheless, as is shown Figure 7.39, the pressure has in fact done so, only it is much smaller than at inside of the pipe and therefore it cannot be seen in Figure 7.40.

### 7.2.3 Discussion

Although the evolution of the pressure appears reasonable at first sight, both with and without reflecting boundaries at the location of the pipe, it is greatly underestimated. Nevertheless, reflecting boundaries provide much better results as the pressures are both increased, and better resemble the characteristic blast wave. A parametric study has been performed only for the model with the non-reflecting boundaries. It is found that unless a sufficiently low time step scaling factor is chosen, the analyses abort prematurely. The necessary size of the time step scaling factor varies when the different parameters are examined. For every simulation, some trial and error is therefore required to determine which time step scaling factor is just low enough. For it is not desirable that the time step scaling factor is unnecessarily low as this increases the computational cost. Even though some inexplicable differences were observed when varying the parameters, the magnitude of the differences was small with regard to pressure. The only parameters that proved to be of any obvious significance was the use of symmetry and reflecting boundaries. It would therefore be interesting to perform a second parametric study for the model with the reflecting boundaries, but due to time limitations, this is not done.
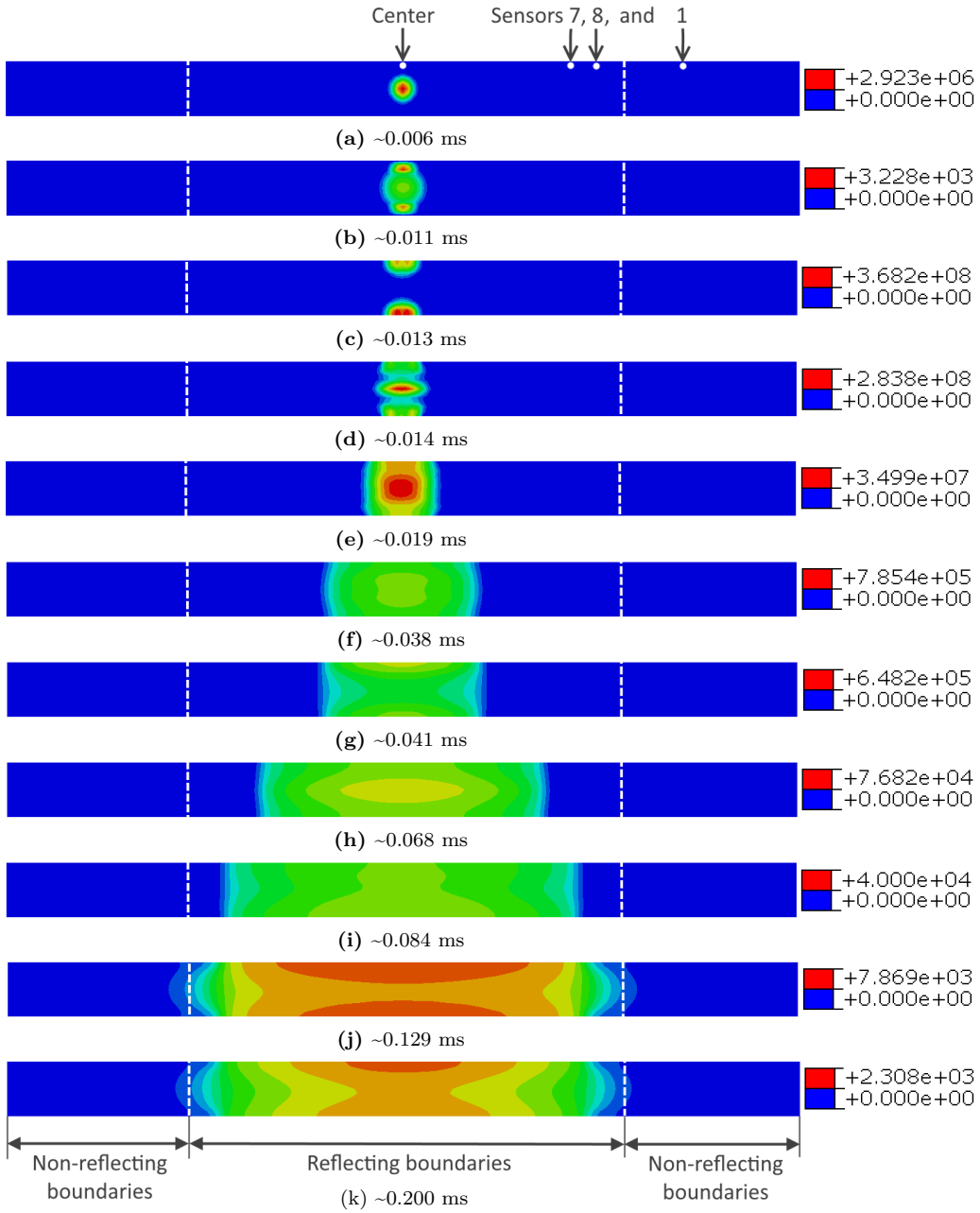
**Figure 7.40:** Time series of pressure in Eulerian analysis of blast with reflecting boundary conditions at the location of the pipe, including a scale for its magnitude with units in Pascals.

## 7.3 Coupled Eulerian-Lagrangian Analyses of Pipe and Blast

By introducing coupling, the Eulerian and Lagrangian parts can interact. Such analyses are therefore often referred to as coupled Eulerian-Lagrangian (CEL) analyses. CEL analyses are well suited to model e.g. fluid-structure interaction where there is strong interaction between the fluid (Eulerian mesh) and the structure (Lagrangian mesh). However, CEL analyses are computationally expensive.

The pipe will firstly be modeled as rigid for eased assessment of how the fluid behaves once a structure is added to the analysis. Theoretically, it should be similar to the pure Eulerian analysis with reflecting boundary conditions. A parametric study is then conducted for the rigid pipe in order to evaluate the importance of single parameters. At last, the pipe is made deformable with a concrete material.

### 7.3.1 Reference Model

A reference model is established in ABAQUS using an explicit method.

The fluid is modeled with an Eulerian domain precisely the same as for the Eulerian reference model in the previous section. Its geometry extends outside that of the pipe, allowing the pipe to move and deform when it later will be made non-rigid.

The pipe is modeled using Lagrangian elements. Since symmetry is used to reduce the computational cost, only one-eighth of the pipe is modeled and with a constant wall thickness, i.e. the end sections of the pipe are simplified to have the same cross-section as the rest of the pipe. At the pipe's symmetry planes boundary conditions are applied, fixing the appropriate translational and rotational degrees of freedom.

Solid brick elements of type C3D8R with reduced integration and default hourglass control are used for the pipe, just as in Section 7.1. Since it, for now, is desirable for the pipe to be rigid, it is assigned a basic steel material with the same properties as the reinforcement steel in Section 7.1. In addition, all pipe nodes are fixed against all displacements and rotations. It is decided to do it this way such that the pipe can later easily be made deformable by altering its material and removing the boundary conditions.

To ensure adequate contact between the fluid and the structure, without gaps or overlaps, the Eulerian fluid mesh should not be larger than the Lagrangian structural mesh. For the reference model, a coarse 20 mm mesh is therefore used for both the Eulerian and Lagrangian domain.

In ABAQUS it is not possible to choose which coupling method to use between the Eulerian and Lagrangian mesh. However, the interaction between the fluid and the structure needs to be defined. This is done using general contact with a penalty formulation. For the reference model, it is used rough friction formulation for the tangential contact behavior, and linear normal contact behavior with a contact stiffness that is ten times higher than Young's modulus of the pipe's material.

Just as for the Eulerian reference model, the 14 g charge of C4 is modeled using JWL. The simulation time is also equal to that of the Eulerian analyses, namely 0.2 ms. A

time step scaling factor of 0.67 is chosen since it proved to be adequately small for the corresponding Eulerian analysis with no pipe. To best possible render the sudden peak pressure, one thousand field outputs are requested for the analyses which are all run using four CPUs and double precision.

Although the simulation starts smoothly and works its way through the first increments efficiently, trouble soon arises. Figure 7.42 displays a time series of how the blast pressure evolves in the CEL analysis of the reference model. Note that a maximum amount of averaging has been used for the pressure and that the time difference between the images is non-constant. Also note that since only one-eighth of the problem was modeled, the results have been mirrored for better visualization. Figure 7.42 therefore displays the pressures at the center of the pipe in the longitudinal direction and the grey horizontal lines are the pipe walls.

Symmetry is probably also the cause of the first problem that is observed, namely the somewhat peculiar shapes of some of the blast pressures in Figure 7.42. Nevertheless, before reaching the pipe wall, the pressure still propagates in a, to some extent, spherical manner (Figure 7.42a). When reaching the pipe wall, the pressure is reflected and is therefore higher near the pipe wall (Figure 7.42e). The reflected pressure propagates towards the center of the pipe where it once again interacts with itself (Figure 7.42f). The pressure then starts propagating inside the pipe in its longitudinal direction (7.42g-h).

When the simulation reaches approximately 0.017 ms (Figure 7.42g), a second issue reveals itself. The pressure no longer seems to be confined by the pipe and therefore leaks outside the pipe. There are two possible explanations for this. Firstly, the pressure leakage could be due to fracture in the pipe. The pipe is therefore more closely inspected from other angles, and its stresses are examined, but nothing is found that indicates that the pipe is breached. The second possible explanation is thus more likely, namely that there is a problem with the contact definition in the model. The contact definition is therefore one of the parameters that will be investigated in the parametric study. Nevertheless, after a while (Figure 7.42m) the pressure leakage seems to stop spreading and gradually once again seems more and more confined by the pipe, although not quite (Figure 7.42p).
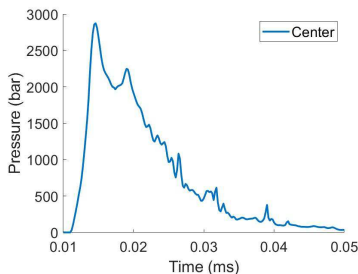


**Figure 7.41:** Pressures simulated at the center of pipe for reference model for CEL analysis.

The last image of the time series in Figure 7.42 is also the last output from the analysis. For even though the analysis was efficient to begin with, it soon became very slow. After a while, the stable time increment of the analysis became so small (of order $10^{-17}$ s) that the analysis stagnated and it was determined to terminate it manually. It took a little more than 1 hour and 45 minutes to complete the first 26.3 % of the analysis.

Because the analysis was aborted prematurely, the blast pressure never reached the location of any of the sensors. In Figure 7.41 the pressure is therefore only plotted at the pipe wall in the center of the pipe. It is observed that the peak pressure is higher (of approximate magnitude ten) than what was measured at the sensors inside the pipe for the experimental testing. The pressure-time curve resembles the characteristic blast wave, and some fluctuations are present, most likely due to the reflections.
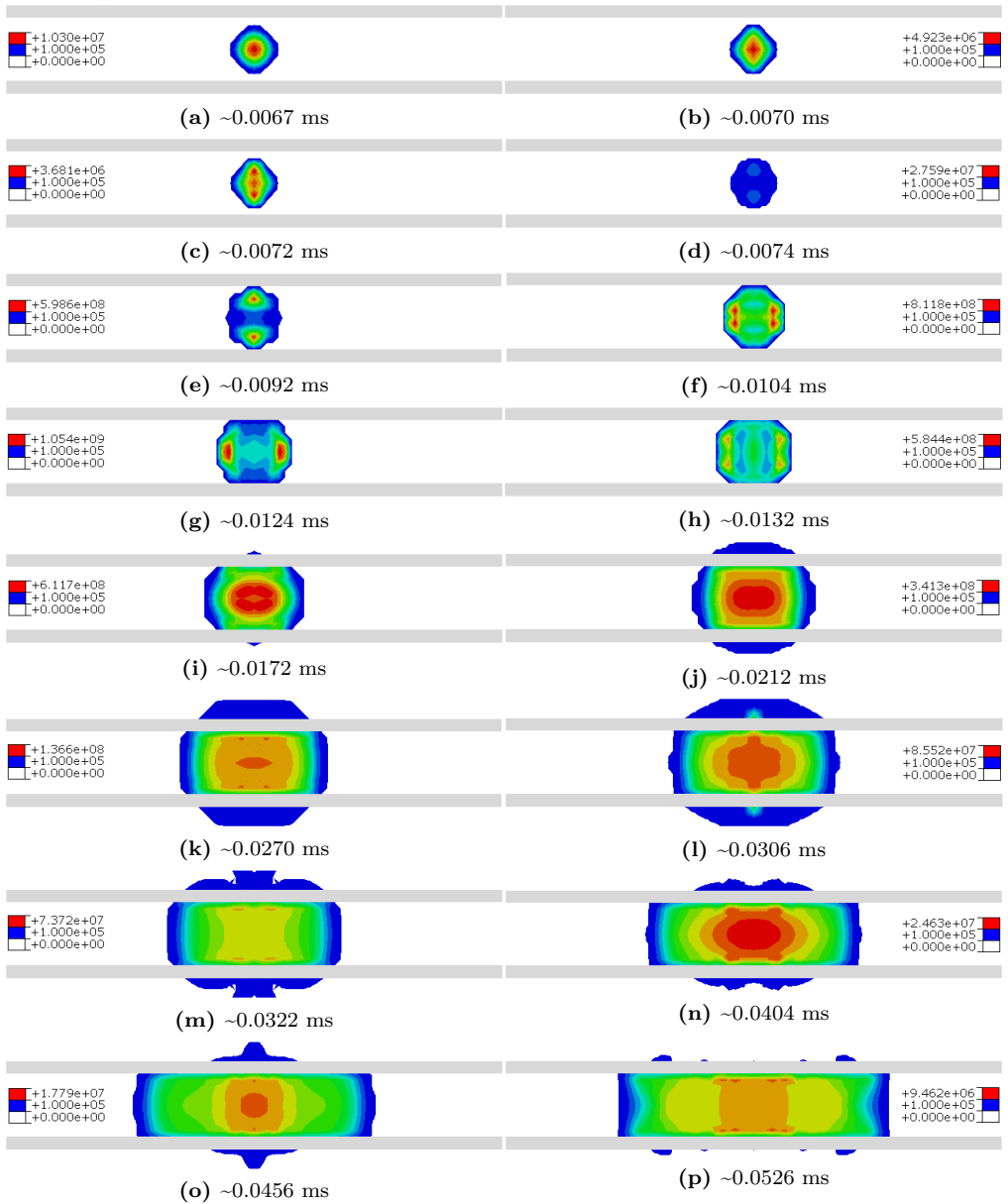
**Figure 7.42:** Time series of pressure in CEL analysis of blast with rigid pipe, including a scale for its magnitude with units in Pascals.

## 7.3.2   Parametric Study

Although the pressure curve at the center of the pipe for the reference model could appear to be reasonable, a parametric study is performed in an attempt to find a solution to the mentioned problems.

### *Contact*

Since the contact definition was suggested a possible reason for the pressure leakage, it is the first parameter to be examined. The normal behavior is attempted made hard instead of linear, but the analysis aborts after completing only 7.4 % with an error message that says that the ratio of deformation speed to wave speed exceeds 1. This may indicate that a lower time step scaling factor is required and a new simulation is therefore run with a time step scaling factor of 0.3. However, also this analysis aborts with the same error, but this time after completing 15.9 %. By lowering the time step scaling factor even further the analysis would probably be able to run longer, but no further attempt of this is made. The tangential behavior is altered from rough to frictionless, but also this analysis stagnates, and it is therefore decided to terminate it after it has completed 37.3 %.
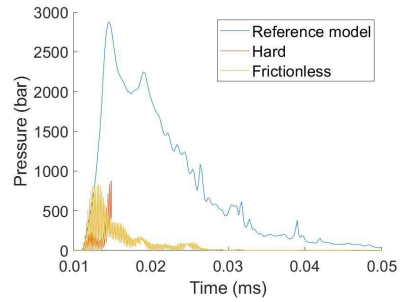


**Figure 7.43:** Pressures simulated at the center of pipe for CEL analysis of blast with various contact definitions.

The pressure-time curves obtained with different contact behaviors are provided in Figure 7.43. For the hard normal contact definition, it is the pressure with the time step scaling factor of 0.67 that is plotted. The reason for this is that it is desirable to only alter one parameter at a time in order to obtain a better basis for comparison. It is observed that the pressure obtained with the reference model is significantly higher than the other two, although it is unknown if the model with the hard normal contact perhaps would have continued to increase had it not aborted. Since it is only the pressure of the reference model that is higher than the experimental pressure measured at the sensors for the 14 g charge, the reference model shows the most potential. Besides, the pressure for the reference model fluctuates remarkably less.

### *Charge Size*

Another parameter that is evaluated is the charge size, i.e. the amount of explosive. A charge of 12 g C4 is considered, but also this analysis stagnates and is therefore terminated after completing 27.2 %. The blast pressure propagation behaves similarly to that of the reference model in Figure 7.42. Although the pressure at the pipe center is of the same magnitude as for the reference model with 14 g of C4, for 12 g of C4 it fluctuates a lot (see Figure 7.44). Why the pressure-time curve fluctuates so much more for the smaller of the two charges, is unknown.
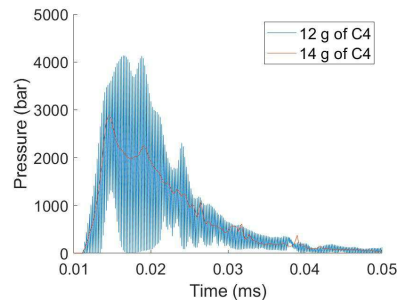


**Figure 7.44:** Pressures simulated at the center of pipe for CEL analysis with various charge sizes.

### *Mesh Size*

For the reference model, both the Eulerian and Lagrangian parts had 20 mm meshes. For better contact, the Eulerian mesh size should presumably be smaller than that of the Lagrangian mesh. In Figure 7.45 different scenarios are explored where the fluid mesh is smaller than, equal to, or greater than, the structural mesh. All analyses stagnate after a while, and they are therefore manually terminated. Note that a time step scaling factor of 0.4 was required for the analyses with 8 mm fluid mesh to not abort.
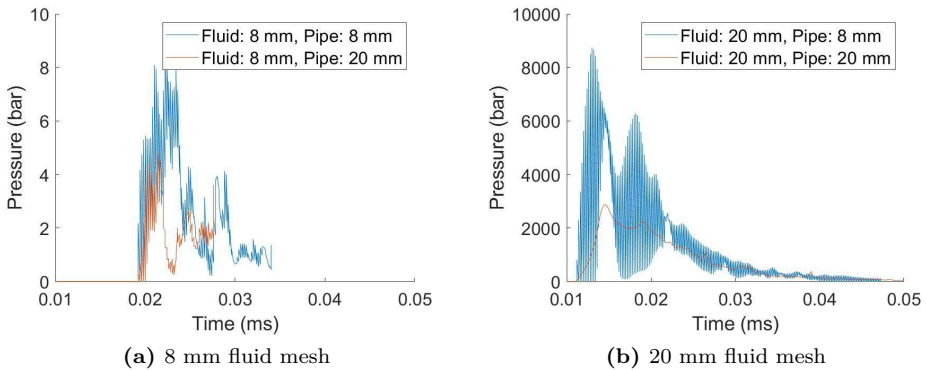


**(a)** 8 mm fluid mesh  **(b)** 20 mm fluid mesh

**Figure 7.45:** Pressures simulated at the center of pipe for CEL analysis with various mesh sizes.

The first observation that is made from Figure 7.45, is that all pressure curves oscillate considerably more than the reference model. The second observation that is made, is that the pressure decreases a lot when the mesh is refined. In fact, for the 8 mm Eulerian mesh, the pressure simulated in the center of the pipe is lower than what was measured at the sensors inside the pipe for the experimental test. Furthermore, refining the mesh of only the fluid, and not the pipe, does not appear to solve to solve the pressure leakage problem.

### *Time Step Scaling Factor*

A time step scaling factor of 0.67 was chosen for the reference model based on recommendations for blast loads in LS-DYNA [80]. Yet, for some simulations, the analyses abort with an error message saying that the ratio of deformation speed to wave speed exceeds 1. Recall that this happened for e.g. the hard contact definition and for the 8 mm fluid mesh. By lowering the time step scaling factor, it was then found that the analyses were able to proceed further.



**Figure 7.46:** Pressures simulated at the center of pipe for CEL analysis with various time step scaling factors (TSF).

In Figure 7.46, the effect of altering only the time step scaling factor is therefore examined. This is done by running the reference model with a much lower time step scaling factor of 0.3. The analysis
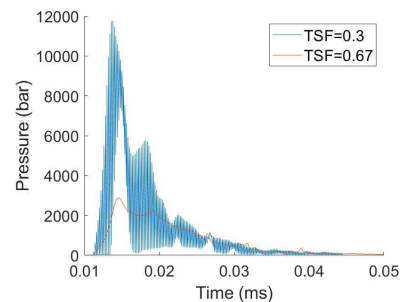
stagnates and is therefore terminated after completing 22.2 %. It is observed substantial oscillations for the pressure-time curve with the 0.3 time step scaling factor. The cause of the significantly increased amount of fluctuations that occur when decreasing the time step scaling factor is unidentified.

### Symmetry

For the reference model, the symmetry of the problem was exploited in an attempt to decrease the computational cost. It was also suspected that this was the cause of the at times peculiar looking shape of the blast pressure. For the sake of comparison also the full problem is modeled. The analysis was aborted after a little less than 32 hours when the computer it was run on crashed. It had then completed 42.1 %. A second attempt was made of running the analysis. After running for 97.5 hours and completing 80.8 %, the analysis aborted with the same error message as before. No attempt was made of re-running the analysis with a smaller time step scaling factor due to the excessive CPU time.
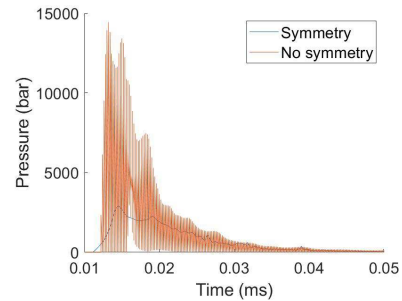


**Figure 7.47:** Pressures simulated at the center of pipe for CEL analysis with and without making use of the problem's symmetry.

In Figure 7.47 the simulated pressure at the pipe wall in the center of the pipe, is compared for the reference model which uses symmetry and the model which does not. Like for many of the other parameters that were checked, the pressure for the whole problem, i.e. no symmetry, fluctuates greatly. In addition, the pressure is higher when the full problem is simulated. Modeling the whole problem does neither solve the issue with pressure leakage. The suspicion that it was the symmetry which caused the odd-looking blast pressure is proved correct. Since the analysis of the full model was able to complete more before aborting, the shock front reaches the location of sensors 7, 8, and 1+4 where peak pressures of 25.7, 117.5, and 21.8 bar are registered. Recall that sensors 7 and 8 are located in the pipe wall, with sensor 7 closest to the charge, while sensor 1+4 is located at the outside of the pipe. It is therefore illogical that the simulated pressure is so much larger at sensor 8 than at sensor 7, and that the pressures at sensors 7 and 1+4 are almost the same. Additionally, the simulated pressure-time curves at the sensors are completely off and difficult to make sense of, and thus they have not been included.

### Deformable Pipe

Lastly, the pipe is made deformable by changing the material of the pipe in the reference model to concrete and removing the boundary conditions which fixed all the degrees of freedom for all the pipe nodes. The concrete material is identical to that of the Lagrangian reference model. Also, this analysis stagnates and is therefore manually terminated after completing 27.3 %.
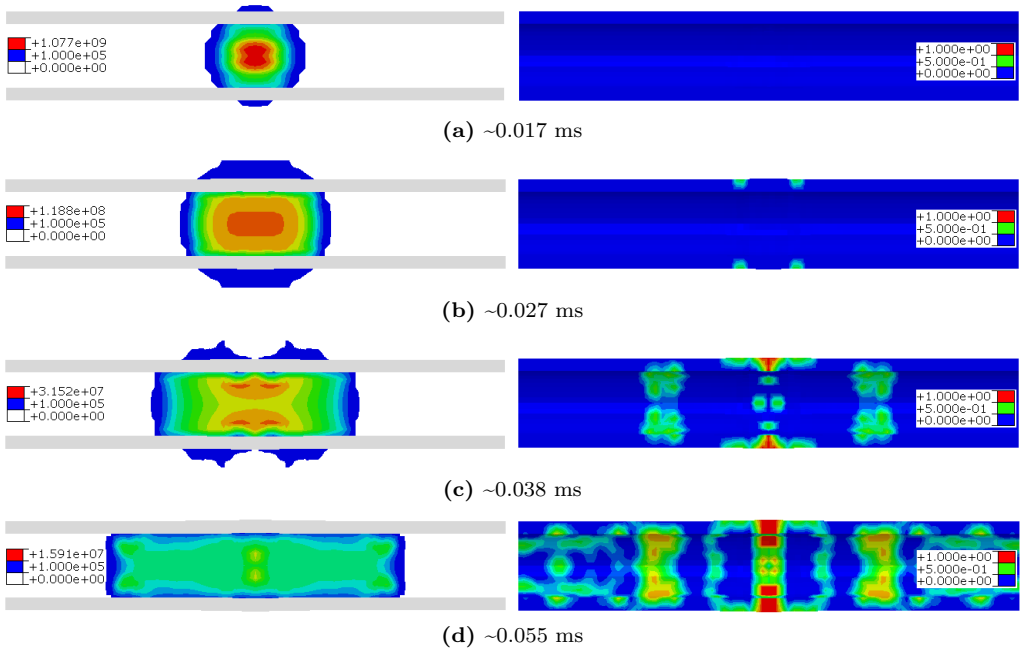
**(a)** ~0.017 ms



**(b)** ~0.027 ms



**(c)** ~0.038 ms



**(d)** ~0.055 ms

**Figure 7.48:** *Left:* Time series of the pressure for blast from the CEL analysis of a deformable pipe, including a scale for its magnitude with units in Pascals. *Right:* Tensile damage of the inside of the pipe from the same analysis, including a scale for the damage.

To the left in Figure 7.48 the pressures are displayed for the blast at various times of the CEL analysis with the deformable pipe. Just as for the reference model with the rigid pipe, the pressure leaks out of the pipe. However, since the pipe is no longer rigid, the leakage could be due to damage of the pipe. Therefore, to the right in Figure 7.48 the tensile damage of the pipe is displayed for the same time steps. However, there seems to be no correlation between the pressure leakage and the pipe damage. The pressure leaks when the pipe is intact (Figure 7.48a) and does not when the pipe is breached (Figure 7.48d). The tensile damage of the outside of the pipe is displayed in Figure 7.49. It is observed that this damage is larger than on the inside of the pipe, which is reasonable since an internal blast load would cause scabbing on the outside of the pipe. The compressive damage has also been inspected, but since it was smaller than the tensile damage it has not been included.
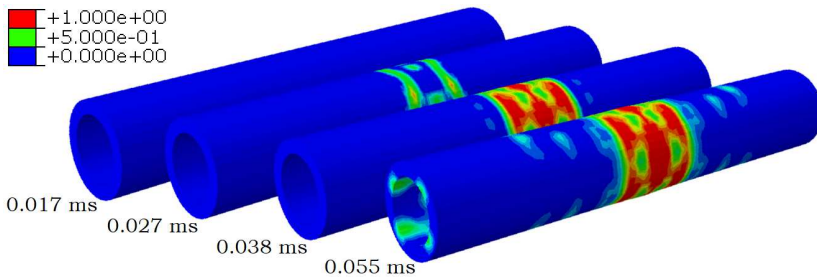


**Figure 7.49:** Tensile damage of the outside of the deformable pipe from the CEL analysis, including a scale for the damage.

Just as for the other parameters that have been in-spected, the pressure from the simulation of the de-formable concrete pipe is compared to that of the ref-erence model which had a rigid pipe (see Figure 7.50). Also just as for the other parameters that have been in-spected, the pressure for the deformable pipe oscillates significantly. In addition, the peak pressure for the de-formable pipe is larger than that of the rigid pipe, even though the deformable pipe is more damaged. The rea-son for this is unknown.



**Figure 7.50:** Pressures simu-lated at the center of pipe for CEL analysis with both a rigid and a deformable pipe.

An analysis with a deformable concrete pipe and a 12 g charge is also run. This is done in order to check whether the CEL analysis is able to predict that this pipe was not breached. However, the simulation revealed that also this pipe would be severely damaged. The pressure-time curve for the 12 g charge was very similar to that for the 14 g charge in Figure 7.50, but the peak pressure was approximately 1000 bar lower.

### 7.3.3    Discussion

The CEL analyses performed in ABAQUS for pipes subjected to internal blast loading, have not provided the results which were hoped for. There are four main problems with the analyses.

The first problem with the CEL analyses is the choice of an appropriate time step scaling factor. It has been found that a time step scaling factor is essential for the analyses to run without aborting with the same error message saying that the speed of deformation is higher than the wave speed. However, it is also not desirable to use a lower time step scaling factor than necessary as the time step scaling factor increases the computational cost of the analysis. Besides, it has been showed that the time step scaling factor affects the solution. Deciding on a time step scaling factor is therefore challenging.

The second problem with the CEL analyses is that the simulations eventually become very slow and stagnate as the step sizes become minuscule. If the analyses did not stagnate, they aborted due to an insufficiently low time step scaling factor. The analysis that was able to complete the most before aborting was the one where the full problem was modeled, i.e. without exploiting the symmetry of the problem.

A third problem is that pressure seems to leak outside the pipe. Different definitions of the boundary between the fluid and the structure have been investigated, but with no luck. The ratio of mesh sizes for the Eulerian and Lagrangian part have also been explored, but also this without luck. However, it was found that refining the Eulerian mesh seemed to cause the peak pressure to decrease remarkably. It is possible that a different coupling between the Eulerian and Lagrangian parts could resolve the problem with pressure leakage, but In ABAQUS it is not possible to choose the coupling mechanism.

The fourth main problem is that for most of the CEL analyses, the pressure-time curves oscillate a lot. In fact, it is only the reference model which does not cause excessive oscillations. Some fluctuations are to be expected due to e.g. reflections, but perhaps not to this extent.
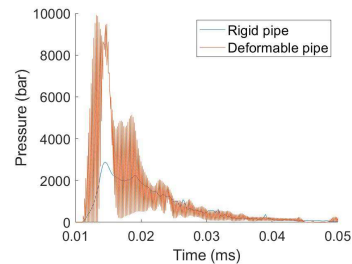
## 7.4 Discussion

In conjunction with the experimental testing of concrete pipes subjected to blast loading, numerical simulations have been performed. Three different types of analyses have been evaluated, namely Lagrangian analyses of the pipe, Eulerian analyses of the blast, and coupled Eulerian-Lagrangian analyses of both the pipe and blast.

It was found that due to its simplicity and ability to predict the locality of a blast load, ConWep was the most promising way of applying the blast load for the Lagrangian analyses. Nevertheless, ConWep is not intended for complex blast environments and does not account for reflections. Therefore, the blast pressure was underestimated, yet the damage of the concrete pipe was overestimated. This observation was made for both the analyses conducted in ABAQUS and LS-DYNA, and may indicate that neither the CDP or K&C concrete models are suitable for simulations involving blast loads. Although overpredicting the damage, the LS-DYNA simulations with the K&C concrete model provided cracking that appeared more realistic than in ABAQUS. In addition, the damage in ABAQUS did not seem to stop evolving. However, for this problem, LS-DYNA was considerably more expensive with regard to CPU time, and this was the main reason for using ABAQUS in the following Eulerian and CEL analyses.

For the Eulerian analyses of the blast using the JWL equation of state, it was found that deciding on an appropriate time step scaling factor can be challenging. If the time step scaling factor was too high, the analysis aborted as the deformation speed was higher than the wave speed. Some trial and error was therefore necessary in order to get a working model. Once an applicable time step scaling factor had been obtained and the analyses were run, it was found that the pressures were greatly underestimated compared to the experimental results. Reflecting boundaries at the location of the pipe were essential to obtain a blast pressure that resembles the characteristic one. Even though the pressures were also considerably increased when using reflecting boundaries, they were still too low compared with the experimental results.

As there were challenges with both the Lagrangian and Eulerian analyses, it was not unexpected that there would be trouble with the coupled Eulerian-Lagrangian analyses. The problems with the underpredicted loads and choice of time step scaling factor from the Eulerian analyses, and the problem with the overpredicted damage from the Lagrangian analyses, could also be observed for the CEL analyses. However, other problems were presumably more prominent. These problems included unaccounted for oscillations, pressure leakage, and that the analyses became extremely slow and stagnated. Yet, it was found that the full problem should be modeled without exploiting symmetry as this perhaps seemed to solve the issue with the analyses stagnating.

By coupling the Eulerian and Lagrangian analyses, the computational cost increased immensely. For example, while the Lagrangian (ABAQUS) and Eulerian reference models only took 6.5 minutes and 18 seconds to complete, respectively, the coupled analysis of the reference model took 1 hour and 45 minutes to complete only the first 26.3 %.
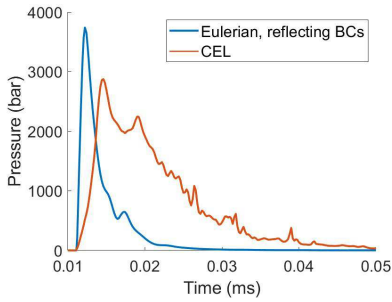
**Figure 7.51:** Pressures simulated at the center of pipe for CEL analysis with rigid pipe and Eulerian analysis with reflecting boundaries.

The Eulerian reference model produced a peak pressure of only 0.005 bar at the center of the pipe. By adding the reflecting boundary conditions at the location of the pipe, the same value increased tremendously to 3741 bar. The corresponding values for the Lagrangian and CEL reference models were 55 and 2875 bar respectively. Since the Eulerian analysis with the reflecting boundaries and the CEL analysis with the rigid pipe, should theoretically produce similar results, they are compared in Figure 7.51. It is observable that they do indeed produce pressures of the same magnitude, but that the peak pressure is lower for the CEL analysis although the impulse is larger. At sensor 7, the Eulerian analysis with the reflecting boundaries simulated a peak pressure of 0.15 bar. The CEL analysis which did not make use of symmetry was the only one of the CEL analyses where the blast pressure reached sensor 7 and this it did with a peak pressure of 25.7 bar. Compared to the corresponding experimental test which measured 400.5 bar, this is therefore too low, despite the high pressures simulated at the pipe center.

# Chapter 8

# Concluding Remarks

There is little use in trying to numerically simulate complex problems such as submerged floating tunnels (SFT) subjected to blast loads, without being certain that the material model behaves as expected. Experimental concrete compression tests have therefore been performed in order to validate the compressive behavior, which is perhaps the single most important property of concrete, of numerical concrete models. Once this was done, one could move on to the more complicated problem of concrete pipes subjected to blast loading. Experimental testing was performed with the purpose of assessing the behavior of tubular concrete structures subjected to blast loading, and to form a basis of comparison for numerical modeling.

For the concrete compression tests, the engineering stress-strain curves obtained using the displacement directly logged from the test rig, seemingly provided too high strains. The reason for this was most likely rig stiffness as the forces were large and the displacements small. Despite an extensive amount of cracking in the concrete, the digital image correlation (DIC) analyses, on the other hand, provided reasonable results. For one of the cubes, the DIC analysis was even able to render the whole post-peak, strain-softening behavior. Given that an appropriate mesh size and multiscaling are used, DIC shows promising potential for tests like these.

The concrete compression tests can be rather difficult to simulate numerically as they are highly dependant on material models with many parameters. Thus, knowing what each parameter controls and the effect of altering it, can be challenging. Nevertheless, after some trial and error, both the concrete damaged plasticity (CDP) model in ABAQUS and the Karagozian & Case (K&C) model in LS-DYNA provided promising results. The CDP model needs extensive experimental testing to determine all its parameters, but an alternative approach which proved efficient, is to scale the parameters which have been obtained in previous research. The K&C model, on the other hand, is much easier to use as the only necessary input is the concrete's compressive strength. However, it was found that an unnaturally low friction coefficient was needed in LS-DYNA in order to obtain reasonable results. Additionally, the LS-DYNA model displayed nonphysical post-peak behavior due to complete damage of the concrete. While the CDP model showed a clear pathological mesh dependency, but little sensitivity to the amount of time scaling, the opposite was observed for the K&C model.

From the experimental testing of the concrete pipes, it was found that the charge placement greatly affects both the failure mode and the minimum charge size required to damage the pipe severely. In most cases, the Kingery-Bulmash equations were found to be non-conservative. The amplification of the blast due to confinement was evident as the internal contact charge caused much more damage than an equivalent external contact charge. The effect of stand-off distance was also clear as the internal contact charge caused more damage than the equivalent internal centrically placed charge. In a potential SFT, however, it will be difficult to affect the stand-off distance since it at most will be equal to the internal diameter of the SFT. Nevertheless, from the experimental tests, it was also found that increasing the wall thickness and adding reinforcement steel, both appear to be effective measures for design with regard to blasts. These measures are also very applicable for an SFT which would anyhow require reinforcement.

Simulating the pipes subjected to blast loads proved to be challenging. For both ABAQUS and LS-DYNA, the Lagrangian analyses overpredicted the damage, despite ConWep underestimating the blast pressure. This indicates that it might be the concrete models which quantitatively do not perform well for blast loads. Other concrete models may therefore need to be considered.

Eulerian analyses were also performed in ABAQUS using John-Wilkins-Lee (JWL) equation of state to model the detonation of C4 in air. However, these analyses underestimated the blast pressure as well. Adding reflecting boundaries at the location of the pipe, significantly improved the results. The pressure-time curve then resembled that of a characteristic blast and the peak pressure was much higher, though still way too low compared to the experimental test results.

The blast experiments were also simulated in ABAQUS using coupled Eulerian-Lagrangian (CEL) analyses. However, there were several problems with these analyses. The CEL analyses eventually stagnated completely, there were high pressures outside the intact pipe due to leakage, and the pressure-time curves fluctuated significantly. It was unsuccessfully attempted to solve these issues as their causes, or cause, are unknown. One possible explanation could be how the Lagrangian and Eulerian meshes are coupled, but since there is no way of determining this coupling in ABAQUS, it is difficult to know if this is the reason. The simulated damage of the pipe was still overpredicted for the charge that did not cause any visible damage in the experimental tests. Only one of the CEL analyses was able to run long enough for the blast to reach the location corresponding to the sensors, namely the one which did not exploit the problem's symmetry. For this simulation, the peak pressure was very high at the center of the pipe, but still the blast pressure at the sensors was too low.

For both the Eulerian and CEL analyses it was a challenge deciding on a proper time step scaling factor as the result, CPU time, and the analysis' ability to complete, was affected by it.

The work of Hillestad and Pettersen [48] with incorporating the statistical variation of concrete, has been further investigated. Their methods of random element strength and mesoscale modeling have been investigated, modified, and expanded for the use in ABAQUS and for the pipes. Including these methods for the modeling of the compression tests, showed that they did in fact provide variation in the results. For the Lagrangian analyses of the pipes, the methods provided some decrease in the damage, but the effect was greater in LS-DYNA.

Thus, in conclusion, the main findings of this thesis are:

- DIC shows promising potential for application for concrete compression tests.

- Both concrete models, CDP for ABAQUS and K&C for LS-DYNA, provide adequate results when modeling the concrete compression tests. CDP displays pathological mesh dependency and is slightly more tedious as it requires scaling. K&C is very simple to use as it only requires the compressive strength, but an unnaturally low friction coefficient is needed and it does not render the concrete's residual strength.

- Experimental tests of concrete pipes subjected to blast loads verify that confining a blast and decreasing its stand-off distance, greatly increases the blast pressure. The tests also show that increasing the wall thickness and adding reinforcement steel are both highly effective design measures with regard to blast loads.

- Lagrangian analyses, both in ABAQUS and LS-DYNA, of the concrete pipes subjected to blast loading, showed that the damage was overestimated even when the blast pressure was very low, suggesting that quantitatively neither of the concrete models are suitable for blast loads.

- The methods of modified random element strength and mesoscale modeling decrease the amount of damage in the Lagrangian analyses of the pipes.

- The blast pressure generated using Eulerian analyses in ABAQUS, only resembles the characteristic blast if the there are reflecting boundaries present.

- It is difficult to get a working ABAQUS CEL model of the concrete pipes subjected to internal blast loads, and there are several unresolved problems including pressure leakage, pressure fluctuations, and stagnation of the analyses. In addition, the damage is overpredicted.

- The performed Lagrangian, Eulerian, and CEL analyses of the pipe and the blast, all underestimate the peak blast pressure.

- For Eulerian and CEL analyses it is essential to choose an appropriate time step scaling factor, a task which can prove challenging.

- It should be avoided making use of symmetry for the Eulerian and CEL analyses, and the whole problem should be modeled.

# Chapter 9

# Further Work

Submerged floating tunnels subjected to blast loading is a complex issue. This is perhaps reflected in the diversity of topics in this thesis which includes everything from blast load theory, DIC, statistical variation in concrete modeling, to CSD, CFD, and FSI analyses. Yet this covers merely a fraction of all the fields of research that are linked to the issue with SFTs and blast loads. Making the construction of an SFT possible with respect to blast loads, requires further work. In the following paragraphs, some topics are suggested that could be interesting to examine more closely.

Since the numerical simulations of the pipes in this thesis indicated that the CDP and K&C concrete models might not be suitable for blasts, it could be an idea to explore other concrete models. For instance, the Holmquist-Johnson-Cook (HJC) concrete model is widely used to model penetration in concrete and may therefore be interesting with regard to modeling contact charges. Additionally, for this thesis, the input for the CDP model was taken from Jankowiak and Lodygowski [79], but since there have also been others who have calibrated these material parameters, one could consider also evaluating these. Due to time limitations, reinforced concrete was not evaluated using the K&C model, but doing so should certainly be considered.

Because the simulated blast pressures were too low compared to the experimental tests, other approaches than JWL should perhaps be investigated. Granum and Løken, for example, used temperature differences to acquire the desired blast pressure in their master's thesis [98]. Another option could be to evaluate the parameters of the JWL EOS. A third option, which is perhaps the most relevant one, would be to perform the analyses using different software, e.g. LS-DYNA, IMPETUS, or possibly even better, Europlexus which is more commonly used for CEL analyses of blasts. If it for some reason is desirable to continue using ABAQUS for the Eulerian analyses, a parametric study should be conducted for when the reflecting boundaries are used.

The parametric studies for this thesis have only focused on a single parameter at a time. To fully understand the effect of the parameters they can be cross-examined. However, this is an extensive amount of work which has not been prioritized in this thesis.

Lastly, it should be mentioned, although it might be obvious, that the main goal for further work on the topic, should be to numerically simulate a full SFT cross-section.

However, before this is done, one must be certain that the concrete, the blast, and the two of them interacting, can be appropriately modeled. For this thesis, it was initially intended to use the results from the numerical study of the pipes, as a basis for numerical simulations of an SFT. An ABAQUS model was even prepared with a concrete which was scaled to have an appropriate strength, and a plausible charge size and placement was decided upon. However, since the numerical simulations of the pipes were rather unsuccessful, the SFT simulations were discarded for now.

# References

[1] L. Skarzynski, J. Kozicki, and J. Tejchman, "Application of DIC Technique to Concrete—Study on Objectivity of Measured Surface Displacements," *Experimental Mechanics*, vol. 53, no. 9, pp. 1545–1559, 2013.

[2] T. M. Fayyad and J. M. Lees, "Application of Digital Image Correlation to Reinforced Concrete Fracture," *Procedia Materials Science*, vol. 3, pp. 1585–1590, 2014.

[3] E. Fagerholt, T. Børvik, and O. S. Hopperstad, "Measuring discontinuous displacement fields in cracked specimens using digital image correlation with mesh adaptation and crack-path optimization," *Optics and Lasers in Engineering*, vol. 51, pp. 299–310, 2013.

[4] Y. Sümer and M. Aktas, "Defining parameters for concrete damage plasticity model," *Challenge Journal of Structural Mechanics*, vol. 1, no. 3, pp. 149–155, 2015.

[5] S. Michal and W. Andrzej, "Calibration of the CDP model parameters in Abaqus," Conference paper for the 2015 World Congress on Advances in Structural Engineering and Mechanics, Incheon, Korea, 2015.

[6] Y. Nikaido, Y. Mihara, S. Sawada, and Y. Takahashi, "Improvement and Enhancement of Concrete Damage Plasticity Model," Paper.

[7] S. V. Chaudhari and M. A. Chakrabarti, "Modeling of concrete for nonlinear analysis Using Finite Element Code ABAQUS," *International Journal of Computer Applications*, vol. 44, no. 7, pp. 14–18, 2015.

[8] V. Birtel and P. Mark, "Parameterised Finite Element Modelling of RC Beam Shear Failure ," Conference paper for 2006 ABAQUS Users' Conference, 2006.

[9] B. L. Whahalathrantri, D. P. Thambiratnam, T. H. T. Chan, and S. Fawzia, "A material model for flexural crack simulation in reinforced concrete elements using ABAQUS," Conference paper for Proceedings of the First International Conference on Engineering, Designing and Developing the Built Environment for Sustainable Wellbeing, 2011.

[10] W. Ren, L. H. Sneed, Y. Yang, and R. He, "Numerical Simulation of Prestressed Precast Concrete Bridge Deck Panels Using Damage Plasticity Model," *International Journal of Concrete Structures and Materials*, vol. 51, no. 1, pp. 45–54, 2015.

[11] M. P. Zappitellia, E. I. Villaa, J. Fernández-Sáezb, and C. Roccoa, "Cracking Development Prediction in Concrete Gravity Dams Using Concrete Damage Plasticity Model," *Mecánica Computacional*, vol. 33, pp. 909–921, 2014.

[12] Y. Tao and J. F. Chen, "Concrete Damage Plasticity Model for Modeling FRP-to-Concrete Bond Behavior," *Journal of Composites for Construction*, vol. 19, no. 1, 2015.

[13] Y. Kawamoto and J. Stepan, "Analytical Study of Reinforced Concrete Slab Subjected to Soft Missile Impact," Conference paper for the SMiRT23 Conference, Manchester, United Kingdom, 2015.

[14] O. Martin, "Comparison of different Constitutive Models for Concrete in ABAQUS/Explicit for Missile Impact Analyses," Technical report for European Commission, Joint Research Centre, Institute for Energy, 2010.

[15] L. J. Malvar, J. E. Crawford, J. W. Wesevich, and D. Simons, "A plasticity concrete material model for DYNA3D," *International Journal of Impact Engineering*, vol. 19, no. 9–10, pp. 847–873, 1997.

[16] N. Markovich, E. Kochavi, and G. Ben-Dor, "An improved calibration of the concrete damage model," *Finite Elements in Analysis and Design*, vol. 47, no. 11, pp. 1280–1290, 2011.

[17] R. M. Brannon and S. Leelavanichkul, "Survey of Four Damage Models for Concrete," Technical report for the United States Department of Energy by Sandia Corporation, 2009.

[18] Y. Wu and J. E. Crawford, "Numerical Modeling of Concrete Using a Partially Associative Plasticity Model," *Journal of Engineering Mechanics*, vol. 141, no. 12, 2015.

[19] M. Xu and K. Willie, "Calibration of K&C Concrete Model for UHPC in LS-DYNA," *Advanced Materials Research*, vol. 1081, pp. 254–259, 2014.

[20] A. Shukla, Y. D. S. Rajapakse, and M. E. Hynes, *Blast Mitigation: Experimental and Numerical Studies.* Springer Science & Business Media, 2013.

[21] X. Z. Kong, Q. Fang, Q. M. Li, H. Wu, and J. Crawford, "Modified K&C model for cratering and scabbing of concrete slab under projectile impact," *International Journal of Impact Engineering*, vol. 108, pp. 217–228, 2017.

[22] S. B. Kim, H. W. Kim, and Y. H. Yoo, "Penetration analysis of projectile with inclined concrete target," Conference paper for DYMAT 2015 - 11th International Conference on the Mechanical and Physical Behaviour of Materials under Dynamic Loading, 2015.

[23] C. Wu, J. Li, and Y. Su, *Development of Ultra-High Performance Concrete against Blasts: From Materials to Structures.* Woodhead Publishing, 2018.

[24] Y. Hor, S. Kzutaka, and T. Wee, "Numerical Assessment of Ultra-high Performance Concrete Material," Conference paper for 5th Asia Conference on Mechanical and Materials Engineering, 2017.

[25] X. Q. Li, J. F. Chen, and Y. Lu, "Meso-Scale Modelling of FRP-to-Concrete Bond Behaviour Using LSDYNA," Conference paper for CICE 2010 - The 5th International Conference on FRP Composites in Civil Engineering, Beijing, China, 2010.

[26] P. Grasl and M. Jirasek, "Meso-scale approach to modelling the fracture process zone of concrete subjected to uniaxial tension," *International Journal of Solids and Structures*, vol. 47, no. 7–8, pp. 957–968, 2010.

[27] X. Q. Zhou and H. Hao, "Mesoscale modelling of concrete tensile failure mechanism at high strain rates," *Computers & Structures*, vol. 86, no. 21–22, pp. 2013–2026, 2008.

[28] L. Wang and T. Ueda, "Mesoscale Modelling of the Chloride Diffusion in Cracks and Cracked Concrete," *Journal of Advanced Concrete Technology*, vol. 9, no. 3, pp. 241–249, 2011.

[29] Z. Xu, H. Hao, and H. N. Li, "Mesoscale modelling of fibre reinforced concrete material under compressive impact loading," *Construction and Building Materials*, vol. 26, no. 1, pp. 274–288, 2012.

[30] X. Q. Zhou and H. Hao, "Mesoscale modelling and analysis of damage and fragmentation of concrete slab under contact detonation," *International Journal of Impact Engineering*, vol. 36, no. 12, pp. 1315–1326, 2009.

[31] A. K. Tiwari, A. K. Tiwary, and A. Dhiman, "Analysis of Concrete Wall under Blast Loading," Conference paper for International Conference on Advances in Emerging Technology, 2016.

[32] G. C. Mays, J. G. Hetherington, and T. A. Rose, "Response to Blast Loading of Concrete Wall Panels with Openings," *Journal of Structural Engineering*, vol. 125, no. 12, pp. 1448–1450, 1999.

[33] T. Ngo, P. Mendis, and T. Krauthammer, "Behavior of Ultrahigh-Strength Prestressed Concrete Panels Subjected to Blast Loading," *Journal of Structural Engineering*, vol. 133, no. 11, pp. 1582–1590, 2007.

[34] T. S. Lok and J. R. Xiao, "Steel-Fibre Reinforced Concrete Panels Exposed to Air Blast Loading," *Proceedings of the Institution of Civil Engineers - Structures and Buildings*, vol. 134, no. 4, pp. 319–331, 1999.

[35] X. Lin, Y. X. Zhang, and P. J. Hazell, "Modelling the response of reinforced concrete panels under blast loading," *Materials & Design*, vol. 56, pp. 620–628, 2014.

[36] Z. S. Tabatabaei, J. S. Volz, J. Baird, B. P. Gliha, D. I, and Keener, "Experimental and numerical analyses of long carbon fiber reinforced concrete panels exposed to blast loading," *International Journal of Impact Engineering*, vol. 57, pp. 70–80, 2013.

[37] W. Wand, D. Zhang, fangyun Lu, S.-C. Wang, and F. Tang, "Experimental study on scaling the explosion resistance of a one-way square reinforced concrete slab under a close-in blast loading," *International Journal of Impact Engineering*, vol. 49, pp. 158–164, 2012.

[38] G. Kravchenko, E. Trufanova, D. Kostenko, and S. Tsurikov, "Analysis of blast load on a reinforced concrete column in the time domain," Conference paper for

International Scientific Conference Energy Management of Municipal Transportation Facilities and Transport EMMFT 2017, 2017.

[39] K. Xu and Y. Lu, "Numerical simulation study of spallation in reinforced concrete plates subjected to blast loading," *Computers & Structures*, vol. 84, no. 5–6, pp. 431–438, 2006.

[40] M. Foglar and M. Kovar, "Conclusions from experimental testing of blast resistance of FRC and RC bridge decks," *International Journal of Impact Engineering*, vol. 59, pp. 18–28, 2013.

[41] R. Tiwari, T. Chakraborty, and V. Matsagar, "Dynamic Analysis of Tunnel in Soil Subjected to Internal Blast Loading," *Geotechnical and Geological Engineering*, vol. 35, no. 4, pp. 1491–1512, 2017.

[42] Martin Kristoffersen, "Experimental data on plain concrete tubes loaded with C-4 charges."

[43] M. Kristoffersen, K. O. Hauge, G. Valsamos, and T. Børvik, "Blast loading of concrete pipes using spherical centrically placed C-4 charges,"

[44] M. Kristoffersen, K. Osnes, S. R. Haug, V. Aune, and T. Børvik, "Shock tube testing and numerical simulations of concrete slabs," Conference paper for the 1st International Conference on Impact Loading of Structures and Materials, Turin, Italy, May 2016.

[45] M. Kristoffersen, J. E. Pettersen, V. Aune, and T. Børvik, "Experimental and numerical study on blast loading of normal strength concrete slabs," 2017.

[46] M. Kristoffersen, A. Minoretti, and T. Børvik, "Submerged floating tunnels subjected to internal blast loading," Conference paper for Proceedings of 7th Transport Research Arena TRA 2018, Vienna, Austria, April 2018.

[47] S. R. Haug and K. Osnes, "Submerged floating tunnels subjected to internal blast loading," Master's thesis, Norwegian University of Science and Technology, Trondheim, 2015.

[48] E. Hillestad and J. E. Pettersen, "Experimental and Numerical Studies of Plain and Reinforced Concrete Plates Subjected to Blast Loading," Master's thesis, Norwegian University of Science and Technology, Trondheim, 2016.

[49] Norwegian Public Roads Administration, "Project Overview: Coastal Highway Route E39." `https://www.vegvesen.no/_attachment/300340/binary/527486`. [Accessed: 13.01.2018].

[50] Norwegian Public Roads Administration, "Ferjefri E39. (Norwegian) [Ferry-Free E39]." `https://www.vegvesen.no/vegprosjekter/ferjefriE39`. [Accessed: 21.01.2018].

[51] Encyclopædia Britannica, "Akashi Strait Bridge." `https://www.britannica.com/topic/Akashi-Strait-Bridge`. [Accessed: 20.01.2018].

[52] American Infrastructure, "The Longest Floating Bridge: SR 520." `https://americaninfrastructuremag.com/longest-floating-bridge-sr-520/`. [Accessed: 20.01.2018].

[53] Norwegian Public Roads Administration, "Ferjefri E39: Hovedrapport. (Norwegian) [Ferry-Free E39: Main Report]." `https://www.vegvesen.no/_attachment/415285/binary/711216`, 2012. [Accessed: 20.01.2018].

[54] Encyclopædia Britannica, "Archimedes' principle." `https://www.britannica.com/science/Archimedes-principle`, December 2017. [Accessed: 20.01.2018].

[55] A. B. Kawade and S. P. Meghe, "Submerged Floating Tunnel." `http://www.idc-online.com/downloads/Submerged_Floating_Tunnel.pdf`. [Accessed: 20.01.2018].

[56] B. Jakobsen, "Design of the Submerged Floating Tunnel operating under various conditions," *Procedia Engineering*, vol. 4, pp. 71–79, 2010.

[57] M. G. Garathun for *Teknisk Ukeblad*, "Ubåtteknologi skal bidra til å finne optimal bruløsning på ferjefri E39. (Norwegian) [Submarine Technology is to Contribute in Finding the Optimal Bridge Solution on Ferry-Free E39]." `https://www.tu.no/artikler/ferjefri-e39-ubatteknologi-skal-bidra-til-a-finne-optimal-brulosning/358715`, October 2016. [Accessed: 20.01.2018].

[58] P. Nikolaisen for *Teknisk Ukeblad*, "Superbru over Norges dypeste fjord skal tåle en skipskollisjon. (Norwegian) [Super-Bridge over Norway's Deepest Fjord Shall Withstand a Ship Collision]." `https://www.tu.no/artikler/superbru-over-norges-dypeste-fjord-skal-tale-en-skipskollisjon/231565`, April 2014. [Accessed: 21.01.2018].

[59] H. Østlid, "When is SFT competitive?," *Procedia Engineering*, vol. 4, pp. 3–11, 2010.

[60] Norwegian Public Roads Administration, "Mulighetsstudie - Kryssing av Sognefjorden: Oppsummering etter idéfasen. (Norwegian) [A Feasibility Study - Crossing of the Sognefjord: Summary of the Thinking Phase]." `https://www.vegvesen.no/_attachment/207480/binary/399909`, March 2011. [Accessed: 21.01.2018].

[61] L. Winkless for *Forbes*, "Could Norwegian Engineers Really Build A Floating Tunnel In A Fjord?." `https://www.forbes.com/sites/lauriewinkless/2016/07/22/could-norwegian-engineers-really-build-a-floating-tunnel-in-a-fjord/#4528cba126bf`, July 2016. [Accessed: 21.01.2018].

[62] F. Perotti, G. Barbella, and M. D. Pilato, "The dynamic behaviour of Archimede's Bridges: Numerical simulation and design implications," *Procedia Engineering*, vol. 4, pp. 91–98, 2010.

[63] M. G. Garathun for *Teknisk Ukeblad*, "Verdens første rørbru kan stå ferdig i 2025. (Norwegian) [The World's First SFT May Be Finished in 2025]." `https://www.tu.no/artikler/verdens-forste-rorbru-kan-sta-ferdig-i-2025/275689`, September 2015. [Accessed: 21.01.2018].

[64] Norwegian Public Roads Administration, "Håndbok 400 - Bruprosjektering. (Norwegian) [Handbook 400 - Design of Bridges]." `https://www.vegvesen.no/_attachment/865860/binary/1030718?fast_title=H%C3%A5ndbok+N400+Bruprosjektering.pdf`, 2015. [Accessed: 23.01.2018].

[65] R. Lunnis and J. Baber, *Immersed Tunnels.* Boca Raton, Florida US: CRC Press, 2013.

[66] W. D. Callister, *Materials Science and Engineering - An Introduction.* John Wiley & Sons, Inc., 7th ed., 2007.

[67] University of Memphis, "Lecture notes in CIVL 1101 - Civil Engineering Measurements: Properties of Concrete." `http://www.ce.memphis.edu/1101/notes/concrete/section_3_properties.html`.

[68] National Concrete Pavement Technology Center, "Development of Performance Properties of Ternary Mixtures and Concrete Pavement Mixture Design and Analysis (MDA): Effect of Paste Quality on Fresh and Hardened Properties of Ternary Mixtures ," , Iowa State University, Institute for Transportation, June 2012.

[69] M. M. Islam, M. A. Chowdhury, A. Z. Mustaiz, M. K. Uddin, P. Mondal, and A. Siddique, "Critical Investigation of the Finite Element Models of Steel Fiber Reinforced Concrete (SFRV): Evaluation of the Governing Parameters to Predict the Flexural Capabilities," Conference paper for the 2nd International Conference on Civil Engineering for Sustainable Development, February 2014.

[70] H. C. Fu, M. A. Erki, and M. Seckin, "Review of Effect of Loading Rate on Concrete in Compression," *Journal of Structural Engineering*, vol. 117, no. 12, pp. 3645–3659, 1991.

[71] J. Weiss, "Stress-Strain Behaviour of Concrete." `http://www.theconcreteportal.com/cons_rel.html`. [Accessed: 22.05.2018].

[72] "Eurocode 2: Design of concrete structures - Part 1-1: General rules and rules for buildings," Eurocode, Standard Norge, December 2004.

[73] T. L. Anderson, *Fracture Mechanics: Fundamentals and Applications.* Boca Raton, Florida, US: CRC Press, 3rd ed., 2005.

[74] "ABAQUS 3DEXPERIENCE User Assistance R2017x," , Dassault Systèmes.

[75] T. Krauthammer, *Modern Protective Structures.* Boca Raton, Florida, US: CRC Press, Taylor & Francis Group, 2008.

[76] T. Børvik, O. S. Hopperstad, and M. Langseth, "Lecture Notes in TKT4128 Impact Mechanics: An Introduction to Penetration and Perforation Mechanics," September 2017.

[77] J. Lubliner, S. J. Oliver, and E. Oñate, "A Plastic-Damage Model for Concrete," *International Journal of Solids and Structures*, vol. 25, no. 3, pp. 229–326, 1989.

[78] J. Lee and G. L. Fenves, "Plastic-Damage Model for Cyclic Loading of Concrete Structures," *Journal of Engineering Mechanics*, vol. 124, no. 8, pp. 892–900, 1998.

[79] T. Jankowiak and T. Lodygowski, "Identification of parameters of concrete damage plasticity constitutive model," *Foundations of civil and environmental engineering*, vol. 6, no. 1, pp. 53–69, 2005.

[80] "LS-DYNA Keyword User's Manual Volume II: Material Models (revision: 5442)," , Livermore Software Technology Corporation, Livermore, California, May 2014.

[81] V. Aune, T. Børvik, and M. Langseth, "Lecture Notes in TKT4128 Impact Mechanics: An Introduction to Blast Mechanics," November 2016.

[82] UN SaferGuard, "IATG 01.80:2015[E]. International Ammunition Technical Guideline, Formulae for ammunition management," IATG, February 2015.

[83] "Risk Assessment: A How-To Guide to Mitigate Potential Terrorist Attacks Against Buildings," FEMA 452, Federal Emergency Management Agency, January 2005.

[84] P. S. Bulson, *Explosive Loading of Engineering Structures.* London, UK: E & FN Spon, an imprint of Chapman & Hall, 1st ed., 1997.

[85] Military Story, "Nuclear Detonations in Urban and Suburdban Areas." `http://www.militarystory.org/nuclear-detonations-in-urban-and-suburban-areas/`, 2017. [Accessed: 07.02.2018].

[86] Department of Defense, "Ammunition and Explosive Safety Standards, Directive 6055.9-STD," August 1997.

[87] L. Albright, *Albright's Chemical Engineering Handbook.* Boca Raton, Florida, US: CRC Press, Taylor & Francis Group, 2008.

[88] Accident Investigation Board Norway, "Report on fire in tank trailer in the Skatestraum tunnel in Sogn og Fjordane county 15 July 2015," , November 2016.

[89] "Eurocode 1: Actions on structures - Part 1-7: General actions - Accidental actions," Eurocode, Standard Norge, Oslo, Norway, May 2008.

[90] B. M. Dobratz and P. C. Crawford, "LLNL Explosives Handbook: Properties of Chemical Explosives and Explosive Simulants," Handbook, Lawrence Livermore National Laboratory, University of California, Livermore, California, January 1985.

[91] W. E. Baker, P. A. Cox, P. S. Westine, J. J. Kulesz, and R. A. Strehlow, *Explosion Hazards and Evaluation.* Amsterdam, Netherlands: Elsevier Science, 1983.

[92] A. Spicher, O. Michel, and J.-L. Giavitto, "Interaction-Based Modeling of Morphogenesis in MGS," 2001.

[93] O. S. Hopperstad and T. Børvik, "Lecture Notes in TKT4128 Impact Mechanics: Modelling of plasticity and failure with explicit finite element methods," 2017.

[94] K. M. Mathisen, "Lecture Notes for lecture 7 in TKT4197 Nonlinear Finite Element Analysis: Solution of the Dynamic Equilibrium Equations by Explicit Direct Integration," 2017.

[95] B. G. Rabbat and H. G. Russell, "Friction Coefficient of Steel on Concrete or Grout," *Journal of Structural Engineering*, vol. 111, no. 3, 1985.

[96] ABAQUS, "Lecture 1: Overview of ABAQUS/Explicit." `http://imechanica.org/files/0-overview%20Explicit.pdf`, 2005. [Accessed: 04.03.2018].

[97] LS-DYNA Support, "Hourglass." `http://www.dynasupport.com/howtos/element/hourglass`. [Accessed: 07.03.2018].

[98] H. M. Granum and L. M. Løken, "Experimental and Numerical Study on Perforated Steel Plates Subjected to Blast Loading," Master's thesis, Norwegian University of Science and Technology, Trondheim, 2016.

# Appendix A: Pressure Readings from Experimental Testing of Concrete Pipes Subjected to Blast Loading

The pressure-time curves presented below are from the experimental testing of concrete pipes subjected to blast loading, see Chapter 6. Within every subsection the experimental tests are sorted by C4 charge size.

## A.1 Smaller Pipes
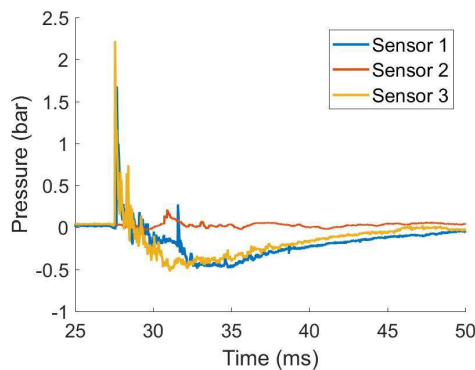
### A.1.1 Centric Charge

*10 g*



**Figure A1:** Pressure-time curves for a smaller plain concrete pipe with a centrically placed 10 g charge of C4 (pipe III).

**(a)** Sensors 1, 2, and 3     **(b)** Sensors 4, 5, and 6     **(c)** Sensors 7 and 8
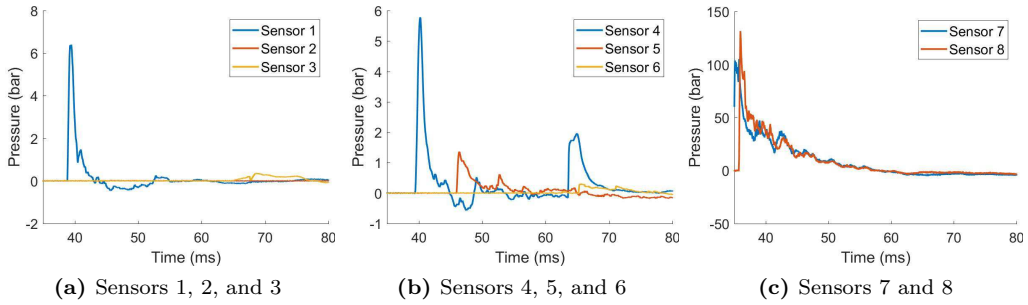
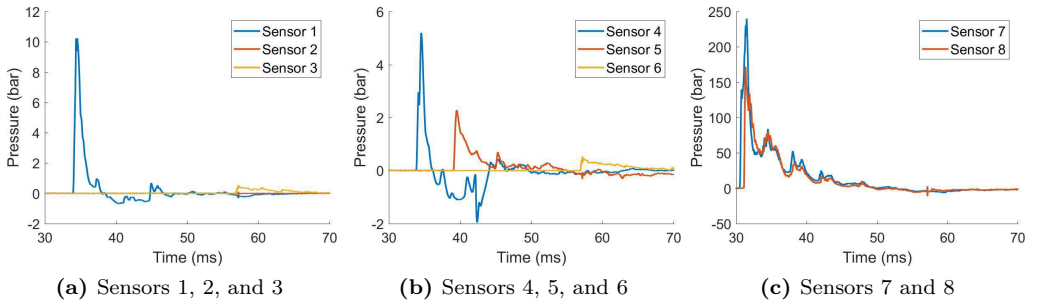**Figure A2:** Pressure-time curves for a smaller plain concrete pipe with a centrically placed 10 g charge of C4 (pipe XVIII).

### 12 g



**(a)** Sensors 1, 2, and 3     **(b)** Sensors 4, 5, and 6     **(c)** Sensors 7 and 8
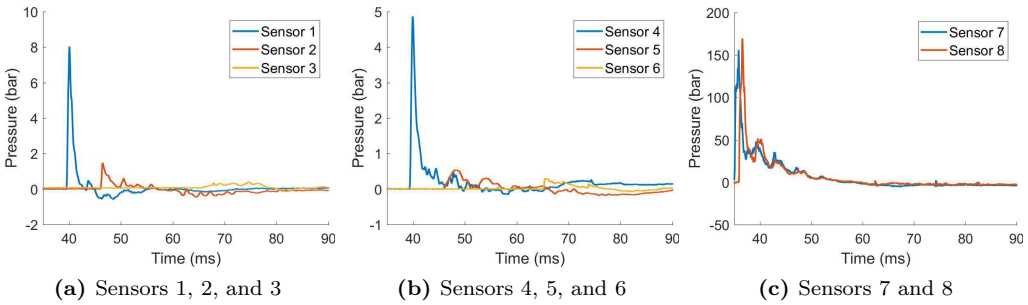
**Figure A3:** Pressure-time curves for a smaller plain concrete pipe with a centrically placed 12 g charge of C4 (pipe XIX).

### 12.5 g
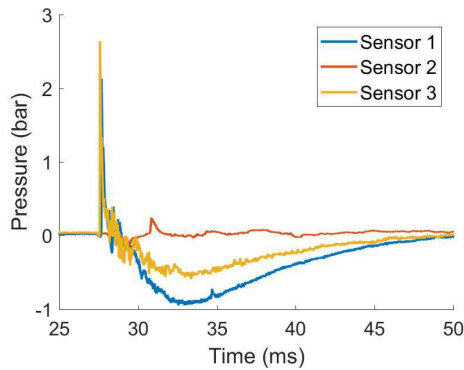


**Figure A4:** Pressure-time curves for a smaller plain concrete pipe with a centrically placed 12.5 g charge of C4 (pipe IV).

*13 g*
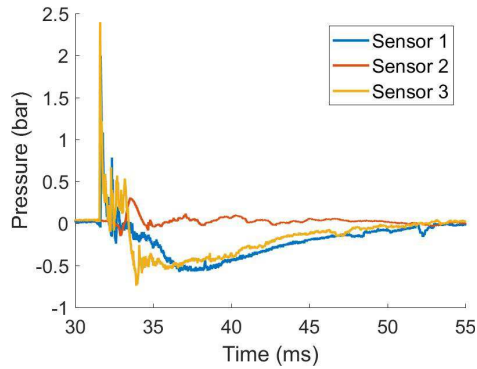


**Figure A5:** Pressure-time curves for a smaller plain concrete pipe with a centrically placed 13 g charge of C4 (pipe XIV).

*13.5 g*
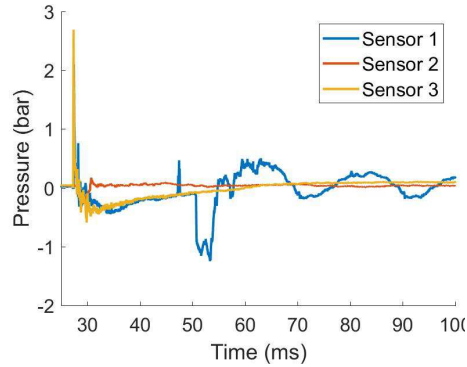


**Figure A6:** Pressure-time curves for a smaller plain concrete pipe with a centrically placed 13.5 g charge of C4 (pipe VI).

*14 g*
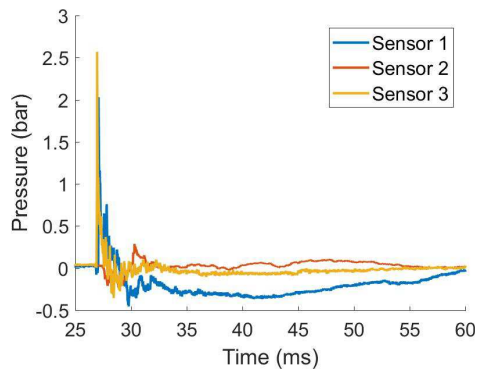


**Figure A7:** Pressure-time curves for a smaller plain concrete pipe with a centrically placed 14 g charge of C4 (pipe V).

**(a)** Sensors 1, 2, and 3  **(b)** Sensors 4, 5, and 6  **(c)** Sensors 7 and 8

**Figure A8:** Pressure-time curves for a smaller plain concrete pipe with a centrically placed 14 g charge of C4 (pipe XX).

*15 g*
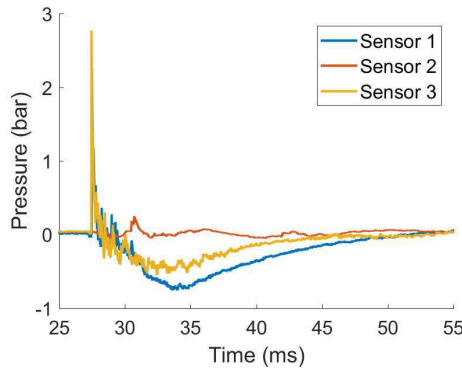


**Figure A9:** Pressure-time curves for a smaller plain concrete pipe with a centrically placed 15 g charge of C4 (pipe II).

*16 g*



**(a)** Sensors 1, 2, and 3  **(b)** Sensors 4, 5, and 6  **(c)** Sensors 7 and 8
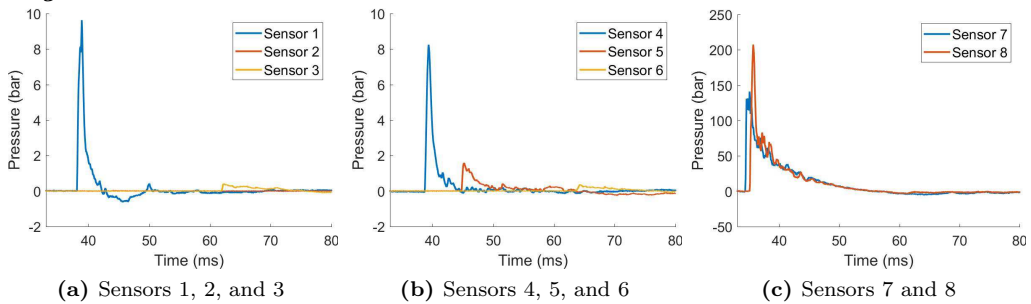
**Figure A10:** Pressure-time curves for a smaller plain concrete pipe with a centrically placed 16 g charge of C4 (pipe XXI).

### 18 g



**(a)** Sensors 1, 2, and 3     **(b)** Sensors 4, 5, and 6     **(c)** Sensors 7 and 8
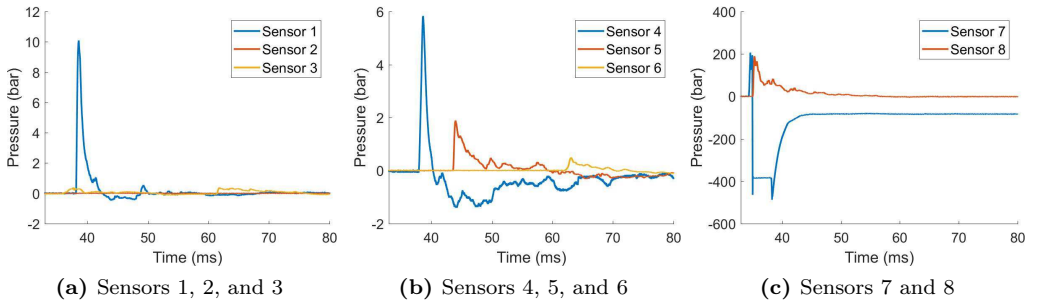
**Figure A11:** Pressure-time curves for a smaller plain concrete pipe with a centrically placed 18 g charge of C4 (pipe XXII).

### 20 g



**(a)** Sensors 1, 2, and 3     **(b)** Sensors 4, 5, and 6     **(c)** Sensors 7 and 8

**Figure A12:** Pressure-time curves for a smaller plain concrete pipe with a centrically placed 20 g charge of C4 (pipe XVII).

### 25 g
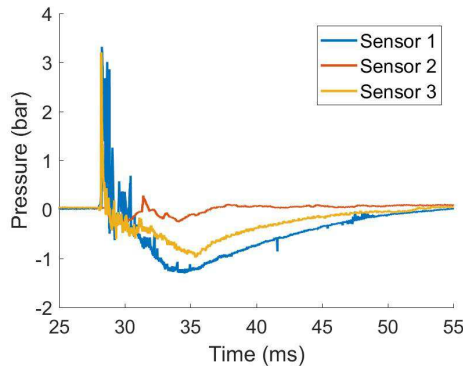


**Figure A13:** Pressure-time curves for a smaller plain concrete pipe with a centrically placed 25 g charge of C4 (pipe I).
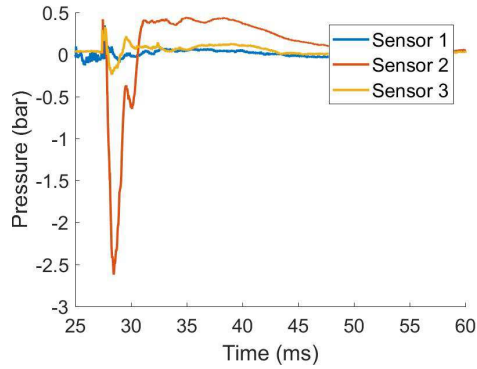
## A.1.2  Internal Contact Charge

*5 g*
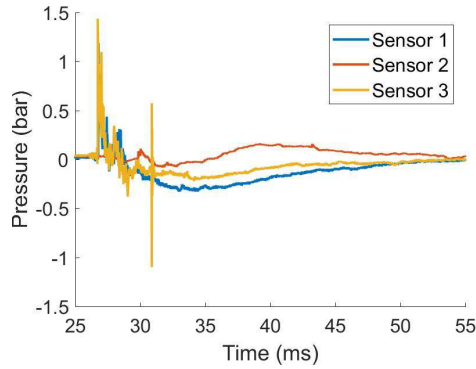


**Figure A14:** Pressure-time curves for a smaller plain concrete pipe with an internal contact charge of 5 g C4 (pipe VIII).
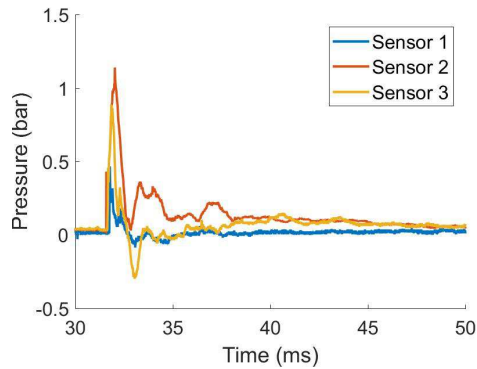
*6 g*
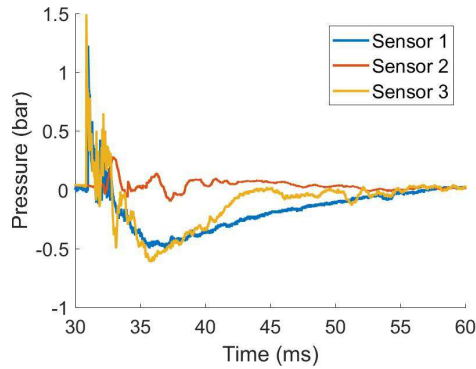


**Figure A15:** Pressure-time curves for a smaller plain concrete pipe with an internal contact charge of 6 g C4 (pipe XV).

*7.5 g*



**(a)** Pipe IX

**(b)** Pipe X
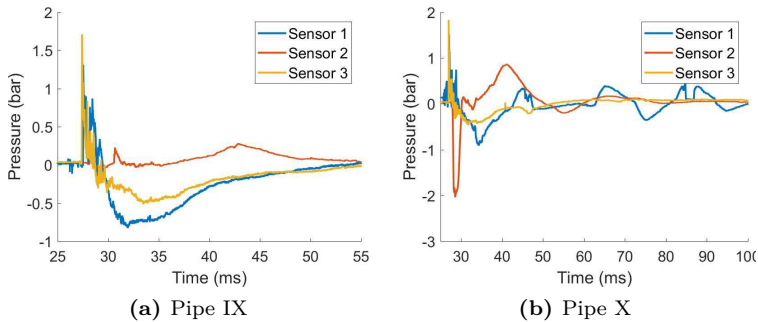
**Figure A16:** Pressure-time curves for smaller plain concrete pipes with internal contact charges of 7.5 g C4.

***10 g***
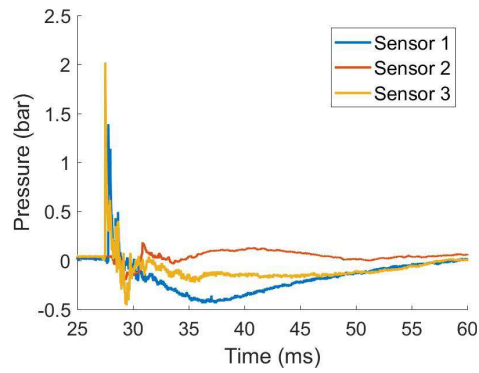


**Figure A17:** Pressure-time curves for a smaller plain concrete pipe with an internal contact charge of 10 g C4 (pipe VII).

## A.1.3    External Contact Charge

*10 g*



**Figure A18:** Pressure-time curves for a smaller plain concrete pipe with an external contact charge of 10 g C4 (pipe XI).

*12.5 g*



**Figure A19:** Pressure-time curves for a smaller plain concrete pipe with an external contact charge of 12.5 g C4 (pipe XVI).
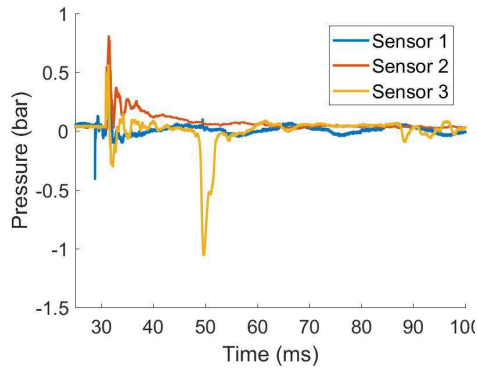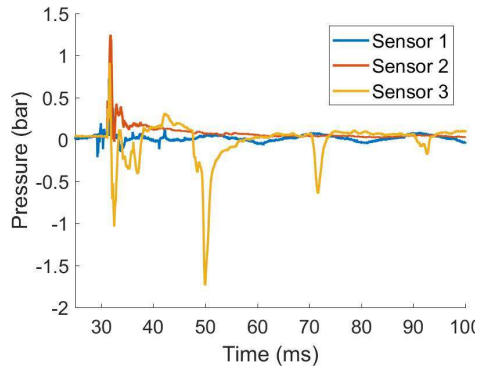
**15 g**



**Figure A20:** Pressure-time curves for a smaller plain concrete pipe with an external contact charge of 15 g C4 (pipe XII).

**20 g**



**Figure A21:** Pressure-time curves for a smaller plain concrete pipe with an external contact charge of 20 g C4 (pipe XIII).
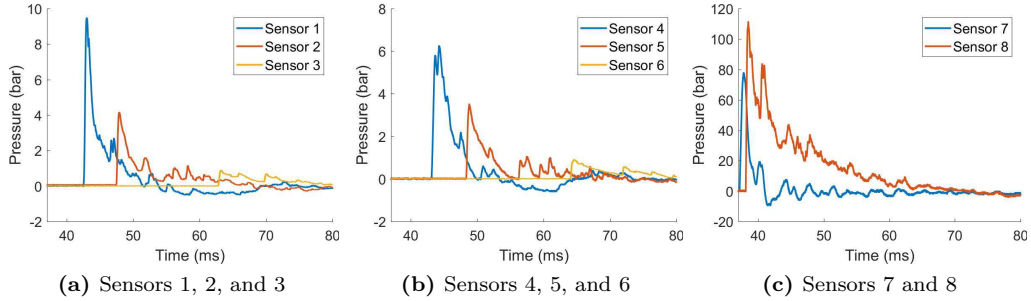
## A.2    Larger Pipes

### A.2.1    Plain Concrete

*50 g*



**(a)** Sensors 1, 2, and 3     **(b)** Sensors 4, 5, and 6     **(c)** Sensors 7 and 8

**Figure A22:** Pressure-time curves for a larger plain concrete pipe with a centrically placed 50 g charge of C4 (pipe VI).
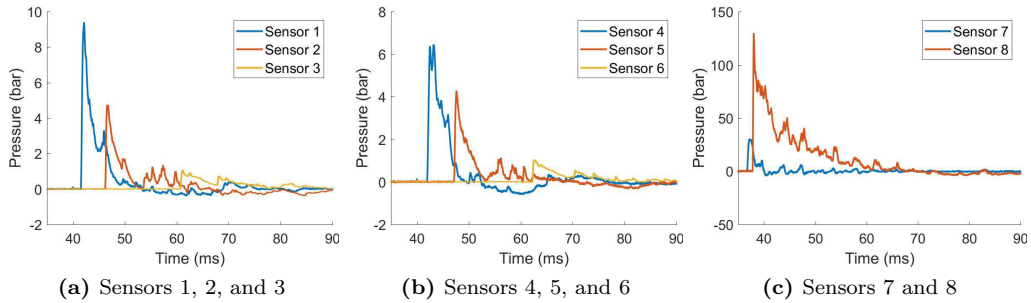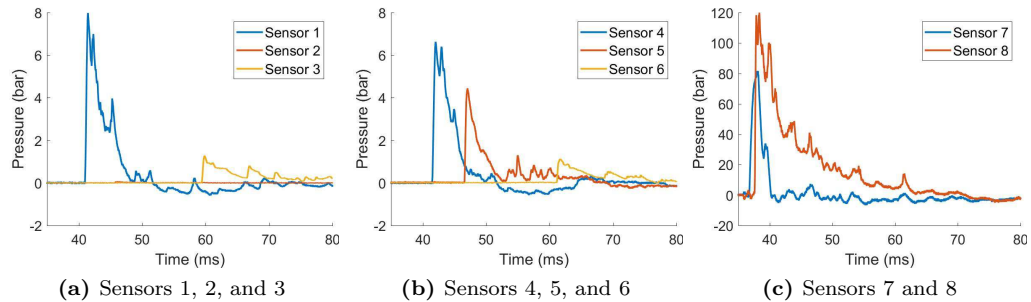
*65 g*



**(a)** Sensors 1, 2, and 3     **(b)** Sensors 4, 5, and 6     **(c)** Sensors 7 and 8

**Figure A23:** Pressure-time curves for a larger plain concrete pipe with a centrically placed 65 g charge of C4 (pipe X).

*75 g*



**(a)** Sensors 1, 2, and 3     **(b)** Sensors 4, 5, and 6     **(c)** Sensors 7 and 8

**Figure A24:** Pressure-time curves for a larger plain concrete pipe with a centrically placed 75 g charge of C4 (pipe VII).

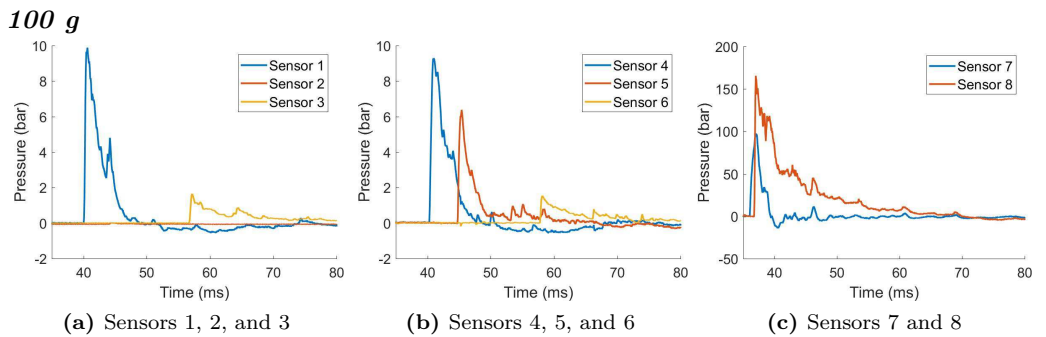**(a)** Sensors 1, 2, and 3 **(b)** Sensors 4, 5, and 6 **(c)** Sensors 7 and 8
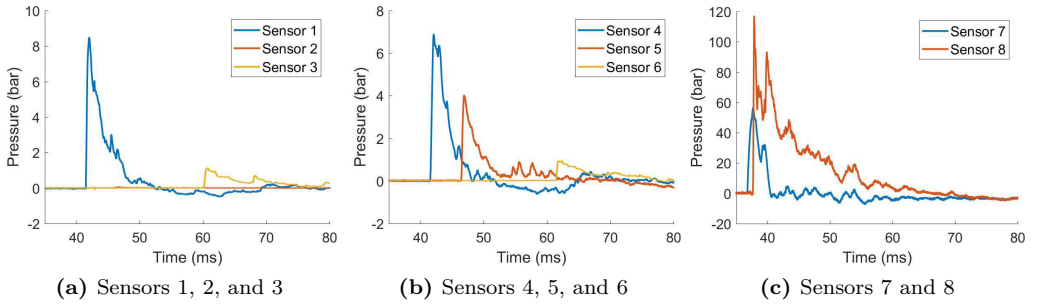
**Figure A25:** Pressure-time curves for a larger plain concrete pipe with a centrically placed 75 g charge of C4 (pipe VIII).

*100 g*



**(a)** Sensors 1, 2, and 3 **(b)** Sensors 4, 5, and 6 **(c)** Sensors 7 and 8

**Figure A26:** Pressure-time curves for a larger plain concrete pipe with a centrically placed 100 g charge of C4 (pipe V).

*150 g*



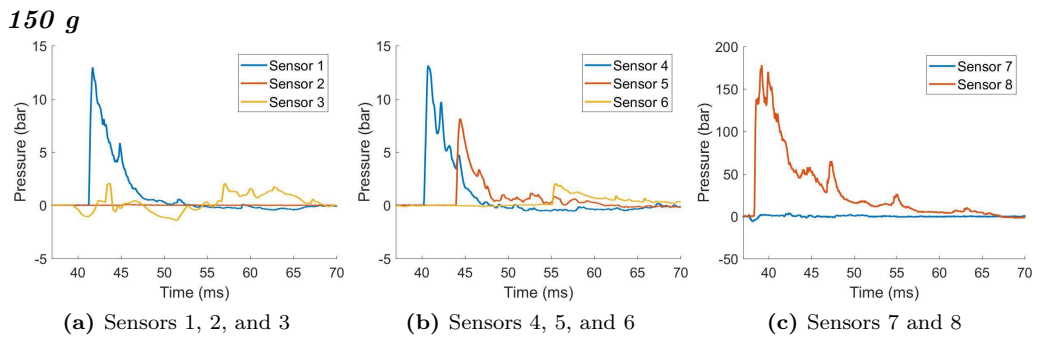**(a)** Sensors 1, 2, and 3 **(b)** Sensors 4, 5, and 6 **(c)** Sensors 7 and 8

**Figure A27:** Pressure-time curves for a larger plain concrete pipe with a centrically placed 150 g charge of C4 (pipe I).
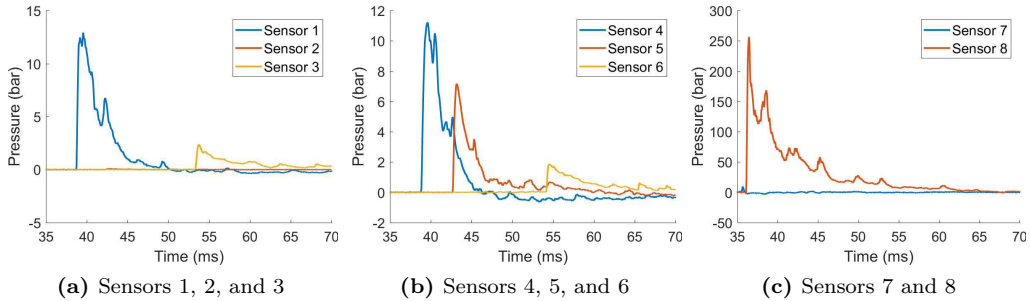
## A.2.2    Reinforced Concrete

*150 g*



**(a)** Sensors 1, 2, and 3



**(b)** Sensors 4, 5, and 6



**(c)** Sensors 7 and 8

**Figure A28:** Pressure-time curves for a larger reinforced concrete pipe with a centrically placed 150 g charge of C4 (pipe II).

*200 g*



**(a)** Sensors 1, 2, and 3
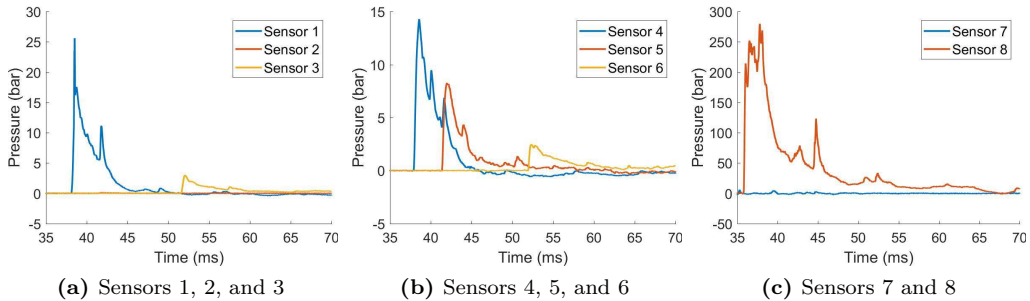


**(b)** Sensors 4, 5, and 6



**(c)** Sensors 7 and 8

**Figure A29:** Pressure-time curves for a larger reinforced concrete pipe with a centrically placed 200 g charge of C4 (pipe III).
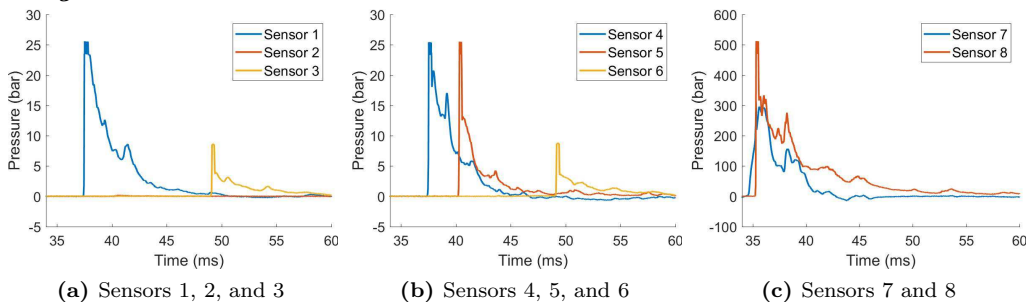
*300 g*



**(a)** Sensors 1, 2, and 3



**(b)** Sensors 4, 5, and 6



**(c)** Sensors 7 and 8

**Figure A30:** Pressure-time curves for a larger reinforced concrete pipe with a centrically placed 300 g charge of C4 (pipe IV).

## 400 g



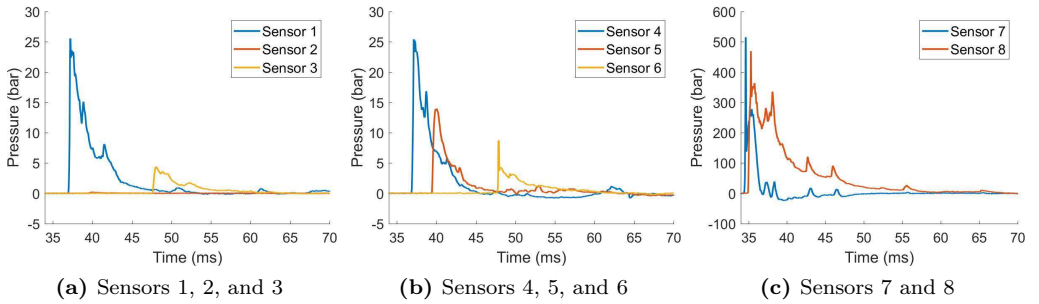**(a)** Sensors 1, 2, and 3     **(b)** Sensors 4, 5, and 6     **(c)** Sensors 7 and 8

**Figure A31:** Pressure-time curves for a larger reinforced concrete pipe with a centrically placed 400 g charge of C4 (pipe IX).

For pipe XXII which also was a larger reinforced concrete pipe with a centrically placed 500 g charge of C4, the pressure-time curves are missing.
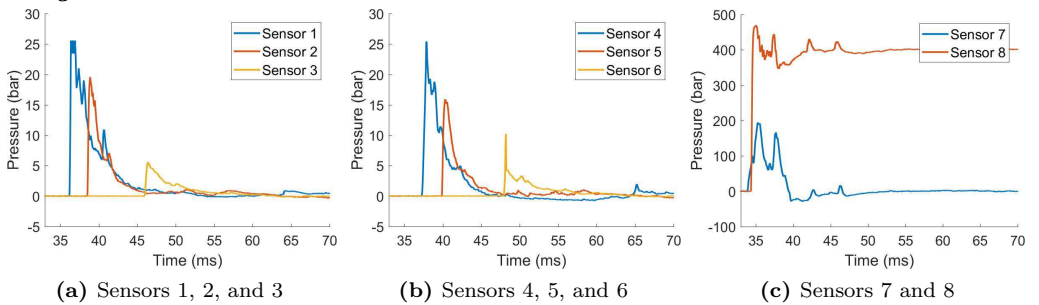
## 500 g



**(a)** Sensors 1, 2, and 3     **(b)** Sensors 4, 5, and 6     **(c)** Sensors 7 and 8

**Figure A32:** Pressure-time curves for a larger reinforced concrete pipe with a centrically placed 500 g charge of C4 (pipe XI).